

Exploring Nature's  
Fingerprints with Isotopic  
Distributions

Thesis by  
Timothy Csernica

In Partial Fulfillment of the Requirements for  
the Degree of  
Doctor of Philosophy

The Caltech logo is displayed in a bold, orange, sans-serif font. The word "Caltech" is centered within a light orange rectangular background.

CALIFORNIA INSTITUTE OF TECHNOLOGY  
Pasadena, California

2024  
(Defended May 22, 2024)

© 2024

Timothy Csernica  
ORCID: 0000-0002-5273-0721

## ACKNOWLEDGEMENTS

*Sine qua non*, Bushra

I am greatly indebted to so many people for their help and support with this thesis. First, I'd like to thank John Eiler, my Ph.D. advisor. John, thank you for pushing me intellectually and personally and for granting me the space to pursue my own interests. I'm especially grateful for your flexibility and understanding as I've worked and lived in five different states while completing my degree. I'm also grateful to the other members of my committee. Geoff Blake both possesses a deep knowledge of a dozen different fields and is an enthusiastic and supportive mentor. Brian Stoltz has encouraged and enabled the interdisciplinary science that makes up the core of my thesis. And Rudy Marcus' extensive knowledge of chemical physics and generosity with his time have been an invaluable aid. I'd also like to thank the other mentors I've had who have nurtured my scientific career: Steve Sibener, who gave me space to explore as an undergraduate, and Tamar Segal-Peretz, who helped me develop and generalize my scientific approach. Likewise, Jonathan Raybin's guidance was crucial to my development as a scientist. I constantly remember advice from each of you. A special thanks to Katsuyuki Wakabayashi, for giving me my first opportunity to work in a research environment.

My day-to-day experiences have been enriched by my colleagues and friends in both GPS and CCE. To Elle Chimiak—you were my first exposure to stable isotope geochemistry, and your enthusiasm and skill continue to inspire me. To Renée Wang and Sarah Zeichner—I'm grateful for both your great skill as scientists and your efforts towards building a stronger lab community, especially through periods of remote work. To Gabriella Weiss and Elliott Mueller—I can't imagine pushing through the early days of ESI-Orbitrap development without your collaboration, and I'm happy to have gone through that experience with you both. To Alexander Meshoulam, Hannah Dion-Kirschner, and Hao Xie—each of you have been generous with your time and energy while helping me with my projects, and I'm grateful to have had the chance to work with you. To Guannan Dong—I

always find our conversations enlightening and enriching. To Noam Lotem—I've loved watching you explore your own Orbitrap measurements, and I can't wait to see what you discover. To Nithya Thiagarajan—I'm grateful for having had the chance to watch and learn from you. To Jennah Colburn—your visualization work was a highlight of my time here, as I could see these ideas coming to life. To my other colleagues in the Eiler lab, especially Lubna Shawar, Xinchu Wang, Josh Anadu, Evie Harel, Anastasia Yanchilina, and Surjyendu Bhattacharjee—it has been a pleasure to work with every one of you. I'm also glad to know Amy Hofmann, for both her scientific rigor and love of the universe. And I'm thankful for Simon Andren, whose enthusiasm and knowledge promise a bright future for 'isotomics.'

I'd also like to thank the scientists and collaborators I've had the privilege of working with over the past several years. I've had great experiences working with the Caltech Proteome Exploration Lab, first with Spiros Garbis and Annie Moradian, who helped me on my first adventure with ESI-Orbitrap, and later with Ting-Yu Wang and Tsui-Fen Chou, who have continued to build a robust and stimulating collaboration. Nils Kuhlbusch, Andreas Hilker, and the rest of the Orbitrap folks at Bremen are rigorous and thoughtful scientists, and their work has been extremely valuable to my understanding of the instrument; I always look forward to our conversations. Nami Kitchen, Nathan Dalleska, Scott Virgil, and Fenfang Wu, have been crucial to various instrument troubleshooting sessions, and my work would not have been possible without their aid. I'm grateful for the opportunity to work with Jim Moran and Carlos Fraga, whose experience in chemical forensics were crucial to the arguments in Chapter V. Finally, Alex Sessions and Kate Freeman have both been supportive and insightful mentors.

I'd next like to thank the administrative staff who have helped run the university—nothing gets done without their efforts. I'm especially grateful for Kacey Gibson, who has managed the logistics for equipment and reagent orders as well as conference travel. I'd also like to thank Alison Ross, Julie Lee, Jen Shechet, Julia Zuckerman, and Ruth Martinez, who have each assisted me time and time again.

Life doesn't begin and end at the lab, and during my time here, there have been many friends and supporters who made my time in Pasadena enjoyable. First, to my gaming groups, especially Kevin, Zach, Neil, and John, as well as Lance, Jose, Alex, Brandon, and Carolyn; I look forward to every one of our nights together and hope for many more. Among the Caltech Chemistry group, I'd like to thank Skyler for her organizational work, as well as Brian, Jake, Zak, Wendy, Kiki, Sam, Sean, and many others I've had the pleasure of spending time with. Then, to my other friends at Caltech: Jorge and Hayley, for hosting me more times than I can count; Maria, for her warmth and honesty; Stephanie, Elizabeth, Joanie, Joaquin, Alessandra, Lauren, Daniel, and Nick, for helping me find community here; Trevor and Caroline, for every one of our discussions; and May, for exploring Los Angeles with me.

I never would have started at Caltech without many friends I've made along the way. Bronson, Nate, and Tom helped me start on this path long ago, through our conversations about science, economics, and society, and I look forward to a lifetime of their company. Likewise, Liza is one of my oldest friends and I greatly enjoy our time together. Ellie has encouraged me to go new places and experience new things, and I am a better person for her friendship. Olivia's spontaneity and love of adventure have added so much to my life. Lexie has been a constant source of encouragement and guidance, and I am grateful for her support. My thanks to Ian, for his creativity and dedication, and to Sydney, Will, and Kristy for all the good times together. Nicholas is a good spades partner and a better wedding guest. I'm also thankful for Samuel, Sara, Amy, and Rebecca, for our conversations. Finally, I'd like to thank Marjan, Priya, Sakshi, Anagha, Jessica, and Shira, for welcoming me into their lives; I look forward to knowing all of them for a very long time.

A Ph.D. degree is decades in the making, and I am thankful to the dozens (or hundreds?) of teachers who have guided me over the years. I especially want to thank Angela Gockley, my first chemistry teacher, and Michael Creeger, the first to encourage the kind of independence that I'd experience in graduate school. I'd also like to thank Jeremy Lauver, Jonathan Clark, and Jennifer Boyer-Switala, for providing a rich environment for

intellectual exploration. My time at the University of Chicago was stimulating and rewarding, in part because of the excellent mentors and faculty members there. I especially want to thank David Egan, Kyle Gardner, John Woods, and Stephen Kent; I remember every one of your classes, and I am grateful for having had the opportunity to study with you.

Finally, I'd like to thank my family. My parents have been a constant source of support and gave me the time and resources to pursue whatever I desired. I'm eternally grateful for their love. I can't remember a time without my godparents, Luigi and Ellen, and I'm thankful for all of our memories. Finally, I'd like to thank Peter, Kelly, Laura, and Ean, for spending a lifetime with me. I love you all.

## ABSTRACT

This thesis examines the measurement and interpretation of isotopic distributions and the application of these techniques to forensic questions. Stable isotope abundances are a powerful tool for examining a compound's history. However, their use is complicated by the fact that 1) isotope substitutions can occur at many positions of a molecule, resulting in a combinatorial increase in possible combinations of isotopes (or isotopologues) with molecule size, and 2) it is difficult to experimentally distinguish between isotopologues, so observational data averages over many isotopologues with distinct properties and histories. We here develop experimental and theoretical strategies to address these questions via observations of the isotopic distributions of small organic compounds obtained by Orbitrap mass spectrometry. In Chapter II, we develop mathematical procedures for manipulating and tracking isotopologues through various experimental designs, allowing us to make precise statements about how observable quantities are affected by underlying physical and chemical processes. Chapters III and IV explore corresponding experimental methods: Chapter III presents a sample introduction technique for the long duration observations required to measure rare, multiply substituted isotopologues, while Chapter IV applies these to observe 146 isotopic properties of methionine, a model analyte. We then explore the use of these Orbitrap methods to applied science problems. In Chapter V, we characterize the  $^{13}\text{C}$  and  $^2\text{H}$  enrichment of methylphosphonic acid, a breakdown product of sarin precursors, and examine the signatures of its synthesis methods. In Chapter VI, we apply these techniques to extraterrestrial, abiotic syntheses of nucleobases, focusing on the chemistry of adenine. These results are interpreted in the context of proposed extraterrestrial syntheses of adenine and other purine nucleobases and used to predict the isotopic distributions of these compounds.

## PUBLISHED CONTENT AND CONTRIBUTIONS

Csernica, T., and Eiler, J. M. (2023) High-dimensional isotomics, part 1: A mathematical framework for isotomics. *Chem. Geol.* 617, 121235. doi: 10.1016/j.chemgeo.2022.121235

T.C. participated in conceptualization, methodology, software development, validation, formal analysis, investigation, writing – original draft, writing – review & editing, visualization, and product administration.

Csernica, T., Bhattacharjee, S., and Eiler, J. (2023) Accuracy and precision of ESI-Orbitrap-IRMS observations of hours to tens of hours via reservoir injection. *Int. J. Mass Spectrom.* **490**, 117084. doi: 10.1016/j.ijms.2023.117084

T.C. participated in conceptualization, methodology, software development, validation, formal analysis, investigation, writing – original draft, writing – review & editing, visualization, and product administration.

Csernica, T., Session, A. L., and Eiler, J. M. High-dimensional isotomics part 2: Observations of over 100 constraints on methionine's isotome. *Chem. Geol.* 642, 121771. doi: 10.1016/j.chemgeo.2023.121771

T.C. participated in conceptualization, methodology, software development, validation, formal analysis, investigation, writing – original draft, writing – review & editing, visualization, and product administration.



## TABLE OF CONTENTS

Acknowledgements .....	iii
Abstract .....	iv
Published Content and Contributions.....	vi
Table of Contents.....	vii
Nomenclature.....	viii
Chapter I: Physical and Chemical Origins of Isotopologue Distributions.....	1
Chapter II: A Mathematical Framework for Isotomics .....	6
Chapter III: Accuracy and Precision of ESI-Orbitrap-IRMS Observations Of Hours to Tens of Hours via Reservoir Injection.....	96
Chapter IV: Observation of Over 100 Constraints on Methionine's Isotome.....	137
Chapter V: Simultaneous Observation of $2\text{H}$ and $^{13}\text{C}$ Enrichment of Methyl Phosphonic Acid via Orbitrap-IRMS with Applications to Nerve Agent Forensics .....	196
Chapter VI: Isotopic Signature of a Prebiotic Adenine Synthesis and Consequences for Meteoritic Nucleobases .....	233
Bibliography .....	274

# NOMENCLATURE

## GENERAL TERMS

---

**Abundant Isotope:** The isotope of a chemical element with the highest natural **isotope concentration**.

**Atomic position:** A subset of atoms of the same element within a molecule which are symmetrically equivalent.

**Fragmentation Vector:**  $f_{CM}$ . A vector, where the entries are either "1" or "x." "1" gives a site that is passed from the parent molecule to the derived fragment ion during ionization, and "x" gives a site that is lost upon fragmentation. The subscript "CM" gives the cardinal mass of the **unsubstituted isotopologue** of the fragment ion in question.

**Identity Number:** The number of ways to construct an **isotopologue** given a specified division of **sites**. For example, if  $N_2O$  is defined with sites  $N_{outer+inner}$  and  $O_3$ , the **isotopologue**  $[ (^{14}N^{15}N), ^{16}O ]$  can refer to  $^{14}N^{15}N^{16}O$  or  $^{15}N^{14}N^{16}O$  and has an identity number of 2. The identity number of an isotopologue can be found by multiplying the multinomial coefficient for each **site**.

**Isotome:** The set of all **concentrations of isotopologues** in a sample of a molecule.

**Isotope Concentration:** The mole fraction of an isotope within a molecule. Written using brackets; the concentration of  $^{15}N$  is written  $[^{15}N]$ .

**Isotopologue:** A version of a molecule with a unique set of isotopes in the **sites**. E.g., for the  $N_2O$  molecule,  $^{15}N^{14}N^{16}O$ ,  $^{14}N^{15}N^{16}O$ , and  $^{15}N^{15}N^{17}O$  are three different isotopologues. Note that subdividing **sites** differently may change the number and identity of **isotopologues** of a molecule; e.g., if we define  $N_2O$  to have two sites,  $N_{outer+inner}$  and  $O_3$  (perhaps because our experiment does not distinguish between the nitrogen **sites**), then  $^{15}N^{14}N^{16}O$ ,  $^{14}N^{15}N^{16}O$  are indistinguishable and treated as the same **isotopologue**.

**Isotopologue Concentration (or Relative Abundance):** The mole fraction of an **isotopologue** within a sample. Written using brackets; the concentration of  $^{15}N^{14}N^{16}O$  is written  $[^{15}N^{14}N^{16}O]$ . Multiatomic **sites** are written in parentheses; if we treat  $N_2O$  as having two **sites**,  $N_{outer+inner}$  and  $O_3$ , we write  $[ (^{14}N^{15}N) ^{16}O ]$  for the concentration of the **singly-substituted isotopologue**.

**Multiply-substituted Isotopologue:** An **isotopologue** with multiple **rare isotopes**.

**Rare Isotope:** Any isotope of an element other than the **abundant isotope**.

**Set of All Possible Isotopologues:**  $A$ . The set containing all possible **isotopologues** of a molecule (for some specified division of sites).

**Set of element isotopes,  $E_x$ :** A set giving the possible isotopes for any chemical element  $x$ . Generally, this will include only the naturally occurring stable isotopes of that element. For example, for nitrogen,  $E_N = \{^{14}\text{N}, ^{15}\text{N}\}$ ; the synthetic, short-lived isotope  $^{13}\text{N}$  is omitted. In principle,  $E_N$  can include any isotopes of interest.

**Set of site isotopes:  $S_k$ .** The possible combinations of isotopes at **site**  $k$ . For example, for a nitrogen site with two nitrogen atoms:  $S_N = \{(^{14}\text{N}^{14}\text{N}), (^{14}\text{N}^{15}\text{N}), (^{15}\text{N}^{15}\text{N})\}$ . For a **site**  $k$  with  $n$  atoms of element  $x$ ,  $S_k$  is the multinomial expansion of the corresponding set  $E_x$  to the  $n$ -th power.

**Set of site multinomial coefficients:  $\Phi_k$**  The number of ways to construct each combination of isotopes within **site**  $k$ . For example, for a nitrogen site with two nitrogen atoms:  $C_N = \{1, 2, 1\}$ , corresponding to the set  $S_N$  above. For a **site**  $k$  with  $n$  atoms of element  $x$ ,  $\Phi_k$  is the set of the multinomial coefficients from the expansion of the set  $E_x$  to the  $n$ -th power.

**Singly-substituted Isotopologue:** An **isotopologue** with a single **rare isotope**.

**Site:** An arbitrary subset of atomic positions with the same chemical element within a molecule. Often, a **site** will include the same atoms as an **atomic position**; however, it may combine or subdivide these arbitrarily (doing so may be mathematically useful, especially for the interpretation of fragmentation experiments).

**Site-specific isotope concentration:** The mole fraction of an isotope within a **site(s)**. The **site(s)** are indicated with a subscript, i.e., the concentration of  $^{15}\text{N}$  at **site**  $N_1$  is written  $[^{15}\text{N}]_{N_1}$ .

**Stochastic Assumption:** The assumption that the **rare isotope** content at each **site** of a molecule is randomly distributed across all possible **isotopologues** of that molecule. If we write  $[x_i]$  for the concentration of isotope  $x$  at the  $i$ th **site** of a molecule, and  $[a]$  for the concentration of an **isotopologue**, we may calculate the **isotopologue concentration** as the product of the **site-specific isotope concentrations**:  $[a] = \prod_{i=1}^n [x_i]$ .

**Unsubstituted Isotopologue:** The **isotopologue** where every **site** contains only the **abundant isotope**.

## OPERATIONS ON SETS OF ISOTOPOLOGUES:

---

**Addition of New Atoms:** Define new site(s) for the new atoms and take their cartesian product with the current set of all isotopologues.

**Cardinal Mass Change:** Compute the cardinal mass difference of each **isotopologue** relative to the **unsubstituted isotopologue**.

**Isotopic Substitutions:** Gives the **rare isotopes** present in each **isotopologue**.

**Loss of Atoms/Fragmentation,  $f_{CM}$ :** Applies a **fragmentation vector** to a set of **isotopologues**.

**Mass Selection, M+N:** Selects a subset of a set of **isotopologues** with N cardinal mass units greater than the **unsubstituted isotopologue**.

## REPORTING METHODS

---

**Clumped-Isotope Ratio:**  $R^i = \frac{[\text{isotopologues } i]}{[\text{reference isotopologue}]}$ . The numerator may be a specific **isotopologue**, two or more **isotopologues** containing the same **rare isotope** substitutions, or two or more **isotopologues** having the same cardinal mass, while the denominator is often the **unsubstituted isotopologue**. For example, for  $N_2O$  we may report:

$$R^{^{15}N^{14}N^{18}O + ^{14}N^{15}N^{18}O} = \frac{[^{15}N^{14}N^{18}O] + [^{14}N^{15}N^{18}O]}{[^{14}N^{14}N^{16}O]}$$

**Clumped U Value:** As the clumped isotope ratio where the reference isotopologue is the **unsubstituted isotopologue**.

**Delta value:** Used to report differences between two isotope ratios, for samples 'j' and 'k'; we give the enrichment of 'j' relative to 'k' as:

$$\delta_k^i = \left( \frac{R_j^i}{R_k^i} - 1 \right) * 1000.$$

We can also define delta values using U values, instead of ratios, i.e.,:

$$\delta_k^i = \left( \frac{U_j^i}{U_k^i} - 1 \right) * 1000.$$

**Isotope-specific U value:** A U value where the numerator equals the sums of the concentrations of the **singly-substituted isotopologues** for a given element. For  $N_2O$ , we may report:

$$U^{15N} = \frac{[^{15}N^{14}N^{16}O] + [^{14}N^{15}N^{16}O]}{[^{14}N^{14}N^{16}O]}.$$

**Isotopologue-specific U value:** A U value where the numerator is a single isotopologue.

**Molecular-average isotope ratio:**  $R^i = \frac{[\text{isotope } i]}{[\text{reference isotope } j]}$ . Typically, i is a **rare isotope** while j is the **abundant isotope**. For example, for nitrogen, we may report  $R^{15} = \frac{[^{15}N]}{[^{14}N]}$ .

**Site-specific Isotope ratio:**  $R_k^i = \left( \frac{[\text{isotope } i]}{[\text{reference isotope } j]} \right)_k$ . As the **molecular-average isotope ratio** but calculated across **site(s) k**. For example, the site-specific isotope ratio for the site  $N_1$  in  $N_2O$ :

$$R_{N_1}^{15} = \frac{[^{15}N]_{N_1}}{[^{14}N]_{N_1}}.$$

**Site-specific U value:** A U value where the numerator equals the concentration of the **singly-substituted isotopologue** at a given **site**. For the  $N_{\text{outer}}$  **site** of  $N_2O$ , we have:

$$U^{N_{\text{outer}}} = \frac{[^{15}N^{14}N^{16}O]}{[^{14}N^{14}N^{16}O]}.$$

**“U” Value:**  $U^i = \frac{[\text{isotopologues } i]}{[\text{Unsubstituted Isotopologue}]}$ . The numerator can be any set of **isotopologues**, while the denominator is always the **unsubstituted isotopologue**. Similar to the **clumped-isotope ratio**, the U value differs because 1) the numerator can include **singly substituted isotopologues** and 2) the denominator is always the **unsubstituted isotopologue**.

**$U^{M+N}$  value:** A U value where the numerator equals the sums of the concentrations of the M+N values. This may be used to transform results from M+N relative abundance space to U value space. For  $N_2O$  and M+1:

$$U^{M+1} = \frac{[^{15}N^{14}N^{16}O] + [^{14}N^{15}N^{16}O] + [^{14}N^{14}N^{17}O]}{[^{14}N^{14}N^{16}O]}.$$

## ORBITRAP MASS SPECTROMETRY TERMS

---

**Microscan:** An observation of a single packet of ions within the Orbitrap which records an individual transient.

**Transient:** The time-varying image current observed by the Orbitrap.

**Scan:** A single observation reported from the Orbitrap software to the user, consisting of the result of a Fourier transform applied to a transient to present a mass spectrum. The transient may be from a single microscan or from a combination of several microscans.

**Acquisition:** A single experiment performed on a compound of interest, consisting of many individual scans.

**Mass Resolution:** The mass resolution (FWHM) of the Orbitrap at  $m/z = 200$ ; scales as  $(m/z)^{1/2}$ .

**Automatic Gain Control Target (AGC Target):** A target number of ions to permit into the Orbitrap for each scan.

**Total Ion Current (TIC):** The sum of ion intensities observed by the Orbitrap.

**Number of Ions Observed ( $N_{IO}$ ):** The number of ions observed for an individual peak in an individual scan.

**Zero Scan:** A scan which returns  $N_{IO} = 0$  for a specific peak.

## ORBITRAP-IRMS ERROR MEASURES

---

**Acquisition Error ( $\sigma_{AE}$ ):** The observed relative standard error of an observed isotope ratio (i.e., a R value) across all scans of a single acquisition. Reported in ‰.

**Shot Noise Limit ( $\sigma_{SN}$ ):** A prediction of the relative standard error of an observed isotope ratio (i.e., a R value) across all scans of a single acquisition assuming that the precision of that observation was limited only by shot noise error. Reported in ‰.

**Propagated Acquisition Error ( $\sigma_{PAE}$ ):** The error of a standardized isotope ratio (i.e., a  $\delta$  value) calculated using a sample acquisition and one or more standard acquisitions. Computed by adding the  $\sigma_{AE}$  on the sample to the error on the standard in quadrature. Elsewhere in the literature, the error on the standard may be a  $\sigma_{AE}$  value (Eiler et al., 2017; Wilkes et al., 2022; Mueller et al., 2022a). Here, it is a confidence interval around a linear fit to several standard acquisitions. Strictly greater than  $\sigma_{AE}$  for the sample. Reported in ‰.

**Experimental Reproducibility ( $\sigma_{ER}$ ):** The standard deviation of the standardized isotope ratios (i.e.,  $\delta$  values) for multiple sample observations. Reported in ‰.

## *Chapter 1*

### INTRODUCTION

The forensic question—where did a compound come from? What processes were active in its formation? To what extent has it been degraded or changed?—are crucial across scientific disciplines. They inform our understanding of the Earth's past, present, and future, telling us where and how our planet was formed, how anthropogenic activity is altering our environment, and how we can expect its biosphere to develop. They can tell us about our own history, revealing when humans developed certain agricultural techniques, what sorts of diets they ate, and how cultural practices began. And they have much to say about current problems, revealing if patients are healthy or diseased or if athletes are using performance enhancing drugs.

Stable isotopes are one of our core tools for answering these sorts of questions. Most elements can exist in multiple forms, or isotopes, with different numbers of neutrons. Different isotopes have subtly different physical and chemical properties, and the abundances of these isotopes in a sample will differ with its physical and chemical history. Measurements of isotope abundances can therefore reveal a compound's history. For example, carbon fixation proceeds more rapidly for CO<sub>2</sub> with the <sup>12</sup>C isotope of carbon than the <sup>13</sup>C isotope, causing the carbon incorporated into living creatures to be depleted in <sup>13</sup>C relative to atmospheric carbon. A measurement of the relative abundances of <sup>13</sup>C and <sup>12</sup>C in a sample can thus be used to distinguish whether it originated from an organic or inorganic source.

However, the application of stable isotopes is immediately complicated by the fact that molecules have many atoms, and isotopic substitutions can occur at any of these. Moreover, these substitutions can occur simultaneously; there are versions of alanine, for example, with <sup>13</sup>C substitutions at both the amine and methyl carbon. Because substitutions can occur at any combination of positions, there is a combinatorial explosion in the number

of isotopologues which exist for a molecule. Molecules with as few as 20 atoms (e.g., small fatty acids, or moderate-sized amino acids) can have millions of possible isotopic forms, or isotopologues. Just as different atoms have different chemical properties, isotopic substitutions at different positions have different effects: every one of these isotopologues has its own unique properties, and the abundances of each will differ with the compound's history.

The combinatorial explosion presents both a challenge and an opportunity for the application of isotopic arguments. The presence of so many isotopologues with their own unique properties can allow investigators to distinguish different scenarios in minute detail. However, the difficulty in separating and observing so many isotopologues makes it hard to use any of this information; indeed, previous investigators have concluded that "it is impossible to determine the relationships among all the isotopic forms of a polyatomic compound experimentally" (Galimov, 1985). Traditional experimental techniques will instead average over a large number of isotopologues; for example, they will combust a sample to CO<sub>2</sub> and observe the <sup>13</sup>C/<sup>12</sup>C content of the resulting gas, losing any information about <sup>13</sup>C at different positions and the cooccurrence of multiple <sup>13</sup>C substitutions. This more analytically tractable approach is useful; however, as there may be dozens of processes affecting the isotopic content of a compound, it is often insufficient to fully solve a problem. As one investigator put it: "It often seems that isotopic fractionations provide *too much* information about *too many* processes, combining it all in a package that is unmanageably intricate" (Hayes, 2001). Making progress in this regard therefore requires a two-pronged approach: first, we must develop experimental techniques which can distinguish between the many different isotopologues of a compound, and second, we must have the theoretical means for understanding and interpreting the resulting data.

This thesis attempts to make progress on both experimental and theoretical aspects of this problem, which we term 'isotomics.' Crucial to our approach is the new measurement technique of Orbitrap isotope ratio mass spectrometry (Orbitrap-IRMS). Orbitrap-IRMS methods have been developed only recently but are very promising tools for



isotope measurements because of their high mass resolution and ability to observe many fragments of larger organic molecules, which allows us to determine the positions of isotopic substitutions. While powerful, there are many outstanding questions regarding the use of this technology and the amount of isotopic information which can be extracted. We explore these questions via both fundamental method development (Chapters II-IV) and application to science questions (Chapters V-VI). We conclude this section with an overview of the remaining chapters.

Chapter II explores the mathematical foundations of isotope calculations. Here, the key questions are: how can we understand the data obtained from an arbitrary experiment applied to a small molecule? How can we relate this data to other experiments, and a more holistic understanding of the molecule? Which properties are expected to differ with which processes? And which targets should we choose for isotopic measurements? It settles on an explicit isotopologue-tracking strategy, in which all of the isotopologues of a molecule are enumerated and traced through an experiment. We then apply this strategy to a particular type of Orbitrap-IRMS experiment, called a 'M+N' experiment, which is conceptually challenging but enables the investigator to extract a much greater amount of isotopic information. Our analysis allows us to reframe this experiment in much simpler terms, obtaining an analytical method to compute the results, an improvement over the previous numerical approach.

Chapter III moves to experiment, developing techniques for the long duration Orbitrap-IRMS measurements required for isotomics. One of the core challenges of isotomics is the rarity of the many of the species it wishes to observe; these may have abundances of  $<10^{-5}$ . Moreover, to make meaningful statements about forensics, investigators must characterize *deviations* in their abundances at the level of 1 ‰. Observed precisions are limited by counting statistics, so the target must be observed many times (e.g.,  $10^6$ ) to make these statements. In order to observe such rare species so many times, our experiments must occur over long durations, hours to tens of hours. However, prior Orbitrap-IRMS measurements used much shorter timescales, minutes to tens of

minutes. We therefore implemented an alternate sample introduction method which was capable of such long duration measurements and characterized its stability and accuracy. We find that it is sufficient for a certain level of precision,  $\approx 1 \text{ ‰}$ , but insufficient to move much beyond this.

Chapter IV combines the sample introduction method developed in Chapter III and the mathematics developed in Chapter II to explore the bounds of isotopic measurements using current technology. We selected methionine as an analyte, because it is a good model compound: it has C, H, N, O, & S, the most common elements for which we would like to recover isotopic information, and it forms many fragments with well-constrained geometries, which is useful for computing its site-specific structure. We are able to observe 146 different isotopic properties of methionine, including double and triple-substitutions. Moreover, we were able to associate these measurements with certain locations in the molecule. An important takeaway from this experiment is that measurements of multiple substitutions in organic compounds must move beyond easier-to-understand interpretations (e.g., “the enrichment of the  $^{13}\text{C}^{13}\text{C}$  isotopologue with  $^{13}\text{C}$  at the methyl and carboxyl positions”) to statements that are more closely tied to experiment (e.g., “the enrichment of the  $^{13}\text{C}^{13}\text{C}$  isotopologues which contribute to the fragment with cardinal mass 61”). We also comment on the theoretical limits of this technology based on the abundances of rare isotopologues.

Chapters V and VI shift the focus from method development to application. Chapter V develops a comparatively simple isotopic measurement of just two properties: the  $^2\text{H}$  and  $^{13}\text{C}$  content of methylphosphonic acid ( $\text{CH}_5\text{O}_3\text{P}$ ). Methylphosphonic acid is the hydrolysis product of key precursors used to synthesize sarin, including methylphosphonic difluoride ( $\text{CH}_3\text{POF}_2$ ) and methylphosphonic dichloride ( $\text{CH}_3\text{POCl}_2$ ). Methylphosphonic difluoride has been used to make sarin on the battlefield within the past decade. Both  $^2\text{H}$  and  $^{13}\text{C}$  contain valuable forensic evidence for these compounds and have been measured individually; our Orbitrap-IRMS method explores them more rapidly and using less sample. While more

routine than our other analyses, this chapter helps demonstrate the validity of Orbitrap-IRMS to applied science targets.

Chapter VI presents another application: the extraterrestrial, abiotic, syntheses of nucleobases. Many of the core compounds present in living systems—amino acids, sugars, and nucleobases—have been found in extraterrestrial environments, and a significant amount of evidence suggests these were formed abiotically. However, associating a specific compound with a specific synthesis pathway is challenging. Isotomics is therefore a valuable tool for these purposes. We explored the isotope effects associated with a laboratory-scale abiotic synthesis of adenine, beginning from formamide and cyanide, with an eye towards interpreting the isotopic signatures of meteoritic purines. Adenine is a rich target for isotomics, forming nine distinct fragments observable via Orbitrap, but simultaneously reveals many of the challenges encountered with Orbitrap-IRMS methods: it is difficult to standardize our observations, the fragments are formed via complex pathways, and the core reaction occurs via multiple mechanisms. We discuss these challenges and possible resolutions. We then interpret our results in the context of the only previous measurement of the isotopic content of extraterrestrial purines. Comparing our results to currently proposed scenarios for meteorite organics, we suggest the most parsimonious explanation for these compounds—that they were formed from cyanide—is only plausible in a specific set of conditions, where the nucleobases were highly degraded prior to observation. We suggest some alternative mechanisms for the observations and make predictions of the isotopic content of 11 purine nucleobases under these scenarios.

## Chapter 2

### A MATHEMATICAL FRAMEWORK FOR ISOTOMICS

Csernica, T., and Eiler, J. M. (2023) High-dimensional isotomics, part 1: A mathematical framework for isotomics. *Chem. Geol.* 617, 121235. doi: 10.1016/j.chemgeo.2022.121235

#### Abstract

Molecules can exist in a variety of isotopic forms, called **isotopologues**, with varying numbers of isotopic substitutions at symmetrically nonequivalent atomic positions. The concentrations of these **isotopologues** in a sample, referred to here as the sample's **isotome**, encodes information about that sample's physical and chemical history. While much of this information remains inaccessible due to experimental challenges, recent advances have enabled the measurement of many new constraints on a sample's **isotome**. These constraints, which may be obtained from several different technologies, currently consist of ratios of subsets of the **isotome** and in almost all cases fail to directly observe most isotopologues. Thus, it is challenging to relate the set of all measured constraints to the abundances of all possible isotopologues. We here develop a mathematical framework for understanding how various measurements of a sample's **isotome** relate to one another. We first show a method for tracking **isotopologues** through complicated experimental designs, to rigorously and precisely state what subsets of the **isotome** are being measured. We then propose the generalization of the so-called 'clumped' isotope ratios to a new ratio type, the "U" value, which gives the concentration of any set of **isotopologues** relative to the **unsubstituted isotopologue**; this is a more appropriate way to report many **isotopologue** measurements. The U value can be used to compare and combine clumped, molecular-average, and site-specific measures of isotopic content; we demonstrate that for molecules with near-stochastic distributions of isotopes (and thus for many cases of interest), the molecular-average or site-specific U values are approximately equal to the corresponding molecular-average or site-specific isotope ratio. The U values therefore

provide a convenient framework for comparing and manipulating many different types of observations. To demonstrate our work in practice, we apply it to a MS/MS experiment in which a subset of **isotopologues** with a given cardinal mass is selected, subjected to collisional fragmentation, and then observed in an Orbitrap mass spectrometer. This design, which is now practical, offers many constraints on a sample's **isotome** that are conceptually difficult to relate to concentrations of individual isotopologues. We analyze a simulated MS/MS experiment offering over 100 constraints on a methionine **isotome** (we plan to present our experimental results from this experiment in a companion publication). Our framework enables us to report conventional data products, such as overall molecular  $\delta_{PDB}^{13C}$  values, as well as measurements of various singly and multiply-substituted (including triply-substituted) isotopologues, demonstrating the efficacy and generalizability of our mathematical methods.

## 2.1. Introduction

Molecules can have a variety of isotopic structures due to varying numbers and locations of isotopic substitutions. These structures, called **isotopologues**, have subtly different physical and chemical properties caused by their different isotopic substitutions. Physical and chemical processes thus affect **isotopologues** in subtly different ways, leading to changes in the relative abundance of the **isotopologues** of a sample (Eiler, 2013). The relative abundances of a compound's **isotopologues** therefore encode its physical and chemical history.

Conventional studies of isotopic diversity observe variation along a few compositional dimensions, such as the total  $^{13}C$  or  $^{15}N$  content of a molecule. However, much more information is present. For example, consider a small organic molecule like methionine ( $C_5H_{11}NO_2S$ ; Figure 2.1); it contains five elements with possible isotopic substitutions; two of these, C and H, may contain substitutions at symmetrically nonequivalent positions; furthermore, combinations of any set of these positions may have substitutions simultaneously ("clumped" **isotopologues**). Collectively, there are some hundreds of thousands (depending on which atoms we choose to treat as indistinguishable;

this may differ depending on the experiment of interest; see below for a detailed discussion) of **isotopologues** of methionine; their concentrations constitute the **isotome** of a methionine sample.

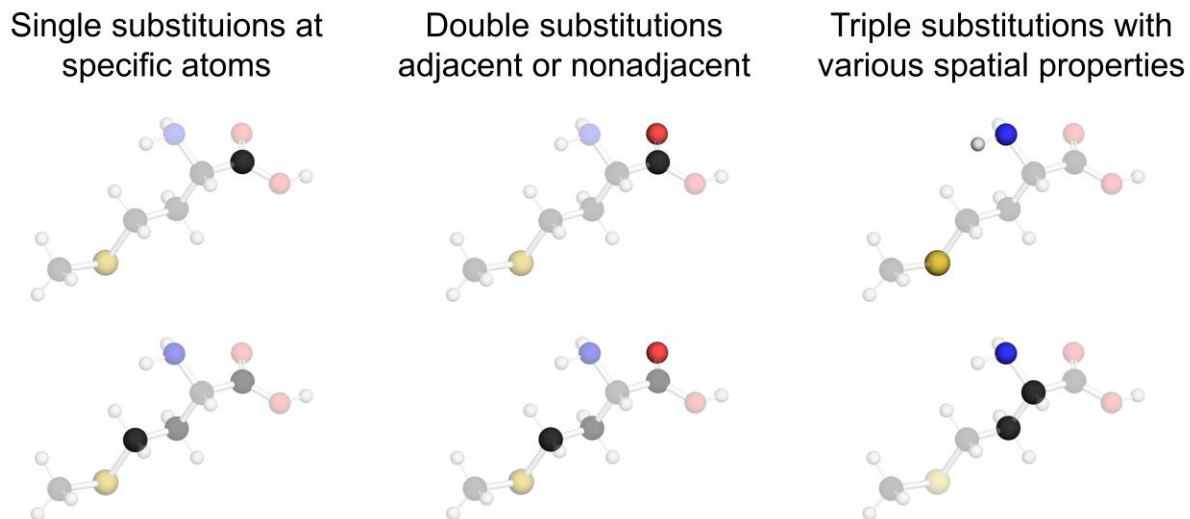


**Figure 2.1:** Some isotopologues of methionine. Substitutions are shown with bolded atoms. Note that O and S can have multiple rare substitutions, so images with these can represent more than one isotopologue. Left column, top: a single substitution at the carboxyl carbon; bottom: a single substitution at the gamma carbon. Center, top: an adjacent C-O clump at the carboxyl site; bottom: a nonadjacent C-O clump at the gamma carbon and one oxygen. Right, top: A triple substitution with adjacent N-D clumping and a sulfur substitution; bottom: a triple substitution at the amine, alpha, and beta carbons. These six illustrated isotopologues, and many more, are represented in the methionine **isotome**.

The information present in an **isotome** is valuable but can be difficult to measure and understand. Many **isotopologues** have low concentrations; for example, doubly- $^{13}\text{C}$  substituted **isotopologues** in methionine, one of the more common variants, occur at a rate of about 1 in 1000 (Each carbon position has approximately a 1% chance of being substituted; two carbons simultaneously have substitutions about 0.01 % of the time; as there are 10 nonequivalent arrangements, about 0.1% of methionine **isotopologues** are doubly- $^{13}\text{C}$  substituted). Moreover, physical and chemical processes which select for or against certain **isotopologues** are often subtle, leading to enrichments or depletions at level of parts per thousand (per mil, “‰”), relative; thus, effectively measuring an **isotome** requires distinguishing small variations in the concentrations of already rare species. When they can be made, measurements of these variations have widespread applications. For

example, observations of multiply substituted isotopologues have constrained paleoclimate temperatures, vertebrate body temperatures, atmospheric budgets of CO<sub>2</sub> and O<sub>2</sub>, the nitrogen cycle, and biological cycling of oxygen and methane (Wang et al., 2004; Yeung et al., 2009, 2015, 2017; Eagle et al., 2010; Eiler, 2011; Douglas et al., 2017) (among other applications). Similarly, position-specific effects in isotopes have been observed in the biological formation of amino acids, glucose and lipids, abiotic organic reactions responsible for formation of extraterrestrial organics, and the sources and sinks of petroleum hydrocarbons (Abelson and Hoering, 1961; DeNiro and Epstein, 1977; Singleton and Thomas, 1995; Singleton et al., 1999; Singleton and Szymanski, 1999; Gonzalez-James et al., 2010; Gilbert et al., 2011; Cesar et al., 2019; Chimiak et al., 2021). Progress in this area has been driven, and limited, by experimental advances—physical processes affecting clumped **isotopologues** of CO<sub>2</sub>, for example, were predicted by Harold Urey in 1947 but not measured until the mid-2000s (Urey, 1947; Eiler and Schauble, 2004).

A number of techniques developed in the past two decades have improved our ability to study a sample's **isotome**; these include site-specific NMR, gas-source isotope ratio mass spectrometry (IRMS), Orbitrap<sup>TM</sup> mass spectrometry (Orbitrap<sup>TM</sup> MS), and optical spectroscopy (Eiler et al., 2013, 2017; Chaintreau et al., 2013; Prokhorov et al., 2019). It can be challenging to compare and integrate the data from different experimental designs, as they may sample different (often subtly different) populations of **isotopologues** to make similar measurements. For example, a **site-specific** NMR measurement determines the <sup>13</sup>C/<sup>12</sup>C ratio of carbon at a specific position (Caytan et al., 2007), while a **site-specific** MS experiment determines the ratio between the singly-substituted **isotopologue** with a <sup>13</sup>C at that position and the **unsubstituted isotopologue** — for reasons explained below, these similar-sounding observations are subtly but importantly different as constraints on the proportions of isotopologues and thus the overall structure of the **isotome**.

We can illustrate these difficulties with a hypothetical (but currently possible) tandem mass spectrometry (MS/MS) technique, which selects and fragments a subset of **isotopologues** with a cardinal mass N units greater than the monoisotopic mass. Following the IUPAC recommendations, the monoisotopic mass is calculated using the

masses of the **most abundant** isotope of each element, and is therefore the mass of the **unsubstituted isotopologue** (Murray et al., 2013). We call this technique an “M+N experiment” for “monoisotopic mass + N.” As our analysis focuses on small volatile and organic molecules where the **most abundant** isotopes are the lowest mass isotopes and the monoisotopic peak is the most abundant peak, we find this notation clear; for molecules incorporating elements with rare isotopes lighter than the **most abundant** isotope or where the monoisotopic peak is low in abundance, we suggest the more precise “M0+N” or “M0-N” be employed. We emphasize that we consider “M+N” to include *all isotopologues* with qualifying cardinal masses, following previous usage (Brownawell and San Filippo, 1982; Sleno, 2012; Neubauer et al., 2018).

For example, consider an experiment where we introduce an N<sub>2</sub>O sample, mass select **isotopologues** weighing one cardinal mass unit greater than the **unsubstituted isotopologue**, <sup>14</sup>N<sub>2</sub><sup>16</sup>O (i.e., the “M+1” isotopologues), subject them to collisional fragmentation such that they lose the outer nitrogen (N-N-O) to form NO<sup>+</sup> ions, and observe the resulting mass spectrum (Figure 2.2) (in actual N<sub>2</sub>O fragmentation, a scrambling effect may cause NO<sup>+</sup> to sample ≈ 10% of outer nitrogen; we omit this for our example) (Ostrom and Ostrom, 2012; Toyoda et al., 2017). In this case, we can observe three ion beams, <sup>14</sup>N<sup>17</sup>O<sup>+</sup>, <sup>15</sup>N<sup>16</sup>O<sup>+</sup>, and <sup>14</sup>N<sup>16</sup>O<sup>+</sup>, produced by fragmentation of the <sup>14</sup>N<sup>14</sup>N<sup>17</sup>O, <sup>14</sup>N<sup>15</sup>N<sup>16</sup>O, and <sup>15</sup>N<sup>14</sup>N<sup>16</sup>O **isotopologues**, respectively. Observations of the relative intensities of these fragments constrain the relative abundances of those **isotopologues**. However, these constraints do not directly map onto traditional measurements that give <sup>15</sup>N/<sup>14</sup>N, <sup>17</sup>O/<sup>16</sup>O, or <sup>18</sup>O/<sup>16</sup>O ratios across the entire sample or more specialized measurements which give **isotopologue** ratios for singly-substituted <sup>15</sup>N **isotopologues**, e.g.,  $\frac{{}^{15}\text{N}^{14}\text{N}^{16}\text{O}}{{}^{14}\text{N}^{14}\text{N}^{16}\text{O}}}$  or  $\frac{{}^{14}\text{N}^{15}\text{N}^{16}\text{O}}{{}^{14}\text{N}^{14}\text{N}^{16}\text{O}}$ , with <sup>15</sup>N at the outer or inner position (Toyoda et al., 2017). Underlying the experimental challenges involved in measuring **isotomes**, then, is a theoretical issue—how are we to understand the ways in which various experimental designs sample **isotomes**, how can we combine information from different experiments, and how should this



information be presented? To do so, we must have a detailed, general understanding of the composition space of **isotomes** (or **isotomics**).

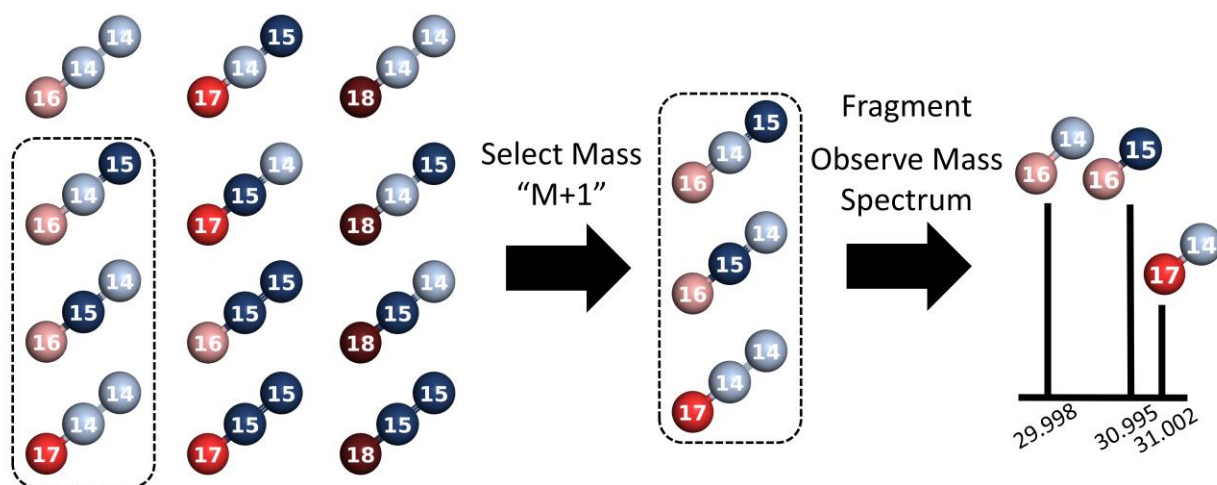


**Figure 2.2:** A hypothetical mass selection/fragmentation experiment applied to  $\text{N}_2\text{O}$ . The original set of isotopologues is shown on the left. After mass selection, only those weighing 1 cardinal mass unit greater than the common monoisotopic form remain; they are then fragmented and observed, resulting in the mass spectrum on the right (not to scale). For larger molecules with more fragments, it is difficult to determine how the resulting mass spectrum relates to the original isotopologue population.

Several aspects of a similar but subtly different problem—the prediction of isotopic distributions arising from various mass spectrometry experiments as an aid to molecular identification—have been studied in detail and reviewed previously (Valkenburg et al., 2012; Rockwood and Palmblad, 2020). These studies include both isotopic distributions of a whole molecule and MS/MS experiments like that in Figure 2.2. Assuming the natural abundances are constant for atoms of the same element, whole molecule isotopic distributions can be computed exactly using a ‘polynomial expansion method,’ where all combinations of isotopes are calculated and their concentrations computed as the product of the corresponding isotopic abundances (Brownawell and San Filippo, 1982; Yergey, 1983; Hsu, 1984). As molecular size increases, the computational complexity required increases combinatorially, and these exact methods cannot be applied (e.g., for proteins with masses of several kilodaltons); subsequent work in this community has therefore focused on the rapid calculation of isotopic distribution for molecules on the order of 10s to 100s of kilodaltons. Effective solutions include the construction of ‘superatoms,’ i.e., a combination

of many instances of the same element with a precalculated isotopic distribution (Kubinyi, 1991), as well as the description of the polynomial expansion in terms amenable to fast Fourier transform; these generally omit calculation of the isotopic fine structure (i.e., they only calculate abundance of a single peak at each cardinal mass), although with some modification fine structure can be recovered (Rockwood, 1995; Rockwood et al., 1996; Rockwood and Van Orden, 1996; Fernandez-de-Cossio, 2010). More recently, Markov process-based methods which can recover isotopic structure for such large molecules have been described (Snider, 2007; Li et al., 2008). Algorithms to predict the isotopic distributions arising in product ions from tandem MS/MS experiments have also been developed and, e.g., compute the relative probabilities with which isotopically substituted product ions contribute to the isotopically substituted parent ion (Singleton et al., 1983; Lehmann, 1998; Rockwood et al., 2003; Ramaley and Herrera, 2008; Böcker et al., 2009; Dührkop et al., 2019). Thus far, all MS/MS algorithms assume that isotopes of the same cardinal mass could not be distinguished and that isotopic abundance is the same across all positions (although generalizations of these algorithms may relax these rules). This prior work on the study of isotopic distributions is instructive; however, as these methods do not explicitly track isotopologues, are not concerned with natural abundance position-specific or clumped isotope effects, and do not provide a way to compare different types of isotopic analysis experiments (e.g., MS experiments with NMR or optical spectroscopy), our applications require a more general framework.

To this end, we develop a framework for treating a sample's **isotome** and understanding the constraints different experiments offer, outlined in Figure 2.3. Our strategy is to explicitly track all **isotopologues** of a molecule through an experiment and understand the observed data in terms of **isotopologues**, and then to simplify this understanding to give a practical statement of how the data relate to the molecular **isotome**. We begin in section 2.1 by suggesting a way to divide a molecule into **sites**, conceive of **isotopologues** in terms of these **sites**, and calculate the **set of all isotopologues** for a molecule using an adaption of the polynomial expansion method. In section 2.2, we develop several operations one may apply to this **set of all isotopologues** to track

**isotopologues** through various experimental designs. In section 2.3, we discuss how to report data from these experiments, and suggest that a generalization of the nomenclature previously used to describe clumped isotope ratios is broadly applicable and effective for comparison between different measurements. We then apply our framework to some experimental designs. In section 2.4, we analyze both fragmentation and M+N experiments using our methods, and in section 2.5 we perform a detailed analysis of experimental issues raised by the M+N experiment. To demonstrate our methods in practice, we apply them to a M+N measurement of methionine which offers over a hundred constraints on methionine's **isotome**, using them to reconstruct site-specific and clumped isotope composition. A planned companion paper will present experimental results from this measurement; we find that the modeling developed here is essential to interpreting experimental results. Finally, we use an accessible N<sub>2</sub>O mixing model to emphasize that the direct measurements of an M+N experiment may be useful even without reconstruction of the proportions of isotopologues in the analyzed compound. Our work gives both a general framework that can be applied to many experimental designs and a specific algorithm for understanding M+N experiments. Throughout, we develop new nomenclature; terms of interest are listed in our glossary (glossary terms are bolded in the text).

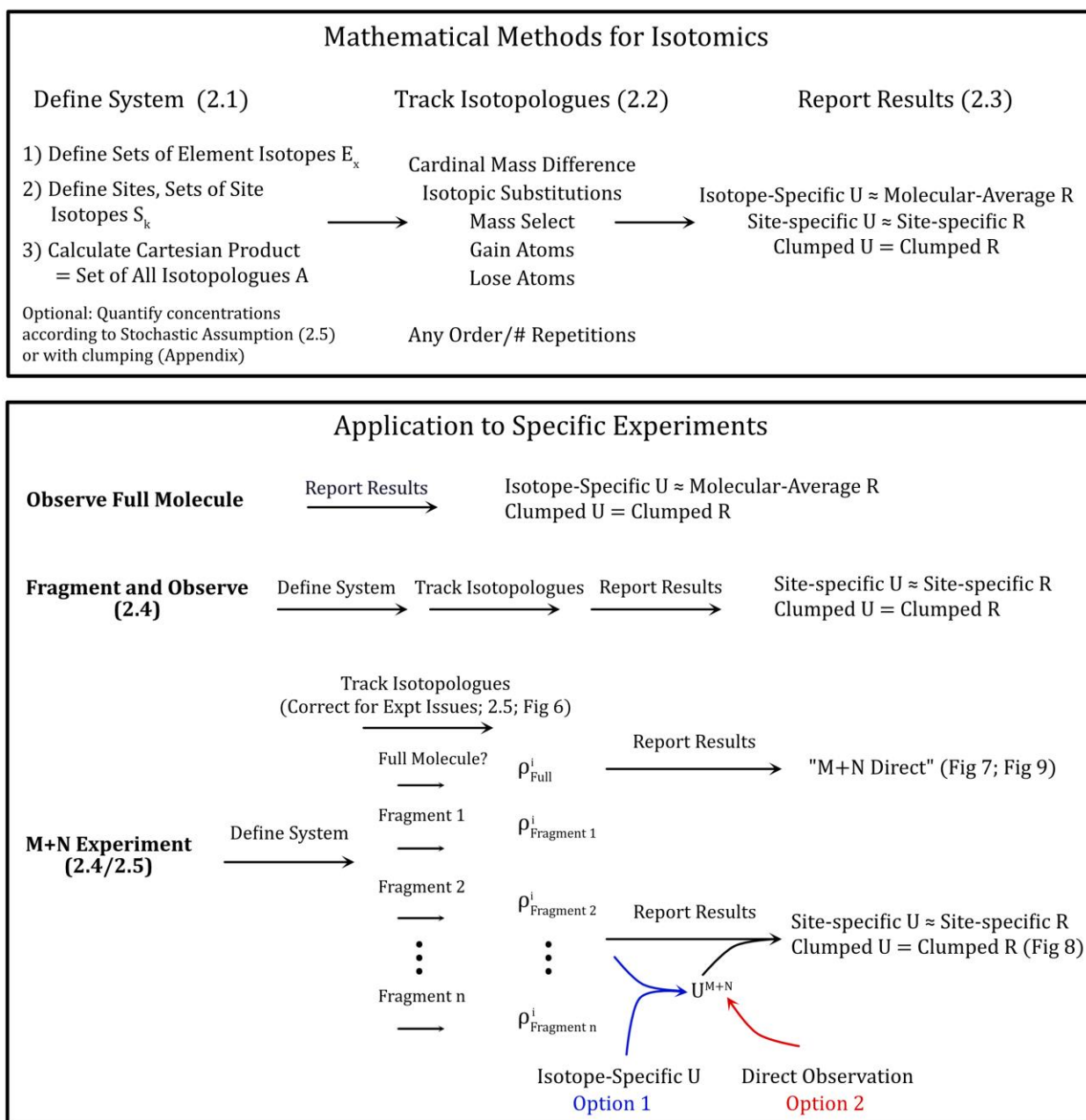


**Figure 2.3:** An outline of the methods and applications described in this article. We first define our mathematical methods for calculating isotopologues (2.2.1), tracking them through experiment (2.2.2), and reporting observations of their abundances (2.2.3). We then apply this framework to several experimental designs, including a fragmentation experiment (2.2.4) and a M+N experiment (2.2.4), as well as to analyze specific experimental issues raised by the M+N experiment (2.2.5).

Some terms and components in this figure are introduced in following sections of the text. Each M+N experiment begins by defining a system and analyzing observations of an arbitrary number of fragments (where the full molecule is formally considered a ‘fragment,’

albeit one that loses no **sites**). The observations are reported as M+N relative abundances  $\rho^i$  for each isotope  $i$  in that fragment. These results can be reported directly or combined with a  $U^{M+N}$  value to reconstruct site-specific or clumped  $U$  values. The  $U^{M+N}$  value can either be calculated from an isotope-specific  $U$  value and the combined M+N relative abundance of all atoms of that element or observed directly.

## 2.2. Materials & Methods

### 2.2.1 A Mathematical Foundation for Tracking Isotopologues

To understand how mass spectrometric analytical technologies manipulate and observe the **isotopologues** of a molecule, it is helpful to track these **isotopologues** through an experiment. We immediately reach a conceptual hurdle—what should we consider an **isotopologue**? One possible definition is the IUPAC standard, which defines **isotopologue** as: “a molecular entity that differs only in isotopic composition (number of isotopic substitutions)” (McNaught et al., 1997). In some circumstances, e.g., fragmentation experiments, we may wish to distinguish between isotopic substitutions at symmetrically distinct atomic positions, i.e., “An **isotopologue** is a version of a molecule with a specific set of isotopic substitutions at each symmetrically unique **atomic position**” (the term *isotopocule* has been suggested for this purpose; see the note in the appendix) (Coplen, 2011). For example,  $^{15}\text{N}^{14}\text{N}^{16}\text{O}$  and  $^{14}\text{N}^{15}\text{N}^{16}\text{O}$  are two different **isotopologues** of  $\text{N}_2\text{O}$  as the two nitrogen positions at which an  $^{15}\text{N}$  substitution occurs are structurally nonequivalent; in contrast,  $^{12}\text{C}^{17}\text{O}^{16}\text{O}$  and  $^{12}\text{C}^{16}\text{O}^{17}\text{O}$  are the same **isotopologue** of  $\text{CO}_2$  as the oxygen positions are symmetrically equivalent. However, this definition adds unnecessary complexity when we cannot analytically distinguish symmetrically non-equivalent substitutions, e.g., a mass spectrometric observation of  $\text{N}_2\text{O}$  without fragmentation. The proper definition to use, then, depends on the specifics of the experiment in question.

Motivated by these concerns, we adopt an alternative definition. First, we define the term “**site**” to refer to any subset of atoms of the same element within a molecule. For example, for  $\text{N}_2\text{O}$ , we may use a single nitrogen **site** to refer to both nitrogen atoms or we may use two nitrogen **sites**, each referring to one atom. In both cases, we have a single **site**

for the oxygen atom. We then define an **isotopologue** as “a version of a molecule with a specific set of isotopic substitutions at each **site**,” noting that the **isotopologues** of a molecule will differ if its **sites** are defined differently. We choose this definition for its flexibility: we may define **sites** such that we recover the “symmetrically equivalence” definition of **isotopologue** (i.e., each **site** by our nomenclature would correspond to a symmetrically unique atomic position), or to distinguish only those atoms which we distinguish in a mass spectrometry experiment (i.e., such that **isotopologues** are versions of a molecule that can be operationally distinguished, given the limitations of a certain analytical technology), or for some other purpose. We continue to use the word **isotopologue** throughout; we trust the reader will appreciate how our definition will take on different specific meanings (based on how analytically distinguishable isotopologues map onto the family of symmetrically equivalent isotopologues) depending on how we define the **sites** of a molecule. Finally, a note on **site** naming: we will label **sites** with the element and an arbitrary subscript, appropriate to the problem of interest; for example,  $N_1$ ,  $N_{outer}$ ,  $N_{amine}$ , or  $N_{nitro+amine}$  are all acceptable **site** labels; the only important criterion is that the labels clearly distinguish different **sites** (though some labels may require effort to define clearly).

With **isotopologue** defined as such, we proceed to calculate the **isotopologues** of a molecule (and optionally their abundances; see section 2.2.5) using an adapted version of the polynomial expansion method (Brownawell and San Filippo, 1982; Yergey, 1983; Hsu, 1984). While this technique is computationally expensive, it is sufficient for molecules of the size we treat here; we discuss computational complexity in more detail in the discussion.

First, for each chemical element, we define a **set of element isotopes**,  $E_x$ , where  $x$  indicates the chemical element. For example, for N we write  $E_N = \{^{14}N, ^{15}N\}$  and for O we write  $E_O = \{^{16}O, ^{17}O, ^{18}O\}$ . In general, we only include the most common stable isotopes of an element in  $E_x$ . We could relax this restriction—for example, if we wanted to include the short-lived isotope of oxygen,  $^{19}O$ , we would write  $E_O = \{^{16}O, ^{17}O, ^{18}O, ^{19}O\}$ . To simplify notation and to facilitate the matrix operations we develop below, we use a

shorthand: We write “0” for the **abundant isotope**, or isotope of an element with the largest natural abundance (e.g.,  $^{14}\text{N}$  or  $^{16}\text{O}$ ); for **rare isotopes**, we write the integer giving the cardinal mass difference between the **rare isotope** and the **abundant isotope**. For example,  $E_{\text{O}} = \{^{16}\text{O}, ^{17}\text{O}, ^{18}\text{O}\}$  becomes  $E_{\text{O}} = \{0,1,2\}$ . In some cases, e.g., Fe with isotopes  $^{54}\text{Fe}$ ,  $^{56}\text{Fe}$ ,  $^{57}\text{Fe}$ , and  $^{58}\text{Fe}$ ,  $E_x$  may include negative numbers;  $^{56}\text{Fe}$  is the **abundant isotope**, and  $E_{\text{Fe}} = \{-2,0,1,2\}$ .

Now, for **site k**, we define the **set of site isotopes**  $S_k$  to give the possible combinations of isotopes at that **site** (recalling that a **site** may include one or more atomic positions in a molecule of interest). For **sites** with only one atom  $S_k$  is equivalent to the **set of element isotopes**  $E_x$  for the corresponding chemical element. An example of this instance is  $\text{N}_2\text{O}$  defined with three sites (which we label  $N_{\text{outer}}$ ,  $N_{\text{inner}}$ , and  $\text{O}_1$ ), we have:

$$S_{N_{\text{outer}}} = \{0,1\} \quad (2.1)$$

$$S_{N_{\text{inner}}} = \{0,1\} \quad (2.2)$$

$$S_{\text{O}_1} = \{0,1,2\}. \quad (2.3)$$

Multiatomic **sites** are more complicated; we begin by examining a **site** with two atoms. Suppose we define the multi-atomic **site**  $N_{\text{outer+inner}}$  for  $\text{N}_2\text{O}$ ; in this case, our set of element isotopes is  $E_{\text{N}} = \{^{14}\text{N}, ^{15}\text{N}\}$ . We can compute the possible combinations of isotopes at this **site** via a binomial expansion:

$$(^{14}\text{N} + ^{15}\text{N})^2 = ^{14}\text{N}^{14}\text{N} + 2 * ^{14}\text{N}^{15}\text{N} + ^{15}\text{N}^{15}\text{N}. \quad (2.4)$$

There are three terms, corresponding to the number of distinguishable substitutions at **site**  $N_{\text{outer+inner}}$ . The coefficient of each term gives the number of ways to construct that substitution; i.e., for  $^{14}\text{N}^{15}\text{N}$ , the coefficient is 2, as this substitution may occur with  $N_{\text{inner}} = ^{14}\text{N}$  and  $N_{\text{outer}} = ^{15}\text{N}$  or vice versa. We define an ordered **set of site isotopes** as the set of these terms, and an associated ordered **set of site multinomial coefficients**  $\Phi_k$  to track their coefficients:

$$S_{N_{\text{outer+inner}}} = \{^{14}\text{N}^{14}\text{N}, ^{14}\text{N}^{15}\text{N}, ^{15}\text{N}^{15}\text{N}\} \quad (2.5)$$

$$\Phi_{N_{\text{outer+inner}}} = \{1, 2, 1\}. \quad (2.6)$$

We conceptually separate these sets, but they are closely related, and should always be thought of as associated with each other. By convention, we order by writing the lowest

cardinal mass substitutions first, and then increase by cardinal mass. Any order is acceptable, as long it is maintained between  $S_k$  and  $\Phi_k$ . In shorthand, our set of site isotopes is:

$$S_{N_{outer+inner}} = \{ (0,0), (0,1), (1,1) \}. \quad (2.7)$$

We can generalize this procedure for other multi-atomic **sites**, finding  $S_k$  via a multinomial expansion of  $E_x$ . We write  $E_x = \{x_1, x_2, \dots, x_n\}$ , where the  $x_i$  correspond to individual isotopes. For a **site** with  $m$  atoms, our expansion is:

$$(x_1 + x_2 + \dots + x_n)^m = \sum_{l_1+l_2+\dots+l_n=m} \binom{m}{l_1, l_2, \dots, l_n} \prod_{i=1}^n x_i^{l_i}. \quad (2.8)$$

Here,  $l_i$  corresponds to the number of instances of isotope  $x_i$ ,  $\prod_{i=1}^n x_i^{l_i}$  gives the content of the isotopic substitutions at the **site**, and

$$\binom{m}{l_1, l_2, \dots, l_n} = \frac{m!}{l_1! l_2! \dots, l_n!} \quad (2.9)$$

is a multinomial coefficient giving the number of ways to make that substitution. For example, for a hydrogen **site** with 6 hydrogens (perhaps for a measurement of ethane, where each H atomic position is analytically indistinguishable and so operationally equivalent), we have  $E_H = \{^1H, ^2H\} = \{H, D\}$ , (writing H, D so we may omit the superscript) and:

$$\begin{aligned} (H + D)^6 &= \sum_{l_{1H}+l_{2D}=6} \binom{6}{l_{1H}, l_{2D}} (H^{l_{1H}} * D^{l_{2D}}) = \\ &= H^6 + 6 * H^5D + 15 * H^4D^2 + 20 * H^3D^3 + 15 * H^2D^4 + 6 * H^1D^5 + D^6. \end{aligned} \quad (2.10)$$

The number of terms in this expansion, corresponding to the number of distinguishable isotopic substitutions at the **site**, is

$$\binom{n+m-1}{m} = \frac{(n+m-1)!}{m!(n-1)!}. \quad (2.11)$$

The set  $S_k$  is the set of these terms, dropping the coefficients, while  $\Phi_k$  contains the coefficients. In this case,

$$S_{ethane} = \{H^6, H^5D, H^4D^2, H^3D^3, H^2D^4, HD^5, D^6\} \quad (2.12)$$

$$\Phi_{ethane} = \{1, 6, 15, 20, 15, 6, 1\}. \quad (2.13)$$



We now have the tools to calculate the **set of all isotopologues**, denoted **A**. We compute **A** by taking the cartesian product of all sets  $S_k$ , i.e., by taking all combinations of one element from each set. Returning to our example case of N<sub>2</sub>O defined with 3 **sites**, and using  $\otimes$  to denote cartesian product, we have:

$$\mathbf{A} = S_{N_{outer}} \otimes S_{N_{inner}} \otimes S_{O_1} = \begin{matrix} N_{outer} & N_{inner} & O_1 \\ \left. \begin{array}{l} {}^{14}\text{N} & {}^{14}\text{N} & {}^{16}\text{O} \\ {}^{14}\text{N} & {}^{14}\text{N} & {}^{17}\text{O} \\ {}^{14}\text{N} & {}^{14}\text{N} & {}^{18}\text{O} \\ {}^{14}\text{N} & {}^{15}\text{N} & {}^{16}\text{O} \\ {}^{14}\text{N} & {}^{15}\text{N} & {}^{17}\text{O} \\ {}^{14}\text{N} & {}^{15}\text{N} & {}^{18}\text{O} \\ {}^{15}\text{N} & {}^{14}\text{N} & {}^{16}\text{O} \\ {}^{15}\text{N} & {}^{14}\text{N} & {}^{17}\text{O} \\ {}^{15}\text{N} & {}^{14}\text{N} & {}^{18}\text{O} \\ {}^{15}\text{N} & {}^{15}\text{N} & {}^{16}\text{O} \\ {}^{15}\text{N} & {}^{15}\text{N} & {}^{17}\text{O} \\ {}^{15}\text{N} & {}^{15}\text{N} & {}^{18}\text{O} \end{array} \right\} & = & \left. \begin{matrix} N_{outer} & N_{inner} & O_1 \\ \begin{array}{l} 0 & 0 & 0 \\ 0 & 0 & 1 \\ 0 & 0 & 2 \\ 0 & 1 & 0 \\ 0 & 1 & 1 \\ 0 & 1 & 2 \\ 1 & 0 & 0 \\ 1 & 0 & 1 \\ 1 & 0 & 2 \\ 1 & 1 & 0 \\ 1 & 1 & 1 \\ 1 & 1 & 2 \end{array} \end{matrix} \right\}$$

Each column refers to a specific **site**  $k$ ; we track these labels along with the set **A**. The ordering of these columns is arbitrary and may be chosen according to application (We suggest the following convention for ordering: sites with elements other than hydrogen first, in order of increasing atomic weight, followed by hydrogen sites). Here, **A** gives the identity of each **isotopologue**; it says nothing about how many ways an **isotopologue** can be constructed. We additionally define an **identity number**, giving the number of equivalent ways to construct an **isotopologue**. We may compute this by multiplying across the multinomial coefficients associated with the isotopic substitutions at each **site**, i.e., the cartesian product of  $\Phi_k$ . For single-atomic **sites**, the multinomial coefficients are all 1, and thus the **identity numbers** are all 1. If we instead defined a single **site** for N<sub>2</sub>O that includes both nitrogen atoms:

$$\mathbf{A} = S_{N_{inner+outer}} \otimes S_{O_1} = \left. \begin{array}{cc} N_{inner+outer} & O_1 \\ \left( \begin{array}{c} (0,0) \\ (0,0) \\ (0,0) \\ (0,1) \\ (0,1) \\ (0,1) \\ (1,1) \\ (1,1) \\ (1,1) \end{array} \right) & \left( \begin{array}{c} 0 \\ 1 \\ 2 \\ 0 \\ 1 \\ 2 \\ 0 \\ 1 \\ 2 \end{array} \right) \end{array} \right\} \left| \Phi_{N_{inner+outer}} \otimes \Phi_{O_1} = \left( \begin{array}{c} 1 \\ 1 \\ 1 \\ 2 \\ 2 \\ 2 \\ 1 \\ 1 \\ 1 \end{array} \right) \right.$$

The sum of the identity numbers is 12, the same as the number of **isotopologues** we calculated with single atomic **sites**; even if we define the **sites** differently, we are referring to the same underlying set of **isotopologues**. We track these identity numbers along with our set of **isotopologues**.

### 2.2.2 Tracking Isotopologues Through Mass Spectrometry Experiments

Next, we develop some operations we can perform on sets of **isotopologues** to track **isotopologues** through mass spectrometry experiments. We expect that other experimental designs can use the same nomenclature and develop operations specific to their methodology.


#### 2.2.2.1 Matrix Operations: Cardinal Mass Difference and Isotopic Substitutions

We define the **unsubstituted isotopologue** as the **isotopologue** containing the **abundant isotope** at every site, (i.e.,  $[0,0, \dots, 0]$ ). Then, we can compute the cardinal mass difference  $\Delta_{CM}$  between any **isotopologue** and the **unsubstituted isotopologue** by summing across cardinal mass differences of each site in its shorthand representation. We can likewise find the isotopic substitutions present in each **isotopologue** by looking up the chemical element and corresponding substitution for any nonzero entry of the vector. As an example, we return to our representation of  $N_2O$  with three **sites**; the first column gives the cardinal mass difference of each **isotopologue** relative to the **unsubstituted isotopologue**, and the second gives the isotopic substitutions present in that **isotopologue**.

$N_{outer}$	$N_{inner}$	$O_1$	$\Delta_{CM}$	Substitutions
0	0	0	0	$Unsub$
0	0	1	1	$^{17}O$
0	0	2	2	$^{18}O$
0	1	0	1	$^{15}N$
0	1	1	2	$^{15}N^{17}O$
0	1	2	3	$^{15}N^{18}O$
1	0	0	1	$^{15}N$
1	0	1	2	$^{15}N^{17}O$
1	0	2	3	$^{15}N^{18}O$
1	1	0	2	$^{15}N^{15}N$
1	1	1	3	$^{15}N^{15}N^{17}O$
1	1	2	4	$^{15}N^{15}N^{18}O$

### 2.2.2.2 Matrix Operations: Mass Selection

The **mass selection** operation allows us to select a subset of **isotopologues** based on cardinal mass. To perform a **mass selection**, we select only the **isotopologues** with the mass difference(s) of interest. For example, if we mass select the population having a mass difference of 1 ('the M+1 population'), we get:

$N_{outer}$	$N_{inner}$	$O_1$	$\Delta_{CM}$		$N_{outer}$	$N_{inner}$	$O_1$
0	0	0	0	Mass Select M+1 	0	0	1
0	0	1	1		0	1	0
0	0	2	2		1	0	0
0	1	0	1		0	0	0
0	1	1	2		0	1	0
0	1	2	3		0	0	0
1	0	0	1		1	0	0
1	0	1	2		0	1	0
1	0	2	3		0	0	0
1	1	0	2		1	0	0
1	1	1	3		0	1	0
1	1	2	4		0	0	0

### 2.2.2.3 Matrix Operations: Addition of New Atoms

As molecules are manipulated through mass spectrometry experiments, they may gain additional atoms. For example, in electrospray ionization (ESI) experiments it is common for molecules to gain adducts, such as hydrogen, sodium, potassium, or

ammonium (Kruve and Kaupmees, 2017; Zhang et al., 2019). Alternatively, reactions may occur during gas-phase collisional dissociation which add new atoms to the compound (Van Stipdonk et al., 2003; Bubas et al., 2021). Importantly, the stage of the experiment at which adduct formation occurs will influence the resulting population of **isotopologues**. For example, consider a (hypothetical) experiment where the M+1 population of N<sub>2</sub>O is selected (as above) and collisionally fragmented (an ‘M+1 experiment’; see below) to yield the NO<sup>+</sup> fragment ion. Imagine we then observe NOH<sup>+</sup>, a version of the expected fragment ion but with addition of a hydrogen adduct atom. If we gain the hydrogen *prior* to mass selection, we would select only <sup>14</sup>N<sup>14</sup>N<sup>16</sup>OH and observe <sup>14</sup>N<sup>16</sup>OH; if we gain the hydrogen *following* mass selection, we would select <sup>15</sup>N<sup>14</sup>N<sup>16</sup>O, <sup>14</sup>N<sup>15</sup>N<sup>16</sup>O, and <sup>14</sup>N<sup>14</sup>N<sup>17</sup>O and observe both the hydrogen and deuterium adduct for each. To deal with these different processes, we must be able to add atoms to our set at any step of the process.

To implement an **addition of atoms**, we define new **sites** and take the cartesian product of these **sites** with the current set of **isotopologues**. For example, take the case where hydrogen is gained prior to fragmentation: we write H<sub>adduct</sub> for the new **site**, which has a single hydrogen, and we have  $S_{H_{adduct}} = \{0, 1\}$  and  $\Phi_{H_{adduct}} = 1$ . We mass select N<sub>2</sub>O as above; then compute the cartesian product as follows:

$$\begin{array}{ccc} N_{outer} & N_{inner} & O_1 \\ \left\{ \begin{array}{ccc} 0 & 0 & 1 \\ 0 & 1 & 0 \\ 1 & 0 & 0 \end{array} \right\} \otimes S_{H_{adduct}} & = & \begin{array}{ccc} N_{outer} & N_{inner} & O_1 & H_{adduct} \\ \left\{ \begin{array}{cccc} 0 & 0 & 1 & 0 \\ 0 & 1 & 0 & 0 \\ 1 & 0 & 0 & 0 \\ 0 & 0 & 1 & 1 \\ 0 & 1 & 0 & 1 \\ 1 & 0 & 0 & 1 \end{array} \right\} \end{array} \end{array}$$

We track the identity numbers and multinomial coefficients as before.

#### 2.2.2.4 Matrix Operations: Loss of Atoms (Fragmentation)

Molecules may also lose atoms during mass spectrometry experiments, for example due to fragmentation during the ionization process or collision-induced dissociation. We define a **loss of atoms** as a single event where a molecule loses some subset of **sites**; as this

will generally be due to fragmentation, we call this a **fragmentation** operation, but note it describes a more general process. For each **fragmentation**, we specify that each **site** must be wholly retained or wholly lost. For example, we would not permit **fragmentation** where one hydrogen of a methyl H **site** containing three hydrogens is lost. In this scenario, we choose to split those hydrogens into two **sites** (e.g., H<sub>retained</sub> and H<sub>lost</sub>) rather than treating them as a single **site** where 1/3 of the atoms in the **site** are lost. We find this choice simplifies our analysis, because it means each **isotopologue** pre-loss corresponds to a single **isotopologue** (and a single observed ion beam) post-loss. If we treated the methyl group as a single **site**, the **isotopologue** with a D substitution could either retain or lose the deuterium substitution upon fragmentation, contributing to two separate **isotopologues** and observed ion beams. This scheme allows us to track any exotic fragmentations; when combined with the **addition of atoms** operation, it also allows us to model exchanges (a loss followed by a gain) which occur during experiments.

To model this process, we write a **fragmentation vector** (or **loss vector**)  $f_{CM}$  where the subscript “CM” gives the cardinal mass of the unsubstituted fragment (if there are fragments with distinct stoichiometries at the same mass, the subscript can be expanded as necessary). The entries of  $f_{CM}$  are then either “1,” indicating a **site** that is kept, or “x,” indicating a **site** that is lost (we were tempted to use 1 and 0; in our shorthand, 0 also refers to the **most abundant** isotope of an element, and we found this re-use of notation confusing. We also considered using multiple letters (e.g., x, y) but found these harder to scan visually). For example, if we fragment N<sub>2</sub>O to lose the oxygen atom, the **fragmentation vector** is

$$f_{28} = [1, 1, x]. \quad (2.14)$$

Note the fragmentation vector depends on our definition of **site**; if we defined N<sub>2</sub>O to have a combined N<sub>inner+outer</sub> **site**, we would have  $f_{28} = [1, x]$ .

To fragment a set of isotopologues **A**, we take the element-wise product (denoted  $\circ$ ) of a **fragmentation vector** and the **isotopologue** vectors of **A**, specifying that any **site** multiplied by “x” returns “x.” For example:

$$\begin{matrix} N_{outer} & N_{inner} & O_1 \\ \left( \begin{array}{ccc} 0 & 0 & 0 \\ 0 & 0 & 1 \\ 0 & 0 & 2 \\ 0 & 1 & 0 \\ 0 & 1 & 1 \\ 0 & 1 & 2 \\ 1 & 0 & 0 \\ 1 & 0 & 1 \\ 1 & 0 & 2 \\ 1 & 1 & 0 \\ 1 & 1 & 1 \\ 1 & 1 & 2 \end{array} \right) \circ [1, 1, x] = & \begin{matrix} N_{outer} & N_{inner} & O_1 \\ \left( \begin{array}{ccc} 0 & 0 & x \\ 0 & 0 & x \\ 0 & 0 & x \\ 0 & 1 & x \\ 0 & 1 & x \\ 0 & 1 & x \\ 1 & 0 & x \\ 1 & 0 & x \\ 1 & 0 & x \\ 1 & 1 & x \\ 1 & 1 & x \\ 1 & 1 & x \end{array} \right) \end{matrix}
 \end{matrix}$$

One conceptual difficulty remains: the same fragment may be formed *via* multiple pathways. For example, consider a case where N<sub>2</sub>O fragments to form NO, and the observed NO corresponds to some combination of N<sub>inner</sub>O<sub>1</sub> and N<sub>outer</sub>O<sub>1</sub> (Toyoda et al., 2017). In this case, we compute each fragmentation separately, defining a unique fragmentation vector for each physical process. Thus, we can see which **isotopologues** contribute to the observation via what pathway.

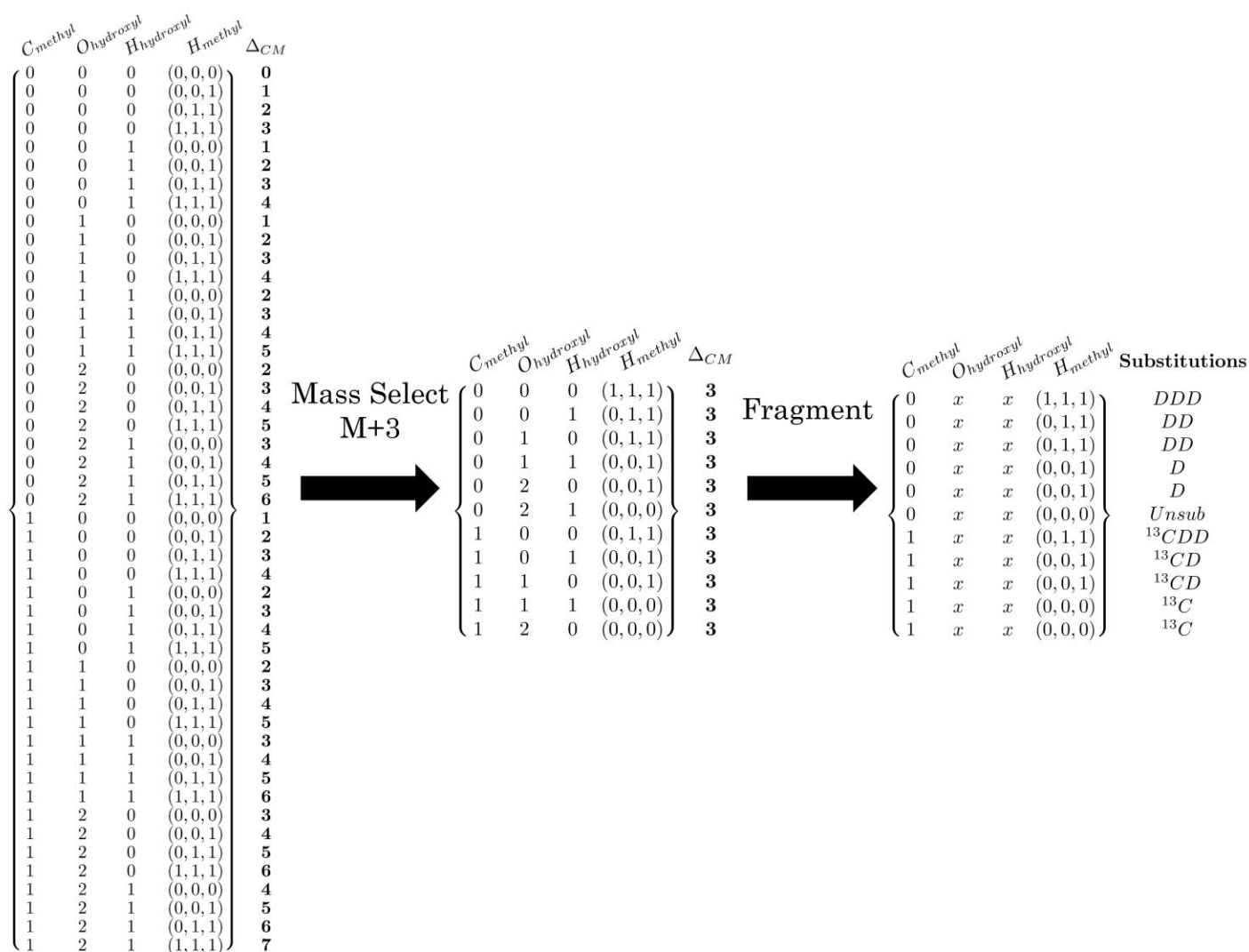
### 2.2.2.5 Quantification of Masses and Abundances

After tracking individual **isotopologues**, we can quantify exact masses and approximate abundances to predict the mass spectrum we will obtain for various experiments. The exact mass calculation is straightforward; we compute the mass of the **unsubstituted isotopologue** based on the isotopes present, then compute the masses of other **isotopologues** based on the mass differences of their **rare isotopes** relative to the **most abundant** isotopes of the corresponding elements. Abundances are more difficult as these will vary from sample to sample; indeed, observing small differences in abundance is the entire point of our approach! We also note that if one is interested in predicting abundances without tracking **isotopologues**, alternative algorithms which scale more readily should be employed (Rockwood et al., 2003). With this qualification, our approach can be used to quantify abundances, either approximately to obtain a rough prediction of a spectrum or more precisely to understand small variations in abundance. We deal with

the latter below; for the approximate approach, we note that variations in **isotope** and **isotopologue abundances** will often be small (e.g., < 10 %); we can therefore take plausible natural abundances for each isotope (e.g., 1% for  $^{13}\text{C}$ ) and compute approximate abundances for each **isotopologue** as the product of these.

### 2.2.2.6 A Worked Example for Methanol

By applying our operations, we can track of **isotopologues** through various experimental designs. To demonstrate this process, consider an experiment where we mass select the M+3 population (i.e., species having a cardinal mass difference of 3 relative to the **unsubstituted isotopologue**) of methanol, then fragment to lose the -OH group (a “M+3” experiment). We first split methanol into 4 **sites**, which we label and order  $C_{\text{methyl}}$ ,  $O_{\text{alcohol}}$ ,  $H_{\text{methyl}}$ , and  $H_{\text{alcohol}}$ , and then calculate **A** (Figure 2.4; the  $H_{\text{methyl}}$  site contains three atoms whereas all other sites contain one atom each). Then, we define the **fragmentation vector**,  $f_{15} = [1, x, 1, x]$ . Next, we mass select the M+3 population and fragment that selected population. The resulting ion beams and their masses in a mass spectrum are shown in Figure 2.5.



1

2 **Figure 2.4:** The Matrix operations for a M+3 fragmentation experiment of methanol. On the left, we enumerate all **isotopologues** of methanol and calculate  
3  $\Delta_{CM}$ . In the center, we mass select only those with  $\Delta_{CM} = 3$ . On the right, we fragment to lose the -OH hydroxyl group. The final substitutions observed for each  
4 mass selected **isotopologue** are shown.



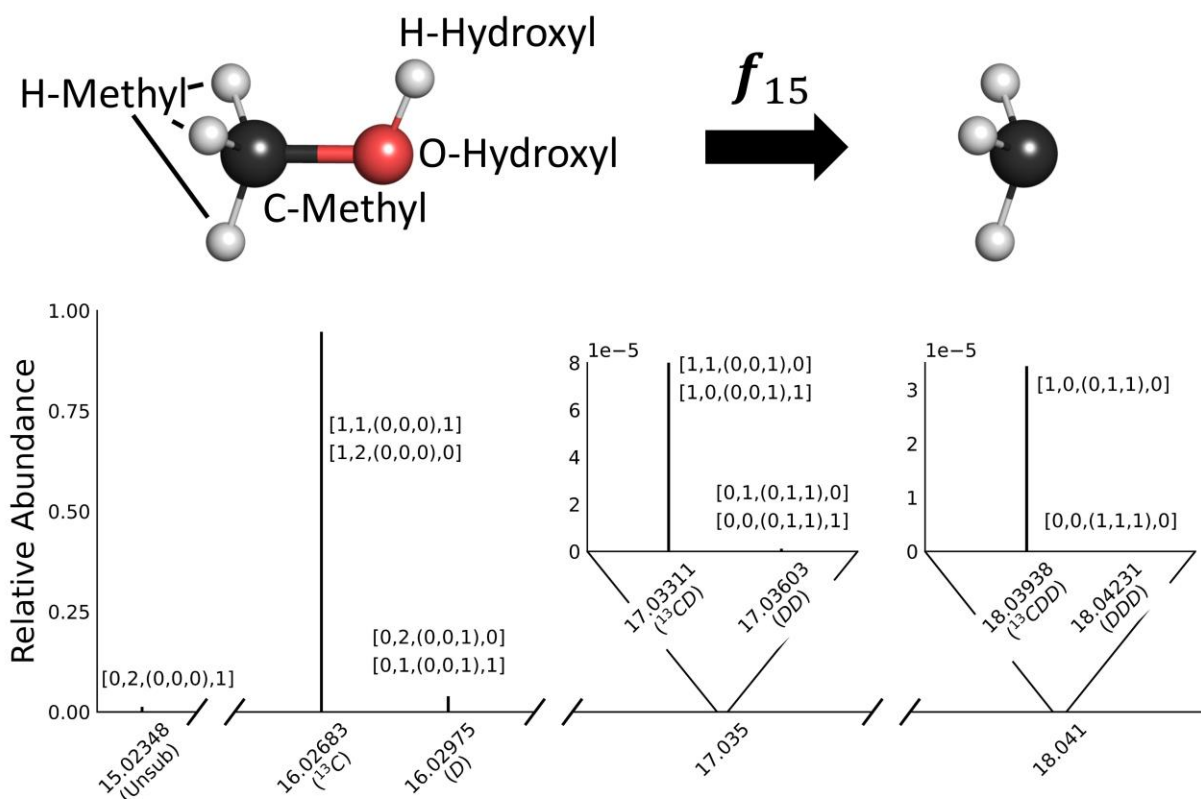


**Figure 2.5:** The M+3 fragmentation experiment applied to methanol. Top: Our definition of the **sites** of methanol and a depiction of its fragmentation. Bottom: The **isotopologues** and corresponding ion beams of methanol after an M+3 experiment where the -OH group is lost. There are seven observable fragments resulting from the 11 isotopologues from the parent population. By applying our basic operations in sequence, we can determine which **isotopologues** contribute to which ion beams for various experimental sequences.

### 2.2.3. Reporting Isotopologue Measurements and the U Value

With an understanding of how the ion beams of a mass spectrometry (MS) experiment sample **isotopologues**, we next discuss how to report these measurements. While our focus is on MS experiments, the methods we outline are applicable to data generated by other types of experiments. We begin by surveying some current methods of reporting isotopic content.

#### 2.3.1 Molecular-Average Isotope Concentrations and Ratios

When reporting information about a sample's **isotome**, there are two related but distinct properties of fundamental interest: **isotopologue concentrations**, which give the

mole fraction of an individual **isotopologue** relative to all instances of the molecule, and **isotope concentrations**, which give the mole fraction of an isotope of a given element relative to all atoms of that element in a molecule. Because individual concentrations are difficult to measure, ratios of **isotopologue** or **isotope concentrations** are typically reported rather than concentrations themselves. These ratios are typically normalized to known or assumed ratios of reference materials so that the subtle differences among natural materials are more readily expressed.

We first examine the **molecular-average isotope ratio**, the most used reporting method. We write **isotope concentrations** using brackets, e.g., the **concentration** of  $^{15}\text{N}$  in  $\text{N}_2\text{O}$  is written  $[\text{}^{15}\text{N}]$ . An **isotope concentration** is a complicated data product of **isotopologue concentrations** (also written in brackets; note the concentrations are given relative to *atoms of an element* for isotopes and *instances of a molecule* for isotopologues). For  $\text{N}_2\text{O}$ :

$$[\text{}^{15}\text{N}] = \frac{[\text{100}] + [\text{101}] + [\text{102}] + [\text{010}] + [\text{011}] + [\text{012}] + 2 * [\text{110}] + 2 * [\text{111}] + 2 * [\text{112}]}{2}. \quad (2.15)$$

The **molecular-average isotope ratio** compares these isotope concentrations for a molecule of interest, and is written as:

$$R^i = \frac{[\text{isotope } i]}{[\text{reference isotope } j]}. \quad (2.16)$$

Typically,  $i$  corresponds to a **rare isotope** (i.e.,  $^{15}\text{N}$ ) and  $j$  corresponds to the **abundant isotope** (i.e.,  $^{14}\text{N}$ ). We can write these ratios in terms of **isotopologue concentrations**:

$$R^{15} = \frac{[\text{}^{15}\text{N}]}{[\text{}^{14}\text{N}]} = \frac{[\text{100}] + [\text{101}] + [\text{102}] + [\text{010}] + [\text{011}] + [\text{012}] + 2 * [\text{110}] + 2 * [\text{111}] + 2 * [\text{112}]}{[\text{100}] + [\text{101}] + [\text{102}] + [\text{010}] + [\text{011}] + [\text{012}] + 2 * [\text{000}] + 2 * [\text{001}] + 2 * [\text{002}]}. \quad (2.17)$$

The choice to report ratios of **isotope concentration** rather than ratios of **isotopologue concentration** is a result of the experimental techniques used for these measurements. They are often measured by chemically transforming, e.g., combusting, a sample into one of a small set of easily analyzable molecules, such as  $\text{N}_2$  or  $\text{CO}_2$ , then measuring that molecule with an isotope-ratio mass spectrometer. These techniques transform

complicated distributions of **A** into simple forms where **isotope concentrations** can be directly measured. Because of the widespread use of **molecular-average isotope ratios**, methods for reporting **isotopologue concentrations** must be conversant with **molecule-average isotope ratios**.

### 2.3.2 Clumped-Isotope (Isotopologue) Ratios

A recently developed method for reporting ratios of **isotopologue** concentrations is the **clumped-isotope ratio**, written (Eiler and Schauble, 2004; Eiler, 2013):

$$R^i = \frac{[\text{isotopologues } i]}{[\text{reference isotopologue}]} \quad (2.18)$$

The numerator can be a specific **isotopologue** (the original intent being that it is always a multiply substituted isotopologue), several **isotopologues** containing the same **rare isotope(s)**, or two or more **isotopologues** of the same cardinal mass but possibly differing in the number and identity of rare isotopes, while the denominator is often (but not required to be) the **unsubstituted isotopologue**. One example of this nomenclature applied to N<sub>2</sub>O is a measurement of <sup>14</sup>N<sup>15</sup>N<sup>18</sup>O and <sup>15</sup>N<sup>14</sup>N<sup>18</sup>O, written in shorthand as:

$$R^{012+102} = \frac{[012] + [102]}{[000]} \quad (2.19)$$

Another example is the ratio reporting the proportion of all isotopologues of N<sub>2</sub>O with cardinal mass M+3:

$$R^{M+3} = \frac{[012] + [102] + [111]}{[000]} \quad (2.20)$$

### 2.3.3 Site-specific Isotope Ratios

A third useful reporting method is the **site-specific isotope ratio**. This takes a ratio of **site-specific isotope concentrations**, which give the mole fraction of an isotope of interest, relative to all atoms of a given element, at some subset of **sites**; for example, for the N<sub>outer</sub> **site** of N<sub>2</sub>O:

$$[^{15}\text{N}]_{N_{\text{outer}}} = [100] + [101] + [102] + [110] + [111] + [112]. \quad (2.21)$$

The site-specific ratio is analogous to the **molecular-average isotope ratio** and written  $R_k^i$ , where  $k$  gives the **site(s)**,  $i$  gives the isotope of interest, and  $j$  gives a reference isotope:

$$R_k^i = \left( \frac{[\text{isotope } i]}{[\text{reference isotope } j]} \right)_k. \quad (2.22)$$

For example, the **site-specific isotope ratio** for the  $N_{\text{outer}}$  **site** of  $N_2O$ :

$$R_{N_1}^{15} = \left( \frac{[^{15}N]}{[^{14}N]} \right)_{N_{\text{outer}}} = \frac{[100] + [101] + [102] + [110] + [111] + [112]}{[000] + [001] + [002] + [010] + [011] + [012]}. \quad (2.23)$$

### 2.3.4 A New Reporting Method: The “U” value

While each of the methods discussed above is useful for certain types of measurements, they typically do not apply to the observed spectra of mass spectrometric experiments that consider isotopic forms of fragment ions; furthermore, merging or translating between measurement types can be challenging, as **isotopologue** and **isotope** ratios use fundamentally different reference frames.

Motivated by these concerns, we define the “U” value for reporting measurements. The “U” value is a ratio where the numerator is the sum of the concentrations of any set of **isotopologues** and the denominator is the concentration of the **unsubstituted isotopologue**. The letter “U” stands for “unsubstituted” and clearly differentiates this ratio from others. We write:

$$U^k = \frac{[\text{isotopologues } k]}{[\text{Unsubstituted Isotopologue}]}. \quad (2.24)$$

Our definition has several advantages relative to previous reporting methods. Its numerator is more general than the **clumped-isotope ratio**, allowing us to define U values for **singly-substituted isotopologues** (and sums of those). The denominator is fixed, simplifying comparison across different measurements. The U value has a clear relation to the **clumped-isotope ratio**. And as we will see, it has a clear relation to the **site-specific isotope ratio** and can be used to interpret fragmentation experiments (it could also apply to data generated by optical spectroscopy).

We further define categories of U values of particular interest. We first define an **isotope-specific U value**, where the numerator equals the sums of the concentrations of

the **singly-substituted isotopologues** for a given isotopic substitution. For example, in N<sub>2</sub>O, we have:

$$U^{15N} = \frac{[100] + [010]}{[000]}. \quad (2.25)$$

The **isotope-specific U value** is useful from an experimental perspective because it can be measured directly, requires observation of only two ion beams, and is easy to interpret and use. We also define a **site-specific U value**, where the numerator equals the sums of the concentrations of the **singly-substituted isotopologues** at given **site(s)**. For example, we may write the N<sub>outer</sub> **site** of N<sub>2</sub>O as:

$$U^{N_{outer}} = U^{100} = \frac{[100]}{[000]}. \quad (2.26)$$

We can define a **site-specific U value** for a multi-atomic **site** like N<sub>outer+inner</sub>:

$$U^{N_{outer+inner}} = U^{(0,1)0} = \frac{[(0,1)0]}{[000]}. \quad (2.27)$$

One note that deserves comment: ratios of U values may be used to represent the ratio of any combination of **isotopologues** in a sample; for example, in N<sub>2</sub>O:

$$\frac{[110]}{[100]} = \frac{[110]}{[100]} * \frac{[000]}{[000]} = \frac{U^{110}}{U^{100}}. \quad (2.28)$$

This observation may be useful when making measurements which do not measure the unsubstituted **isotopologue** directly. Finally, we may refer to an **isotopologue-specific** or **clumped U value**, where the numerator is a single **isotopologue** or **clumped isotopologue**.

#### 2.2.3.5 Connecting the U Value to the other isotope ratios; the Stochastic Assumption

We may relate U values to **site-specific** and **molecular average** isotope ratios. We begin by comparing the **site-specific U value** and the **site-specific isotope ratio**. Suppose we know the **site-specific isotope concentration** across every **site** of a molecule. We may write these concentrations  $[x_i]$ , where  $x_i$  gives the  $i$ -th **site** of the molecule. Now, assume these isotopes are randomly distributed across all **isotopologues**; we call this the **stochastic assumption** (or **stochastic distribution**). Then, we can compute the

concentration of any **isotopologue**, **a**, as the product of the **site-specific isotope concentrations**  $[x_i]$ :

$$[\mathbf{a}] = \prod_{i=1}^n [x_i] . \quad (2.29)$$

For example, for the **isotopologue** [102] of  $N_2O$ :

$$[102] = [^{15}N]_{N_{outer}} [^{14}N]_{N_{inner}} [^{18}O]_{O1}. \quad (2.30)$$

Under the **stochastic assumption**, the **site-specific isotope ratio** of a single-atom **site** is equivalent to the **site-specific U Value**. For example, for  $N_2O$ , we can expand  $U^{N_{outer}}$  to yield:

$$U^{N_{outer}} = \frac{[100]}{[000]} = \frac{[^{15}N]_{N_{outer}} [^{14}N]_{N_{inner}} [^{16}O]_{O1}}{[^{14}N]_{N_{outer}} [^{14}N]_{N_{inner}} [^{16}O]_{O1}} = \frac{[^{15}N]_{N_{outer}}}{[^{14}N]_{N_{outer}}} = R_{N_{outer}}^{15} \quad (2.31)$$

demonstrating  $U^{N_{outer}}$  and  $R_{N_{outer}}^{15}$  are equal. This holds in the general case, as the singly-substituted **isotopologue** and the **unsubstituted isotopologue** differ only at the **site** of interest. We write:

$$R_k^i \approx U^k \quad (\text{single atom site}). \quad (2.32)$$

Which is exact under the **stochastic assumption**. As we diverge from the **stochastic assumption**,  $R_k^i$  and  $U^k$  values will diverge; however, for clumped isotope anomalies in small molecules with amplitudes typical of natural samples, this divergence will be small. For a range of  $^{13}C$ ,  $^{15}N$ ,  $^{17}O$ , & D-containing clumped isotopologues, we find clumped isotope anomalies of  $\sim 100$  ‰ (measured as departures from the stochastic clumped isotope ratio) lead to divergences between R and U values of  $\leq 1$  ‰ for the **sites** which are rare-isotope substituted in the clumped isotope species in question, and much smaller for other **sites**. We are often justified in treating these ratios as identical. We direct the interested reader to our Appendix for a more detailed discussion of the limits of this approximation.

We can generalize this result to multi-atomic **sites** in the following way. Suppose we now treat  $N_{outer+inner}$  as a multi-atomic **site** of  $N_2O$ . Although we are assuming  $N_{outer}$  and  $N_{inner}$  are experimentally indistinguishable, we can still define **site-specific ratios**  $R_{N_{outer}}^{15}$  and  $R_{N_{inner}}^{15}$ , which exist but are not measurable. The **site-specific ratio**  $R_{N_{outer+inner}}^{15}$  may be approximated as the average of these, that is:

$$R_{Nouter+inner}^{15} \approx \frac{R_{Nouter}^{15} + R_{Ninner}^{15}}{2}. \quad (2.33)$$

The errors induced by this approximation will be small in most circumstances; for example, if  $\delta_{Nouter,AIR}^{15} = -50$  and  $\delta_{Ninner,AIR}^{15} = 50$ , then  $\delta_{Nouter+inner,AIR}^{15} = -0.009 \text{ ‰}$  (see Nomenclature for a definition of  $\delta$  values). This approximation is exact when the **site-specific isotope ratios** are equal,  $R_{Nouter}^{15} = R_{Ninner}^{15}$ ; we also comment that violations of this assumption are the origin of combinatorial isotope effects (Yeung, 2016). Under the **stochastic assumption**, we may replace the R values with U values, and conclude:

$$R_{Nouter+inner}^{15} \approx \frac{U^{Nouter} + U^{Ninner}}{2} = \frac{U^{Nouter+inner}}{2}. \quad (2.34)$$

We see the **site-specific isotope ratio** approximates the **site-specific U value** normalized by the number of atoms in the **site** of interest. A similar argument holds in the general case: consider a **site** with  $n$  atoms and let  $j$  index across these atoms. The **site-specific isotope ratio** is approximated *via*:

$$R_k^i \approx \frac{\sum_{j=1}^n R_j^i}{n} \quad (2.35)$$

where  $R_k^i$  is the **site-specific isotope ratio** and the  $R_j^i$  give the isotope ratios at each atom,  $j$ , within the **site**. As the isotope ratio for each atom is approximated by the U value for each atom, we may write:

$$\frac{\sum_{j=1}^n R_j^i}{n} \approx \frac{\sum_{j=1}^n U^j}{n} = \frac{U^k}{n} \quad (2.36)$$

where the approximation is exact under the **stochastic assumption**. We therefore conclude

$$R_k^i \approx \frac{U^k}{n} \quad (\text{multiatomic site}).(2.37)$$

The approximation is exact when the **stochastic assumption** holds and the isotope ratio at each atom within the **site** is identical. Our multi-atomic formula can be applied to the **molecular-average isotope ratio** by defining **site**  $k$  to include all  $n$  atoms of a particular element:

$$R^i \approx \frac{U^i}{n} \quad (\text{molecular average}). \quad (2.38)$$

#### 2.2.4. Calculating U Values From Mass Spectrometry Experiments

We next show how to relate U values to various MS experiments. U values are natural to use for MS experiments without fragmentation which observe many isotopic peaks simultaneously. Because isotopic peaks are observed based on mass and because the **unsubstituted isotopologue** has a unique mass, U values for the **isotopologues** corresponding to any observed ion beam may be computed by taking a ratio with the ion beam corresponding to the **unsubstituted isotopologue**. For example, if we looked at the methanol spectrum (without fragmentation), we could compute the **isotope-specific U values** for  $^{13}\text{C}$ , D,  $^{17}\text{O}$ , &  $^{18}\text{O}$  based on the intensity ratios of the relevant molecular ions; we could also compute U values for any clumped species we observed (experimentally, we may have to account for fractionation of different **isotopologues** via standardization; we discuss this further below). Moreover, U values are useful for experiments involving fragmentation of all **isotopologues** of a molecule (the entire **isotome**) and especially for experiments with mass selection and fragmentation (M+N experiments). In these cases, the appeal lies in the ease of calculation of U values from various measurements; because all U values have the same structure, it is simple to convert between, e.g., **isotope-specific U values** and **site-specific U values** for a given isotope, as well as between more unconventional data products and U values. We will now examine some specific cases of interest.

##### 2.2.4.1 Fragmentation and Observation

For fragmentation experiments where the entire **isotome** is fragmented and observed (Eiler et al., 2017; Cesar et al., 2019; Chimiak et al., 2021), the observed peaks give neither U values nor traditional isotope ratios, but closely approximate both. Suppose, for example, we wanted to measure  $U^{N_{inner}}$  by fragmenting  $\text{N}_2\text{O}$  to lose  $\text{N}_{outer}$  and observing the  $^{15}\text{N}$  and unsubstituted ion beams. Tracking fragmentation, our set is:



$$\mathbf{A} = \begin{array}{c} N_{outer} \quad N_{inner} \quad O_1 \\ \left( \begin{array}{ccc} 0 & 0 & 0 \\ 0 & 0 & 1 \\ 0 & 0 & 2 \\ 0 & 1 & 0 \\ 0 & 1 & 1 \\ 0 & 1 & 2 \\ 1 & 0 & 0 \\ 1 & 0 & 1 \\ 1 & 0 & 2 \\ 1 & 1 & 0 \\ 1 & 1 & 1 \\ 1 & 1 & 2 \end{array} \right) \xrightarrow{\text{Fragment}} \begin{array}{c} N_{outer} \quad N_{inner} \quad O_1 \quad \text{Substitutions} \\ \left( \begin{array}{ccc} x & 0 & 0 \\ x & 0 & 1 \\ x & 0 & 2 \\ x & 1 & 0 \\ x & 1 & 1 \\ x & 1 & 2 \\ x & 0 & 0 \\ x & 0 & 1 \\ x & 0 & 2 \\ x & 1 & 0 \\ x & 1 & 1 \\ x & 1 & 2 \end{array} \right) \left( \begin{array}{l} Unsub \\ {}^{17}O \\ {}^{18}O \\ {}^{15}N \\ {}^{15}N^{17}O \\ {}^{15}N^{18}O \\ Unsub \\ {}^{17}O \\ {}^{18}O \\ {}^{15}N \\ {}^{15}N^{17}O \\ {}^{15}N^{18}O \end{array} \right) \end{array}$$

Measuring the ratio of the observed  ${}^{15}N$  peak to the observed unsubstituted peak of the NO fragment yields:

$$\frac{\alpha_{15N}}{\alpha_{Unsub}} = \frac{[010] + [110]}{[000] + [100]} \quad (2.39)$$

where we write  $\alpha_x$  to give the observed abundance of the ion beam with substitution  $x$  (in a real experiment, this equality will be approximate due to fractionation). Under the **stochastic assumption**, we have

$$\frac{[010]}{[000]} = \frac{[110]}{[100]} \quad (2.40)$$

Using the fact that

$$\frac{a}{b} = \frac{c}{d} \Rightarrow \frac{a+c}{b+d} = \frac{a}{b} \quad (2.41)$$

we see

$$\frac{[010] + [110]}{[000] + [100]} \approx \frac{[010]}{[000]} = U^{Ninner} \approx R_{Ninner}^{15} \quad (2.42)$$

Thus, the measurement closely approximates the  $U$  value of interest.

If multiple atoms contribute to the numerator (via different **sites** or a single multi-atomic **site**), a similar argument holds. For example, if we instead fragmented and lost the  $O_1$  **site**, then measured the  ${}^{15}N$  and unsubstituted ion beams to compute  $U^{Ninner+outer}$ , then we have:

$$\frac{\alpha_{15N}}{\alpha_{U_{sub}}} = \frac{[100] + [101] + [102] + [010] + [011] + [012]}{[000] + [001] + [002]} \quad (2.43)$$

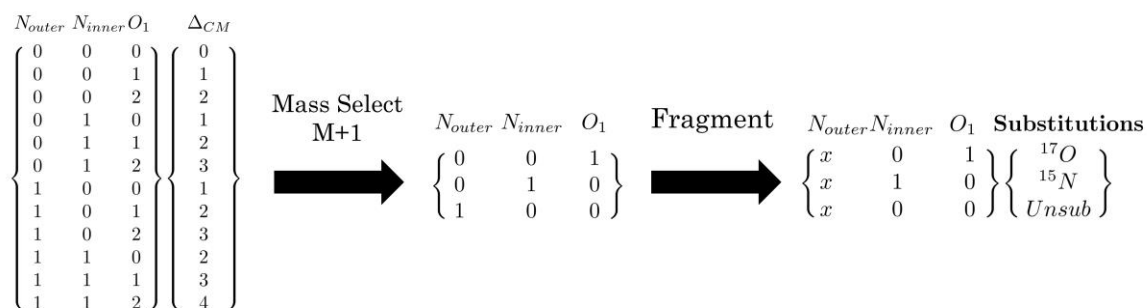
which we rewrite as

$$\frac{[100] + [101] + [102]}{[000] + [001] + [002]} + \frac{[010] + [011] + [012]}{[000] + [001] + [002]} \approx U^{100} + U^{010} = U^{Ninner+outer} \approx 2 * R_{Ninner+outer}^{15} \quad (2.44)$$

following the same logic employed above; as before, we approximate the U value of interest. In this case, the first equality is approximate as it depends on the **stochastic assumption**, while the third is approximate both because  $R_{Ninner}^{15}$  and  $R_{Nouter}^{15}$  may differ and due to the **stochastic assumption** (see eq 2.33). For the interested reader, a general version of this argument is presented in Chapter 3.

#### 2.2.4.2 Mass Selection, Fragmentation and Observation (“M+N Experiment”)

Next, we discuss the “M+N” experiment, where some subset of an **isotome**, with cardinal mass difference N relative to the **unsubstituted isotopologue**, is mass selected, fragmented, and observed via a MS/MS experiment (Neubauer et al., 2018). For example, suppose we performed a M+1 measurement with N<sub>2</sub>O where we fragment to lose the N<sub>1</sub> **site**. Following the nomenclature and ordering established above, we define  $f_{30} = [x, 1, 1]$ , where “30” gives the cardinal mass of the unsubstituted NO ion. Using the operations discussed above:



We observe three ion beams. We may calculate the **M+1 relative abundances** within the fragment ion population,  $\rho_{30, M+1}^x$  (or M+N relative abundance, for other experiments; 30 is the cardinal mass of the fragment) by taking the intensity of each ion beam z relative to the sum of the intensities of all ion beams of this fragment.

$$\rho_{30,M+1}^{17O} = \frac{Z_{17O}}{Z_{17O} + Z_{15N} + Z_{Unsub}} \quad (2.45)$$

$$\rho_{30,M+1}^{15N} = \frac{Z_{15N}}{Z_{17O} + Z_{15N} + Z_{Unsub}} \quad (2.46)$$

$$\rho_{30,M+1}^{Unsub} = \frac{Z_{Unsub}}{Z_{17O} + Z_{15N} + Z_{Unsub}} \quad (2.47)$$

We interpret these abundances as corresponding to **isotopologue concentrations**, noting again that when instrument fractionation occurs, this relationship will be approximate:

$$\rho_{30,M+1}^{17O} = \frac{[001]}{[001] + [010] + [100]} \quad (2.48)$$

$$\rho_{30,M+1}^{15N} = \frac{[010]}{[001] + [010] + [100]} \quad (2.49)$$

$$\rho_{30,M+1}^{Unsub} = \frac{[100]}{[001] + [010] + [100]} \quad (2.50)$$

Next, we define a “ $U^{M+1}$  value,” a U value where the numerator gives the sum of the concentrations of all M+1 substituted **isotopologues** (and likewise for M+2, M+3, ... M+N):

$$U^{M+1} = \frac{[100] + [010] + [001]}{[000]} \quad (2.51)$$

and thereby calculate **site-specific U values**:

$$\rho_{30,M+1}^{17O} * U^{M+1} = U^{001} \quad (2.52)$$

$$\rho_{30,M+1}^{15N} * U^{M+1} = U^{010} \quad (2.53)$$

$$\rho_{30,M+1}^{Unsub} * U^{M+1} = U^{100} \quad (2.54)$$

The  $U^{M+N}$  value is a mathematical trick which allows us to relate unconventional measurements to **site-specific U values** (and thus **site-specific isotope ratios**). Note, however, the implication—the M+N relative abundance measurements we make in a M+N experiment are directly proportional, and with the same proportionality constant, to the U values for the associated **isotopologues** (and approximately proportional to the corresponding **site-specific isotope ratios**, cf. eq 2.37). By manipulating U values, we can therefore understand the M+N measurement in terms of physically meaningful and widely understood isotope ratios.

To proceed, we must determine the  $U^{M+N}$  value. We suggest two ways to do so. First, we could measure  $U^{M+N}$  directly by performing an experiment which observes all

M+N peaks simultaneously with the unsubstituted peak, taking their ratio; e.g., for N<sub>2</sub>O,  $U^{M+N} = U^{15N} + U^{17O}$ . Second, we could measure some other  $U$  value (i.e., isotope-specific) and use it in conjunction with M+N relative abundance measurements to calculate  $U^{M+N}$ . For example, suppose we independently measured  $U^{15N}$ . Suppose also we know  $\rho_{M+1}^{15N} = \frac{[100]+[010]}{[100]+[010]+[001]}$ , the M+N relative abundance of the <sup>15</sup>N substituted **isotopologues** within the M+1 population (here, we omit the cardinal mass subscript as we are talking about the unfragmented population of **isotopologues**). Then, using the fact that

$$\rho_{M+1}^{15N} * U^{M+1} = \frac{[100] + [010]}{[100] + [010] + [001]} * \frac{[100] + [010] + [001]}{[000]} = \frac{[100] + [010]}{[000]} = U^{15N}. \quad (2.55)$$

We find

$$U^{M+1} = \frac{U^{15N}}{\rho_{M+1}^{15N}}. \quad (2.56)$$

For the experiment outlined above,  $\rho_{M+1}^{15N}$  is the sum  $\rho_{30,M+1}^{15N} + \rho_{30,M+1}^{Unsub}$ , so we can use this approach. In general, calculating  $U^{M+N}$  in this way requires that we can calculate  $\rho^x$  and  $U^x$  for some isotope  $x$ . In some cases, this may be possible using one of the fragments, e.g., fragment 30 here; in other cases, this can be done by observing  $U^x$  via direct measurement, then measuring the M+N spectrum of the compound *without* fragmentation, giving  $\rho^x$ .

Some implications of this strategy deserve further comment. First, we emphasize that  $U^{M+N}$  values do not depend on the fragment studied; for molecules with many fragments of interest, one may use the same  $U^{M+N}$  value for every fragment. This (perhaps counterintuitive) fact is a function of the M+N experimental design, which causes every fragment to sample the same set of **isotopologues**. We show this process in more detail in the following section. Second, a point of interest for M+1 and M+2 mass selections: as noted above, **isotope-specific U values** are closely approximated by **molecular average isotope ratios**. Many **molecular average isotope ratios** (<sup>13</sup>C or <sup>15</sup>N for M+1, <sup>18</sup>O or <sup>34</sup>S for M+2) can be measured at high precision. We can therefore use these

measurements to approximate  $U^{M+1}$  or  $U^{M+2}$  and apply this information to a M+N experiment. For example, with the  $N_2O$  measurement outlined above, our  $U^{15N}$  measurement may be an approximation based on a measurement of  $R^{15N}$ .

For a more involved example, suppose we perform an M+1 experiment on methanol, fragmenting to lose the -OH (as before). Following mass selection (the reader can verify), our set of **isotopologues** is:

$$\left\{ \begin{array}{cccc} C_{methyl} & O_{hydroxyl} & H_{hydroxyl} & H_{methyl} \\ 1 & 0 & 0 & (0,0,0) \\ 0 & 1 & 0 & (0,0,0) \\ 0 & 0 & 1 & (0,0,0) \\ 0 & 0 & 0 & (0,0,1) \end{array} \right\} \xrightarrow{\text{Fragment}} \left\{ \begin{array}{cccc} C_{methyl} & O_{hydroxyl} & H_{hydroxyl} & H_{methyl} \\ 1 & x & x & (0,0,0) \\ 0 & x & x & (0,0,0) \\ 0 & x & x & (0,0,0) \\ 0 & x & x & (0,0,1) \end{array} \right\} \left\{ \begin{array}{c} {}^{13}C \\ Unsub \\ Unsub \\ D \end{array} \right\}$$

Fragmentation results in 3 observed ion beams; for each, we may report M+1 relative abundances. Now, suppose that we have observed  $R^{13C}$  of methanol via some other mechanism; in this case, we may approximate  $R^{13C} \approx U^{13C}$ . From our measurement of the  $^{13}C$  ion beam, we know  $\rho_{M+1}^{13C}$ . Therefore, we may calculate:

$$U^{M+1} = \frac{U^{13C}}{\rho_{M+1}^{13C}}. \quad (2.57)$$

We may then apply  $U^{M+1}$  to our other M+1 measurements:

$$\rho_{15,M+1}^D * U^{M+1} = \frac{[0, 0, (0,0,1), 0]}{[0, 0, (0,0,0), 0]} = U^{Dmethyl} \quad (2.58)$$

$$\rho_{15,M+1}^{Unsub} * U^{M+1} = \frac{[0, 1, (0,0,0), 0] + [0, 0, (0,0,0), 1]}{[0, 0, (0,0,0), 0]} = U^{17O} + U^{Dhydroxyl}. \quad (2.59)$$

Commenting again that if we observed another fragment (e.g.  $COH^+$ ), we could apply the same  $U^{M+1}$  value to these results. In eq (58), we have used a  $R^{13C}$  measurement in combination with a M+1 experiment to constrain the site-specific isotope content of deuterium. That we can do so is a key benefit of the M+N experiment; we may rely on high-precision measurements of well-known properties to constrain more exotic ones. In eq (59), we constrain a sum of two U values; this represents actual knowledge about the isotopic structure of a molecule but is not interpretable in terms of commonly used isotope ratios. In some cases, we will have to interpret these constraints directly. In others, we may be able to use additional information to tease apart these constraints. For example, if we observed  $U^{17O}$  directly, we could calculate  $U^{Dhydroxyl}$  from eq (59). We

next discuss a common way to make (and combine) multiple information sources, *via* observation of multiple fragments of the same molecule.

### 2.2.4.3 Multiple Observations of a M+N Experiment

When making a M+N experiment with many fragments, we can combine information from multiple measurements using a linear system of equations to gain more in-depth knowledge about the **isotome**. For example, suppose we perform an M+1 mass selection/fragmentation experiment on N<sub>2</sub>O and observe  $f_{30} = [x, 1, 1]$  and  $f_{28} = [1, 1, x]$  as fragments. As before, the ordering is N<sub>outer</sub>, N<sub>inner</sub>, O<sub>1</sub>, and the fragments are NO and N<sub>2</sub>, respectively; the subscripts give the associated unsubstituted cardinal masses.

We begin by writing a vector  $I_{expt}$  for the M+N relative abundances of the **isotopologues** observed during the measurement; in this case, they are the M+1 substituted **isotopologues**:

$$I_{expt} = \begin{bmatrix} [100]_{M+1} \\ [010]_{M+1} \\ [001]_{M+1} \end{bmatrix} \quad (2.60)$$

where the subscript M+1 denotes a M+1 relative abundance, e.g.,

$$[100]_{M+1} = \frac{[100]}{[100] + [010] + [001]}. \quad (2.61)$$

Now, for each fragment, we have some set of M+N relative abundance measurements. We may write these as a vector  $\rho_{CM}$ , where CM gives the cardinal mass of the unsubstituted fragment:

$$\rho_{30} = \begin{bmatrix} \rho_{30}^{Unsub} \\ \rho_{30}^{15N} \\ \rho_{30}^{17O} \end{bmatrix} \quad \rho_{28} = \begin{bmatrix} \rho_{28}^{Unsub} \\ \rho_{28}^{15N} \end{bmatrix} \quad (2.62)$$

Finally, for each fragment, we may define a composition matrix  $C_{CM}$  taking relative abundances  $I_{expt}$  to the observed values in  $\rho_{CM}$  (i.e.,  $C_{CM}I_{expt} = \rho_{CM}$ ). For example:

$$C_{30} = \begin{bmatrix} 1 & 0 & 0 \\ 0 & 1 & 0 \\ 0 & 0 & 1 \end{bmatrix} \quad C_{28} = \begin{bmatrix} 0 & 0 & 1 \\ 1 & 1 & 0 \end{bmatrix} \quad (2.63)$$

For the  $f_{30}$  fragment, we have:

$$\begin{bmatrix} 1 & 0 & 0 \\ 0 & 1 & 0 \\ 0 & 0 & 1 \end{bmatrix} \begin{bmatrix} [100]_{M1} \\ [010]_{M1} \\ [001]_{M1} \end{bmatrix} = \begin{bmatrix} \rho_{30}^{Unsub} \\ \rho_{30}^{15N} \\ \rho_{30}^{17O} \end{bmatrix} \quad (2.64)$$

Which is the same system of equations given in eqs 48-50, above.

To combine information from multiple fragments, we concatenate the composition matrices and measurement vectors. As **isotopologue** concentrations are reported relative to the M+N population, we know their concentrations sum to 1 and may add a row to satisfy this principle of closure. Our final system of equations is:

$$\begin{bmatrix} 1 & 1 & 1 \\ 1 & 0 & 0 \\ 0 & 1 & 0 \\ 0 & 0 & 1 \\ 0 & 0 & 1 \\ 1 & 1 & 0 \end{bmatrix} \begin{bmatrix} [100]_{M1} \\ [010]_{M1} \\ [001]_{M1} \end{bmatrix} = \begin{bmatrix} 1 \\ \rho_{30}^{Unsub} \\ \rho_{30}^{15N} \\ \rho_{30}^{17O} \\ \rho_{28}^{Unsub} \\ \rho_{28}^{15N} \end{bmatrix}. \quad (2.65)$$

We can solve this matrix inversion problem through a variety of computational methods, e.g., a least-squared inversion algorithm or via Gauss-Jordan elimination. This will yield the M+1 relative abundances of any **isotopologues** we can constrain; we may compute the associated U values by using the  $U^{M+N}$  as discussed above. Finally, we note a conceptual point—the special case where we observe the full molecule may be formally treated as a “fragment,” i.e.,  $f_{full} = [1, 1, \dots, 1]$ , and we may combine this observation with observations of fragments as shown.

### 2.2.5. Experimental Issues Raised by the M+N Experiment

Thus far, our mathematically rigorous framework for M+N experiments has been developed using hypothetical examples and ignoring experimental issues; we next demonstrate how one might apply this framework to a real experiment to acquire detailed knowledge of a molecule’s **isotome**. To do so, we take methionine as a test molecule, as it has previously been studied by M+N measurements and because it has several fragments and many elements present (Neubauer et al., 2018). We begin by broadly outlining the experimental issues one encounters in making this measurement and

suggesting methods for dealing with these; in the appendix, we examine these issues in greater detail. We then present a simulated dataset for M+1 through M+4 measurements of methionine, giving over 100 constraints on its isotopic composition, and demonstrate what information can be gleaned from these observations. This exercise is guided by the authors' experimental observations of methionine; in a planned companion paper, we will apply this algorithm to experimental methionine data. The source code for our implementation of the algorithm and the simulated methionine datasets is available as a github repository; our code is generalizable to other M+N experiments and includes a tutorial for setting up new measurements (see Research Data, below).

To guide our discussion of experimental issues, we will examine a M+1 experiment for methionine where we observe the fragment at cardinal mass 61 ( $C_2SH_5$ ) (Figure 2.6). This ion beam has four isotopic peaks: Unsubstituted,  $^{33}S$ ,  $^{13}C$ , and D. We would like to report measurements of these ion beams using the nomenclature developed above for M+1 relative abundances, e.g.,

$$\rho_{61,M+1}^{13C} = \frac{Z_{13C}}{Z_{13C} + Z_D + Z_{15N} + Z_{Unsub}}. \quad (2.66)$$

We identify three main experimental issues—fractionation of observed ion beams, unobserved ion beams, and unresolved ion beams.



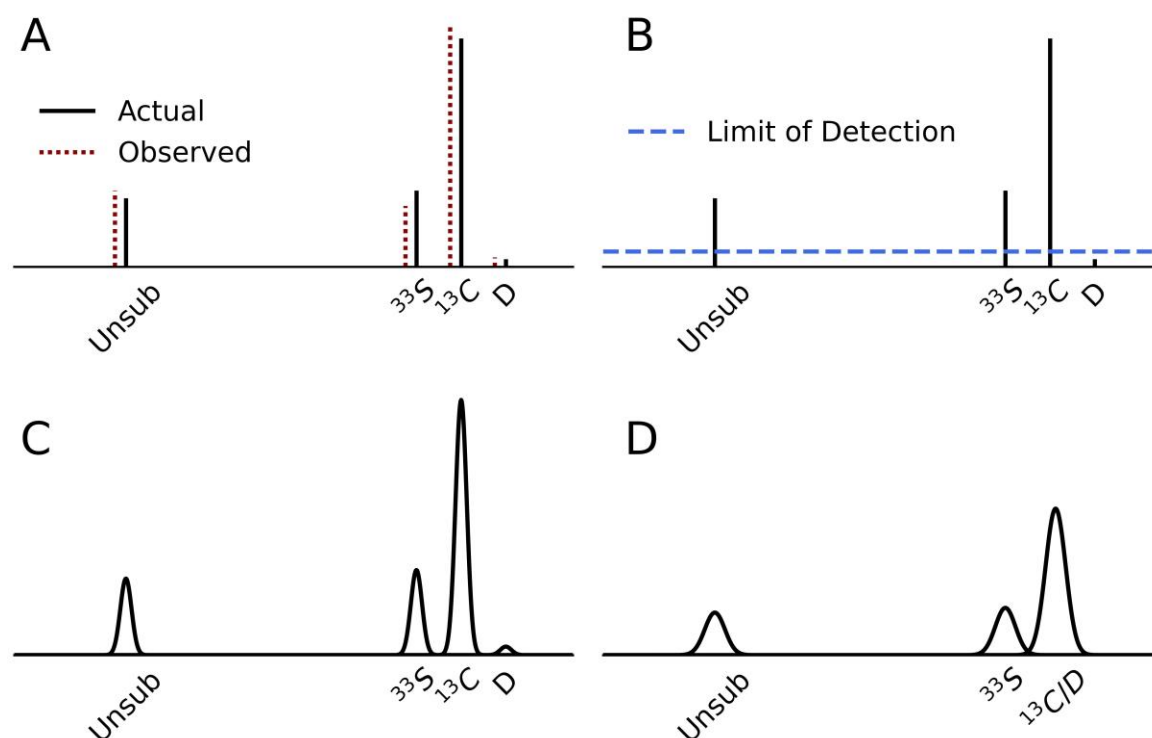


**Figure 2.6:** Some of the experimental issues encountered when making M+N measurements. A: Due to peculiarities of each instrument, the observed abundance for each ion beam will differ from its actual abundance. To deal with this, correction factors may be determined by measuring a standard; the sample composition may then be reported relative to that standard. B: In some cases, certain peaks may not be observed due to insufficient abundance. However, calculation of relative abundances assumes the denominator includes abundance of all peaks. Some correction factor must be applied to account for this difference. C: A spectrum with sufficient resolution to observe each peak. D: The same spectrum at lower resolution; in this case the  $^{13}\text{C}$  and D peaks are unresolved. It is not obvious how the abundances of these peaks combine; it could be a simple linear addition, or something more complex. We report this ion beam as belonging to the most abundant substitution ( $^{13}\text{C}$ ) and correct for the contribution from D as part of our correction for instrument fraction. If the heights of unresolved beams are similar or the sample and standard differ substantially, more involved correction schemes may be necessary.

First, we consider fractionation. Measurements of ion beam intensities in a mass spectrometer will generally not reflect the true abundances of relevant molecular isotopic species but may increase or decrease due to preferential production, transmission and/or detection of some ion beams relative to others (sometimes called ‘instrumental mass fractionation,’ though we refer here to any phenomenon that might bias relative ion beam intensities; Figure 2.6, A). For this reason, isotope ratio experiments compare measurements of a sample to measurements of a standard with known or assumed isotopic composition observed on the same instrument under the same conditions and

using the same methods, usually directly before and/or after a sample measurement. Standardizing in this manner for M+N experiments is difficult due to the premise that the standard has a known isotopic composition. In a M+N experiment, the M+N relative abundance of an ion beam (e.g.,  $^{13}\text{C}$ ) depends on the abundance of all other substitutions ( $^{33}\text{S}$ , D,  $^{15}\text{N}$ , etc.) as well as (for fragment ions) their distribution across non-equivalent sites; this kind of detailed knowledge of a standard will generally not be available. Nevertheless, we find we can effectively standardize by (1) hypothesizing the standard composition assuming plausible abundances for isotopic substitutions at every **site**; (2) calculating a spectrum for the standard in the absence of fractionation; (3) comparing this spectrum with the observed abundances to calculate fractionation factors for each ion beam of the standard; and (4) applying these fractionation factors to the sample. While this method uses a hypothesized standard composition which will often be wrong, we find it is sufficient to report accurate comparisons of U values between sample and standard and the data products downstream of these (site-specific and clumped delta values, such as  $\delta_{STD}^{13C}$  for carbon **sites**); if specific U values of the standard are known in a separate reference frame (e.g.,  $\delta_{PDB}^{13C}$  of a specific carbon **site**), we can report the calculated values of the sample in the same reference frame.

The interested reader is directed to the appendix for a detailed analysis.

Second, we address experimental difficulties caused by unobserved ion beams. Reporting results using the nomenclature developed above for M+N relative abundances assumes that we observe every ion beam of a particular fragment (else we cannot calculate the denominator of the  $\rho_{CM}$  value); however, certain ion beams may be sufficiently rare that they cannot be observed (Figure 2.6, B). For example, in the 61 ion beam of methionine, we may be unable to observe the D ion beam due to low abundance; rather than relative abundances, we can only calculate results of the form:

$$\frac{Z_{13C}}{Z_{13C} + Z_{15N} + Z_{Usub}}, \quad (2.67)$$

i.e., the actual result multiplied by

$$\frac{Z_{13C} + Z_D + Z_{15N} + Z_{Usub}}{Z_{15N} + Z_{Usub} + Z_{13C}}. \quad (2.68)$$

To change these results into M+N relative abundance we apply a correction factor, which will be equal to (assuming fractionation has been corrected for):

$$\frac{Z_{15N} + Z_{Unsub} + Z_{13C}}{Z_{13C} + Z_D + Z_{15N} + Z_{Unsub}}. \quad (2.69)$$

Generally, we will not know this correction factor, but we can approximate it. We may do so by using a forward model of the isotopic abundance, using experimental constraints from other observations, or by combining the two to iteratively update our forward model. These methods are discussed in detail in the appendix.

Third, we address the issue of unresolved peaks. Often, two peaks will be close enough in mass that they cannot be distinguished by our mass spectrometer; rather than observing either peak individually, we observe them in combination (Figure 2.6, C & D). This issue is perhaps the most difficult to address; the best correction depends on some knowledge of which ion beams combine and how they combine, which will necessarily differ from instrument to instrument and possibly from sample to sample. We suggest the following general correction, which we expect to fail in certain scenarios, but believe will be broadly applicable to many experiments: we assign observed peaks to the most abundant ion beam observed near that mass and treat changes in height caused by unresolved ion beams as instrumental fractionation, folding our correction of it into our calculation of the fractionation factors. This method assumes that (1) unresolved beams combine in the same way across sample and standard (which we think is plausible and allows us to proceed without knowing precisely how this occurs); (2) that the relative abundances of the less abundant peaks are broadly similar across sample and standard (e.g., if a  $^{13}\text{C}$  and D ion beam are unresolved, the D content of sample and standard are assumed to be similar); and (3) that the less abundant peaks are small in magnitude relative to the larger ones (meaning changes in their abundance from sample to standard will have a small effect on the observation). The key benefit of our approach is the ease of application to many new targets—we do not have to assume anything about which peaks are unresolved, how they combine with each other, or what the isotopic abundance of any species is. If one had more detailed knowledge of the system in question, one could suggest better correction schemes. For example, consider the  $^{17}\text{O}$  correction performed

for CO<sub>2</sub> carbon isotope measurements (Brand et al., 2010). In this scenario, the <sup>13</sup>C and <sup>17</sup>O ion beam are unresolved; however, because they are assumed to combine additively, e.g.,  $Z_{13C \& 17O} = Z_{13C} + Z_{17O}$ , and because the <sup>17</sup>O content can be closely approximated *via* measurement of <sup>18</sup>O, a reasonable approximation of the <sup>17</sup>O signal can be subtracted out of the <sup>13</sup>C beam. We suspect these sorts of correction schemes will be applicable to M+N measurements in the future, for specific cases where similarly useful constraints can be assumed. At present, because our algorithm must correct for many unresolved beams simultaneously (~100s, across all M+N experiments for the methionine dataset) and because not all of the experimental details are known for the method we are using to execute the actual measurement (Orbitrap<sup>TM</sup>-MS; e.g., do unresolved ion beams combine additively?), we leave these more detailed corrections for future work. A more detailed discussion of this topic is presented in the appendix.

### 2.3. Results

To demonstrate the amount of information one may extract, the accuracy and precision of the reconstructed isotopic structure, and the effects of the experimental issues outlined above, we simulated methionine datasets under a range of conditions and applied our methods to these data. We simulated M+1, M+2, M+3, and M+4 experiments for a sample and standard, measuring fragments at cardinal mass 56, 61, 102, 104, and 133, in addition to the full molecule (Figure 2.7). We additionally computed U values for  $U^{13C}$ ,  $U^{34S}$ ,  $U^{15N34S}$ , and  $U^{36S}$ , which we use to calculate  $U^{M+N}$  values. Our choice of which measurements to simulate are guided by experiment; these fragments have well-studied fragmentation pathways, meaning the **sites** they sample are well known, and they have previously been used to constrain methionine's isotopic structure (Neubauer et al., 2018; Zhang et al., 2019). Moreover, we have successfully made observations for each M+N experiment we examine, and plan to present these results in a companion paper.

To evaluate the experimental issues discussed above, we generated simulated datasets modeling these issues. We present six datasets, each including the full suite of M+N measurements (Table 2.1). These include 1) an "ideal" dataset with all peaks

observed precisely and accuracy; 2) the same with measurement errors of 1 ‰ on all M+N observations and 0.1 ‰ for the  $U$  values; including these measurement errors, we then evaluated 3,4,5) each experimental issue (instrument fractionation, low abundance peaks, unresolved peaks) individually and then 6) evaluated all issues in combination. The sample and standard compositions used throughout are shown in Table 2; clumped species were computed following the **stochastic assumption** (Table 2.2).

We modeled the experimental issues as follows. For instrument fractionation, we assumed each ion beam fractionated identically for the sample and standard, multiplying its intensity by a factor randomly chosen from  $\mathcal{N}(1,0.05)$ . For low abundance peaks, we assumed any peak with a M+N relative abundance of < 1% within the family of peaks associated with an individual fragment was not observed. For unresolved peaks, we assumed our experimental resolution was 120,000 at every mass; peaks with insufficient mass separation to be distinguished at this resolution were combined linearly in our observed spectrum.

**Table 2.1: Description of Simulated Datasets**

<b>Synthetic Dataset</b>	<b><i>Standard Composition Known?</i></b>	<b><i>Instrument Fractionation Occurs?</i></b>	<b><i>Omit Low Abundance Peaks?</i></b>	<b><i>Unresolved Peaks?</i></b>	<b><i>Experimental Error?</i></b>
<b>1) Perfect Measurement</b>	Yes	No	No	No	No
<b>2) Experimental Error</b>	Yes	No	No	No	Yes
<b>3) Instrument Fractionation Test</b>	No	Yes	No	No	Yes
<b>4) Low Abundance Test</b>	Yes	No	Yes	No	Yes
<b>5) Unresolved Test</b>	Yes	No	No	Yes	Yes
<b>6) All Issues Combined</b>	No	Yes	Yes	Yes	Yes

**Table 2.2: Simulated Methionine Structure**

Site	# Atoms	$\delta_{STD}$	$\delta_{SMP}$
C <sub>methyl</sub>	1	-30	-45
C <sub>gamma</sub>	1	-30	-35
C <sub>alphabeta</sub>	2	-30	-30
C <sub>carboxyl</sub>	1	-30	-25
O <sub>carboxyl</sub> (17/18)	2	0/0	-13/-25
S <sub>sulfur</sub> (33/34/36)	1	0/0/0	2.5/4.854367/9.223391
N <sub>amine</sub>	1	0	10
H <sub>methyl</sub>	3	0	-250
H <sub>gamma</sub>	2	0	-100
H <sub>alphabeta</sub>	3	0	0
H <sub>amine</sub>	2	0	100
H <sub>hydroxyl</sub>	1	0	250
H <sub>protonated</sub>	1	0	0

The scope of this M+N measurement strategy can be seen *via* the dataset with all experimental issues, which is most representative of a real dataset. This synthetic measurement gives a total of 170 constraints on our sample's **isotome**; 4 full molecule U values as well as 24 M+1, 35 M+2, 48 M+3, and 58 M+4 observations. Some of these constrain the same property; for example, observations of the abundance of  $^{15}\text{N}$  in the 56, 102, 104, and full fragments of the M+1 experiment all give  $\rho_{M+1}^{15\text{N}}$ , the M+1 relative abundance of  $^{15}\text{N}$ . By counting only unique observations of new properties, we have 17 M+1, 29 M+2, 44 M+3, and 50 M+4 constraints; combined with the full molecule U values, this gives us 144 unique observations. These constraints are visualized in Figure 2.7, C, which shows which ion beams were observed and indicates those which were not observed due to low abundance or poor resolution. An isotopic substitution is only included in Figure 2.7, C if at least one ion beam with that isotopic substitution is observed for that M+N experiment; certain isotopic substitutions may not be included (e.g., *DDD* in the M+3 experiment). This illustrative example demonstrates how much information is available for a single molecule and how an M+N measurement strategy can yield high-dimensional information about a sample's **isotome**.

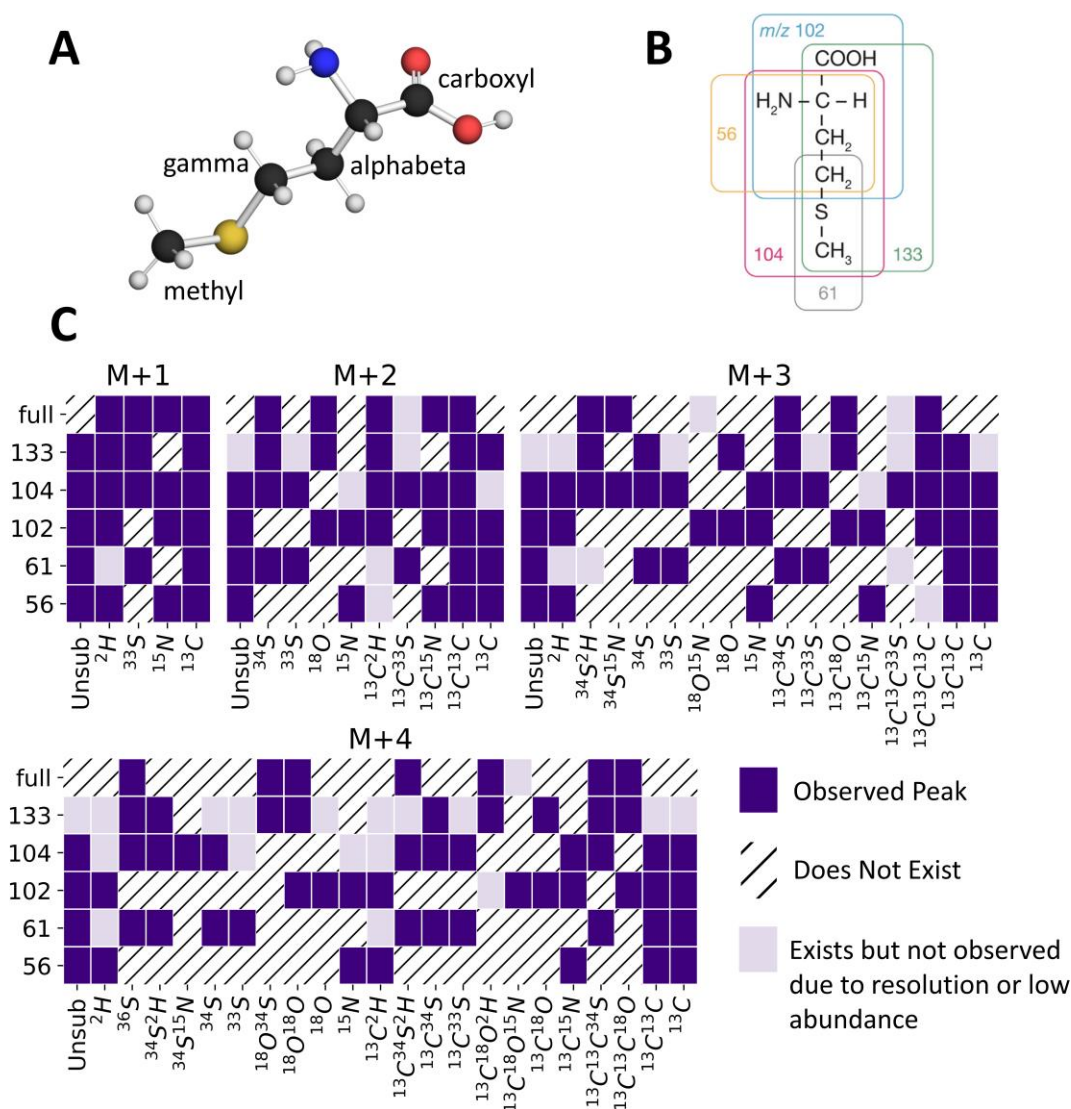


**Figure 2.7:** The observations for our simulated experiment. A: The methionine molecule and our definition of the sites of methionine. Sulfur, nitrogen, and oxygen each have a single site for all atoms of those elements. Carbon and hydrogen **sites** are defined according to the labels. There is also a hydrogen “protonated” site, for the proton picked up in an electrospray ionization mass spectrometry experiment, the experimental technique used in measurements for the companion paper. B: The subgeometries sampled by the fragments of methionine. Reprinted from Neubauer et al. 2018; used with permission. C: Observed isotopic peaks for each fragment of each M+N experiment. Purple boxes give observed peaks. Light purple boxes give substitutions that exist in the fragment but are unobserved due to insufficient resolution and/or abundance. Hatched boxes give substitutions which do not exist in those fragments.

We next evaluated the effect of experimental issues on our methodology. In Figure 2.8, we show computed results after processing each simulated dataset. We first

show a representative result for the simplest data product we can provide, the directly observed sample/standard comparison of  $\rho_{M+N}$  values. We here show results for the 61 fragment; there are no data for deuterium when low abundance is taken into account. These data show which errors are present in the raw data themselves; for many reported **isotopologue-specific U values**, the errors will be larger due to the convolution of errors from multiple observations used to constrain that **isotopologue**. Next, we show the **site-specific** and **clumped isotopologue ratios** we constrain; in all cases, these results are given after applying our corrections for the experimental issues present (a “theoretical,” “iterated” correction process with  $N = 50$  and  $\sigma=0$  for  $M+1$ , and a “theoretical” correction process with  $N = 1$  and  $\sigma = 0.001$  for the remaining  $M+N$ ; see Appendix for details). We only show values that are constrained in all simulations; in certain cases, e.g., the simulation with no experimental problems, we constrain other **clumped isotopologues** as well. For the **isotopologues** we present, the sample/standard comparisons ( $\delta_{STD}^{SMP}$ ) are reported as the ratio between U values for the relevant **isotopologues**, e.g.,

$$\delta_{STD}^{SMP} C_{methyl} = 1000 * \left( \frac{U_{SMP}^{C_{methyl}}}{U_{STD}^{C_{methyl}}} - 1 \right).$$

In cases where the U value of the standard is known, these could be given relative to widely used isotope standards (VPDB for carbon, AIR for nitrogen, VSMOW for oxygen and hydrogen, etc.) As the standard is not known in all cases, we give results only relative to the standard (i.e., by definition, the standard represents 0 on the delta scale for that property, and only relative differences between samples, each measured vs. that standard, could be said to have interpretable significance).

## 2.4. Discussion

### 2.4.1. Recovered Constraints from M+N Experiment

Our results for the synthetic M+N experiment on methionine (Figure 2.8) show how our recovered values change with different experimental issues. First, we examine the directly observed  $\rho_{M+N}$  values. For the 61 ion beam, accounting for instrument fractionation causes no noticeable increase in error. There are no unresolved peaks for



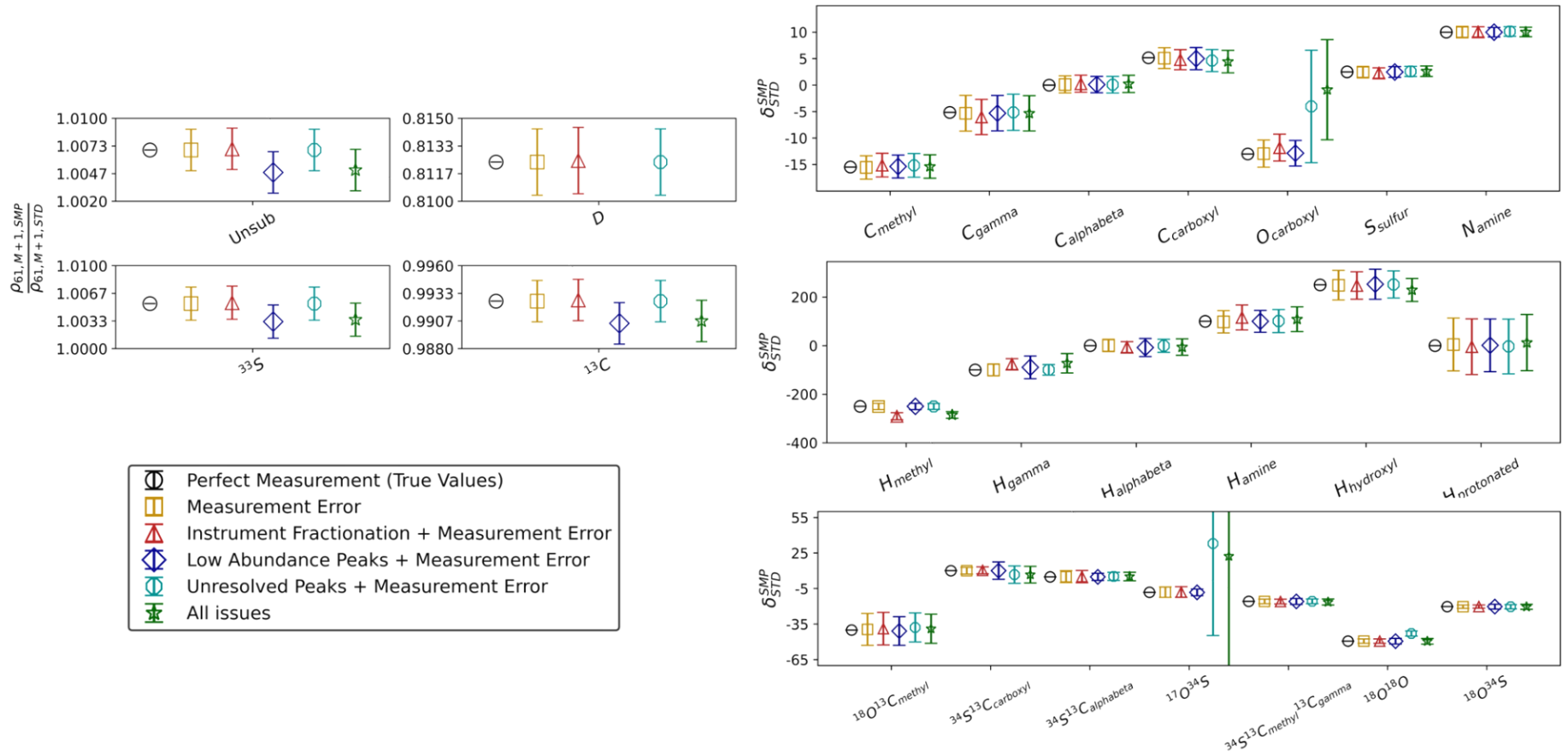
this measurement, so that issue does not affect these results. The loss of the deuterium beam when low abundance peaks are accounted for does decrease our accuracy—in this case, by decreasing the observed ratio by  $\approx 1\sigma$  for all other observed substitutions. This is due to differences in the M+1 relative abundance of deuterium between sample and standard; in the sample it accounts for  $\sim 0.9\%$ , while in the standard it is  $\sim 1.1\%$ , with the lower value for the sample coming primarily from its lesser content of deuterium at the **sites** ( $H_{\text{methyl}}$  and  $H_{\text{gamma}}$ ) sampled in this fragment. Our observed M+1 relative abundances in the case of the sample are multiplied by a factor  $\approx \frac{1}{1-0.009}$ , while for the standard by  $\approx \frac{1}{1-0.011}$  (c.f. eq (68), substituting  $\rho$  for  $z$  and noting the sum of the  $\rho$  equals 1). The larger factor for the standard shifts the observed M+1 relative abundances for the standard closer to those for the sample, causing the size of the difference to decrease (we correct for this effect when computing site-specific values, but not for this raw data product). As this error is a mathematical consequence of unobserved peaks, it will be consistent and replicable across the same experimental design. Therefore, while we caution against interpreting these values directly as accurate comparisons of M+N relative abundance ratios, they will still be useful for high dimensional chemical forensics. Finally, we note that for fragments where unresolved peaks are an issue, they present both the same issue (the M+N relative abundance of unresolved peaks is not observed) and an additional one (when unresolved peaks combine, if the height of the minor, unobserved, peak differs notably between sample and standard, this will be measured as a change in the height of the major, observed peak). Our interpretation is similar; without correcting for these effects, these results should not be interpreted as accurate M+N relative abundance ratios; however, they remain useful for distinguishing different samples of the same compound and may be applicable for determining fingerprints of different physical or chemical processes.

Next, we turn to the **site-specific** values. For most **sites**, experimental issues do not noticeably affect our results; our corrections effectively deal with these problems. Notable exceptions are 1) the  $O_{\text{carboxyl}}$  **site**, which is poorly constrained in the case of unresolved peaks; this is unsurprising, as  $^{17}\text{O}$  cannot be directly observed for any fragment

at a resolution of 120,000, so that  $O_{\text{carboxyl}}$  is not constrained by any measurement, but only by closure, in this scenario; and 2) the  $H_{\text{methyl}}$  **site**, where the result is low by  $\approx 30\%$  due to instrument fractionation. In no case do the deviations observed for low abundance peaks in the  $\rho_{M+N}$  values result in a missed **site-specific** result, although there is an increase in error for  $H_{\text{gamma}}$  due to this effect. The results for the clumped **isotopologues**, which are basically analogous; the  $^{17}\text{O}^{34}\text{S}$  result becomes poorly constrained when resolution is considered, for the same reason as the  $O_{\text{carboxyl}}$  **site**. Overall, we find our correction scheme is robust for most experimental issues for most **sites**. The issues that do occur appear idiosyncratic to the problem of interest—we suggest that future experimental work include this sort of theoretical analysis to examine which experimental issues create problems for that system.

The recovered error bars for each constraint convolve errors from several different sources; this includes 1) experimental error on the  $\rho_{M+N}$  value for both sample and standard; 2) errors inherent to our correction process for the  $\rho_{M+N}$  values for each experimental issue; 3) errors from each  $\rho_{M+N}$  value used to calculate the composition of a single **isotopologue**; and 4) errors on the  $U^{M+N}$  value used to compute **site-specific** or **clumped** U values. As noted, the errors in our simulation from (1) are  $1\%$  for both sample and standard, hence their ratio has an error of  $1.41\%$  ( $\sqrt{2}$ ). From Figure 2.8, we find errors induced by (2), at least for the 61 fragment, to be minor. (3) accounts for much of error in our final values, and depends on the **site**; for example, for carbon, some error bars ( $C_{\text{alphabet}}$ ) are close to those for the direct measurements, while others ( $C_{\text{gamma}}$ ) are notably larger. The error from (4) is minor in our results, as we asserted an error of  $0.1\%$  for each  $U^{M+N}$  value. Increases in the error of the  $U^{M+N}$  value used will cause proportionally larger errors in the reported results; for example, if the error of the  $U^{M+3}$  value were  $3\%$ , we would expect an increase of  $\approx 3\%$  in the error of the  $^{34}\text{S}^{13}\text{C}_{\text{carboxyl}}$  result.

1



2 **Figure 2.8:** Several data products from the M+N experiment on methionine evaluated with a range of experimental issues. Top Left: A representative sample of  
 3 the raw data product, a sample/standard comparison of the M+N relative abundances for the different isotopes of the 61 ion beam in the M+1 experiment. We  
 4 find instrument fractionation causes no notable increase in error, while there are no unresolved peaks that would cause an effect. The loss of the deuterium  
 5 ion beam shifts the other results down by  $\approx 1\sigma$ , due to the difficulty of estimating the right correction factor (see the Appendix for a detailed discussion). Right:  
 6 The sample standard comparisons of **site-specific** and **clumped** U values. In general, our treatment of experimental issues is robust and we recover accurate  
 7 values despite these problems. Exceptions are the  $\text{O}_{\text{carboxyl}}$  and  $^{17}\text{O}^{34}\text{S}$  results, which become poorly constrained at our simulated resolution of 120,000 because  
 8 the associated ion beams are not directly observed, and the **isotopologues** must be computed via closure. We also see deviations for  $\text{H}_{\text{methyl}}$  due to instrument  
 9 fractionation.

### 2.4.2. Using Directly Measured Constraints: Application to Mixing

In some cases, the involved process of reconstructing **isotopologue concentrations** may be unnecessary, and the directly observed data from a M+N experiment may be used; an example case is the mixing of two isotopically distinct reservoirs of the same compound. Mixing of two reservoirs will cause subtle deviations from the **stochastic distribution** in the mixed product, and these deviations can be seen directly in an M+N experiment. To show this, we examine hypothetical measurements of mixed N<sub>2</sub>O samples (Table 2.3). As endmembers, we take tropospheric N<sub>2</sub>O and soil-derived N<sub>2</sub>O; the latter's composition varies based on local conditions, so we select one possible composition which differs significantly from the troposphere, that of N<sub>2</sub>O from Amazon rainforest soil examined by Pérez et Al. (Pérez et al., 2006; Toyoda et al., 2013). We compute three separate mixed populations (Table 2.3) with varying amounts of each endmember. Deviations from the **stochastic distribution** for each isotopologue in the mixed population are shown in Figure 2.9, left. Here,  $\delta_{STOCH}^{MIX} = 1000 \left( \frac{[a]_{MIX}}{[a]_{STOCH}} - 1 \right)$  where [a] gives the concentration of an **isotopologue** of interest. The tropospheric endmember is enriched at each **site** relative to the soil population, so in the mixture, concentrations of **isotopologues** with two or more heavy substitutions are increased relative to the **stochastic distribution**. (If this is nonobvious, imagine mixing two **stochastically distributed** N<sub>2</sub> endmembers, where one has [<sup>15</sup>N] = 0, and the other has [<sup>15</sup>N] = 2x. The mixed product has [<sup>15</sup>N] = x. If this were distributed stochastically, [<sup>15</sup>N<sup>15</sup>N] = x<sup>2</sup>. However, in the mixture, [<sup>15</sup>N<sup>15</sup>N] =  $\frac{1}{2} [^{15}N^{15}N]_{FIRST} + \frac{1}{2} [^{15}N^{15}N]_{SECOND} = \frac{1}{2} (0)^2 + \frac{1}{2} (2x)^2 = 2x^2$ . Hence, the mixture is enriched in the clumped isotopologue). The size of this increase is a function of the amount of enrichment at each individual **site** and hence largest for the doubly-<sup>15</sup>N substituted **isotopologues**. These deviations may be measured in an M+N experiment; in Figure 2.9, right, we show the increases in M+N relative abundances which would be observed by a sample/standard comparison of the mixture (sample) versus N<sub>2</sub>O with the same **site-specific**

concentrations and the **stochastic distribution** (standard); note the effects could be observed with a different standard. The magnitudes of the effect are smaller—in some cases substantially smaller—than the relative changes in concentrations themselves. One example of this is the  $^{15}\text{N}^{18}\text{O}$  **isotopologue**, where the increase in concentration of the  $^{15}\text{N}^{18}\text{O}$  substituted **isotopologues**,  $\sim 0.5\text{‰}$ , is not observed in the M+3 experiment. We attribute this to the large absolute abundance of the  $^{15}\text{N}^{18}\text{O}$  **isotopologue** in that experiment,  $>99.9\%$ , which suppresses changes in the relative abundance of this **isotopologue**. There is some dependence on mixing ratio, with a 50/50 ratio causing the largest deviations. The changes are apparent for multiple **isotopologues** across a range of mixing ratios, and this type of measurement may be useful in confirming the existence of and constraining the amount of mixing in a sample.

We do not intend this example to be a definitive discussion of this topic—indeed, we anticipate that M+N experiments can show deviations between samples and the **stochastic distribution** for that sample for all sorts of reasons, including diffusion, mixing, photochemistry, reaction history, and more. The peculiarities of how each process will affect the **isotome**, and how that will be observed *via* this measurement strategy, must be developed for each of these cases. However, we believe this example shows a ‘tip-of-the-iceberg,’ hinting at new possibilities—and recall that for some samples, we may have an order of magnitude more measurements than we show for  $\text{N}_2\text{O}$ . Consider, for example, the mixing of an amino acid highly enriched at a certain carbon position with another with moderate or no enrichment at a single carbon, as might happen in extraterrestrial environments (Chimiak et al., 2021)—the M+N experiment may show that mixing occurred, constrain the proportions of mixing, and determine the content of the endmembers. More work must be done to investigate the applicability and limitations of this method.

Table 2.3: Mixing of N<sub>2</sub>O Endmembers

Site-specific Composition <sup>i</sup>	Tropospheric N <sub>2</sub> O (Toyoda et al., 2013)	An Amazon Rainforest Soil N <sub>2</sub> O (Pérez et al., 2006)	25 % soil, 75% troposphere	50 % soil, 50% troposphere	75 % soil, 25% troposphere
$\delta_{N_{outer}}^{15}$	-11.76	-72.7	-27.0	-42.2	-57.5
$\delta_{N_{inner}}^{15}$	25.14	-54.4	5.3	-14.6	-34.5
$\delta_O^{18}$	44.28	14.7	36.9	29.5	22.1

i:  $\delta_O^{17}$  was set by mass scaling with  $^{18}\text{O}$  assuming a mass exponent of 0.52.

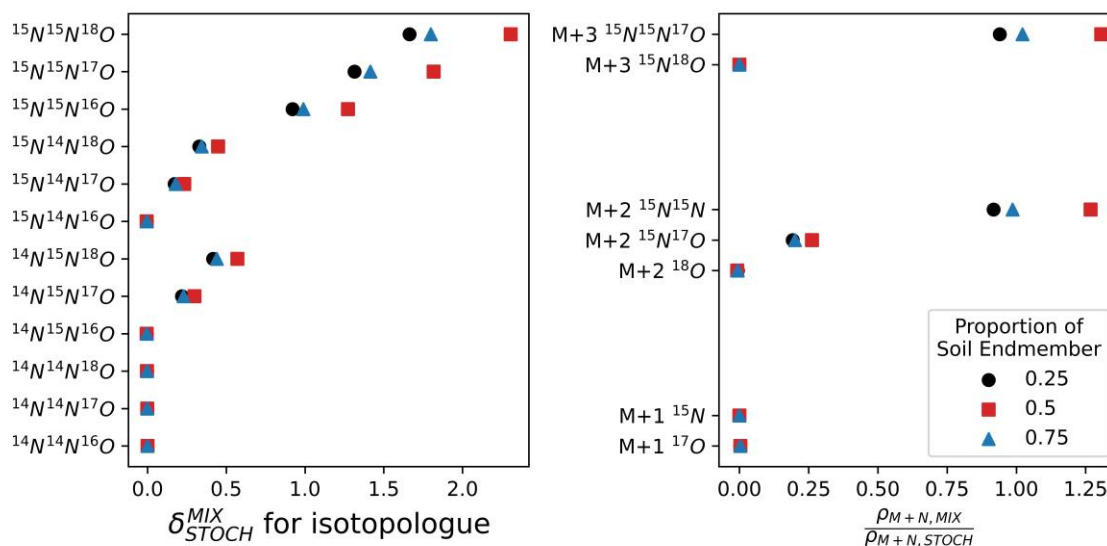


**Figure 2.9:** Comparison between N<sub>2</sub>O isotomes with the same site-specific concentrations; MIX comes from mixing of tropospheric and soil derived N<sub>2</sub>O, while STOCH follows the stochastic assumption. Left: Delta values for the change in concentration of each isotopologue;  $\delta_{STOCH}^{MIX} = 1000 \left( \frac{[a]_{MIX}}{[a]_{STOCH}} - 1 \right)$  where [a] gives the concentration of the isotopologue. Right: Comparisons in M+N relative abundance space for three experiments: M+1, M+2, and M+3. M+N relative abundance space is defined above, eq (45-47). Changes are largest for those observations associated with isotopologues with large changes, e.g.,  $^{15}\text{N}^{15}\text{N}$ , and smaller for substitutions that contribute more of the M+N relative abundance for an experiment (e.g.,  $^{15}\text{N}^{18}\text{O}$ , which is >99.9% of the signal for a M+3 experiment).

### 2.4.3 Computational Speed

An unavoidable problem with studies of molecular isotomes is the rapid increase in the number of isotopologues of a molecule as molecular size increases; this has made the

polynomial expansion method for spectrum prediction, which we adapt, intractable for, e.g., proteins. To demonstrate typical complexities for different molecular sizes, consider that methionine, with **sites** defined as we do, has 663,552 **isotopologues**; a small protein, insulin, has somewhere between  $1.44 \times 10^{12}$  and  $3.8 \times 10^{252}$  **isotopologues**, depending on how we define the **sites**. Our treatment is feasible for molecules the size of methionine—computing all **isotopologues** takes on the order of 30 seconds on a personal computer—but fails for larger molecules. At this point, we note another benefit of the M+N approach—as we mass select a small subset of the **isotopologues**, we need only compute and store information about that population. Computing the M+1 population for methionine (13 **isotopologues**) is essentially instant, while the M+1 population of insulin has at most 789 **isotopologues**—and likely fewer given that many **atomic positions** will be indistinguishable and can be treated as the same **site**—so this style of experiment may be applicable even to such targets. At the same time, for many applications, we may use the directly measured composition space, the  $\rho_{M+N}$  values, rather than computing **isotopologue-specific concentrations**, further simplifying the problem. We expect computational complexity to be an ongoing but often tractable concern.

## 2.5. Conclusions

There are two main ideas presented in this work: first, a generalized framework for treating measurements of molecular **isotomes**, which is applicable to a broad range of experiments; second, a specific treatment of the M+N experiment, which will enable further measurements of this type. Our framework for tracking **isotopologues** is applicable to a wide variety of experiments on small molecules and we expect will provide a unified way to understand diverse measurements. With respect to the M+N measurements, the most practicable insight is that the M+1 algorithm can immediately be applied to many small molecules; it is conceptually straightforward (and computationally easy) and deals with no more than a few dozen isotopologues, while the algorithm is general and can be used for many different targets on many different instruments. We expect this sort of

experimental design to become more widespread in the near future. Beyond this, the results from our M+2, M+3, and M+4 experiments suggest a diverse range of measurable properties. The isotope effects caused by mixing are a clear target, and other processes, such as diffusion or photochemical destruction, will have signature effects on molecular **isotomes**. Sorting out how these processes affect measured values requires a rigorous understanding of what **isotopologues** are being measured and how; we hope that the mathematics developed here will be useful in analyzing future work.

### **Acknowledgements**

We thank Cajetan Neubauer, Gabriella Weiss, Elliott Mueller, Guannan Dong, Elise Wilkes, Laura Chimiak, Nivedita Thiagarajan, Sarah Zeichner, Renée Wang, and Surjyendu Bhattacharjee for their helpful discussion on the content of this manuscript. We also thank Fenfang Wu for the assistance with the EA-IRMS measurements. Finally, we thank Max Lloyd, Guannan Dong, Peter Martin, and Sarah Zeichner for their contributions to the data processing scripts used in this article.

### **Funding**

This work was supported by the Simons Foundation, Award Number 626103 and DOE-BES funding to JME.

### **Data Availability**

Research data associated with this article, including simulated datasets and code to run our algorithm, can be accessed at <https://doi.org/10.5281/zenodo.6415852> as well as at <https://github.com/Csernica/Isotomics/tree/v1.0.0>. We include a tutorial that guides new users through the software to apply to their own projects.



## Supplementary Material for Chapter 2

### S2.1. “Isotopologue” vs “Isotopocule” and our Definition of Site

Recent definitions for describing isotopic content distinguish between “isotopologue” and “isotopocule” as:

- 1) Isotopologue: Molecular species that differ only in isotopic composition (number of isotopic substitutions) and relative molecular mass, e.g.,  $C^{35}Cl_4$ ,  $C^{35}Cl_3^{37}Cl$ ,  $C^{35}Cl_2^{37}Cl_2$ .
- 2) Isotopocule: Molecular species that only differ in either the number or positions of isotopic substitutions.

Both definitions are from (Coplen, 2011). Our definition of **site** and our definition of **isotopologue** put us in between these definitions. If we define a single site for each element, we recover the above definition of isotopologue, while if we define a different site for every position, we recover the above definition of isotopocule.

### S2.2. Deviations from the Stochastic Assumption Cause Small Differences Between Site-specific U and R values

We here show empirically that typical clumps at natural abundance do not cause significant deviations between **site-specific U values** and **isotope ratios**.

First, a word about how introducing multiply substituted, or ‘clumped’ isotopologues affects these values. When we introduce an anomalous enrichment, relative to the stochastic proportion, of a doubly substituted clumped isotopologue (containing two rare substitutions) and keep **site-specific concentrations** identical, we change the concentrations of four **isotopologues**: 1) The **clumped isotopologue**; 2/3) Both related singly-substituted **isotopologues**; and 4) The **unsubstituted isotopologue**. For a clumped anomaly of size  $x$ , we increase the concentration of (1) by  $x$ , decrease (2) and (3) by  $x$ , to keep site-specific concentrations the same, and then increase (4) by  $x$ , to maintain closure. For example, for  $N_2O$ :

$$[110]_{new} = [110]_{stoch} + x \quad (S2.1)$$

$$[100]_{new} = [100]_{stoch} - x \quad (S2.2)$$

$$[010]_{new} = [010]_{stoch} - x \quad (S2.3)$$

$$[000]_{new} = [000]_{stoch} + x. \quad (S2.4)$$

This transformation does not change any **isotope ratios**. For example, consider  $R_{N1}^{15}$  for  $N_2O$ , given by:

$$R_{N1}^{15} = \frac{[^{15}N]_{N1}}{[^{14}N]_{N1}} = \frac{[100] + [101] + [102] + [110] + [111] + [112]}{[000] + [001] + [002] + [010] + [011] + [012]}. \quad (S2.5)$$

Here, the changes in the [110] and [100] terms in the numerator cancel, and likewise for [010] and [000] denominator; this is a consequence of us keeping the **site-specific concentrations** identical.

However, the clumped anomaly does change U values; the size of this change depends on stochastic concentrations of both the **isotopologue** of interest and the **unsubstituted isotopologue** as well as the size of the clumped anomaly.

It is hard to draw general conclusions, as the degree to which a **clumped anomaly** causes **site-specific U values** and **isotope ratios** to deviate from the stochastic assumption will be case specific. To empirically test some examples and illustrate the general concepts, we calculated U and R values for  $N_2O$ , methionine, and ethane, with various **clumped anomalies** present. For each **clumped anomaly**, we calculated the **site-specific U values** and **site-specific isotope ratios** for every atomic **site**, reporting our results as a per mil difference between U and R values, i.e.,

$$\Delta_{\frac{U}{R}} = \left( \frac{U^i}{R^i} - 1 \right) * 1000. \quad (S2.6)$$

For our synthetic datasets, we assumed **site-specific concentrations** corresponding to a  $\delta$  value of “0” relative to a given reference for each element (VPDB for carbon, AIR for nitrogen, CDT for sulfur, VSMOW for oxygen and hydrogen). Our results are depicted in Figure S2.1:

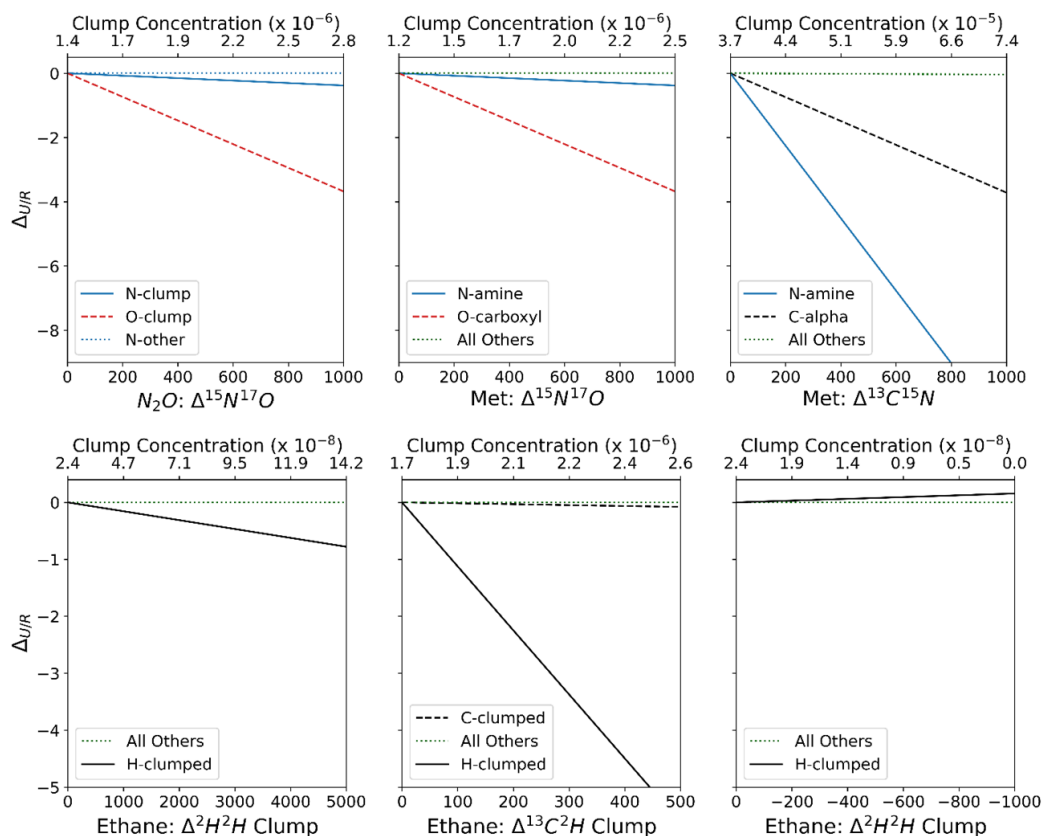


**Figure S2.1:** Top: The  $\Delta_{U/R}$  values of individual **sites** within  $N_2O$  and Methionine as a function of the  $\Delta^i$  value of a **clumped anomaly** between two atoms. Plots were made by creating synthetic datasets for both molecules, introducing the clump of interest, and tracking the resulting **site-specific U values** and **isotope ratios**. For natural abundance clumps with  $\Delta^i < 10$  ‰, the **U values** and **isotope ratios** for **sites** involved in the clump differ by  $\approx 0.1$  per mil or less. For much larger clumped isotope anomalies, i.e., 100-1000 ‰, we observe deviations in  $\Delta_{U/R}$  of 1-10 ‰. **Sites** without rare isotope substitution in the clumped isotopologue have very small differences between U and R values even for massive very large clumped isotope anomalies. Bottom: The  $\Delta_{U/R}$  for ethane with various clumps as well as an anticlump. The largest errors are caused by a  $^{13}C$  **clumped anomaly**, and are  $\sim 1$  ‰ for the hydrogen **site** for every 100 ‰ for the **clumped anomaly**. Our results indicate we are justified in assuming **site-specific U values** and **isotope ratios** are equal for all commonly expected cases without extraordinary enrichments in clumped isotope species.

These calculations demonstrate some key points about how breaking the stochastic assumption affects  $\Delta_{U/R}$  values. First, for these small molecules and for natural clumped isotope anomalies of  $< 10 \text{ ‰}$ , the deviation between **site-specific U** and **R** values is small, on the order of  $0.1 \text{ ‰}$  or less. Second, the magnitude of the  $\Delta_{U/R}$  value depends on the concentration of the **singly-substituted isotopologue** of interest; in methionine, the magnitude of the  $\Delta_{U/R}$  values for  $^{17}\text{O}$  substitutions is greater than that of  $^{15}\text{N}$  substitutions, due to the lesser abundance of  $^{17}\text{O}$ . Third, the magnitude of the  $\Delta_{U/R}$  value depends on the absolute size  $x$  of the clumped isotope anomaly. For example, in methionine, comparing the nitrogen site of the NO clump and NC clump, we see a larger  $\Delta_{U/R}$  for the same clumped  $\Delta^i$  value for the NC clump. This difference exists because the same relative clumped anomaly corresponds to a greater absolute clumped anomaly for NC than for NO, due to the greater natural abundance of  $^{13}\text{C}^{15}\text{N}$  compared to  $^{15}\text{N}^{17}\text{O}$ . Fourth, we see *an identical  $\Delta_{U/R}$  value* for all **sites** not involved in the clump. This error results from the change in concentration of the **unsubstituted isotopologue**. Suppose, for example, that one looks at the  $U^{001}$  value of  $\text{N}_2\text{O}$ . We have:

$$U_{stoch}^{001} = R^{001} = \frac{[001]_{stoch}}{[000]_{stoch}}. \quad (\text{S2.7})$$

Using the subscript “stoch” to indicate a value calculated under the **stochastic assumption**. We introduce a clump of size  $x$  between  $\text{N}_1$  and  $\text{N}_2$ :

$$U_{clump}^{001} = \frac{[001]_{stoch}}{[000]_{stoch} + x}. \quad (\text{S2.8})$$

If we take the ratio:

$$\frac{U_{clump}^{001}}{R^{001}} = \frac{\frac{[001]_{stoch}}{[000]_{stoch} + x}}{\frac{[001]_{stoch}}{[000]_{stoch}}} = \frac{[001]_{stoch}[000]_{stoch}}{[001]_{stoch} * ([000]_{stoch} + x)} = \frac{[000]_{stoch}}{[000]_{stoch} + x} \quad (\text{S2.9})$$

and then compute  $\Delta_{U/R}$ :

$$\Delta_{\frac{U}{R}} = \left( \frac{[000]_{stoch}}{[000]_{stoch} + x} - 1 \right) * 1000, \quad (S2.10)$$

we see  $\Delta_{U/R}$  depends only on  $[000]$  and the size of  $x$ , regardless of which **site** we are looking at. This holds for any **site** not involved in the clump. We therefore conclude that the  $\Delta_{U/R}$  value is identical for any **singly-substituted isotopologue** with a substitution at a **site** which does not participate in the clumped isotope anomaly. While our results suggest we are generally justified in operating under this assumption, there may be some cases where we wish to break it; we give an example of how to modify our algorithm in such an instance, below.

### S2.3 A General Solution for Fragmentation Experiments Without Mass Selection

In section 2.4.1, we analyzed an experiment where all **isotopologues** of  $N_2O$  are fragmented and observed. Here, we generalize this argument to any molecule, as follows. Suppose a molecule has  $n$  distinct chemical elements,  $\{x_1, x_2, \dots, x_n\}$ . For each chemical element, we may define up to two **sites**,  $S_{x1,lost}$  and  $S_{x1,retained}$  (for fully retained or lost elements we need only one). We can order the **sites**

$$[S_{x1,retained}, \dots, S_{xn,retained}, S_{x1,lost}, \dots, S_{xn,lost}] \quad (S2.11)$$

and write a fragmentation vector

$$f_{CM} = [1, \dots, 1, x, \dots, x]. \quad (S2.12)$$

For example, in the specific case of  $N_2O$  molecule fragmented to lose  $N_{outer}$ , we would write:

$$[S_{Ninner}, S_{O3}, S_{Nouter}] \quad (S2.13)$$

and

$$f_{30} = [1, 1, x]. \quad (S2.14)$$

Now, suppose that **site**  $S_{xi,lost}$  has  $m_i$  atoms. The unsubstituted ion beam is formed by all **isotopologues** of the form  $[(0 \cdots 0), \cdots (0 \cdots 0) \cdots (z_{1,1} \cdots z_{1,m1}) \cdots (z_{n,1} \cdots z_{n,mn})]$  where  $z_{i,j}$  indicates the isotope at the  $j$ th atom of **site**  $S_{xi,lost}$ . We write  $Z$  for the set containing all sets of substitutions  $\{(z_{1,1} \cdots z_{1,m1}) \cdots (z_{n,1} \cdots z_{n,mn})\}$ . If we define  $L(S_k)$  to give the number of possible substitutions for **site**  $S_k$ , then there are  $N = \prod_{i=1}^n L(S_{xi,lost})$  elements of set  $Z$ . For example, in  $N_2O$  (with the **sites** defined here), the unsubstituted ion beam is formed by  $[000]$  and  $[001]$  and  $N = 2$ .

Now, consider an observed ion beam with **rare isotope** substitutions, and suppose that **site**  $S_{xi,retained}$  has  $k_i$  atoms. By similar logic, all **isotopologues** contributing to this ion beam have the form  $[(y_{1,1} \cdots y_{1,k1}), \cdots (y_{n,1} \cdots y_{n,kn}) \cdots (z_{1,1} \cdots z_{1,m1}) \cdots (z_{n,1} \cdots z_{n,mn})]$ , where  $y_{i,j}$  indicates the isotope at the  $j$ th atom of **site**  $S_{xi,retained}$ , and there are  $N$  **isotopologues** of this form. For  $N_2O$ , for example, the  $^{14}N^{18}O$  ion beam is formed by  $[020]$  and  $[021]$ , and again,  $N = 2$ . Note that, by our definition of  $S_{xi,retained}$ ,  $(y_{1,1} \cdots y_{1,k1}), \cdots (y_{n,1} \cdots y_{n,kn})$  is the same for all **isotopologues** in this ion beam.

Suppose we then measure the ratio between an ion beam and the unsubstituted ion beam. Our ratio is

$$\frac{\sum_Z [(y_{1,1} \cdots y_{1,k1}), \cdots (y_{n,1} \cdots y_{n,kn}) \cdots (z_{1,1} \cdots z_{1,m1}) \cdots (z_{n,1} \cdots z_{n,mn})]}{\sum_Z [(0 \cdots 0), \cdots (0 \cdots 0) \cdots (z_{1,1} \cdots z_{1,m1}) \cdots (z_{n,1} \cdots z_{n,mn})]} \quad (S2.15)$$

As numerator and denominator are summed across the same set  $Z$ , each has  $N$  terms. We can write  $N$  pairs where  $z_{i,j}$  are fixed between numerator and denominator, i.e., of the form:

$$\frac{[(y_{1,1} \cdots y_{1,k1}), \cdots (y_{n,1} \cdots y_{n,kn}) \cdots (z_{1,1} \cdots z_{1,m1}) \cdots (z_{n,1} \cdots z_{n,m1})]}{[(0 \cdots 0), \cdots (0 \cdots 0) \cdots (z_{1,1} \cdots z_{1,m1}) \cdots (z_{n,1} \cdots z_{n,mn})]} \quad (S2.16)$$

The ratio of each pair of terms is equal under the **stochastic assumption**. Using

$$\frac{a}{b} = \frac{c}{d} \Rightarrow \frac{a+c}{b+d} = \frac{a}{b}, \quad (S2.17)$$

the ratio in eq (S21) is equal to

$$\frac{[(y_{1,1} \cdots y_{1,m_1}), \cdots (y_{n,1} \cdots y_{n,m_1}) \cdots (0 \cdots 0) \cdots (0 \cdots 0)]}{[(0 \cdots 0), \cdots (0 \cdots 0) \cdots (0 \cdots 0) \cdots (0 \cdots 0)]} = U^Y \quad (S2.18)$$

where  $Y$  gives the substitutions  $(y_{1,1} \cdots y_{1,m_1}), \cdots (y_{n,1} \cdots y_{n,m_1})$ . If  $U^Y$  has an isotope ratio (it would not, for example, if  $Y = {}^{15}\text{N}{}^{17}\text{O}$ ), then we may approximate this using eq (4).

For example, for  ${}^{14}\text{N}{}^{18}\text{O}$ :

$$\frac{[020] + [021]}{[000] + [001]} \approx \frac{[020]}{[000]} = U^{18\text{O}} \approx R_{03}^{18}. \quad (S2.19)$$

Therefore, we conclude that in fragmentation measurements, we can measure the ratio between a substituted and the unsubstituted ion beam and interpret the result as a **site-specific U value** or a scalar multiple (for multiatomic **sites**) of the **site-specific isotope ratio** for the **site**.

## S2.4 A Detailed Analysis of M+N Experimental Issues

Here, we discuss the effects of experimental issues on the M+N algorithm in more detail. We divide our discussion into two sections: first, we discuss our treatment of experimental issues, standardization, and propagation of error. Then, we present the results of several different correction schemes and show how these affect our reported methionine structure.

We begin with a general description of our standardization process, hoping to provide an intuitive understanding. We start with two sets of measurements: the **M+N relative abundances** of the standard,  $\rho_{adj,observed,STD}^i$ , and of the sample,  $\rho_{adj,observed,SMP}^i$ , for each observed substitution  $i$ . Because we will not in general observe all ion beams, these observations are “adjusted” **M+N relative abundances**, i.e., a **M+N relative abundance** where the denominator does not include all substitutions. To

determine instrument fractionation, we calculate an approximation of what the standard should have looked like, assuming some standard composition, and use this to calculate a correction factor  $k^i$  for each substitution:

$$k^i \rho_{adj,observed,STD}^i = \rho_{assumed,STD}^i \quad (S2.20)$$

We next apply these to the sample observations, e.g.,

$$k^i \rho_{adj,observed,SMP}^i = \rho_{computed,SMP}^i \quad (S2.21)$$

Doing so results in a problem which is most clearly illustrated in the special case when we *have* observed all substitutions. In this case, we know the sum of the  $\rho_{actual,SMP}^i$  across all isotopes we observe should equal 1, by definition (if we did not observe all substitutions, as  $\rho_{actual,SMP}^i$  is not observed for some isotope  $i$ , the sum across the isotopes we did observe is  $<1$ ; note  $\rho_{actual,SMP}^i$  is not an ‘adjusted’ **M+N relative abundance**). However, the correction factors do not include knowledge of this constraint; hence after applying the correction factors, the sum of the  $\rho_{computed,SMP}^i$  may subtly differ from 1. We thus renormalize, such that the sum is 1 (this is referred to as a “W correction,” as W is the name of a variable we use when rigorously investigating this correction, below):

$$\frac{k^i \rho_{adj,observed,SMP}^i}{\sum_j k^j \rho_{adj,observed,SMP}^j} = \frac{\rho_{computed,SMP}^i}{\sum_j \rho_{computed,SMP}^j} = \rho_{computed,renormalized,SMP}^i \quad (S2.22)$$

and observe:

$$\sum_i \rho_{computed,renormalized,SMP}^i = 1 \quad (S2.23)$$

If we do not observe all ion beams, we know the sum of the  $\rho_{actual,SMP}^i$  equals some constant  $<1$ , equal to the sum of the **M+N relative abundances** of the ion beams we did observe. We call this constant O, for the “Observed abundance constant”; for example, for the 61 ion beam of methionine in the M+1 experiment, if we do not observe the D ion beam:



$$O = z_{33S} + z_{Unsub} + z_{13C} = 1 - z_D. \quad (S2.24)$$

In this case, we renormalize and scale to the constant O:

$$\rho_{computed,renormalized,SMP}^i = O * \frac{k^i \rho_{adj,observed,SMP}^i}{\sum_j k^j \rho_{adj,observed,SMP}^j}. \quad (S2.25)$$

We may approximate O by various methods, detailed below. In the case that we do not have a clear approximation, we may instead omit this correction, and proceed using eq S2.21.

To make this example more concrete, consider the 61 ion beam of methionine and suppose that the ion beams have the following (unrealistic) abundances: D = 0.02, <sup>33</sup>S = 0.1, <sup>13</sup>C = 0.5, Unsub = 0.38. Suppose that we observe all ion beams, calculate fractionation factors, and standardize via eq S2.21. We end up with four  $\rho_{computed,SMP}^i$  values. We know *a priori* that the sum of these must equal 1; hence, we normalize using S2.22 such that their sum is 1. In a second case, suppose we do not observe the D ion beam. After using S2.21, we end up with three  $\rho_{computed,SMP}^i$  values. Assuming knowledge (or prediction) of  $z_D$ , we know that their sum equals 0.98; hence we set O = 0.98 and apply S2.25 to correct for their abundances.

This process may be clear conceptually, but it is useful to get a more detailed understanding of the issues involved. In particular, one will find that, in the absence of unresolved ion beams, this correction process is *exact*; it gives precisely the right answer,  $\rho_{computed,renormalized,SMP}^i = \rho_{actual}^i$ . This fact may be surprising (it was for the authors) and so we investigated the correction scheme in more detail. Readers who are not interested in the intricacies of this process may safely skip the following discussion.

To rigorously investigate how experimental issues affect our observations, we take a step a back, and begin by defining a relation between the observed and the actual **M+N relative abundance** values. For substitution *i*, we may write:

$$\rho_{adj,observed}^i = \Gamma(\rho_{actual}^i) \quad (S2.26)$$

where  $\Gamma$  is a function. Ultimately, we would like to know how to calculate  $\rho_{actual}^i$  given  $\rho_{adj,observed}^i$ , i.e., to invert  $\Gamma$ . We anticipate that  $\Gamma$  will be a function of time, as effects like instrument fractionation which influence  $\Gamma$  will vary with time. Thus, our solution to this problem must use standardization in some way; we must periodically observe standards of known composition to evaluate the current state of  $\Gamma$ .

A solution to this problem is to treat  $\Gamma$  as a proportionality constant, e.g.,  $\Gamma(\rho_{actual}^i) = \frac{1}{k^i} \rho_{actual}^i$  for some constant  $k^i$ , then use “forward model” standardization to compute  $k^i$ . For example, we would hypothesize the isotopic composition of our standard, use it to compute  $\rho_{predicted,STD}^i \approx \rho_{actual,STD}^i$ , and use this to calculate:

$$k^i = \frac{\rho_{actual,STD}^i}{\rho_{adj,observed,STD}^i} \approx \frac{\rho_{predicted,STD}^i}{\rho_{adj,observed,STD}^i}. \quad (S2.27)$$

Our accurate recovery of the  $k^i$  term depends on the quality of our approximation for the standard. We may apply  $k^i$  to the sample observation:

$$k^i \rho_{adj,observed,SMP}^i = \rho_{actual,SMP}^i. \quad (S2.28)$$

Computing our target,  $\rho_{actual,SMP}^i$ , the actual **M+N relative abundance** of the sample.

This method is but one choice of the function  $\Gamma$ , and folds many different experimental issues into the constant,  $k^i$ . It turns out that applying  $k^i$  in this way will be subtly wrong, due to the specific experimental effects on sample and standard. To show this, we will analyze how different experimental issues affect  $\rho_{observed}^i$ , then return to equation (S2.28) to include these effects. A note to the reader: the following section is complicated, introducing new terminology that may be difficult to grasp without a worked example. We provide a worked example problem in Table S2.1, below, and further examples in a companion spreadsheet. We suggest that the reader refer to that table, start with the actual concentrations of the substitutions, and perform the calculations to follow the logic of the following section.

We begin by writing expressions for these quantities in terms of isotope abundances. Writing  $z^i$  for the actual concentration of **substitution**  $i$  within a given fragment, we have:

$$\rho_{actual}^i = \frac{z_{actual}^i}{\sum_j z_{actual}^j}. \quad (S2.29)$$

Here,  $j$  indexes across all substitutions in the fragment; for example, in a fragment (like the 61 fragment of methionine) with  $^{33}\text{S}$ ,  $^{13}\text{C}$ ,  $D$  and  $Unsub$  ion beams,  $j \in \{^{33}\text{S}, D, ^{13}\text{C}, Unsub\}$ . Of course, if some peaks are lost, the sum should be taken only across the observed substitutions. For example, if we do not observe  $D$ , we should write:  $j \in \{^{33}\text{S}, ^{13}\text{C}, Unsub\}$ . Accounting for this issue gives us what we call “adjusted” **M+N relative abundance**, i.e.,

$$\rho_{adj,actual}^i = \frac{z_{actual}^i}{\sum_{j \in obs} z_{actual}^j} \quad (S2.30)$$

and likewise for our actual observations, which have the form:

$$\rho_{adj,observed}^i = \frac{z_{observed}^i}{\sum_{j \in obs} z_{observed}^j} \quad (S2.31)$$

where we write  $j \in obs$  to note the sum is taken only across those ion beams which we observe. Next, we will show how the  $z_{observed}^i$  in our observations relate to the  $z_{actual}^i$  values. We first account for experimental fractionation. Here, we choose to model all fractionation as proportional—i.e., we can compute the fractionated abundance by multiplying  $z_{actual}^i$  by a fractionation factor:

$$z_{observed}^i = F_{abs}^i z_{actual}^i \quad (S2.32)$$

where  $F_{abs}^i$  is the fractionation factor for substitution  $i$  relating the actual and observed absolute abundances.

Next, we examine the presence of unresolved peaks. First, consider the case where two peaks combine; we choose to treat the combined peak as belonging solely to the more abundant isotope (e.g., an unresolved peak combining  $^{13}\text{C}$  &  $^{17}\text{O}$  is assigned to be a  $^{13}\text{C}$  peak). We may write:

$$z_{observed}^i = F_{abs}^i z_{actual}^i + \beta_{ij} F_{abs}^j z_{actual}^j \quad (S2.33)$$

where  $i$  refers to the first peak,  $j$  the second, and  $\beta_{ij}$  is a constant that accounts for how the intensities of the peaks combine. For example, in an instrument where they combine linearly,  $\beta_{ij} = 1$ ; in an instrument where the  $j$  substitution does not add any intensity to the combined ion beam,  $\beta_{ij} = 0$ . We can generalize by taking a sum over all other substitutions:

$$z_{observed}^i = z_{actual}^i F_{abs}^i + \sum_{j \neq i} \beta_{ij} z^j F_{abs}^j. \quad (S2.34)$$

Note that this sum is taken across ALL peaks, not just the observed ones, as unobserved peaks may contribute to observed ones.

If the  $\beta_{ij}$  terms and abundances of other substitutions can be well-constrained via some method (for example, for a  $^{17}\text{O}$  correction to a  $^{13}\text{C}$  ion beam, we may determine  $z^{17\text{O}}$  from observations of  $^{18}\text{O}$  and assert that  $\beta_{13\text{C}17\text{O}} = 1$ ), then we can correct out the additional abundance. As noted in the paper, we here do not address this scenario. Instead, we treat the many cases in which the  $\beta_{ij}$  will be unknown and may be difficult to determine; our treatment has the advantage of being broadly applicable and requiring minimal user input, but may be less accurate than other methods. To do so, we approximate eq S2.35 in the following way:

$$z_{observed}^i = z_{actual}^i F_{abs}^i + \sum_{j \neq i} \beta_{ij} z^j F_{abs}^j \approx z_{actual}^i F_{unres}^i. \quad (S2.35)$$

replacing the concentrations and fractionation factors for all unresolved ion beams with a single fractionation factor,  $F_{unres}^i$ , accounting for all their contributions. As noted in the main paper, this approximation will fail when the  $\sum_{j \neq i} \beta_{ij} z^j F_{abs}^j$  term differs notably between sample and standard (presumably from differences in the concentrations  $z^j$ ) and when  $\sum_{j \neq i} \beta_{ij} z^j F_{abs}^j$  is large relative to  $z_{actual}^i F_{abs}^i$ .

With an expression for  $z_{observed}^i$  in hand, we may use this approximation to calculate observed **M+N relative abundances** (cf. eq S2.31):

$$\rho_{adj,observed}^i = \frac{z_{observed}^i}{\sum_{j \in obs} z_{observed}^j} \approx \frac{z_{actual}^i F_{unres}^i}{\sum_{j \in obs} (z_{actual}^j F_{unres}^j)}. \quad (S2.36)$$

Obtaining an expression that relates our experimental observation ( $\rho_{adj,observed}^i$ ) to the actual concentrations ( $z_{actual}^i$ ).

Returning now to eq (S2.27), we may expand the expression for  $k^i$  to put it in terms of absolute abundances and fractionation factors.

$$k^i = \frac{\rho_{actual}^i}{\rho_{adj,observed}^i} \approx \frac{\frac{z_{actual}^i}{\sum_j z_{actual}^j}}{\frac{z_{actual}^i F_{unres}^i}{\sum_{j \in obs} (z_{actual}^j F_{unres}^j)}} = \frac{1}{F_{unres}^i} * \frac{\sum_{j \in obs} (z_{actual}^j F_{unres}^j)}{\sum_j z_{actual}^j} \quad (S2.37)$$

Recall from eq (S2.27), that  $k^i$  can also be predicted via forward model standardization:

$$k^i \approx \frac{\rho_{predicted}^i}{\rho_{adj,observed}^i}. \quad (S2.38)$$

Note that  $\rho_{predicted}^i$  is *not* in “adjusted” **M+N relative abundance** space, i.e., we sum across all isotopic peaks, rather than just the observed ones. We may use S2.38 to calculate  $k^i$  values for the standard, then apply them to the sample, hoping to yield  $\rho_{actual,SMP}^i$ . Expanding with (S2.36) (observed for the sample) and (S2.37) (calculated using the standard) we have:

$$k^i \rho_{adj,observed,SMP}^i = \frac{1}{F_{unres,STD}^i} * \frac{\sum_{j \in obs} (z_{actual,STD}^j F_{unres,STD}^j)}{\sum_j z_{actual,STD}^j} * \frac{z_{actual,SMP}^i * F_{unres,SMP}^i}{\sum_{j \in obs} (z_{actual,SMP}^j F_{unres,SMP}^j)}. \quad (S2.39)$$

An expanded version of our proportional correction from S2.21. We see that S2.39 is *not* equal to  $\rho_{actual,SMP}^i = \frac{z_{actual,SMP}^i}{\sum_j z_{actual,SMP}^j}$ , but differs by multiple factors related to

sample and standard composition; simply applying a proportional correction factor misses these! We therefore suggest additional corrections to account for these factors.

To assist in analyzing these factors, we begin by multiplying S2.39 by a factor (equal to 1):

$$\frac{\sum_j z_{actual,SMP}^j}{\sum_j z_{actual,SMP}^j} \quad (S2.40)$$

yielding (upon rearrangement)

$$k^i \rho_{adj,observed,SMP}^i = \frac{z_{actual,SMP}^i}{\sum_j z_{actual,SMP}^j} * \frac{F_{unres,SMP}^i}{F_{unres,STD}^i} * \frac{\sum_j z_{actual,SMP}^j}{\sum_j z_{actual,STD}^j} * \frac{\sum_{j \in obs} (z_{actual,STD}^j F_{unres,STD}^j)}{\sum_{j \in obs} (z_{actual,SMP}^j F_{unres,SMP}^j)} \quad (S2.41)$$

which we may write:

$$\rho_{actual,SMP}^i * \frac{F_{unres,SMP}^i}{F_{unres,STD}^i} * \frac{\sum_j z_{actual,SMP}^j}{\sum_{j \in obs} (z_{actual,SMP}^j F_{unres,SMP}^j)} * \frac{\sum_{j \in obs} (z_{actual,STD}^j F_{unres,STD}^j)}{\sum_j z_{actual,STD}^j}. \quad (S2.42)$$

That is, our desired result of  $\rho_{actual,SMP}^i$  offset by three terms. We interpret these terms as follows. The first is a “fractionation factor” term, dealing with differences between unresolved fractionation factors for sample and standard:

$$\mathcal{F}^i = \frac{F_{unres,SMP}^i}{F_{unres,STD}^i}. \quad (S2.43)$$

Recall that we folded the correction of unresolved peaks into the fractionation factors (the subscript “unres”)—hence, this term captures both drift in instrument fractionation as well as subtle differences in the concentration of unresolved ion beams (for example, if  $^{13}\text{C}$  and  $^{17}\text{O}$  are unresolved, and  $^{17}\text{O}$  differs by 10 ‰ between sample and standard).

The second two are closely related terms for sample and standard. These give the ratio (or its inverse), which we label  $w$ :

$$w = \frac{\sum_j z_{actual}^j}{\sum_{j \in obs} (z_{actual}^j F_{unres}^j)} \quad (S2.44)$$

and can be thought of as answering—how much ion intensity would have been observed in a perfect measurement relative to how much was actually observed, given experimental issues? As an example, suppose we could have observed ion beams with abundances of 2, 8, and 10, but the ion beam at intensity 2 is not observed by our experiment. Assume also no fractionation occurs. For this experiment, the associated term is  $\frac{10+8+2}{10+8} = \frac{20}{18} = 1.111 \dots$ . Putting it all together, we may write S2.42 as:

$$k^i \rho_{adj,observed,SMP}^i = \rho_{actual,SMP}^i * \mathcal{F}^i * w_{SMP} * \frac{1}{w_{STD}}. \quad (S2.45)$$

To deal with these factors in forward model standardization, we propose the following solution. First, we calculate  $k^i$  using S2.38 (i.e., via a forward model), and use it to compute  $\rho_{actual,SMP}^i * \mathcal{F}^i * w_{SMP} * \frac{1}{w_{STD}}$ . Next, we will *assume* that  $\mathcal{F}^i = 1$ ; we do not deal with this factor at present. That leaves us with

$$k^i \rho_{adj,observed,SMP}^i = \rho_{actual,SMP}^i * w_{SMP} * \frac{1}{w_{STD}}. \quad (S2.46)$$

Now, we may take the term:

$$W = w_{SMP} * \frac{1}{w_{STD}} = \frac{\sum_j z_{actual,SMP}^j}{\sum_{j \in obs} (z_{actual,SMP}^j F_{unres,SMP}^j)} * \frac{\sum_{j \in obs} (z_{actual,STD}^j F_{unres,STD}^j)}{\sum_j z_{actual,STD}^j} \quad (S2.47)$$

and note that, although the individual terms are complicated, W itself is a constant. Thus, we have

$$k^i \rho_{adj,observed,SMP}^i = \rho_{actual,SMP}^i * W \quad (S2.48)$$

and may calculate  $\rho_{actual,SMP}^i * W$  for all observed ion beams. Next, note a fact about the sum of the  $\rho_{actual,SMP}^i$  for the substitutions we observe. We may write:

$$\sum_{j \in \text{Obs}} \rho_{\text{actual}, \text{SMP}}^j = \frac{\sum_{j \in \text{Obs}} a_{\text{actual}, \text{SMP}}^j}{\sum_j a_{\text{actual}, \text{SMP}}^j} = O \quad (\text{S2.49})$$

using “O” to denote this as the “observed abundance term.” This term gives the ratio of the abundances of the actual ion beams we do observe relative to the abundances of all ion beams we could have observed for the sample. For example, for the 61 ion beam of methionine in the M+1 experiment, if we fail to observe deuterium, this factor is:

$$O_{61, \text{M}+1} = \frac{Z_{33\text{S}} + Z_{\text{Unsub}} + Z_{13\text{C}}}{Z_{13\text{C}} + Z_{\text{D}} + Z_{33\text{S}} + Z_{\text{Unsub}}} \quad (\text{S2.50})$$

Now, using the fact that W is a constant, we have:

$$\sum_{j \in \text{Obs}} (W * \rho_{\text{actual}, \text{SMP}}^j) = W \sum_{j \in \text{Obs}} \rho_{\text{actual}, \text{SMP}}^j = W * O. \quad (\text{S2.51})$$

This result allows us to correct for the W constant, in the following way, beginning with  $\rho_{\text{adj}, \text{observed}, \text{SMP}}^i$  values. First, assume that O is known (it often will not be, but there are useful ways of approximating it; we will deal with this shortly). Next, we apply the correction factors  $k^i$  for each substitution  $i$  that we observe, obtaining  $(W * \rho_{\text{actual}, \text{SMP}}^i)$  for each. And from (eq S2.51), we see that we can remove the W term by normalizing the sum  $\sum_{j \in \text{Obs}} (W * \rho_{\text{actual}, \text{SMP}}^j)$  and scaling such that it equals O; the values after this process will be the  $\rho_{\text{actual}, \text{SMP}}^i$  values we are interested in. Note that when  $\mathcal{F}^i = 1$  and O is known (most simply if  $O = 1$  because all ion beams are observed), this correction is exact! **We employ this “normalize and scale” strategy for the results presented in the paper.**

Because this process is difficult to grasp without an example, we include a sample calculation for the 61 ion beam of methionine, below (Table S2.1); we recommend the reader work through it and verify the calculations. We also include a more detailed spreadsheet which examines these ion beams under a range of conditions (perfect measurement; D not observed; D unresolved from  $^{13}\text{C}$ ; and D unresolved from  $^{13}\text{C}$  and  $^{33}\text{S}$



lost). Improvements in precision offered by this correction scheme are sometimes, but not always, minor, e.g., ~0.1 ‰ here; in some cases, such a correction can be omitted (but see below; for the data shown in the paper, correction is necessary for the most accurate measurement). The limiting factor tends to be how well the O value can be approximated for the sample. We next move to discuss this process.

**Table S2.1: Sample Calculation for Fractionation<sup>a</sup>**

STANDARD					
	Unsub	D	13C	33S	Sum
$z_{actual, std}^i$	0.034182	0.000562	0.00705	0.019216	0.06101
$\rho_{actual, std}^i$	0.560276	0.009209	0.11555	0.314965	1
$F_{abs}^i$	1.026667	0.985457	0.974324	1.099131	--
$z_{fractionated, std}^i$	0.035094	0.000554	0.006869	0.021121	0.063637
$\rho_{fractionated, std}^i$	0.551469	0.0087	0.107935	0.331895	1
$k^i$	1.01597	1.058457	1.07055	0.948988	--
SAMPLE					
	Unsub	D	13C	33S	Sum
$z_{actual, smp}^i$	0.034043	0.000694	0.007031	0.019414	0.061182
$\rho_{actual, smp}^i$	<b>0.556417</b>	<b>0.011336</b>	<b>0.114927</b>	<b>0.31732</b>	<b>1</b>
$z_{fractionated, smp}^i$	0.034951	0.000683	0.006851	0.021339	0.063824
$\rho_{fractionated, smp}^i$	0.54761	0.010709	0.107341	0.33434	1
$W$ * $\rho_{Smp, calculated}^i$	0.556356	0.011335	0.114914	0.317285	0.999889
$\rho_{Smp, calculated}^i$	<b>0.556417</b>	<b>0.011336</b>	<b>0.114927</b>	<b>0.31732</b>	<b>1</b>

a: Sample calculations for the forward model standardization of the 61 ion beam of methionine. The fractionation factors were randomly drawn from a normal distribution with  $\mu = 1$  and  $\sigma = 0.05$ . Our target values for the sample are the row  $\rho_{actual, smp}^i$ ; our result after correction is the row  $\rho_{Smp, calculated}^i$ . Without correcting out the “W” factor, we obtain  $W * \rho_{Smp, calculated}^i$ . Using the correction gives us  $\rho_{Smp, calculated}^i$ , the correct values. For this example,  $O = 1$ . We examine cases where  $O \neq 1$  in the companion spreadsheet.

There is no way to directly measure the O factor; it must be calculated somehow. We now discuss several ways to do so; as we will see, the method one chooses can have a profound effect on the accuracy and precision of the final reported values. Moreover, the method to calculate the O value is the main *choice* that users will make in how to process their data; having a good understanding of when and why to use various methods is necessary to make a good choice for a particular measurement. Our discussion here should be thought of as a point of departure for future work, which may improve on our suggested methods.

We begin by discussing two basic strategies one may use to compute the O factor; one relying on a forward model (the “theoretical” correction) and another using observations of other ion beams (the “experimental” correction). In the first case, we can specify a predicted isotopic composition and calculate the O factor based on the relative abundances of ion beams for that prediction. For example, with the 61 ion beam of methionine in the M+1 experiment, if we do not observe the deuterium beam, we may calculate:

$$O_{61,M+1,FMSMP} = \frac{Z_{33S,FMSMP} + Z_{Unsub,FMSMP} + Z_{13C,FMSMP}}{Z_{13C,FMSMP} + Z_{D,FMSMP} + Z_{33S,FMSMP} + Z_{Unsub,FMSMP}} \quad (S2.52)$$

using a forward model of the sample FMSMP. In some cases, our predicted isotopic composition will be the same as the forward model of our standard (i.e., the forward model for sample and standard are identical); if we know independently that sample and standard differ, we may hypothesize a different forward model for the sample. Using this approach will give an O factor that is subtly wrong, but close to accurate; hence, we suggest a Monte Carlo approach to estimate the error induced by this approximation. For each fragment, we construct a normal distribution  $N(O, \sigma)$  where the mean is the forward model O factor for the standard and  $\sigma$  is a user-specified parameter (e.g., 1 or 2% of O). We then solve our algorithm N times (typically N = 1000) drawing new correction factors for each fragment each time and report the means and standard deviations of the results. When combined with the Monte Carlo for experimental error

(see below), we pick a new factor each round of that Monte Carlo process (rather than running  $N = 1000$  times for each iteration of the experimental error Monte Carlo).

To gain an understanding of how this process works, it is useful to have a model system; we once again turn to the M+1 measurement of methionine. For the synthetic dataset we present, with low abundance cutoff of 1% and resolution of 120,000, there are four fragments which must be corrected—full, 133, 102, and 61 (the first 3 do not observe  $^{17}\text{O}$  ion beams due to low resolution, while 61 does not observe D due to low abundance). To calibrate our approach, we calculate plausible “extreme” values for the O factors for these beams, in the following way. For each position of methionine, we specify plausible ranges of isotopic composition; we assume we know the molecular avg  $^{13}\text{C}$  to within 0.1 ‰, and that it does not vary by position (this assumption is wrong, but the positional distribution turns out not to matter in this case; we observe every  $^{13}\text{C}$  **site** for each fragment, either in the  $^{13}\text{C}$  or Unsub ion beams; thus, variations in position will not affect how much of the M+1 population we observe, and the site-specific distribution is irrelevant to our calculation of the O factor). For other heavy elements, we allowed a range of -25 to 25 vs AIR, VSMOW, or CDT; for hydrogen, we allowed a range of -250 to 250 vs VSMOW. For each fragment, the minimum extreme O factor was computed with the highest  $\delta$  value for all positions we do *not* observe (e.g., the  $^{17}\text{O}$  for fragment 133) and the lowest value for all positions we *do* observe; the maximum extreme was the opposite.

The results of O factors computed for this theoretical correction and Monte Carlo approach are visualized in Figure S2.2, for the 61, 133, and full ion beams. We observe that the proper width of the distribution depends on the fragment of interest; for the 61 fragment, using  $\sigma = 1$  ‰ of the forward model O factor gives a distribution that reaches the bounds of the extreme values, but does not sample outside them; for the 133 and full fragments,  $\sigma = 1$  ‰ extends far beyond the extreme values, and can be considered overly broad for this problem. Second, we observe that the mean of the distributions; i.e., the computed forward model O factors, can differ from the actual O factor (which will typically be unknown); this is most notable for the 61 fragment, where the majority of the

O factors we sample are below the actual value. In any case, knowledge of the extreme values is helpful in defining the proper width of the distribution. The range of extreme values will be tighter if we know more information about the molecule; for example, if we knew  $^{15}\text{N}$  precisely, rather than varying from -25 to 25, we could achieve tighter bounds. Hence, knowledge of the isotopic composition of other parts of the molecule will assist with this O factor computation.

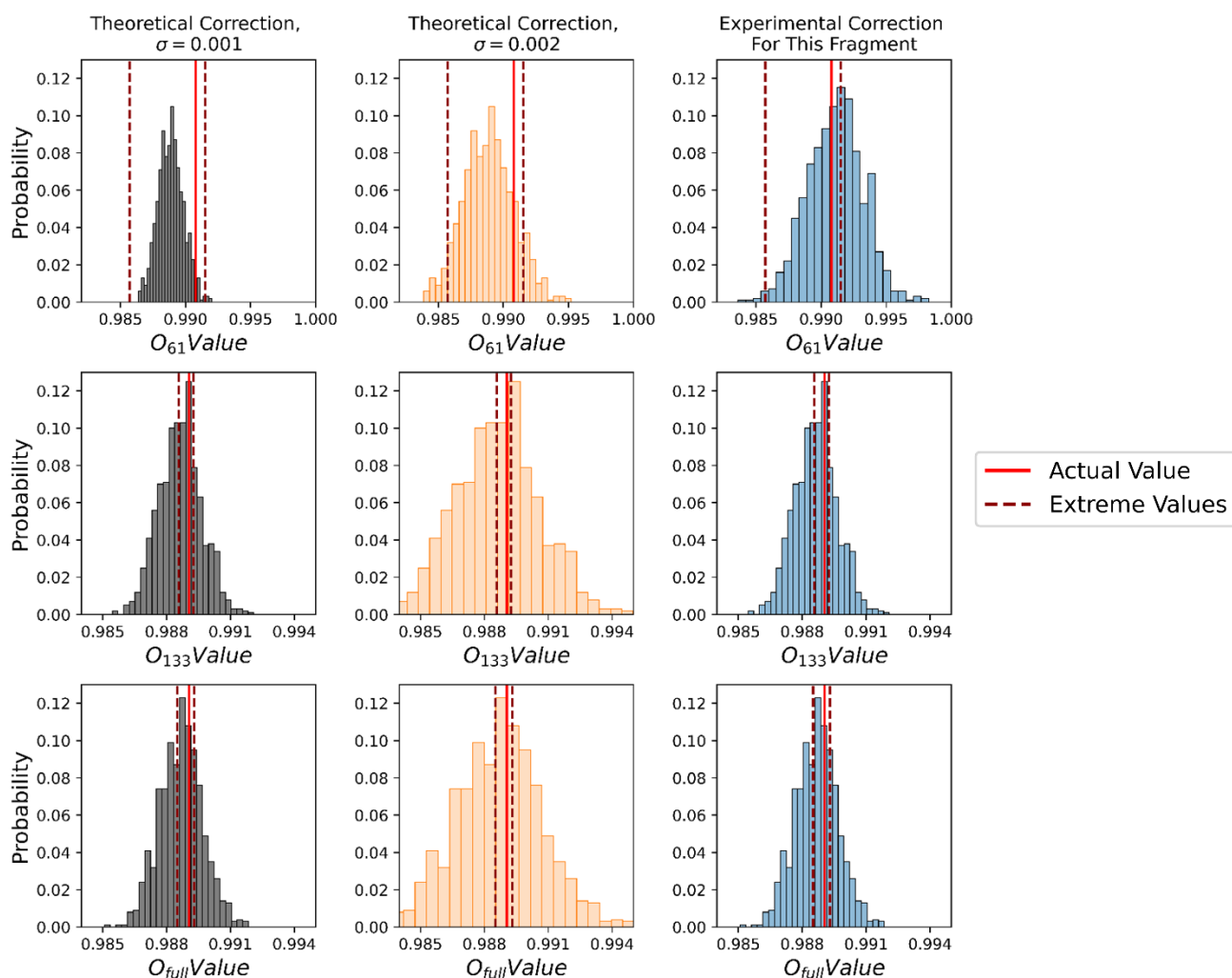


**Figure S2.2:** Histograms of the recovered  $O_{61, \text{SMP}}$  values for three different calculation methods. The correct value is shown by the red solid line. Extreme values, i.e., the highest or lowest possible answer based on reasonable assumptions of the sample's isotopic content, are depicted with dotted red lines. The black bars show results using the "theoretical" calculation method, based on a forward model of the sample, with  $\sigma$  of 1‰; the orange bars show the same, with  $\sigma$  of 2‰; and the blue bars show results using the "experimental" correction, based on observations of the 104 fragment (discussed below).

An alternative method, which we term the “experimental” correction, is to use information from a different observed fragment to constrain the O factor for a target fragment. We do so by taking advantage of a consequence of **M+N relative abundance** space—ion beams from two different fragments containing the same **isotopologues** will have the same **M+N relative abundance**. Suppose, for example, that we do not observe the D ion beam for the 61 fragment, but also measure the 104 fragment of methionine, and observe all of its substitutions:  $^{15}\text{N}$ ,  $^{13}\text{C}$ ,  $^{33}\text{S}$ , D, and Unsub. In this case, the actual **M+1 relative abundance** of  $^{33}\text{S}$  in the 61 ion beam will be the same as the **M+1 relative abundance** as the  $^{33}\text{S}$  ion beam of the 104 fragment. That is, while our observation for the 61 ion beam was:

$$\rho_{61,obs}^{33S} = \frac{z_{61}^{33S}}{z_{61}^{13C} + z_{61}^{33S} + z_{61}^{Unsub}} \quad (S2.53)$$

we independently know that:

$$\rho_{61,actual}^{33S} = \rho_{104,actual}^{33S} \approx \rho_{104,obs}^{33S} = \frac{z_{104,obs}^{33S}}{z_{104,obs}^{13C} + z_{104,obs}^{33S} + z_{104,obs}^{Unsub} + z_{104,obs}^D + z_{104,obs}^{15N}}. \quad (S2.54)$$

Therefore, we may calculate our correction factor as

$$O_{61} = \frac{\rho_{104,obs}^{33S}}{\rho_{61,obs}^{33S}} \approx \frac{\rho_{61,actual}^{33S}}{\rho_{61,obs}^{33S}}. \quad (S2.55)$$

This correction may be appropriate if we do not want to calculate a forward model, or if we have precisely constrained the relevant observations. When accounting for experimental error via a Monte Carlo approach (see below for more detail), we will end up with some range of computed O factors via this approach as well; these distributions are also plotted in Figure S2.2 (we also correct 133 and full, which do not observe the  $^{17}\text{O}$  ion beams, using the  $^{33}\text{S}$  beam of fragment 104). For the specific scenario we model, the range of values we record is broader than the extreme values but centered more closely to the actual value (most obviously for the 61 fragment).

Next, we examine the effects of different correction methods on our final reported **isotopologue-specific** U values. To do so, we computed results for our algorithm with no correction, with the “theory” correction with varying values of  $\sigma$  (0, 1‰, and 2‰), and with the experimental correction for the relevant fragments (full, 133, 61) and the theory correction with  $\sigma = 1‰$  for the other fragment (102). We show our results for the heavy isotopes of methionine in Figure S2.3. These corrections have the most profound effect on  $C_{\text{gamma}}$ , although the changes are qualitatively similar for all affected **sites**. Here, the “theoretical” correction may marginally but not substantially improve the accuracy of our reported values; moreover, if we sample a broad distribution, it can significantly increase our reported error bars. In contrast, the “experimental” correction improves our accuracy, but in this case, harms our precision. We note this may not be the case in all systems (if we had much tighter bounds on  $^{33}\text{S}$ , we may not lose so much precision), and in some instances an experimental correction may give the best result. At this point, it should be clear that *the choice of correction scheme may have a profound effect on our reported results*; as neither correction scheme gives us both accurate and precise results, we next examine some further improvements.

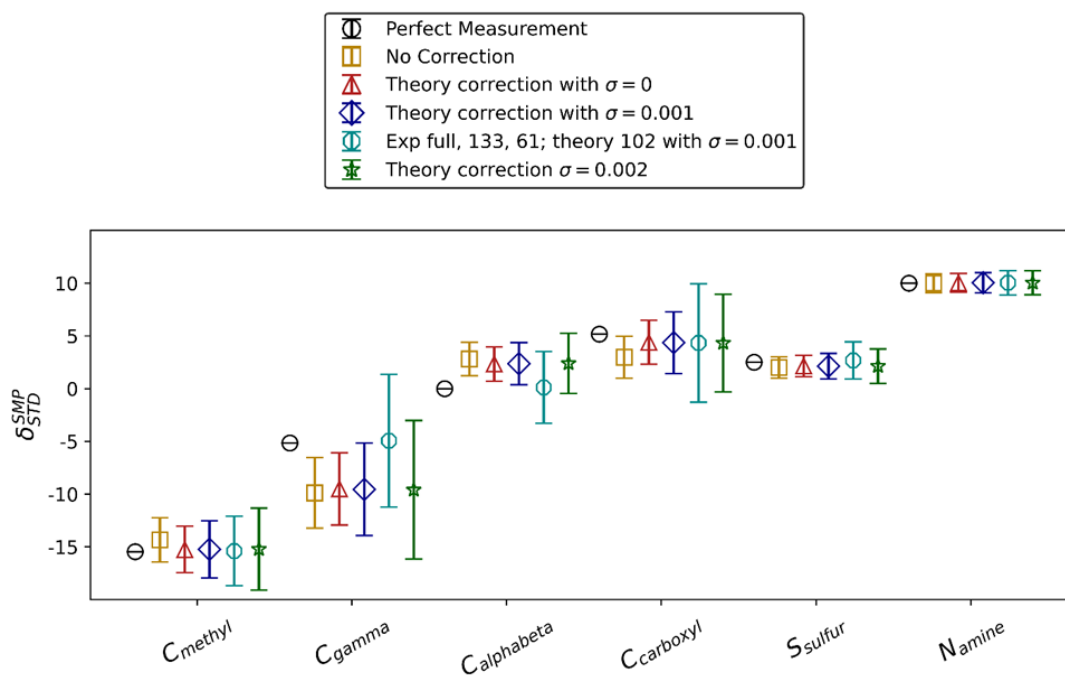


**Figure S2.3:** Results of the theoretical and experimental correction schemes compared to no correction. Each result uses the methionine dataset with all experimental issues shown in the main paper. The “No correction” data points do not include any knowledge of the O values. Remaining points incorporate either theoretical or experimental corrections with various distributions. The experimental correction improves accuracy at the expense of precision; the theoretical correction improves accuracy only slightly, and may harm precision if the chosen distribution is too wide. The correction we choose can powerfully affect our recovered results and errors, but the corrections shown here could be improved.

First, we look at a possible improvement to the theoretical correction scheme. The accuracy of this method depends on the accuracy of the forward model. We suggest an iterated approach to improve the accuracy of our forward model, as follows: first, we specify a forward model for the sample and solve using the theoretical correction, as before. Then, we use the resulting **site-specific** delta values to compute a new forward model for the sample. Using this new forward model, we solve as before. We repeat this process some number of iterations (we have tried  $\approx 50$ ) or until the process converges (i.e., output deltas from one iteration are within some tolerance of deltas from the previous iteration). As before, we may perform this procedure using various values of  $\sigma$ . We show results from this simulation in Figure S2.4, rows 1 and 2, using values of  $\sigma = 0$

and  $\sigma = 1\%$ , respectively. For the 61 fragment and  $\sigma = 0$ , we see a substantial improvement in the accuracy of our  $O_{61}$  value with more iterations; the other fragments do not differ noticeably. When using  $\sigma = 1\%$ , we correspondingly see a shift in the center of the histogram for the 61 fragment, and no noticeable difference for the other fragments.

A second potential improvement we explore is an “extreme value cutoff,” using our calculated extreme values to inform the distribution that we sample. The idea here is that, as O values outside of the accepted range for a given fragment are physically unrealistic, we should not use these results. In our implementation, whenever we compute an O factor outside the allowed bounds, we set it equal to the closest bound. We note that this process is compatible with both theoretical and experimental corrections and with or without iteration. Results from this method applied to the theoretical correction (with  $\sigma = 1\%$ ) and experimental correction are also shown in Figure S2.4; these simulations were performed with the iteration process described above. In this circumstance, as most of the results sampled are outside of the “extreme” values, we find that values at the bounds themselves are highly represented. This issue is more pronounced for the experimental correction, likely due to the wider distribution sampled by this method.



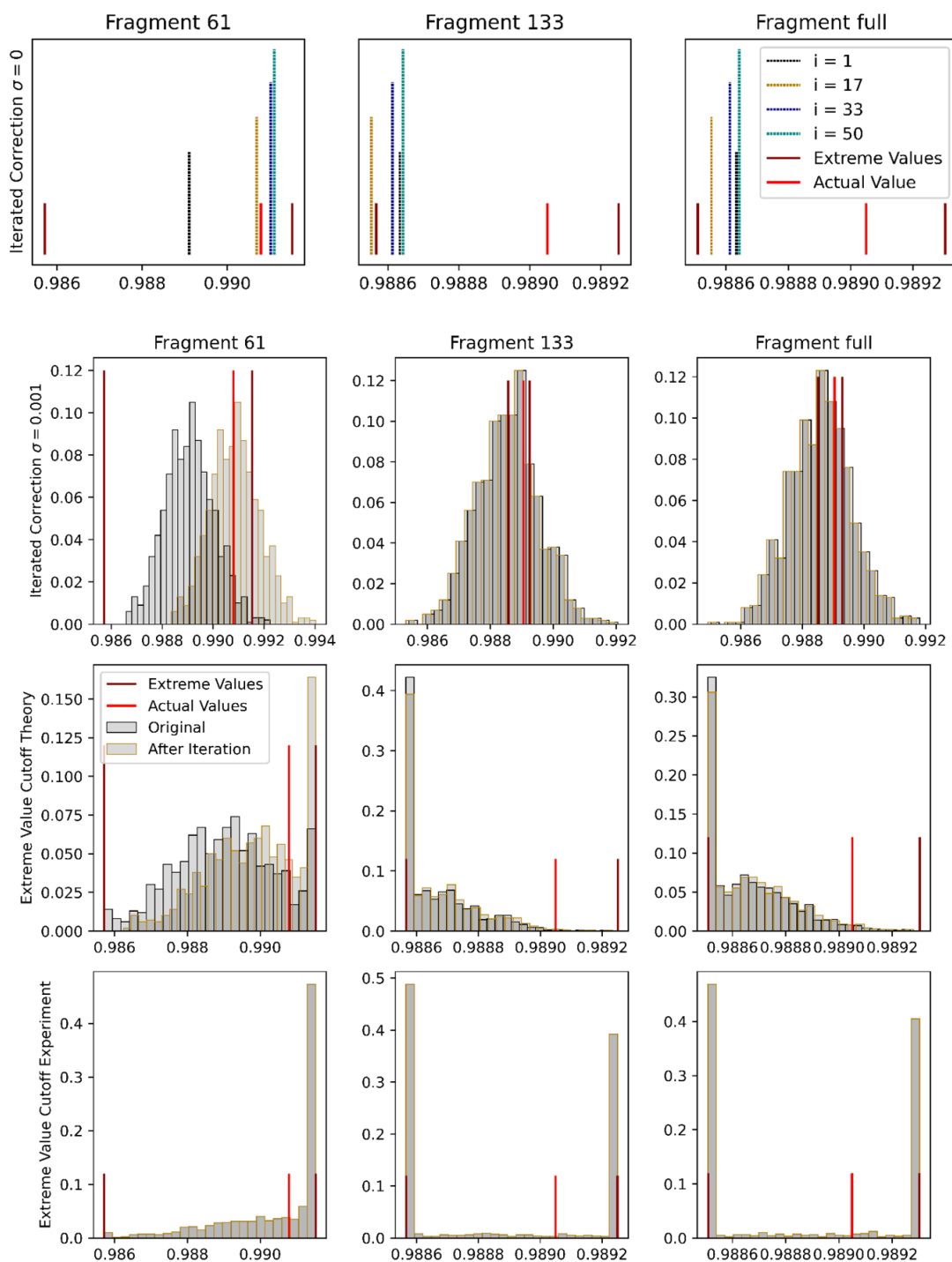


**Figure S2.4:** Histograms of recovered O values for the 61, 133, and full fragments using iterated and extreme value approaches. Top Row: The theoretical correction with  $\sigma = 0$  and 50 iterations; we see substantial improvement for  $O_{61}$  and no significant changes for other fragments. Second Row: The same, with  $\sigma = 1\%$ ; again we see improvement for  $O_{61}$  and no improvement for other fragments. Third Row: The theoretical correction method with an extreme value cutoff, where all values outside the computed bounds are

assigned to be at those bounds, and 50 iterations. Iteration does not substantially change the histograms, and the bounds are heavily sampled. Fourth Row: The experimental correction method with an extreme value cutoff and an iterated solution. Iteration did not result in noticeable changes to the histograms. The bounds are heavily represented due to the width of the experimental correction distributions.

As before, we plot the results from this set of simulations for the heavy isotopes of interest, in Figure S2.5. We find the iterated correction scheme to be the best solution, giving accurate values and smaller error bars than we saw previously for the experimental correction. We find that our results from  $\sigma = 0$  to be the most accurate and precise. Because the O factors sample many values over the course of an iterated solution, we consider it appropriate to use this correction scheme (as opposed to  $\sigma = 0$  and no iteration, which we know samples only an incorrect value). These results come with a tradeoff in terms of computational time; solving a single M+1 solution for methionine takes  $\approx 10$  seconds, while recalculating so iterating 50 times means our algorithm takes around  $\approx 10$  minutes. While this is practical for M+1, for higher order methods (e.g., M+4 which takes  $\approx 2$  minutes) or more complicated systems this may result in intractable computations. **The results in the main paper are presented using this iterated correction scheme for the M+1 dataset and a theoretical correction with  $\sigma = 1 \text{ ‰}$  for the remaining M+N datasets.** We note that there are possible ways to optimize our algorithm—for example, currently we solve the matrix inversion for every Monte Carlo run (e.g., 1000x) so performing this for 50 iterations means 50,000 matrix inversions—and we believe it is possible to substantially reduce this computation time in future work. In contrast, applying the extreme value cutoffs gives a modest benefit and is much cheaper in terms of computational time; improving on this method may be useful much more complex problems.

The number of variations on this correction scheme may seem overwhelming, so we here offer a practical guide to implementing them. When measuring a new system, users should begin by generating simulated sample and standard datasets with the experimental issues they anticipate (low abundance cutoffs, unresolved peaks, fractionation). They should then attempt to compute the **isotopologue** ratios of interest

using 1) no correction scheme; 2) the “theoretical” correction scheme with  $\sigma = 1\%$ ; and 3) the iterated theoretical correction scheme with  $\sigma = 0\%$ ; and compare the results. They may proceed with the simplest correction scheme which gives precise and accurate results for their system of interest. If none of these give appropriate results, and/or computational time with the iterated scheme is a concern, they should then investigate further correction schemes.

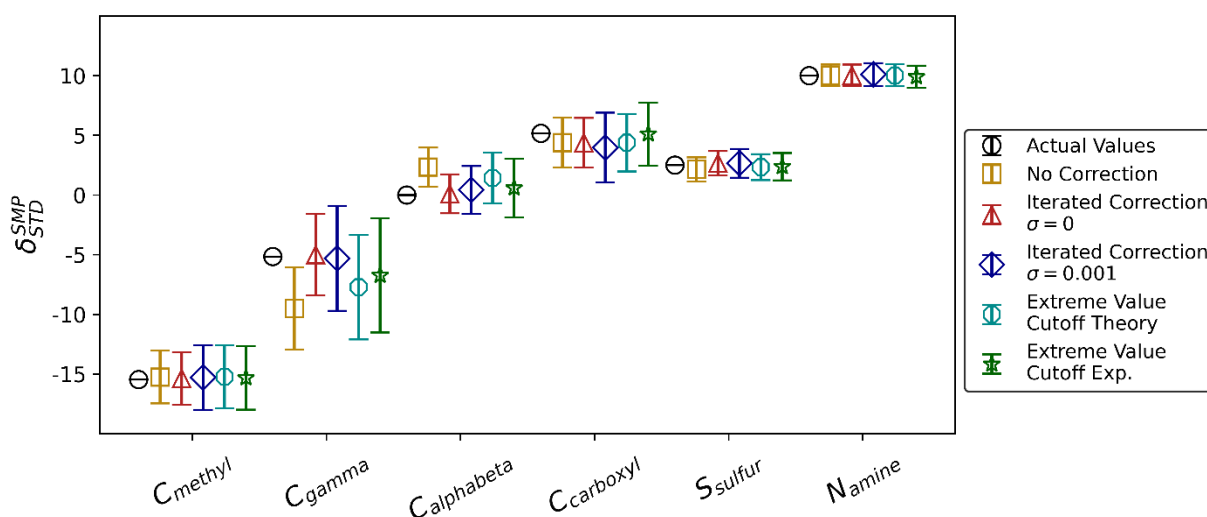


**Figure S2.5:** Results for the M+1 sites with iterated theoretical correction schemes and extreme value cutoffs for both experimental and theoretical correction schemes. The iterated correction scheme with  $\sigma = 0$  gives the best results, recovering the accurate values with error bars comparable to the case of no correction. We use this correction scheme in for the results presented in the main paper and suggest it for future work. The extreme value cutoff method is computationally simpler and results in marginal improvement, so may be considered for some applications.

We conclude this section by explaining the propagation of experimental error, which we achieve by a Monte Carlo simulation. For each iteration, we perturb both sample and standard in the following way. For each fragment, for each substitution, we draw a value from  $\mathcal{N}(\mu, \sigma)$  where  $\mu$  and  $\sigma$  are the mean and standard deviation of the **M+N relative abundance** of that substitution; we then normalize, so the **M+N relative abundances** of all ion beams for each fragment sum to 1 (i.e., as a real observation). We then standardize, following the method above. If we correct using O factors, we generate them as part of the standardization, following either the theoretical or experimental

corrections. We solve for specific  $\rho$  values *via* matrix inversion. We then compute the relevant  $U^{M+N}$ , as discussed in the paper, and report our results as  $\delta$  values relative to the standard. We repeat this process N (typically N = 1000) times, and report means and standard deviations for each recovered value. We take these standard deviations as our error bars. If we are iterating to generate the O factors, we then repeat this entire process, starting by drawing new values from  $\mathcal{N}(\mu, \sigma)$ , and using the updated forward model of the sample to compute new O factors.

All the individual steps have been discussed above, except for the perturbation of sample and standard. We have one comment to make about the normalization step: normalization causes the distributions we use for the Monte Carlo to subtly differ from those specified by the mean and standard deviation alone, as perturbations of one ion beam cause variations in the normalized values of others (Note that there are two normalization steps in the entire process; 1) the normalization here, following perturbation of sample and standard and 2) the normalization for the O factor correction.) To see this, we provide an example of a single normalization in Table S2.2, again using the 61 ion beam of methionine; the values following normalization differ from those following the perturbation itself, and the normalization values are correlated.

**Table S2.2: An Example Perturbation of Experimental Error**

	Measurement	Error	Perturbed	Normalized
D	0.009209	$9.21 \times 10^{-6}$	0.009204	0.009203
33S	0.11555	$1.16 \times 10^{-4}$	0.115526	0.115513
13C	0.314965	$3.15 \times 10^{-4}$	0.315214	0.315179
Unsub	0.560276	$5.60 \times 10^{-4}$	0.560168	0.560105
<b>SUM</b>	1		1.000113	1

A visualization of these effects across many iterations is shown below, in Figure S2.6. The histogram gives the probabilities calculated with normalization (“perturbed distribution”), while the red line gives the distribution without normalization (i.e., the

value if we treated the  $\mu$  and  $\sigma$  from our measurements as uncorrelated). We find that this process broadens the distribution for low abundance peaks (D) and narrows it for high abundance ones (Unsub). There may be more rigorous methods of perturbation— for example, defining a Dirichlet distribution for the ion beams of each fragment, or determining covariances directly from experimental data—which we suggest as avenues for improvement of our algorithm.

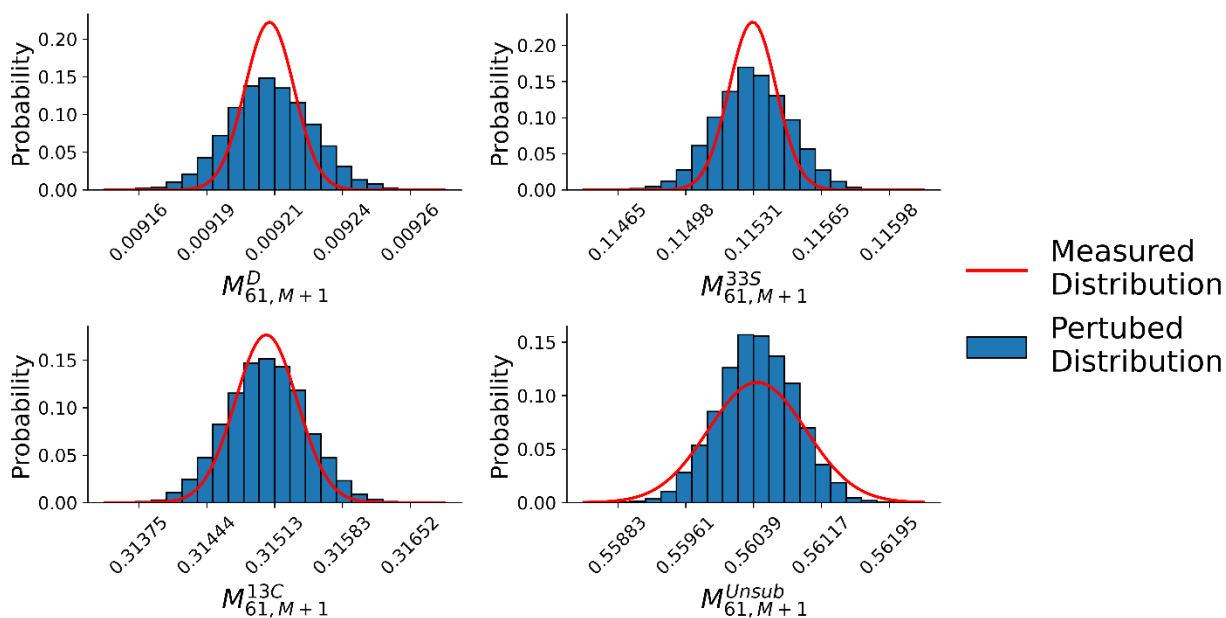


**Figure S2.7:** The sampled values for each peak of the 61 fragment of the M+1 measurement of methionine using our Monte Carlo method. For each iteration, we select a new value for each peak based on experimental error; we then normalize. Because the normalize step correlates errors from each ion beam, the final distribution for an ion beam may differ from its stated distribution based on mean and standard deviation. The histogram plots sampled values following normalize for each peak, while the line plots the distribution we drew from prior to normalize. We find normalize broadens the distribution of low abundance peaks (e.g., D) and narrows it for high abundance peaks (e.g., Unsub).

## S2.5: Additional Simulations and Modifications to the Algorithm

In the main text, we presented the output of our algorithm applied to M+N experiments on methionine with several types of experimental issues. Here, we present some additional results with variations to our algorithm. First, we demonstrate that if the

only experimental issue is instrument fractionation, and the standard is known perfectly, forward model standardization is exact. Next, we show a different method of standardization, which does not rely on a forward model, and demonstrate this is inferior in our case to forward model standardization. Finally, we develop and show a method to correct for large deviations from the stochastic assumption. Source code for these tests is available at <https://github.com/Csernica/Isotomics/tree/v1.0.0>.

### S2.5.1: “Forward Model” Standardization

This test demonstrates that when the only experimental issue is instrument fractionation, forward model standardization is exact. The forgoing section provides a justification of this fact; we here report some representative data from this problem (Table S2.3). We show the recovered values for each **site** of the sample following application of our algorithm. Here, delta values are given relative to the appropriate reference frame (VPDB for carbon, VSMOW for oxygen, CDT for sulfur, AIR for nitrogen, and VSMOW for hydrogen).

**Table S2.3 Forward Model Standardization Methionine Structure**

Site	# Atoms	$\delta_{\text{STD,actual}}$	$\delta_{\text{SMP,actual}}$	$\delta_{\text{Solution}}$
C-methyl	1	-30	-45	-45.00000
C-gamma	1	-30	-35	-35.00000
C- alphabeta	2	-30	-30	-30.00000
C-carboxyl	1	-30	-25	-25.00000
O-carboxyl	2	0/0	-13/-25	-13.00000/-25.00000
S-sulfur	1	0/0/0	2.5/4.854367/9.22339 1	2.500000/4.854369/9.22330 1
N-amine	1	0	10	10.00000
H-methyl	3	0	-250	-250.00000
H-gamma	2	0	-100	-100.00000
H- alphabeta	3	0	0	3.33067e-11

H-amine	2	0	100	100.00000
H-hydroxyl	1	0	250	250.00000
H-protonated	1	0	0	-4.99600e-12

Clumped Measurements	Number	$\Delta_{\text{STOCH,actual}}^{\text{STD}}$	$\Delta_{\text{STOCH,actual}}^{\text{SMP}}$	$\Delta_{\text{STOCH,Solution}}^{\text{SMP}}$
13C methyl   13C gamma	1	0	0	0.00000
13C carboxyl   15 N amine	1	0	0	0.00000
13C methyl   13C gamma   33S sulfur	1	0	0	0.00000
18O carboxyl   15N amine	1	0	0	0.00000
13C methyl   13C gamma   13C alphabeta   13C alphabeta	1	0	0	0.00000
13C methyl   17O carboxyl   18O carboxyl	1	0	0	0.00000

*A representative sample of M+N solutions from the fractionation factor measurement*

## S2.5.2: Alternative Standardization

While the forward model standardization approach does well in many circumstances, in some cases it may be preferable to not have to specify any information about our standard. Attempting to avoid this problem, we also investigated an approach with no forward model. In this case, we do not apply correction factors and use  $\rho_{\text{observed}}^i$  directly for both sample and standard, solving the matrix as in eq 65, then apply  $U^{\text{M+N}}$  values to calculate **isotopologue-specific U values** for both sample and standard (e.g., for  $^{13}\text{C}$ -methyl, we get  $U^{13\text{Cmethyl,SMP}}$  and  $U^{13\text{Cmethyl,STD}}$ ). Then, we report changes between sample and standard for each of these **isotopologue-specific U values**.

Results are shown in Table S2.4. Results for the non-hydrogen **sites** are generally within 2 ‰ of the correct value, while the hydrogen **sites** have errors of hundreds of per mil. The clumped species vary in accuracy; some are accurate, while others differ by up to 10 ‰. We attribute these errors to the interdependencies of the M+N solutions—fractionations in one ion beam (say  $^{13}\text{C}$ ) affect the observed **M+N relative abundances** of

every ion beam of that fragment (D,  $^{33}\text{S}$ , etc.) These interdependencies make a direct comparison between **sites** difficult. We also note that the solution to our matrix inversion gives many negative values for **M+N relative abundances**, a nonphysical result (in the M+1 experiment, this is true for H-gamma, H-alphabeta, and H-protonated). We find these results to be inferior to “forward model” standardization, even when the standard composition is poorly known.

**Table S2.4 Test 5 Methionine Structure**

Site	# Atoms	$\delta_{\text{STD,real}}$	$\delta_{\text{SMP,real}}$	$\delta_{\text{STD,real}}^{\text{SMP}}$	$\delta_{\text{STD,no forward model}}^{\text{SMP}}$
C-methyl	1	-30	-45	-15.46	-14.19
C-gamma	1	-30	-35	-5.15	-6.40
C- alphabeta	2	-30	-30	0	0.35
C-carboxyl	1	-30	-25	5.15	5.83
O-carboxyl	2	0/0	-13/-25 [17/18]	-13/-25	-11.37/-24.82
S-sulfur	1	0/0/0	2.5/4.85/9.22 [33/34/36]	2.5/4.85/9.22	2.52/4.85/9.2233
N-amine	1	0	10	10	9.44
<b>H-methyl</b>	<b>3</b>	<b>0</b>	<b>-250</b>	<b>-250</b>	<b>-138.42</b>
<b>H-gamma</b>	<b>2</b>	<b>0</b>	<b>-100</b>	<b>-100</b>	<b>30.61</b>
H- alphabeta	3	0	0	0	2.77
H-amine	2	0	100	100	29.70
<b>H-hydroxyl</b>	<b>1</b>	<b>0</b>	<b>250</b>	<b>250</b>	<b>14.05</b>
H- protonated	1	0	0	0	-9.68

Clumped Measurements	$\delta_{\text{STD,real}}^{\text{SMP}}$	$\delta_{\text{STD,no forward model}}^{\text{SMP}}$
13C methyl   13C gamma	-20.54	-20.53
13C carboxyl   15 N amine	15.21	16.36
13C methyl   13C gamma   33S sulfur	-18.09	-17.84
18O carboxyl   15N amine	-15.25	-15.25
13C methyl   13C gamma   13C alphabeta   13C alphabeta	-20.54	-20.54



13C methyl   17O carboxyl   18O carboxyl	-52.56	-62.15
---	--------	--------

### S2.5.3: A Method for Dealing with Large Clumped Anomalies

Here, we present an algorithm for dealing with large clumped isotope anomalies. To model this problem, we introduce large clumped isotope anomalies to several positions of methionine while keeping the site-specific delta values the same. As described in S2.2, above, this change will predominately affect the U values for **sites** involved in the clump, decreasing them for a positive clumped anomaly and increasing them for a clumped deficit. Our algorithm for the M+1 experiment gives us the correct **site-specific U values**; however, when we approximate these as **site-specific isotope ratios** using the **stochastic assumption** we introduce substantial error; these errors will make our understanding of the stochastic abundance of various **isotopologues** incorrect, propagating this error into M+2, M+3, or M+4 measurements (if we hope to report deviations from the stochastic abundances).

Before examining methionine, it will be useful to consider a simpler scenario. Consider an N<sub>2</sub> molecule with **site-specific concentrations** of  $[^{15}\text{N}]_{N_1} = [^{15}\text{N}]_{N_2} = 0.1$  and suppose we have a clumped anomaly between N<sub>1</sub> and N<sub>2</sub> of magnitude 0.02.

**Table S2.5: Nonstochastic N<sub>2</sub> Computations**

Isotopologue	Stochastic	Actual	Calculated via Stochastic Assumption
[00]	0.81	0.83	
[01]	0.09	0.07	
[10]	0.09	0.07	
[11]	0.01	0.03	
$U^{N_1} = U^{N_2}$	0.111111...	<b>0.084337</b>	0.084337

$R_{N1}^{15} = R_{N2}^{15}$	0.111111...	0.111111...	0.084337
$U^{N1N2}$	0.012345	<b>0.0361445</b>	0.0060493
$\Delta^{15N15N}$	0	3462.293	5072.46060

*Measured quantities in bold.*

Suppose we first measure **site-specific U values** via an M+1 experiment and approximate the **site-specific isotope ratios** as equal to the **site-specific U values**, i.e., “Calculated via stochastic assumption.” We then observe  $U^{N1N2}$ . When we compute the  $\Delta^{15N15N}$  value, we see it is >5000 per mil, indicating a large clump. Our use of the **stochastic assumption** should therefore be reexamined.

To address this issue, note that, to add a clump of size  $x$  (in concentration space) between the two nitrogen **sites**, while keeping **site-specific isotope concentrations** identical, we perform:

$$[00]_{observed} = [00]_{stoch} + x \quad (S2.56)$$

$$[01]_{observed} = [01]_{stoch} - x \quad (S2.57)$$

$$[10]_{observed} = [10]_{stoch} - x \quad (S2.58)$$

$$[11]_{observed} = [11]_{stoch} + x. \quad (S2.59)$$

Using this fact, we may solve for an unknown clump  $x$  iteratively. First, we approximate the **site-specific isotope ratios** using the **site-specific U values**, for example  $R_{N1}^{15} \approx 0.084337$ . Then, we compute the stochastic population, i.e.,  $[00]_{stoch}$ ,  $[01]_{stoch}$ ,  $[10]_{stoch}$ , and  $[11]_{stoch}$ . We use these to calculate clumped U values, i.e.,  $U^{N1N2} = \frac{[11]_{stoch}}{[00]_{stoch}}$ . Observing that our calculated value for  $U^{N1N2}$  differs from our measured one, we calculate the size of the anomaly  $x$  by solving

$$U_{meas}^{N1N2} = \frac{[11]_{stoch} + x}{[00]_{stoch} + x} \quad (S2.60)$$

for  $x$ . We then use this information to correct our early approximation for the **site-specific isotope ratio**:

$$R_{N1}^{15} = U_{stoch}^{N1} = \frac{[10]_{stoch}}{[00]_{stoch}} = \frac{[10]_{observed}}{[00]_{observed}} * \frac{[00]_{observed}}{[00]_{stoch}} + \frac{x}{[00]_{stoch}} = \frac{[10]_{observed} + x}{[00]_{stoch}}. \quad (S2.61)$$

Our new **site-specific ratios** are still wrong because our original **site-specific isotope ratios** were only approximations. However, by iterating this process, we obtain successively more accurate estimates for the **site-specific ratios**, allowing us to find the size of the clump.

One further tangent: in practice, rather than using eq (S2.60), we may calculate  $x$  via

$$(U_{observed} - U_{stochastic}) * [00]_{stoch} = \left( \frac{[11]_{observed}}{[00]_{observed}} - \frac{[11]_{stoch}}{[00]_{stoch}} \right) * [00]_{stoch} \\ \approx [11]_{observed} - [11]_{stoch} = x. \quad (S2.62)$$

This approximation is reasonable when  $[00]_{stoch}$  and  $[00]_{observed}$  are similar and is easier to implement computationally. We use this approximation for our methionine solution and find the results are sufficiently accurate.

With this algorithm in hand, we proceed to analyze a computed methionine sample with several large clumps, with  $\Delta$  values of 250 ‰ for the methyl/gamma carbons, -250 ‰ for the amine nitrogen and hydrogen, and 100 ‰ for the sulfur and gamma hydrogen (Table S2.6). Our initial solution, i.e., assuming no clumped anomalies were present, misses the **site-specific delta values** for the methyl and gamma **sites** by  $\approx 2.6$  per mil and other **sites** by  $< 1$  ‰. We also overestimate the size of the methyl-gamma clump by about 6 per mil.

Our results are improved by several iterations of our algorithm; our final estimates for **site-specific delta values** are almost all within 0.03 ‰, while the clumped deltas are within 0.1 ‰. We note that our solution does not include a correction for the sulfur-gamma H clump—as this **isotopologue** is not constrained by our solution, we cannot include it in our algorithm. The most difficult case for our algorithm to address will be scenarios with large clumps (> 25 ‰) which cannot be constrained and therefore cannot be corrected for. Systems like  $S_8$ , which contain many atoms with relatively common **rare isotopes** deserve extra caution in this regard. As it is difficult to make strict rules governing all cases, we suggest users with these sorts of systems generate computational datasets with a range of plausible clumps and observe the errors they introduce.

**Table S2.6 Large clumps in Methionine**

Site	# Atoms	$\delta_{SMP}$	$\delta_{Solution}$ (initial)	$\delta_{Solution}$ (6 iterations)
C-methyl	1	-45	-47.617023	-44.973813
C-gamma	1	-35	-37.617313	-34.973528
C-alphabeta	2	-30	-30.028177	-29.972368
C-carboxyl	1	-25	-25.028322	-24.972225
O-carboxyl	2	-13/-25	-13.028671/ 25.028322	-12.971883/ 25.028322
S-sulfur	1	2.5/4.8543 67/9.2233 91	2.456822/4.82 5180/9.22330 1	2.514500/4.82518 0/9.193985
N-amine	1	10	10.013919	9.985502
H-methyl	3	-250	-250.021786	-249.978635
H-gamma	2	-100	-100.738728	-100.686987
H-alphabeta	3	0	-0.029048	0.028487
H-amine	2	100	100.988837	100.031218
H-hydroxyl	1	250	249.963690	250.035609
H- protonated	1	0	-0.029048	0.028487
<b>Clumps</b>	<b>Type</b>	$\Delta^i$		

C-methyl/C-gamma	$^{13}\text{C}/^{13}\text{C}$	250	256.843698	249.931436
N-amine/H-amine	$^{15}\text{N}/^2\text{H}$	-250	-250.683996	-250.010519
S-sulfur/H-gamma	$^{33}\text{S}/^2\text{H}$	100	Not solved for	Not solved for

## ACCURACY AND PRECISION OF ESI-ORBITRAP-IRMS OBSERVATIONS OF HOURS TO TENS OF HOURS VIA RESERVOIR INJECTION

Csernica, T., Bhattacharjee, S., and Eiler, J. (2023) Accuracy and precision of ESI-Orbitrap-IRMS observations of hours to tens of hours via reservoir injection. *Int. J. Mass Spectrom.* **490**, 117084. doi: 10.1016/j.ijms.2023.117084

### Abstract

Orbitrap isotope ratio mass spectrometry (Orbitrap-IRMS) has recently been applied to high-precision, natural-abundance isotope ratio measurements of a diverse range of compounds, including amino acids, oxyanions, fatty acids, and metals. These measurements can characterize many isotope ratios simultaneously at high ( $\approx 1.0$  ‰) precision. In a successful experiment, observed precision will track the shot-noise limit and be limited by experimental time. Some isotope ratios, for example those involving  $^{17}\text{O}$  in organic compounds or multiply-substituted ('clumped') isotopologues, require experimental times of hours to tens of hours to achieve desired precision, while current sample introduction techniques focus on observations on the order of seconds to tens of minutes. In this study, we characterize Orbitrap-IRMS performance for three long duration measurements (individual acquisitions  $\geq 1$  hour and as long as 24 hours) using an automated reservoir injection system coupled to a Q Exactive HF Orbitrap with an electrospray ionization (ESI) source. First, we characterize long-term intra-measurement stability through a 24-hour long measurement of acetone. We report the following isotope ratios and precisions (as acquisition errors, errors on the observed ratio within this measurement ( $\sigma_{\text{AE}}$ )):  $^{13}\text{C}/^{12}\text{C}$  ( $\sigma_{\text{AE}} = 0.07$  ‰),  $^{17}\text{O}/^{16}\text{O}$  ( $\sigma_{\text{AE}} = 1.1$  ‰),  $^{18}\text{O}/^{16}\text{O}$  ( $\sigma_{\text{AE}} = 0.3$  ‰), and  $^{13}\text{C}^{13}\text{C}/^{12}\text{C}$  ( $\sigma_{\text{AE}} = 0.65$  ‰). The  $\sigma_{\text{AE}}$  of each tracks the shot noise limit throughout and is limited by the challenging conditions (high resolution and low numbers of ions per scan) required for  $^{17}\text{O}/^{16}\text{O}$  measurement in the presence of  $^{13}\text{C}$  via Orbitrap. Second, we characterize inter-measurement stability via a sequence of seven 75-minute analyses of perchlorate. We

observe the following ratios and acquisition errors:  $^{37}\text{Cl}/^{35}\text{Cl}$  ( $\sigma_{\text{AE}} = 0.09 \text{ ‰}$ );  $^{17}\text{O}/^{16}\text{O}$  ( $\sigma_{\text{AE}} = 1.6 \text{ ‰}$ );  $^{18}\text{O}/^{16}\text{O}$  ( $\sigma_{\text{AE}} = 0.7 \text{ ‰}$ ),  $^{37}\text{Cl}^{17}\text{O}/^{35}\text{Cl}^{16}\text{O}$  ( $\sigma_{\text{AE}} = 2.7 \text{ ‰}$ ), and  $^{37}\text{Cl}^{18}\text{O}/^{35}\text{Cl}^{16}\text{O}$  ( $\sigma_{\text{AE}} = 1.2 \text{ ‰}$ ). However, we find that inter-measurement drift between acquisitions limits our accuracy and precision for standardized measurements (i.e., error on reported  $\delta$  values) to  $\approx 1 \text{ ‰}$  for the  $^{37}\text{Cl}/^{35}\text{Cl}$  measurement. Hence, the benefits of low  $\sigma_{\text{AE}}$  may not be fully realized. Third, we demonstrate accuracy via sample/standard comparisons of a methionine sample with  $^{13}\text{C}$  enrichment of  $\approx 20 \text{ ‰}$  relative to a known standard. Using a sequence of seven 60-minute analyses, we recover the following isotope ratios and standardized precisions (i.e., error on reported  $\delta$  values, denoted propagated acquisition errors,  $\sigma_{\text{PAE}}$ ):  $^{33}\text{S}/^{32}\text{S}$  ( $\sigma_{\text{PAE}} = 1.0 \text{ ‰}$ ),  $^{34}\text{S}/^{32}\text{S}$  ( $\sigma_{\text{PAE}} = 0.7 \text{ ‰}$ ),  $^{15}\text{N}/^{14}\text{N}$  ( $\sigma_{\text{PAE}} = 2.1 \text{ ‰}$ ),  $^2\text{H}/^1\text{H}$  ( $\sigma_{\text{PAE}} = 3.2 \text{ ‰}$ ),  $^{13}\text{C}/^{12}\text{C}$  ( $\sigma_{\text{PAE}} = 0.4 \text{ ‰}$ ),  $^{18}\text{O}/^{16}\text{O}$  ( $\sigma_{\text{PAE}} = 1.6 \text{ ‰}$ ), &  $^{13}\text{C}^{13}\text{C}/^{12}\text{C}$  ( $\sigma_{\text{PAE}} = 2.8 \text{ ‰}$ ) with confirmation of accurate results for the known  $^{13}\text{C}/^{12}\text{C}$  and  $^{13}\text{C}^{13}\text{C}/^{12}\text{C}$  enrichments. Together, our results demonstrate the viability of Orbitrap-IRMS for long duration measurements of diverse sample types via an automated reservoir injection system. Inter-measurement stability remains a challenge; we expect our methods to be most applicable to extended measurements of hard-to-observe properties, such as  $^{17}\text{O}$  in organics and clumped isotopologues.

### 3.1. Introduction

Orbitrap isotope ratio mass spectrometry (Orbitrap-IRMS) has existed in commercial forms for  $\sim 20$  years and has recently been employed to study natural abundance isotope ratios at high precision (of order per mil, or ‰) (Makarov, 2000; Hu et al., 2005; Hoegg et al., 2017; Eiler et al., 2017; Neubauer et al., 2018). Orbitrap-IRMS is useful for these applications due to its high mass resolution (nominal  $R = m/\Delta m$  of  $> 2$  million has been demonstrated), small sample requirements (often on the order of nmols to pmols, though variable with analyte, target isotopologues and required precision), and its ability to observe fragment ions to constrain site-specific isotopic structure (Eiler et al., 2017; Denisov et al., 2021). Moreover, by interfacing various sources, e.g., electron impact (EI),

electrospray ionization (ESI), or liquid sampling atmospheric pressure glow discharge (LS-APGD), many different types of analytes, including organic compounds, metals, metal oxides, and oxyanions can be observed (Hoegg et al., 2017, 2021; Eiler et al., 2017; Neubauer et al., 2018, 2020; Chimiak et al., 2021; Bills et al., 2021; Hilkert et al., 2021; Wilkes et al., 2022; Mueller et al., 2022a; Zeichner et al., 2022). Thus far, applications include meteoritic alanine, serine from *A. Thaliana* plants, nitrate from river waters as well as acetate, uranium oxide, strontium, rubidium, nitrate, sulfate, and methionine, with many more in active development (Neubauer et al., 2018; Hoegg et al., 2017; Chimiak et al., 2021; Wilkes et al., 2022; Hilkert et al., 2021; Mueller et al., 2022a; Hoegg et al., 2021; Neubauer et al., 2020; Bills et al., 2021; Zeichner et al., 2022).

To be successful, an Orbitrap-IRMS measurement must constrain a target isotope ratio at some desired precision; in most cases, the precision is a function of the number of ions observed throughout the experiment, following counting statistics, and therefore limited by measurement duration. The time required to reach a given precision can vary substantially based on the analyte and isotope ratio of interest and is influenced by the specifics of Orbitrap function (see Nomenclature for a glossary of key terms defined throughout the paper). An Orbitrap measurement consists of many (typically hundreds to tens of thousands) scans, where each scan is a single observation of a packet of ions within the Orbitrap. Observing a large number of ions in a single scan results in space-charge effects that can suppress the signals of low abundance peaks and lead to artifacts such as ‘coalescence’, the merging of peaks with similar  $m/z$  (Hofmann et al., 2020). At the same time, higher mass resolution requires longer scan durations (Eiler et al., 2017). For a given isotope ratio, the number of ions observed in an experiment, and therefore precision, is limited by 1) the number of ions observed per scan, which must be low enough to limit space-charge effects, and 2) the resolution, and therefore the time per scan, required to resolve the target of interest. Once other experimental parameters have been optimized, the only way to improve precision is to observe for a longer time.



In some cases, these constraints demand a measurement of tens of hours. Consider, for example, the observation of the  $^{17}\text{O}/^{16}\text{O}$  ratio in organics, one of the most challenging targets in the stable isotope geochemistry (Clayton, 2008; Miller and Pack, 2021).  $^{17}\text{O}$  is low in abundance ( $\sim 400$  ppm of natural oxygen), generally must be measured simultaneously with other much more abundant ion species (e.g., the unsubstituted and/or  $^{13}\text{C}$ -substituted ions) and must be mass resolved from closely adjacent  $^{13}\text{C}$ -bearing near isobars, generally requiring  $m/\Delta m$  of  $>100,000$ . When observed via Orbitrap-IRMS, these properties demand long scans ( $\approx 250$  ms) which contain few total ions, only a small fraction of which are  $^{17}\text{O}$ . Useful precisions ( $\approx 1\%$ ) therefore require the stable delivery of sample for extended durations of up to tens of hours. Although such long periods of integration are challenging,  $^{17}\text{O}$  is a key target for certain science applications, particularly to study of cosmochemistry and astrobiology, and no other currently recognized technology is capable of precisely measuring  $^{17}\text{O}$  contents of oxygen-bearing organics without chemical conversion and with sensitivities suitable for study of natural samples of interest (Adnew et al., 2019). Similar cases could be made for many 'clumped' (multiply substituted) isotopic measurements of possible interest. Therefore, an understanding of Orbitrap-IRMS performance for long duration experiments and appropriate sample introduction techniques are needed.

Several sample introduction methods have been demonstrated for Orbitrap-IRMS measurements of varying duration, focusing on observations of up to tens of minutes. Marcus and colleagues have developed a LS-APGD system, typically using dual syringe pumps (although optionally using a high performance liquid chromatography (HPLC) pump) interfaced to a six-port valve, typically with liquid flow rates of 5-40  $\mu\text{L}/\text{minute}$  for samples with a concentration of 0.1-10  $\mu\text{M}$  and durations of tens of minutes (Marcus et al., 2011; Hoegg et al., 2016, 2017, 2021; Bills et al., 2021). Several applications use syringe pump injections with an ESI source, with flow rates of 1-20  $\mu\text{L}/\text{minute}$ . These use either a single syringe pump and manually change the syringe between samples (Neubauer et al., 2018, 2020; Mueller et al., 2022a), or a dual-inlet syringe pump connected to a six-port valve, where two syringes are pumped simultaneously, one of the two is selected as active, and

the two are alternated via a pneumatic valve controlled by software commands (Hilkert et al., 2021). In either case, typical experimental durations are tens of minutes. Hilkert et al. have demonstrated an automated “flow injection” system coupled to an ESI ion source, where an autosampler fills a sample loop of 20  $\mu\text{L}$  with analyte for 6 minutes of active measurement; in order to prevent cross contamination, additional time must be spent flowing analyte-free solvent through the system, so each analysis totals 15 minutes (Hilkert et al., 2021). Gas phase introduction methods with an EI source have also been demonstrated for Orbitrap-IRMS (Eiler et al., 2017; Zeichner et al., 2022). These include the direct observation of room temperature gases (e.g.,  $\text{CO}_2$  or Xe) or the vapor associated with liquids or solids for tens of minutes as well as gas chromatography methods. The latter may trap peaks eluting from a GC column in a ‘peak broadener,’ slowly introducing them to the instrument to enable durations of tens of minutes (Eiler et al., 2017; Chimiak et al., 2021). In addition to these and of particular interest here, Eiler et al. present a 24-hour long observation of perfluorotributylamine (PFTBA), a reference gas for the Q Exactive GC mass spectrometer with a dedicated reservoir built into the instrument. This experiment successfully tracked the shot noise limit for the duration, demonstrating the stability of the Q Exactive GC is sufficient for such long durations, but is not generalizable to other sample molecules (Eiler et al., 2017).

Here, we present several long duration Orbitrap-IRMS measurements obtained via a “reservoir injection” sample introduction method that observes diverse target molecules for hours to tens of hours. Our system interfaces a Vanquish Horizon HPLC to a Q Exactive HF Mass Spectrometer with an ESI source. It uses a reservoir size of 250 mL to 1 L (in principle, it may be arbitrarily large) with automated switching between different reservoirs for sample standard comparisons and balancing of sample and standard concentration and flow rate so that signals for sample and standard are closely matched. We characterize the long-term stability and the accuracy of Orbitrap-IRMS using this system. We find that individual acquisition errors ( $\sigma_{\text{AE}}$ ) track the shot noise limit throughout and sample standard comparisons give accurate results with error bars ( $\sigma_{\text{PAE}}$ ) slightly larger than individual  $\sigma_{\text{AE}}$

values (< a factor of 2), up to a limit of  $\sigma_{AE}$  on the order of 1 ‰; beyond this, the benefits of low  $\sigma_{AE}$  are not always realized due to inter-measurement drift. Our results complement the current suite of sample introduction methods and characterize the performance of Orbitrap-IRMS for long duration observations.

## 3.2. Materials and Methods

### 3.2.1 Materials

#### 3.2.1.1 Acetone

HPLC-Plus grade acetone (>99.9%) was acquired from Sigma Aldrich and mixed at a concentration of 500  $\mu$ M with a 90/10 mixture of LC-MS grade methanol (Fischer Scientific) and ultrapure water (Milli-Q IQ 7000 Purification).

#### 3.2.1.2 Perchlorate

Potassium perchlorate (KClO<sub>4</sub>) (>99.99% trace metals basis) was acquired from Sigma Aldrich. A stock solution of 10 mM potassium perchlorate in deionized water was prepared. This stock was then diluted to a 2  $\mu$ M concentration in a solution of 100:1 methanol:ammonium hydroxide (LC-MS Grade, Fischer Scientific; NH<sub>4</sub>OH is >25% in H<sub>2</sub>O). We found adding ammonium hydroxide as an additive improved the ionization stability of perchlorate (appendix, A.1) (Martin, Peter Eckels, 2019)

#### 3.2.1.3. Methionine Standard and Sample

A methionine standard was acquired from Sigma Aldrich and analyzed previously as Met-A by Neubauer et al. (Neubauer et al., 2018). Previously measured aspects of its molecular average isotopic content include  $\delta^{13}C_{VPBD} = -30.0 \pm 0.1$  ‰ and  $\delta^{34}S_{CDT} = 4.3 \pm 0.4$  ‰. A methionine sample was created by mixing this standard with a methyl <sup>13</sup>C-labeled (99 % label at methyl site and natural abundances elsewhere; 98% chemical purity) methionine acquired from Cambridge Isotope Laboratories. To do so, we first dissolved 50 mg of unlabeled methionine in 25 mL of deionized water (13.3 mM) (Milli-Q IQ 7000 Purification)

and 1 mg of labeled methionine in 10 mL of deionized water (0.67 mM). We then added 550  $\mu\text{L}$  of the labeled solution (i.e., 55  $\mu\text{g}$  of labeled methionine, or 0.11% of the combined sample) to the unlabeled solution to create the mixture. The mass of labeled sample added was calculated to give an enrichment of  $\approx 100$  ‰ *relative to the standard* at the methyl site. The combined solution was flash-frozen in liquid nitrogen and freeze dried to obtain a product methionine (the ‘sample’). This sample was characterized using an EA IsoLink™ combustion elemental analyzer system interfaced to a Delta V Plus isotope ratio mass spectrometer (EA-IRMS, Thermo Fischer Scientific), and had a value of  $\delta^{13}\text{C}_{\text{VPDB}} \approx -11.0 \pm 0.1$  ‰. Methionine solutions were made at a concentration of 50  $\mu\text{M}$  in a 70/30 mixture of LCMS-grade methanol and deionized water, with 0.1 % by volume formic acid (Fischer Scientific) added to assist ionization.

The methionine sample was a mixture of two endmembers with partially known isotopic enrichments. Due to the small amount,  $\approx 0.1$  %, of the labeled endmember, and assuming the labeled methionine had natural isotopic abundances for all elements besides C, we expect no differences in isotopic composition between the unlabeled and mixture samples for any non-carbon element (H, N, O, S). The difference in  $\delta^{13}\text{C}_{\text{VPDB}}$  between the unlabeled and mixture samples ( $-30.0$  ‰ &  $-11.0$  ‰, respectively) imply that the mixture measured vs. the unlabeled sample would yield a  $\delta^{13}\text{C}_{\text{unlabeled}}$  of 19.6 ‰ (note differences of delta values are not additive), and a difference in ratio of doubly- $^{13}\text{C}$  substituted to unsubstituted isotopologues ( $^{13}\text{C}_2^{12}\text{C}_3\text{H}_{11}^{14}\text{N}^{16}\text{O}_2^{32}\text{S}/^{12}\text{C}_5\text{H}_{11}^{14}\text{N}^{16}\text{O}_2^{32}\text{S}$ ) between these two samples that is double their difference in  $\delta^{13}\text{C}$  (39.2 ‰). We verified these assumptions by explicitly calculating all isotopologues of each endmember as well as the mixed product; methods for this computation are presented in Csernica and Eiler 2023, and the details are available in the appendix, A.2 (Csernica and Eiler, 2023).

### 3.2.2. Methods

#### 3.2.2.1 *The HPLC-modified sample introduction system*

Our implementation of a reservoir injection system uses a Vanquish Horizon HPLC system (henceforth “Vanquish”) interfaced to a Q Exactive HF Mass Spectrometer (Thermo Fisher Scientific) (Figure 3.1). The Vanquish has two pumps, “A” and “B”; during operation, each pump may pull solution from a single reservoir (typically of 250 mL to 1 L, although in principle much larger) and mix these with some desired composition, e.g., 75% A, 25% B (Figure 3.1). To simplify switching between different solutions, each pump can be attached to three separate reservoirs, e.g., A1, A2, A3, and the active bottle determined via software commands. In a typical HPLC application, these reservoirs contain solvent; the analyte is introduced via a needle injection from a  $\approx 2$  mL vial, then eluted off a column using a solvent gradient defined by varying flow rates through pumps A and B. The reservoir injection method presented here bypasses this process—no sample is injected via the needle and no column is used. Instead, the analyte solution is placed directly into a reservoir (e.g., A1) and introduced to the mass spectrometer. We may optionally apply solvent mixing to adjust the concentration of the analyte online; for example, if we load methionine with a concentration of 50  $\mu\text{M}$  on reservoir A1 and wish to perform an experiment which requires a concentration of 25  $\mu\text{M}$ , we may load reservoir B2 with solvent and inject with a 50/50 mixing ratio of A1 and B2. This strategy can be used to perform multiple experiments which require different concentrations on the same bottle of analyte. Additionally, when performing a sample/standard comparison, it allows us to finely adjust the concentrations of both solutions to closely match intensities for the sample and standard analyte. The system is designed to operate at flow rates of 100  $\mu\text{L}/\text{minute}$  to 8 mL/minute of combined flow through A & B at  $\geq 50$  bar pressure. To minimize sample consumption, we operate near the lower limit of 100  $\mu\text{L}/\text{minute}$  during acquisitions.

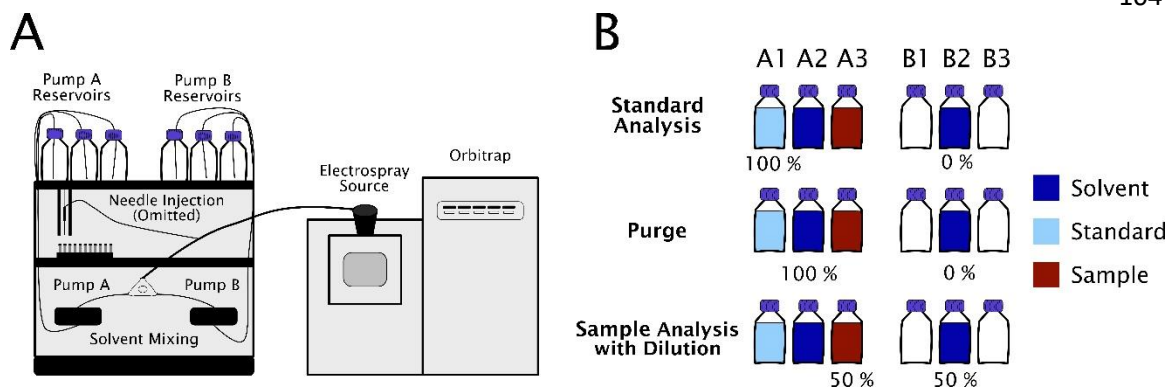


**Figure 3.1:** Setup for the reservoir injection system. A: A depiction of the Vanquish HPLC attached to the Q Exactive HF. The HPLC has two pumps, A and B, each of which is attached to three separate reservoirs. In use, each pump draws from a single reservoir, and the two can be mixed in various proportions before being introduced to the electrospray source. B: Representative reservoir contents and mixing amounts for different purposes. Standard analysis observes the standard via pump A only. A purge sequence pushes solvent through pump A. Sample analysis with dilution observes the sample via pump A while mixing with solvent from pump B to dilute online. In this example, reservoirs B1 and B3 are not used.

Reservoir injection measurements, like most Orbitrap-IRMS measurements, generally involve closely matched comparisons of sample and standard measurements, made under nearly identical instrumental conditions and closely spaced in time. We use this method because the isotope ratio(s) observed in Orbitrap-IRMS differ from their true values due to differences in the efficiencies of ion generation, transmission and detection of different isotopic forms of ions in various stages of the measurement, e.g., delivery of analyte to the ion source, ionization and ion extraction, transmission and pre-selection in the quadrupole system of the Q Exactive platform, trapping in the C-trap, and observation in the Orbitrap; we collectively refer to these processes as “instrument fractionation.” By observing a standard with a known isotope ratio under the same conditions as the sample, we can measure and correct for the instrument fractionation encountered by that analyte. Some instrument fractionations vary with time, so rather than performing a one-time standardization, we alternate sample and standard measurements, interpolating between standard measurements to estimate instrument fractionation during a sample measurement.

Using the reservoir injection method, we can implement sample/standard comparison in two ways—either with both sample and standard flowing through a single

pump, but drawing on different reservoirs, e.g., comparing reservoirs A1 and A3, or with each flowing through separate pumps, e.g., comparing reservoirs A1 and B1. It is possible that using different pumps is better for preventing contamination between sample and standard, as sections of tubing unique to each pump will only see either sample or standard; on the other hand, any difference in equipment and procedures between sample and standard could potentially introduce differences in instrument fractionation and thus systematic error in the sample/standard comparison. Here we chose to use the same pump for both sample and standard. Between observations, we perform a 'purging' step to clear the previous analyte. We purge by flushing the system with pure solvent (e.g., reservoir A2; Figure 3.1), to remove the previous analyte. We start analysis of new analytes with a 'priming' step, as a dead volume of  $\approx 2$  mL must be filled before the analyte reaches the electrospray source. The details of 'purging' and 'priming' steps may differ between samples, but they must be included in any sample/standard comparison. All steps may be automated using the Xcalibur software, allowing measurement sequences of tens of hours without user input.

Details for our analysis are given in Table 2.2, below. The acetone measurement assesses intra-measurement stability and was not standardized through sample/standard comparison. The perchlorate measurements include a sample/standard comparison, but only through a 'zero enrichment' experiment, i.e., the 'sample' and the 'standard' consist of the same perchlorate. For perchlorate, priming is done in a 15-minute step at 0.15 mL/minute, while purging consists of 20 minutes of solvent flow at the same flow rate. The methionine measurements involve standardization with different sample and standard. Here, 'priming' is accomplished by introducing analyte from its reservoir (A1 or A3) mixed 50:50 with pure solvent from reservoir B2 at a rate of 0.5 mL/minute, for a total of 8 minutes. After priming, we adjust the flow rate to the 0.1 mL/minute used for observation. We allow the system to stabilize at this flow rate for two minutes, then observe for the desired amount of time. Finally, we purge the system with solvent from A2 at 0.5 mL/minute. In all cases, the duration of the measurement step can be increased arbitrarily.

For methionine, the mixing ratios for sample (96%, not shown) and standard (95%) differ subtly; we tuned these prior to the measurement, to closely match ion intensities for each. They both include a large amount of solvent because the same solutions were also used for another set of measurements which required higher concentrations and which we intend to present in a forthcoming publication. Both perchlorate and methionine analyses were performed in triplicate, i.e., 7 observations were performed in the order: Standard/Sample/Standard/Sample/Standard/ Sample/Standard.

**Table 2.2: Conditions for Reservoir Injection Experiments**

<b>Acetone 24-Hour Experiment</b>						
<i>Time (minutes)</i>	<i>Concentration of A (uM)</i>	<i>Flow (mL/min)</i>	<i>%B</i>	<i>Pump A</i>	<i>Pump B</i>	<i>Description</i>
0-1440	500	0.1	0	A2: Sample	N/A	Observe
<b>Perchlorate Zero Enrichment Comparisons</b>						
<i>Time (minutes)</i>	<i>Concentration of A (uM)</i>	<i>Flow (mL/min)</i>	<i>%B</i>	<i>Pump A</i>	<i>Pump B</i>	<i>Description</i>
0-15	2	0.15	0	A1: Standard	N/A	Prime
15-90	2	0.15	0	A1: Standard	N/A	Observe
90-110	2	0.15	0	A2: Solvent	N/A	Purge
<i>Repeat as desired, switching between 'Standard' and 'Sample' Reservoirs.</i>						
<b>Methionine Sample Standard Comparisons</b>						
<i>Time (minutes)</i>	<i>Concentration of A (uM)</i>	<i>Flow (mL/min)</i>	<i>%B</i>	<i>Pump A</i>	<i>Pump B</i>	<i>Description</i>
0-8	50	0.5	50	A1: Standard	B2: Solvent	Prime
8-10	50	0.1	95 <sup>a</sup>	A1: Standard	B2: Solvent	Adjust flow
10-70	50	0.1	95	A1: Standard	B2: Solvent	Observe
70-90	50	0.5	0	A2: Solvent	B2: Solvent	Purge
<i>Repeat as desired, switching between 'Standard' and 'Sample' Reservoirs.</i>						

a: For the methionine samples (as opposed to standards), %B was 96% between 8 and 70 minutes.

The ions and isotopologues we monitored are as follows. For acetone, we observed  $C_3H_7O^+$ , including  $^{12}C_3^{1}H_7^{16}O^+$  (the unsubstituted isotopologue) and heavy isotopologues of this ion including  $^{13}C$ ,  $^2H$ ,  $^{17}O$ ,  $^{18}O$ , or  $^{13}C^{13}C$  substitutions. For perchlorate, we observed  $ClO_4^-$ , including  $^{35}Cl^{16}O_4^-$  (the unsubstituted isotopologue) and heavy isotopologues of this ion including  $^{37}Cl$ ,  $^{17}O$ ,  $^{18}O$ ,  $^{37}Cl^{17}O$ , and  $^{37}Cl^{18}O$  substitutions. For methionine, we observed



$C_5H_{12}NO_2S^+$ , including  $^{12}C_5^{1}H_{12}^{14}N^{16}O_2^{32}S^+$  (the unsubstituted isotopologue) and heavy isotopologues of this ion including  $^{33}S$ ,  $^{34}S$ ,  $^{15}N$ ,  $^2H$ ,  $^{13}C$ ,  $^{18}O$ , and  $^{13}C^{13}C$  substitutions.

### 3.2.2.2 Ionization and Data Analysis

The analytes were ionized using an (ESI) source with a HESI-II probe (Thermo Fisher Scientific). Experimental conditions for each analyte are shown in Table 2.3, as well as the observed tics and relative standard deviations (RSD) for samples and standards. For each analyte under these conditions, contaminant peaks in the spectra were less than 10% the height of the unsubstituted isotopologue, minimizing effects on the observed ratios due to these contaminants (Hofmann et al. suggest a threshold of 20% is sufficient to avoid statistically significant effects) (Hofmann et al., 2020).

**Table 2.3: Mass Spectrometer Parameters By Analyte**

	Acetone	Perchlorate	Methionine
Polarity (+/-)	Positive	Negative	Positive
Spray Voltage (kV)	4.5	3.0	4.5
Sheath gas flow rate (arbitrary)	50	10	35
Auxiliary gas flow rate (arbitrary)	10	10	10
Sweep gas flow rate (arbitrary)	2	0	0
Capillary temperature (°C)	320	320	320
S-lens RF level (arbitrary)	50	50	50
Aux gas heater temperature (°C)	40	40	40
Scan Range (m/z)	57.0-62.0	97.5-104.0	149.5-152.5
Microscans (#)	10	1	1
Automatic Gain Control (AGC) (# of ions) <sup>a</sup>	$2 \times 10^5$	$2 \times 10^5$ or $5 \times 10^5$	$10^5$
Mass Resolution (FWHM at m/z = 200) <sup>b</sup>	120,000	120,000	120,000

Maximum Injection Time (ms)	1000	500	1000
Observed TIC Std (Intensity)	2.0e7	4.2e7	1.2e8
Observed TIC relative standard deviation (RSD) Std (%)	15	6.5	5.3
Observed TIC Smp (Intensity)	-	4.2e7 <sup>c</sup>	1.2e8
Observed TIC RSD Smp (%)	-	6.0 <sup>c</sup>	4.3

a: The AGC target is a target number of ions, but note that the number of ions observed in the Orbitrap is an approximation.

b: Orbitrap resolution scales as  $(m/z)^{-1/2}$

c: Perchlorate 'sample' and 'standard' consist of the same solution but are treated as a distinct sample and standard and so noted here.

Ion intensities and noise for selected isotopic peaks were recovered from instrument .RAW files using either FTStatistic (proprietary unpublished software provided by Thermo Fisher Scientific; used for acetone and methionine) or IsoX (a recently developed software; used for perchlorate) (Hilkert et al., 2021). For the <sup>17</sup>O peak of acetone, a targeted extraction procedure using FTStatistic was used to distinguish <sup>17</sup>O from artifacts associated with the close-lying <sup>13</sup>C peak; this is discussed in detail in the appendix, A.3. In either case, this data was used to calculate ion counts following Eiler et al. 2017 (Eiler et al., 2017). Briefly, for each peak, ion counts were calculated following the equation

$$N_{IO} = \frac{S}{N} * \frac{C_N}{z} * \left(\frac{R_N}{R}\right)^{\frac{1}{2}} * \mu^{\frac{1}{2}} \quad (3.1)$$

where  $N_{IO}$  is the number of ions observed in a scan, S is the ion intensity, N is the peak noise,  $C_N$  is an empirical constant measured by Makarov and Denisov relating the signal-to-noise ratio to ion counts, here taken to be 4.4, (Makarov and Denisov, 2009) z is the charge (taken to be 1 in all cases here),  $R_N$  is the reference resolution of 120,000 at which  $C_N$  was determined, R is the mass resolution, and  $\mu$  is the number of microscans (i.e., Orbitrap scans that were averaged before the transient was subjected to fast Fourier transform analysis, Table 3.1). The number of counts calculated with eqn. 3.1 were used to compute observed

isotope ratio(s) for each scan. For example, for scan  $j$  and isotope ratio  $^{13}\text{C}/\text{Unsub}$ , the observed ion beams are  $^{13}\text{C}^{12}\text{C}_2^{16}\text{O}^1\text{H}_7^+$  and  $^{12}\text{C}_3^{16}\text{O}^1\text{H}_7^+$ , and we compute  $R_j^{13\text{C}} = \frac{N_{IO,j}(^{13}\text{C}^{12}\text{C}_2^{16}\text{O}^1\text{H}_7^+)}{N_{IO,j}(^{12}\text{C}_3^{16}\text{O}^1\text{H}_7^+)}$ . For each target isotope ratio  $i$ , we report the average ratio across all  $N$  scans:

$$R^i = \frac{1}{N} \sum_{j=1}^N R_j^i \quad (3.2)$$

and the relative standard error, in per mil, across all scans:

$$\sigma_{AE}^i = \frac{STDEV(R_j)}{\sqrt{N}} * \frac{1}{R_i} * 1000. \quad (3.3)$$

We refer to this error as ‘acquisition error,’ i.e., the error on the observed isotope ratio in a single acquisition.

### 3.2.2.3. Shot Noise Limit

We also calculate the ‘shot noise limit’ for each reported isotope ratio  $i$ , the theoretical limit for how well that ratio could be constrained based on the number of counts observed of each ion beam used to compute that ratio. This was calculated as:

$$\sigma_{SN}^i = \sqrt{\frac{1}{\sum N_{IO,Beam\ 1}} + \frac{1}{\sum N_{IO,Beam\ 2}}} \quad (3.4)$$

where  $\sum N_{IO,Beam\ 1}$  gives the sum of the observed counts of ion beam 1 across all scans of the acquisition. As the number of counts per scan is approximate and based on empirically determined constant ( $C_N$ ) that may not be identical in all scenarios,  $\sigma_{SN}^i$  should be treated as a useful estimate rather than a precise statement of the theoretical limit.

### 3.2.2.4 Standardization

We calculate and report standardized values for isotope ratios of both perchlorate and methionine as delta values, in the following way. Each acquisition sequence consisted of the following measurements:

Standard/Sample/Standard/Sample/Standard/Sample/Standard. We found that variations in the recovered isotope ratios for each standard acquisition varied systematically with acquisition number (equivalent to time, as each acquisition was the same duration). Therefore, for each isotope ratio  $i$ , we performed a linear regression across all four standards and calculated both a predicted standard value  $R_{STD,pred}^i$  and associated confidence interval  $\sigma_{STD,CI}^i$  at the acquisition number of each sample. We report standardized values for the observation of isotope ratio  $i$  as delta values, e.g.,  $\delta^{13}C_{STD} = 1000 \left( \frac{R_{SMP}^i}{R_{STD,pred}^i} - 1 \right)$ . We calculated error bars for each standardized sample acquisition (propagated acquisition error,  $\sigma_{PAE}$ ) by adding  $\sigma_{AE}^i$  for the sample to  $\sigma_{STD,CI}^i$  for the predicted standard in quadrature:

$$\sigma_{PAE}^i = \sqrt{(\sigma_{AE})^2 + (\sigma_{STD,CI}^i)^2}. \quad (3.5)$$

Additionally, across all standardized measurements, we report ‘experimental reproducibility,’ or the mean and standard deviation ( $\sigma_{ER}^i$ ) of  $\delta_{STD}^i$  across all sample observations ( $n=3$ ). We discuss standardization in more detail in the supplement. A summary of our error measures may be found in Table 3.1.

### 3.2.2.5 Data Quality Tests

For all measurements, we perform automated data quality tests to check for and reject anomalous data. Our tests are as follows.

#### 3.2.2.5.1 Acquisition Error to Shot Noise Ratio

Ratios of  $\frac{\sigma_{AE}}{\sigma_{SN}}$  with values  $>2$  have been associated with poor quality data in previous experiments (Eiler et al., 2017); we compute this ratio and reject measurements above the threshold.

### 3.2.2.5.2 Zero Scans

For each observed isotope, we screen for zero scans, where a zero scan returns a value of  $N_{IO} = 0$  for that ion beam. All of our deuterium measurements for both acetone and methionine, as well as observations of  $^{37}\text{Cl}^{17}\text{O}$  in perchlorate, include at least some zero scans. The acetone  $^2\text{H}$  data are complex due to the presence of a nearly isobaric contaminant; we discuss these in detail in the appendix, A.5. For methionine and perchlorate, we attribute the zero counts to the low number of counts ( $\approx 20$ ) of the relevant isotope ( $^2\text{H}$  and  $^{37}\text{Cl}^{17}\text{O}$ ) in each scan. Prior work on previous Orbitrap models has indicated that approximately 30 ions of the same species are required for detection; in our case (and following eq (1)) sensitivity is better, but we are still near the limits of detection and so often fail to detect any ions (Makarov et al., 2005; Olsen et al., 2005).

For  $^2\text{H}$  in the methionine measurements, we report 1.5 – 3.0 % of all scans as zero scans (varying across different observations); the corresponding  $\frac{\sigma_{AE}}{\sigma_{SN}}$  ratios are in the range of 1.15-1.3. We have three options for dealing with these data: first, we may use  $N_{IO} = 0$  for each zero scan and calculate the isotope ratio and error normally; second we may cull these scans and calculate using only nonzero scans; and third, we may reject any dataset including zero scans. The first option will understate the true ratio (as there were likely some small nonzero number of deuterated ions present for that scan) while the second will overstate it (as the culled scans are likely to have contained less than the average number of deuterated ions); the third is most conservative but may cause us to reject usable data. For the  $^2\text{H}$  data, we find that culling zero scans (option 2) results in less replicable sample/standard comparisons, possibly due to differences in the number of zero scans between different observations. We therefore include the zero scans and calculate isotope ratios normally (option 1), noting that these results should be treated with increasing caution as the proportion of zero scans increases. A detailed discussion is available in the supplement, S3.6.

For  $^{37}\text{Cl}^{17}\text{O}$  in the perchlorate measurements, we report  $\approx 0.3\%$  zero scans and  $\frac{\sigma_{AE}}{\sigma_{SN}}$  ratios of 1.15 at an AGC of  $5e5$  and  $\approx 20\%$  zero scans and  $\frac{\sigma_{AE}}{\sigma_{SN}}$  ratios of 2.1 at an AGC of  $2e5$ . Based on  $\frac{\sigma_{AE}}{\sigma_{SN}}$  ratios, we consider the  $5e5$  but not the  $2e5$  data sufficient for measurement. In all cases, results were calculated including the zero scans and calculating isotope ratios normally (option 1, above).

### 3.2.2.5.3 Internal Variability

Datasets with low  $\frac{\sigma_{AE}}{\sigma_{SN}}$  ratios and few to no zero scans may still be compromised due to anomalous changes in the value of an isotope ratio across the measurement. An example of this is shown in Figure 3.2, which depicts two measurements of  $^{15}\text{N}/\text{Unsub}$  in methionine: on the left we show an observation with no obvious evidence of time-dependent variations in the measured ratio, beyond random scan to scan differences; and on the right we present the results of a similar measurement that exhibited two periods of time (centered around  $\sim 4000$  and  $\sim 10000$  scans) when the measured ratio departed significantly from the long-term average, by amounts exceeding random scan-to-scan variations. We note that this second, aberrant measurement was to our knowledge typical in all other respects and did not demonstrate such behavior for any other isotope ratios observed ( $^{33}\text{S}/^{32}\text{S}$ ,  $^{34}\text{S}/^{32}\text{S}$ ,  $^2\text{H}/^1\text{H}$ ,  $^{13}\text{C}/^{12}\text{C}$ ,  $^{18}\text{O}/^{16}\text{O}$ , &  $^{13}\text{C}^{13}\text{C}/^{12}\text{C}$ ). Moreover, other data quality statistics for the two measurements are similar; for the typical measurement,  $\frac{\sigma_{AE}}{\sigma_{SN}} = 1.08$ , while for the failed measurement  $\frac{\sigma_{AE}}{\sigma_{SN}} = 1.1$ ; the aberrant measurement has a small number of 0 scans (8 out of 13,300) and it is not obvious it should be rejected on those grounds alone.

There are a diversity of methods for screening anomalies in univariate time-series data (Braei and Wagner, 2020; Blázquez-García et al., 2021); here we adopt a z score based model, as follows (Figure 3.2). We attempt to find subsequence outliers, i.e., subsequences of scans which differ from the surrounding scans, by defining sliding windows of length  $N = 1000$ , i.e.,  $S_i = S_{j=i}, S_{j+1}, \dots, S_{j+N}$  where  $s_j$  gives the observation of the isotope ratio of interest

in scan  $j$  and  $S_i$  is the sliding window beginning at scan  $i$ . For this window, we define an expected mean  $\mu_{i,predict}$  and standard deviation  $\sigma_{i,predict}$  as the mean and standard deviation of the previous  $N$  scans. We then calculate the average z score across each scan in  $S_i$  using these predicted values and report the absolute value of this as our anomaly score,  $a_i$ . That is:

$$a_i = \left| \frac{1}{N} \sum_{j=i}^{j+i+N} \frac{S_j - \mu_{i,predict}}{\sigma_{i,predict}} \right|.$$

We choose an anomaly score of  $>0.2$  ( $>3$  standard deviations above the expected anomaly score for normally distributed data) as the threshold for identifying anomalous data. Our anomaly score for the typical and aberrant  $^{15}\text{N}$ /Unsub observations in methionine are plotted in Figure 3.2A; both periods of drift are identified using our anomaly score. Note that our anomaly score goes to 0 around the center of each anomalous period; this is due to a sign change in the z score associated with a change in the drift direction; our anomaly score best captures drift towards a new mean. Across all data presented in this chapter, only the methionine nitrogen measurement shown is rejected in this manner.

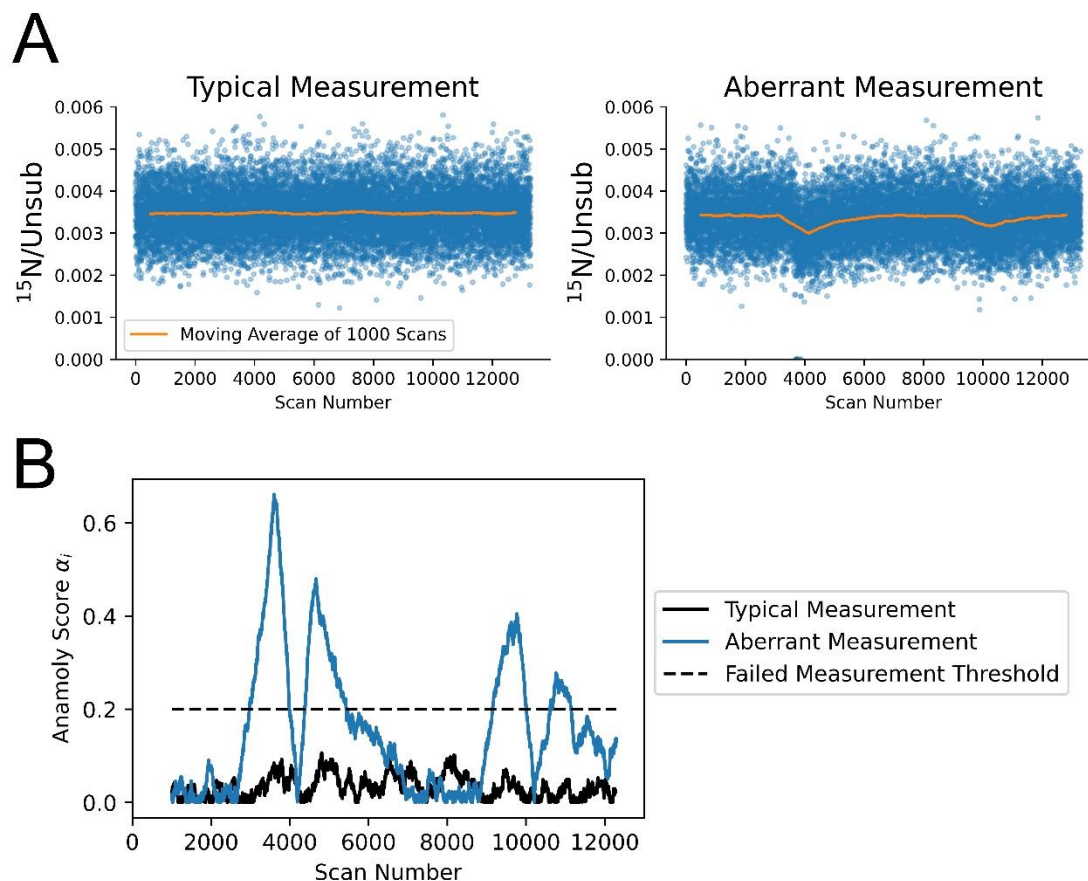


**Figure 3.2:** A subsequence anomaly detection method to screen aberrant measurements. A, left: The recorded ratio for each scan of a typical observation; the moving average is near constant. A, right: The recorded ratio for each scan of an observation with substantial drift during the measurement. B: The calculated anomaly score  $\alpha_i$  for each scan of these measurements together with the threshold of 0.2 for rejected measurement. The aberrant methionine measurement crosses the threshold for both anomalous periods. Note that our anomaly score has a value of 0 where the drift in ratio changes direction, associated with a sign change in the anomaly score. The highest values of anomaly score are associated with the most extreme periods of drift.

### 3.2.2.6 Data and Figure Availability

Data, including .RAW files generated by the instrument and .txt or .isox files generated by either FTStatistic or IsoX, is available on the Caltech data repository (T. Csernica, 2023b). Code for our data processing and for the generation of all figures except Figure 3.1 is available on the open Zenodo repository (Csernica, 2023b). In some cases, multiple plots were generated separately and joined using Microsoft Powerpoint or Affinity Designer. Figure 3.1 was generated using Affinity Designer.



### 3.3. Results & Discussion

#### 3.3.1 Intra-Measurement Stability for Measurements of Arbitrary Duration

To evaluate the stability of reservoir injection methods for measurements of long duration, we analyzed a 24-hour observation of acetone, hoping to observe whether  $\sigma_{AE}$  tracked the shot noise limit throughout. To our knowledge, the only similar long-duration experiment on an Orbitrap™ was a 24-hour measurement of  $^{13}\text{C}$  in reference gas PFTBA by Eiler et al. on a Q-Exactive GC™ instrument (Eiler et al., 2017). This previous experiment found the acquisition error  $\sigma_{AE}$  of the observed ratio tracked shot noise throughout, reaching a value of 0.015 ‰ after 24 hours. In our measurement of acetone, we report the ratios of isotopologues with one of five different isotopic substitutions— $^{13}\text{C}$ ,  $^{17}\text{O}$ ,  $^{18}\text{O}$ ,  $^2\text{H}$  or  $^{13}\text{C}^{13}\text{C}$ —relative to the unsubstituted isotopologue. In Figure 3.3, we show  $\sigma_{AE}$  and the ratio of acquisition error to shot noise,  $\frac{\sigma_{AE}}{\sigma_{SN}}$ , vs time for each isotope ratio. The  $\frac{\sigma_{AE}}{\sigma_{SN}}$  ratio has been suggested as a criterion for data quality, with ratios of  $>2$  indicating systematic problems with the observations (although this threshold is somewhat arbitrary). We interpret increases in  $\sigma_{AE}$  or  $\frac{\sigma_{AE}}{\sigma_{SN}}$  as losses of internal stability. The  $^{13}\text{C}$ ,  $^{18}\text{O}$ , and  $^{13}\text{C}^{13}\text{C}$  data track shot noise throughout, with  $\frac{\sigma_{AE}}{\sigma_{SN}}$  ratios stabilizing around 1.2; we consider these to be representative of ideal measurement. The  $^{17}\text{O}$  also tracks shot noise throughout, stabilizing around a value of 1.6; we attribute the higher value for  $^{17}\text{O}$  to the presence of zero scans and artifacts associated with the close-lying  $^{13}\text{C}$  peak. We consider this sufficient for measurement; the use of additional microscans, which increase signal to noise ratio (we used 10 microscans, the limit for pre-installed software) may offer further improvement (Bills et al., 2021). In contrast, the  $^2\text{H}$  data do not track shot noise, with noticeable increases in the  $\sigma_{AE}$  and  $\frac{\sigma_{AE}}{\sigma_{SN}}$  values around  $\approx 200$  minutes. We attribute this failure to the presence of a contaminant nearly isobaric with the deuterium peak, preventing the recovery of accurate data. Both  $^{17}\text{O}$  and  $^2\text{H}$  data are discussed in more detail in the appendix (A.3, A.5). We report final  $\sigma_{AE}$  of 0.07 ‰, 1.1 ‰, 0.3 ‰, and 0.65 ‰ for  $^{13}\text{C}$ ,  $^{17}\text{O}$ ,  $^{18}\text{O}$ , and  $^{13}\text{C}^{13}\text{C}$ , respectively. Note these limits reflect the long-term system stability of the reservoir method for Orbitrap

IRMS, but that sample/standard comparisons might improve upon them if it is capable of compensating for slow, subtle drift in instrumental fractionations. Our best reported  $\sigma_{AE}$  is worse than the best observed previously (0.015 ‰), likely due to differences in scan settings required to resolve the  $^{17}\text{O}$  peak of acetone. In particular, a high mass resolution is required here to resolve  $^{13}\text{C}$  from  $^{17}\text{O}$  while a lower number of ions per scan (set by the AGC target) is necessary to avoid undesirable space-charge effects; both factors slow the rate at which we can count ions. The behavior of precision with respect to time is identical. Our results demonstrate that, when the observed peaks are clear of contaminants, reservoir injection measurements are stable over periods of  $\geq 24$  hours and precisions of  $< 0.1$  ‰.

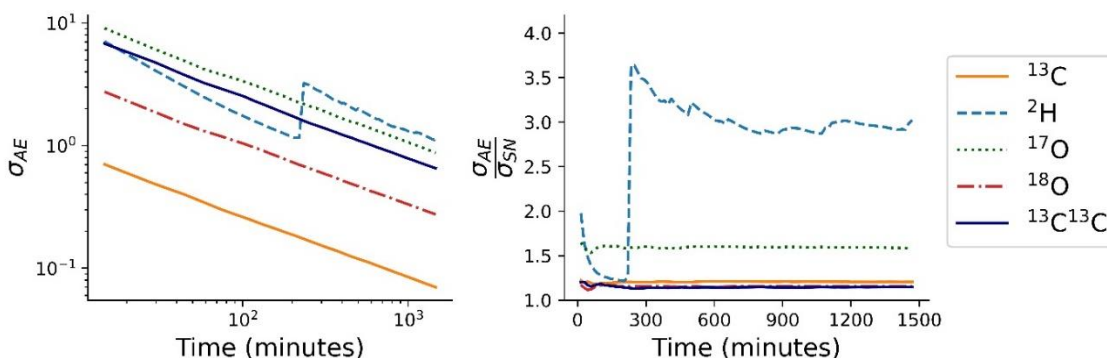


**Figure 3.3:** Long term stability and precision of acetone observed by reservoir injection. Isotopologues with five different isotopic substitutions were observed relative to the unsubstituted isotopologue and the precision of the observed ratios plotted. All ratios except  $^2\text{H}$  decrease continually with time, yielding a ratio  $\frac{\sigma_{AE}}{\sigma_{SN}}$  of 1.2 ( $^{13}\text{C}$ ,  $^{18}\text{O}$ ,  $^{13}\text{C}^{13}\text{C}$ ) or 1.6 ( $^{17}\text{O}$ ). We attribute the higher  $\frac{\sigma_{AE}}{\sigma_{SN}}$  ratio for  $^{17}\text{O}$  to the presence of zero scans in the  $^{17}\text{O}$  measurement ( $\approx 0.2\%$  of all scans) and artifacts associated with the closely adjacent  $^{13}\text{C}$  peak. The  $^2\text{H}$  data are compromised by the presence of a close-lying contaminant. We discuss  $^{17}\text{O}$  and  $^2\text{H}$  data in more detail in the supplement (S3.3, S3.5).

### 3.3.2. Limits of Inter-Measurement Stability Examined Via Perchlorate

After investigating the intra-measurement stability, we evaluated the inter-measurement stability in perchlorate to determine the limits of accuracy and precision for sample/standard comparisons (Figure 3.4). Our main question here is: if we have a low acquisition error for a given measurement, will our precision for reported  $\delta$  values be similarly low, or are there issues associated with standardizing multiple measurements which prevent this? We chose perchlorate due to the abundant  $^{37}\text{Cl}$  substitution, which

allowed us to rapidly reach high precision ( $\sigma_{AE} \approx 0.1 \text{ ‰}$  in 75 minutes) and evaluate the effects of inter-measurement changes. Perchlorate observations consisted of triplicate sample standard comparisons in the order Standard/Sample/Standard/Sample/Standard/Sample/Standard, a total of 7 measurements. Each measurement had a 15 minute ‘priming’ period followed by 75 minutes of measurement and 20 minutes of purging, for a total of 110 minutes (Table 3.1). The entire sequence took  $\approx 13$  hours, was automated, and required no user input for the duration. We present three sequences of this type; all were zero enrichment measurements, i.e., the same perchlorate was used for sample and standard. One was performed at AGC 5e5, while two were performed at AGC 2e5. All drew sample from the same reservoir; the 5e5 and one 2e5 measurement (‘2e5 S’, or same) also used the same tubing for both standard and sample, while the other 2e5 measurement (‘2e5 D’, or ‘different’) used different tubing for standard and sample.

We first examine the  $^{37}\text{Cl}/\text{Unsub}$  data, as this is the highest precision isotope ratio we recover and best able to reveal issues with inter-measurement replicability (Figure 3.4A). Acquisition errors ( $\sigma_{AE}$ ) in individual measurements for  $^{37}\text{Cl}/\text{Unsub}$  were  $\approx 0.09 \text{ ‰}$  (5e5) and  $0.13 \text{ ‰}$  (2e5). As with previous IRMS measurements made using an Orbitrap, we observe significant inter-measurement drift in raw measured isotope ratios, on the order of  $1 \text{ ‰}$  (the average difference between two consecutive observations of  $^{37}\text{Cl}/\text{Unsub}$  is  $0.8 \text{ ‰}$ ) (Figure 3.4A, left) (Chimiak et al., 2021; Hilkert et al., 2021; Mueller et al., 2022a). Our standardization strategy attempts to correct for this inter-measurement drift by performing a linear fit to the standard values and comparing the sample values to this line; results of these comparisons are given in per mil as  $\delta^{37}\text{Cl}_{STD}$ , with the average of the associated  $\sigma_{PAE}$  values given above each plot (Figure 3.4A, center). We also give the experimental reproducibility, or the mean of these three  $\delta^{37}\text{Cl}_{STD}$  values and their standard deviation ( $\sigma_{ER}$ ) (defined in 3.2.2.4) (Figure 3.4A, right). We find our correction scheme does not adequately account for inter-measurement drift; recovered values for  $\delta^{37}\text{Cl}_{STD}$  drift relative to each other and relative to the correct value on the order of  $1 \text{ ‰}$ , substantially

greater than our  $\sigma_{AE}$  values. The effects of this drift are captured both in the  $\sigma_{PAE}$  values (where drift causes broader confidence intervals,  $\sigma_{STD,CI}$  for the standard values used to calculate  $\delta^{37}Cl_{STD}$ ) and the  $\sigma_{ER}$  values (reflecting different values of  $\delta^{37}Cl_{STD}$  for different sample acquisitions, reaching 0.82 ‰ for the 5e5 case). We conclude that drift associated with the changing of samples (i.e., the ‘purge’ and ‘prime’ steps and the introduction of a new sample) leads to variations in standardized ratios on the order of 1 ‰. Therefore, the benefits of  $\sigma_{AE}$  values much lower than 1‰ may not be realized. Future work may examine the causes of this instrument drift to obtain a more accurate measurement.

We close this section by examining the remaining, lower precision perchlorate data, for  $^{17}O/Unsub$ ,  $^{18}O/Unsub$ ,  $^{37}Cl^{18}O/Unsub$ , and  $^{37}Cl^{17}O/Unsub$ . Note that perchlorate  $^{17}O$  is an easier target than acetone  $^{17}O$ , as there is no  $^{13}C$  peak in perchlorate. These data are shown in Figure 3.4B (we omit 2e5\_S, as it is similar to the other datasets; all data are available in the appendix (A.7)). The sizes of  $\sigma_{AE}$  and  $\sigma_{PAE}$  error bars on individual samples are given in the title of each plot. Note that the low abundance of  $^{37}Cl^{17}O$  means that the 2e5 dataset has a substantial number ( $\approx 20\%$ ) of zero scans and a  $\frac{\sigma_{AE}}{\sigma_{SN}}$  ratio  $>2$ , and so we reject this data (in the 5e5 dataset,  $^{37}Cl^{17}O$  has  $\approx 0.3\%$  zero scans and  $\frac{\sigma_{AE}}{\sigma_{SN}} < 2$ , which we consider sufficient for measurement). In all cases, the drift between acquisitions and their divergence from accurate values is within  $2\sigma$  of the  $\sigma_{PAE}$  values. Additionally, the  $\sigma_{PAE}$  values are closer to the observed  $\sigma_{AE}$  values (all within a factor of 2), suggesting that lowering  $\sigma_{AE}$  will result in a more precise error bar for the final reported  $\delta$  value for these precisions. We make one additional comment about  $^{17}O$ : in some mass spectrometric measurements of oxygen isotopes, errors in  $\delta^{17}O$  and  $\delta^{18}O$  arise from mass dependent effects, allowing  $^{17}O$ -excess (or  $\Delta^{17}O = \ln(\delta^{17}O+1) - 0.528\ln(\delta^{18}O+1)$ ) to be constrained more precisely than  $\delta^{17}O$  or  $\delta^{18}O$  individually (Landais et al., 2006; Luz and Barkan, 2010). Our experiment suggests that the error bars for these quantities is following shot noise error, rather than a mass-dependent process; in this case, such a beneficial cancellation of errors will not occur. We conclude that inter-measurement drift is sufficiently small to permit observations with precisions on the order of 1 ‰, including for rare or multiply-substituted species.

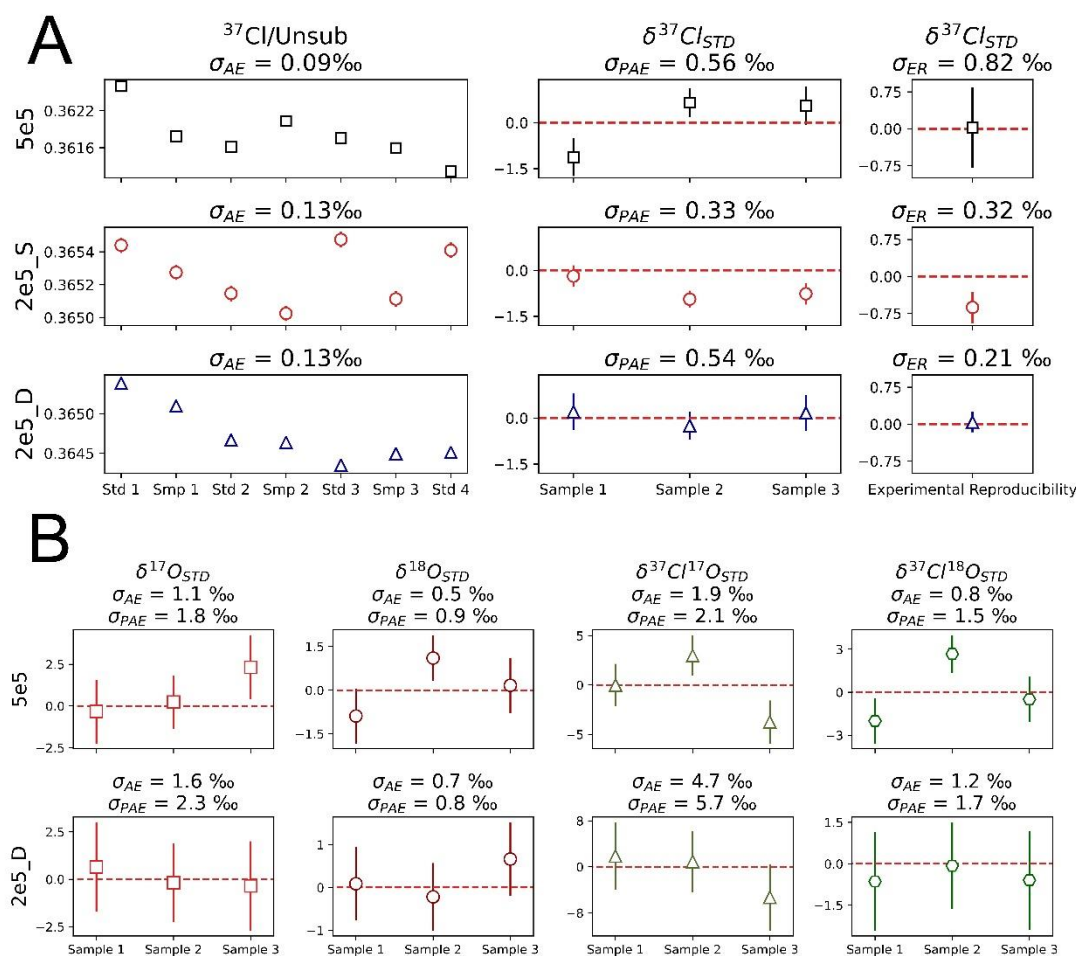


**Figure 3.4:** Inter-measurement variability perchlorate. When error bars are not shown, they are smaller than the size of the points. A: The  $^{37}\text{Cl}$  substitution of perchlorate. A, Left: The raw ratio  $^{37}\text{Cl}/\text{Unsub}$  recovered from each observations. A, Right: The standardized ratios reported as delta values. The red line at 0 per mil indicates the accurate value for this zero-enrichment measurement. We observe drift between sample replicates on the order of 1‰, exceeding the  $\sigma_{AE}$  of  $\approx 0.1\text{‰}$ . This inter-measurement drift prevents the application of reservoir injection methods to such high precisions. B: Remaining data for four other substitutions in perchlorate; these are observed simultaneously with  $^{37}\text{Cl}$ . Only the standardized data are shown, and we omit the  $2e5\_S$  dataset, which is qualitatively similar to the  $2e5\_D$  (remaining data are available in the appendix (A.7)). For substitutions with  $\sigma_{AE}$  on the order of 1‰, inter-measurement drift is sufficiently small to permit accurate and replicable measurements. The red lines indicate the accurate value of 0‰ for a zero-enrichment measurement.

### 3.3.3 Inter-Measurement Accuracy Tests on Methionine

We next perform an accuracy test using standardization via an analysis of a methionine sample spiked to have an enrichment of 19.6‰ in molecular average  $^{13}\text{C}/^{12}\text{C}$  ratio, relative to the standard. This experiment allows us to evaluate whether we return accurate  $\delta$  values for all substitutions, including those with enrichments where scale

nonlinearities may be an issue. We made triplicate standardized measurements, each consisting of a 1-hour integration and each bracketed by measurements of a methionine standard; as in the case of perchlorate, these occurred in the order: Standard/Sample/Standard/Sample/Standard/Sample/Standard. Including the triplicate measurements and purging steps between each analysis, the total measurement sequence took 10.5 hours, was automated, and required no user monitoring or input. For each measurement we simultaneously observed the ratios of isotopologues with one of seven ( $^{33}\text{S}$ ,  $^{34}\text{S}$ ,  $^{15}\text{N}$ ,  $^2\text{H}$ ,  $^{13}\text{C}$ ,  $^{18}\text{O}$ , &  $^{13}\text{C}^{13}\text{C}$ ) substitutions relative to the unsubstituted isotopologue; we plot representative results from  $^{13}\text{C}$ ,  $^{33}\text{S}$ , and  $^2\text{H}$  in Figure 3.5 and give the remainder in Table 3.4. After standardizing, we find that all experimental replicates lie within  $2\sigma$  of each other and our  $\sigma_{\text{PAE}}$  values are within a factor of 2 of the  $\sigma_{\text{AE}}$  values (Table 3.4), suggesting this method of standardization corrects for inter-measurement drift to within the level of precision of our measurements.

Next, we address the relative accuracy and precision of the sample standard comparisons made in this experiment. We report both  $\sigma_{\text{PAE}}$  error bars on individual standardized measurements and  $\sigma_{\text{ER}}$  values representing variation across multiple standardized measurements (see section 2.2.4) (Figure 3.5, Table 3.4). Our results for individual acquisitions and  $\sigma_{\text{PAE}}$  values are successful in that most reported values and errors fall within  $2\sigma$  of our computed enrichments (exceptions: 2<sup>nd</sup> sample:  $^{13}\text{C}$ ,  $^{18}\text{O}$ ,  $^{34}\text{S}$ ; 3<sup>rd</sup> sample,  $^{33}\text{S}$ ). Our experimental reproducibilities and  $\sigma_{\text{ER}}$  values miss the target in more cases ( $^{13}\text{C}$ ,  $^{18}\text{O}$ ,  $^{34}\text{S}$ ,  $^2\text{H}$ , and  $^{13}\text{C}^{13}\text{C}$ ). In some cases ( $^{13}\text{C}$ ,  $^{18}\text{O}$ ,  $^{34}\text{S}$ ), the calculated values are just beyond  $2\sigma$  error bars (0.1 ‰ for all;  $^{13}\text{C}$  hits the target if results are presented to two decimal places). For the others ( $^2\text{H}$  and  $^{13}\text{C}^{13}\text{C}$ ), we attribute this to  $\sigma_{\text{ER}}$  understating our actual error due to the small number of replicates ( $n=3$ ). For example,  $^{13}\text{C}^{13}\text{C}$ , if we compute the shot noise limit using all ions across all acquisitions, we obtain an error bar of  $\approx 2.0$  ‰; hence the reported  $\sigma_{\text{ER}}$  of 0.3 ‰ for this measurement is implausibly low. With the caveat that  $\sigma_{\text{ER}}$  may understate our actual error, we find  $\sigma_{\text{ER}}$  a useful one-number summary for a series of measurements. In all cases, we regard our  $\sigma_{\text{PAE}}$  values as reasonable bounds on

the accuracy and precision of our method. In sum, we find reservoir injection methods can measure many isotope ratios at high precision (on the order of  $\sim 1$  ‰ for  $\sigma_{PAE}$  and  $\sigma_{ER}$ ) for long durations and in an automated fashion.

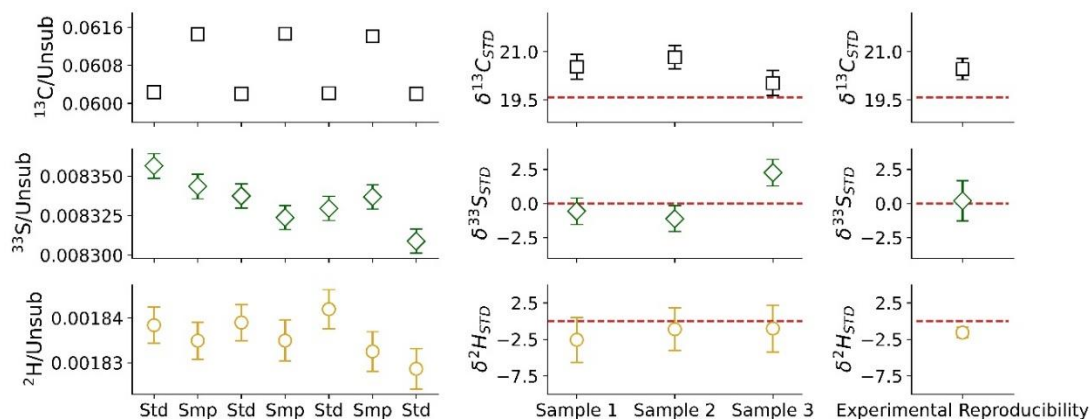


**Figure 3.5:** Inter-measurement drift with  $\sigma_{AE}$  (left), sample standard comparisons with  $\sigma_{PAE}$  (center), and experimental reproducibility with  $\sigma_{ER}$  (right) for several replicate methionine measurements. Inter-measurement drift shows single acquisitions of either sample or standard and the raw reported ratios and errors. Sample standard comparisons show the resulting delta values after taking the average of the ratios of the sample and the predicted standard value at that timepoint. Experimental reproducibility shows the average and standard deviation of the  $n=3$  samples. Red lines show the predicted values for  $\delta^{13}C_{STD}$  (19.6 ‰) and other isotope ratios (0 ‰, as these are zero-enrichment).

**Table 3.4: Results from Methionine Replicates<sup>a</sup>**

	<b>Observed or Approximate Value</b>	<i>Average <math>\sigma_{AE}</math></i>	<i>Sample 1 and <math>\sigma_{PAE}</math></i>	<i>Sample 2 and <math>\sigma_{PAE}</math></i>	<i>Sample 3 and <math>\sigma_{PAE}</math></i>	<i>Average and <math>\sigma_{ER}</math></i>
$\delta^{13}C_{STD}$	<b>19.6 ± 0.1</b>	0.3	20.5 ± 0.4	20.8 ± 0.4	20.0 ± 0.4	20.5 ± 0.3
$\delta^{15}N_{STD}$ <sup>b</sup>	<b>0</b>	1.5	-0.1 ± 2.1	-2.2 ± 2.1	-1.2 ± 3.1	-1.1 ± 0.8
$\delta^{18}O_{STD}$	<b>0</b>	1.3	-1.5 ± 1.6	-4.2 ± 1.5	-1.8 ± 1.6	-2.5 ± 1.2
$\delta^{33}S_{STD}$	<b>0</b>	0.9	-0.6 ± 1.0	-1.1 ± 0.9	2.3 ± 1.0	0.2 ± 1.5
$\delta^{34}S_{STD}$	<b>0</b>	0.4	-0.4 ± 0.7	-1.3 ± 0.6	-1.0 ± 0.7	-0.9 ± 0.4
$\delta^2H_{STD}$	<b>0</b>	2.3	-2.6 ± 3.1	-1.1 ± 2.9	-1.0 ± 3.2	-1.6 ± 0.7
$\delta^{13}C^{13}C_{STD}$	<b>39.2 ± 1</b>	2.5	35.4 ± 2.8	35.1 ± 2.7	35.8 ± 2.8	35.4 ± 0.3

a: All entries in per mil (‰)

b: The final standard was omitted, hence greater error on sample 3

### 3.3.4 Sample Consumption

At present, the biggest limitation on reservoir injection methods is the large sample consumption relative to other Orbitrap-IRMS methods. Reservoir injection uses similar

analyte concentrations (1-500  $\mu\text{M}$ ) to other methods but much faster flow rates (100  $\mu\text{L}/\text{minute}$  vs 3-20  $\mu\text{L}/\text{minute}$ ), and hence consumes more sample per unit time; additionally, a priming step is required prior to each measurement, consuming  $\approx 2$  mL more of sample solution. Final sample requirements were 72  $\mu\text{mol}$  (4.2 mg) for 24 hours of acetone observation; 27 nmol (3.8  $\mu\text{g}$ ) per 75-minute perchlorate observation; and 26 nmol (3.8  $\mu\text{g}$ ) per 60-minute methionine observation. Due to the inherent sensitivity of Orbitrap IRMS, even these relatively high values compare favorably to some alternative technologies. For example, observation of the average  $^{13}\text{C}/^{12}\text{C}$  ratio of methionine via EA-IRMS required 50  $\mu\text{g}$  per replicate, an order of magnitude more than the Orbitrap measurement. In our case, the flow rate limitation was imposed by the HPLC used; we imagine that similar experiments using nano-HPLC systems could reduce sample requirements. We also re-emphasize that the reservoir injection method is designed for the purpose of measuring rare and hard-to resolve isotopic substitutions, such as  $^{17}\text{O}$ -bearing isotopologues of organic molecules, that have never been analyzed directly at useful precision ( $\sim 1$  ‰) by alternative methods.

### 3.4 Conclusion

The results presented here demonstrates that, with our reservoir injection system, Orbitrap-IRMS can observe many isotope ratios simultaneously, at high precisions, and for long durations, across a variety of target compounds. Our results from acetone demonstrate the long-term stability of the system, which does not deviate noticeably from shot noise limits across a 24-hour measurement. Meanwhile our perchlorate results demonstrate that current accuracy limits for  $\delta$  values across standardized replicates are on the order of 1 ‰, despite lower  $\sigma_{\text{AE}}$  values ( $\approx 0.1$  ‰), due to inter-measurement drift. Finally, our methionine observations confirm that automated, accurate, and reproducible measurements of isotopic differences may be made across many isotopes of interest. In their current form, reservoir injection methods are best suited to rare isotopologues or to those with demanding mass-resolution and AGC requirements, such as  $^{17}\text{O}$  in organics or



clumped isotopes, and therefore require observations on the order of hours to tens of hours. Future investigations should evaluate the capability of other sample introduction methods for long duration Orbitrap-IRMS measurements. Additionally, they should improve on the sample requirements and determine and correct for the causes of inter-measurement drift in order to fully take advantage of the reservoir injection platform.

### **Acknowledgements**

We thank Nivedita Thiagarajan for collaborating on the development of long duration measurements, and we thank Gabriella Weiss, Elliott Mueller, and Nivedita Thiagarajan for their comments and discussion on the experiments presented in this manuscript. We also thank Alex Sessions and Fenfang Wu for the assistance with the EA-IRMS measurements. Additionally, we thank Max Lloyd, Guannan Dong, Peter Martin, and Sarah Zeichner for their contributions to the data processing scripts used in this article. Finally, we thank two anonymous reviewers for their helpful comments on this manuscript.

### **Funding**

This work was supported by the Simons Foundation, Award Number 626103 and DOE-BES funding to JME.

## SUPPLEMENTARY MATERIAL FOR CHAPTER 3

**S3.1 Ammonium Hydroxide Additive for Perchlorate**

We found that adding ammonium hydroxide improved the ionization stability of perchlorate. To do so, we injected perchlorate solutions using a syringe pump (Fusion 101, Chemyx Inc.) at a flow rate of 10  $\mu\text{L}/\text{minute}$ . All mass spectrometric conditions were as shown in Table 3.3 except: Sheath gas: 5 Aux gas: 0, AGC target =  $1\text{e}6$ . Perchlorate solutions were all at 2  $\mu\text{M}$  in methanol, and had either 1) 0%, 0.1%, or 0.2% ammonium hydroxide. For 5-minute observations, we found the following tic means, standard deviations, and relative standard deviations:

**0% Ammonium hydroxide:**  $4.0\text{e}7 \pm 1.9\text{e}7$  (RSD of 47%)

**0.1% Ammonium hydroxide:**  $5.4\text{e}7 \pm 2.9\text{e}6$  (RSD of 5.3 %)

**0.2% Ammonium hydroxide:**  $4.5\text{e}7 \pm 2.8\text{e}6$  (RSD of 6.2%)

The resulting tic curves are plotted in Figure S3.1, below. While we did not retest each condition for the reservoir injection methods, the RSD values for those experiments, all of which used 0.1% ammonium hydroxide, were of a similar magnitude (between 3.4% and 7.0%).

In the syringe pump experiments, we observe an increase in the height of a contaminant peak at 101.059 (tentatively assigned as  $\text{C}_5\text{H}_9\text{O}_2^-$ ) with more ammonium hydroxide ( $\sim 2\%$  the height of the unsubstituted perchlorate peak at 0% ammonium hydroxide;  $\sim 10\%$  with 0.1% ammonium hydroxide;  $\sim 20\%$  with 0.2% ammonium hydroxide). However, we did not observe the same contaminant using the reservoir injection methods.

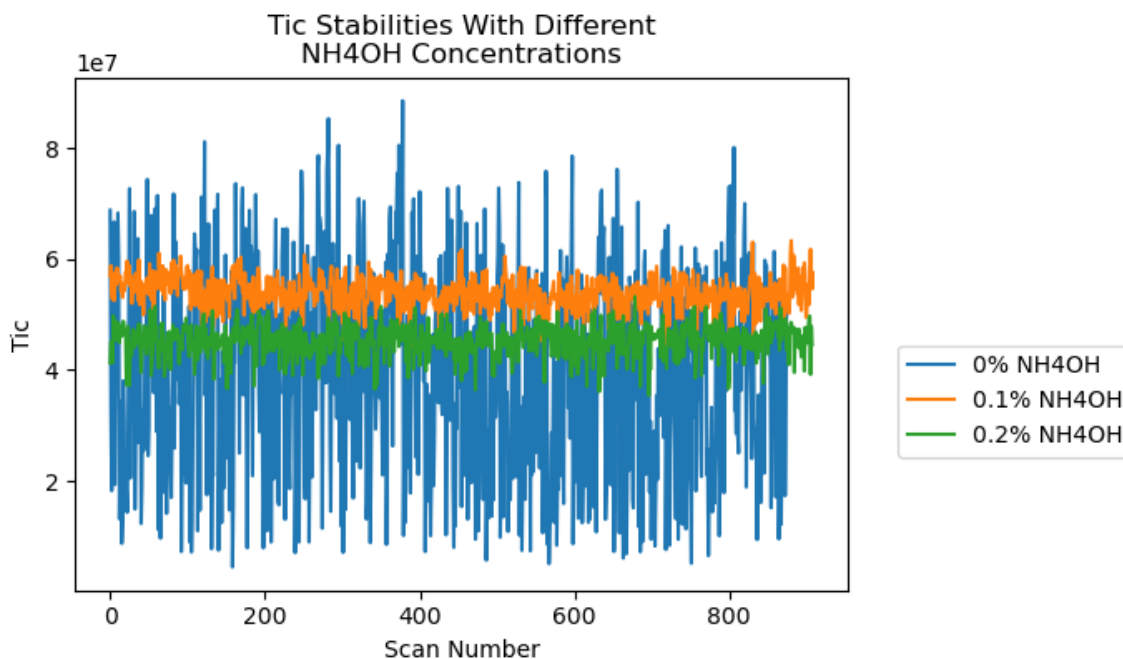


**Figure S3.1:** The tic stability for perchlorate observations using different amounts of  $\text{NH}_4\text{OH}$ . Each observation includes 5 minutes of data.

### S3.2 Methionine Mixing

To confirm that our assumed sample standard comparisons for each isotope of methionine were accurate, we explicitly calculated the concentrations of all isotopologues of methionine for the  $^{13}\text{C}$ -methyl labelled methionine and methionine standard, mixed these on an isotopologue-by-isotopologue basis for the methionine sample, and compared results for the sample and standard, using a range of plausible methionine compositions. This exercise allows us to determine whether unknown variations in the content of either methionine would result in idiosyncratic differences. For example, if the labelled methionine had a high  $^{15}\text{N}$  content, or if its  $^{13}\text{C}$  carboxyl site were substantially enriched, our sample standard comparisons may have differed from our assumptions.

As input for this calculation, we needed an estimate of the site-specific content of each atom in each methionine. For Met-A, the explicitly measured constraints are: -53.9 ‰ (methyl  $^{13}\text{C}$ ), -23.7 ‰ (gamma  $^{13}\text{C}$ ), -24.0 ‰ (average composition of alpha & beta  $^{13}\text{C}$ ), -24.3 ‰ (carboxyl  $^{13}\text{C}$ ), all vs VPDB, and 4.3 (‰  $^{34}\text{S}$ ) vs CDT (Neubauer et al 2018). We have no

independent constraints on the N, H or O isotope composition of Met-A methionine, and so assume compositions of 0 ‰ vs VSMOW (for  $^2\text{H}$ ,  $^{17}\text{O}$  and  $^{18}\text{O}$ ) or AIR (for  $^{15}\text{N}$ ) and set  $^{33}\text{S}$  and  $^{36}\text{S}$  via mass scaling and assuming conventional mass laws for sulfur isotope variations. These assumptions do not cause significant errors in the expected differences between Met-A and our sample for isotopic properties studied in this text. For the  $^{13}\text{C}$ -methyl labelled methionine, we specified a composition of 99%  $^{13}\text{C}$  at the methyl site. For other positions, to test the variability caused by unknown deviations in the labelled methionine's isotopic structure, we specified 'heavy,' 'moderate,' and 'light' compositions, depicted in Table S3.1. We varied the composition of all sites simultaneously and so tested 3 methionines (heavy, moderate, and light); a full description of the sites we defined and used is presented in Csernica and Eiler, 2023.

**Table S3.1: Tested  $^{13}\text{C}$ -Methyl Labelled Methionine Compositions<sup>a</sup>**

Site	Light	Moderate	Heavy
C-methyl	99 %	99 %	99 %
C-gamma	-50	-30	0
C-alphabeta	-50	-30	0
C-carboxyl	-50	-30	0
O-carboxyl <sup>b</sup>	-25	0	25
S-sulfur <sup>c</sup>	-25	0	25
N-amine	-25	0	25
H-methyl	-100	0	100
H-gamma	-100	0	100
H-alphabeta	-100	0	100
H-amine	-100	0	100
H-hydroxyl	-100	0	100
H-protonated	-100	0	100

a: Except for C-methyl, which is given as a concentration of  $^{13}\text{C}$ , values are given as per mil enrichments vs VPDB (carbon) CDT (sulfur), AIR (nitrogen), or VSMOW (oxygen and hydrogen).

b: Composition of  $^{17}\text{O}$ , with  $^{18}\text{O}$  set via mass scaling

c: Composition of  $^{33}\text{S}$ , with  $^{34}\text{S}$  &  $^{36}\text{S}$  set via mass scaling

For all non-carbon substitutions, we find that deviations from the Met-A composition in the mixture to be minor, < 0.001 ‰ for all substitutions. For  $^{13}\text{C}^{13}\text{C}$ , the composition of the remaining carbon sites of the methyl  $^{13}\text{C}$  labelled methionine are more

influential, inducing errors of  $\approx 1$  ‰ in the final value. If some carbon sites of the methyl  $^{13}\text{C}$  labelled methionine differed substantially from our range (e.g., due to some of the label being applied at these sites), it may lead to significant deviations (enrichment, in the case that the  $^{13}\text{C}$  label appeared at multiple sites) of the  $^{13}\text{C}^{13}\text{C}$  composition of the mixture relative to our computation.

### S3.3. $^{17}\text{O}$ Extraction and Zero Scans for Acetone

To avoid an artifact associated with the abundant and nearly isobaric  $^{13}\text{C}$  peak, a targeted extraction procedure for  $^{17}\text{O}$  had to be used with FTStatistic. We begin with a basic overview of how FTStatistic functions. To extract peaks, one defines central masses associated with those peaks and a certain tolerance; e.g., a peak center of  $m/z = 60.05380$  Da and a tolerance of 5 ppm, relative. Then, for each scan, FTStatistic searches for and records the largest peak within the mass range. Typically, a tolerance of 5 ppm is used, leading to extraction of signal centered around a single mass (shown for  $^{13}\text{C}$  in Figure S3.2, top left). When two peaks are very close to each other, i.e., within the tolerance range, the FTStatistic program will report only the more intense of the two, and in cases where the two intensities are relatively similar to each, which of the two is reported might vary from scan to scan. When using a 5 ppm tolerance for  $^{17}\text{O}$  in the presence of  $^{13}\text{C}$ , this problem occurs and data from two close but distinct peaks are observed (Figure S3.2, top right) To remove this problem, the data are reextracted with a narrower mass range. In this case, we defined moving mass windows to target both the higher and lower peaks associated with  $^{17}\text{O}$ . For the higher mass peak, these were  $60.05390 \pm 0.0001$ ,  $60.05392 \pm 0.0001$ , and  $60.05394 \pm 0.0001$  for times of 0-300 minutes, 300-600 minutes, and 600-end minutes, respectively. For the lower mass peak, these were  $60.05370 \pm 0.0001$ ,  $60.05372 \pm 0.0001$ , and  $60.05374 \pm 0.0001$ , for the same times. Results of these targeted extractions are shown in Figure S3.2, center. For the lower mass peak, we see periodic oscillatory behavior, while for the higher mass one, the distribution appears similar to the  $^{13}\text{C}$  peak; moreover, the higher mass peak matches the theoretical mass of  $^{17}\text{O}$  (calculated as a moving average

assuming the same mass error as observed for  $^{13}\text{C}$ ); hence, we conclude the lower mass is an artifact of the Fourier-transform retrieval of the nearly isobaric, intense  $^{13}\text{C}$ -bearing peak, while the higher mass corresponds to the  $^{17}\text{O}$  peak. Quantifying the ratio using the targeted extraction of the higher mass peak results in the distribution shown in Figure S3.2, bottom, which is similar to the expected histogram, having a small number of zero scans (74 out of 33305, or 0.22%) and a similar number where the ratio is noticeably depressed. We consider these artifacts acceptable for observation and note the reported  $\frac{\sigma_{AE}}{\sigma_{SN}}$  ratio (1.6) is less than the arbitrary but useful data-triaging threshold of 2. In our data processing, we include these scans and quantify them with a value of 0 for the  $^{17}\text{O}/\text{Unsub}$  ratio.

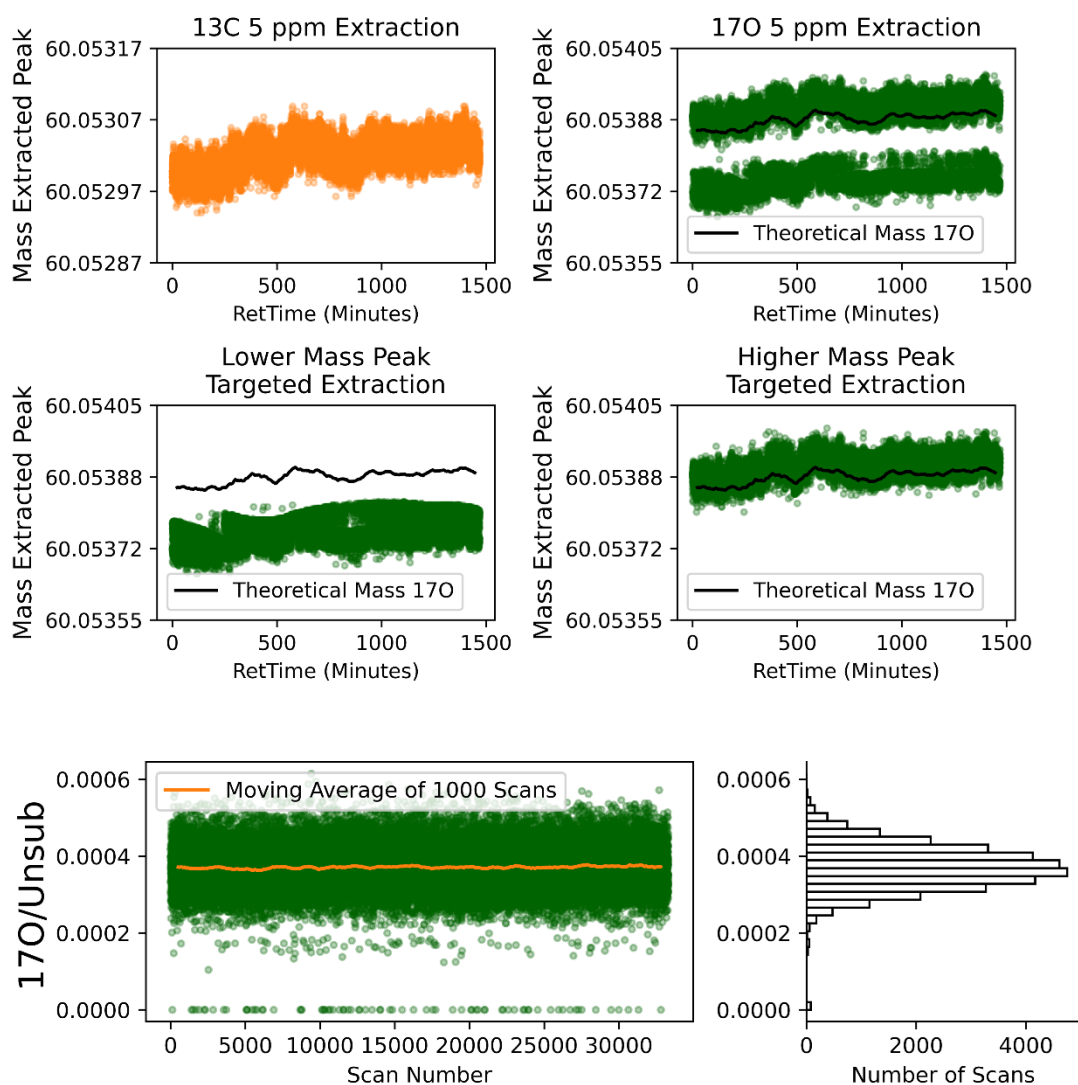


**Figure S3.2:** Targeted extraction of the  $^{17}\text{O}$  peak. Top left: For a typical FTStatistic extraction, a center point with a mass tolerance of 5 ppm is chosen, resulting in a distribution like that for  $^{13}\text{C}$ . Top right: For  $^{17}\text{O}$ , this results in the extraction of two closely related but distinct populations. Center: We redefined targeted mass windows for both, extracting them individually. The higher mass peak more accurately matches the theoretical mass of  $^{17}\text{O}$ , while the targeted lower mass extraction shows periodic behavior unlike the  $^{13}\text{C}$  (and other observed) isotopic peaks, so we identify the higher mass peak as  $^{17}\text{O}$ . Bottom: Our final extraction of the isotope ratio (using the window in the center right panel) has a distribution similar to that for other extracted peaks, with a small number of depressed and/or 0 scans; it also has a  $\frac{\sigma_{\text{AE}}}{\sigma_{\text{SN}}}$  ratio of  $<2$ . We consider the data sufficient for measurement.

### S3.4 Standardization Methods

The methionine and perchlorate data both constituted measurement sequences of 7 acquisitions in the order: Standard/Sample/Standard/Sample/Standard/Sample/Standard. Our results for the acetone 24-hour measurement show that acquisition error continues to decline throughout a single acquisition; we therefore attribute differences between consecutive measurements to the process of switching the analyte—i.e., the ‘purge’ and ‘prime’ steps. To evaluate whether this drift was random or systematic across measurement sequences, we performed the following calculation. For each sequence, and for each isotope ratio observed in that sequence, we took the four standard values observed, averaged them, and computed the deviation of each standard relative to the mean. We collected results for each ratio, and present these in Figure S3.3; each block of ratios corresponds to a single standard acquisition (datapoints are offset around standard number in the plot to allow visualization). Note that we omit the failed  $^{15}\text{N}/\text{Unsub}$  measurement from the final methionine standard acquisition and the failed  $^{37}\text{Cl}^{17}\text{O}/\text{Unsub}$  measurement for the perchlorate acquisitions at 2e5. We then performed a linear regression (using `scipy.stats.linalg`) versus standard number on each dataset, and present the  $R^2$  and p values (for the null hypothesis that the slope is 0) in Figure S3.3. For three of the four datasets, we compute p values  $< 0.05$  and so conclude that systematic error is present.



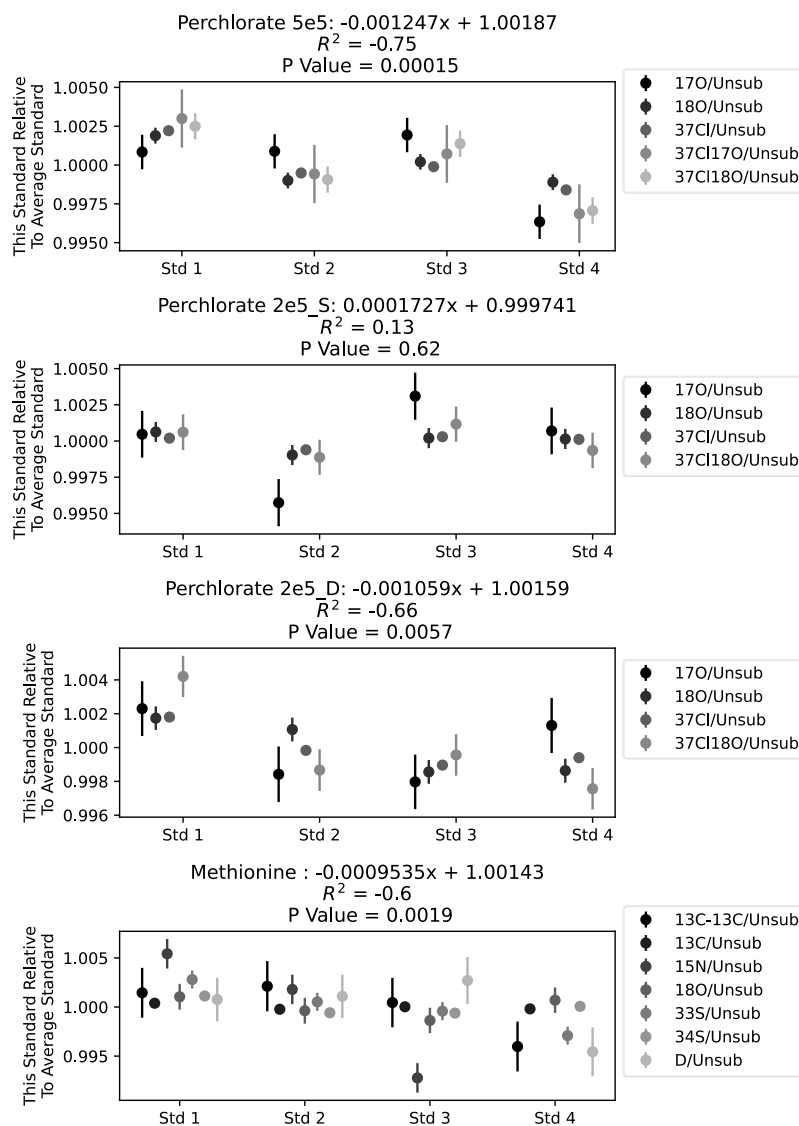


**Figure S3.3:** The isotope ratios recovered for the four standard acquisitions vary systematically with standard number rather than being random. We therefore chose to standardize by assuming a linear trend across each measurement sequence. Trendlines are not shown as the data for different ratios are offset along the x axis, to allow visualization; for the regression, each isotope ratio within a block had the same value for acquisition number ('0' for Std 1, '1' for Std 2, etc.). Values for the linear fit are given in each figure title.

Because we saw evidence of systematic drift in most cases, we chose to standardize versus the linear trend observed for all four standards. To do so, for each isotope ratio, we performed a linear regression across the four recovered standard values. We used this regression to predict the standard value at the time of each sample acquisition and the associated  $1\sigma$  confidence intervals ( $\sigma_{\text{STD,CI}}$ ). We then standardized each sample acquisition

relative to this predicted standard value. Error bars are given by adding the acquisition error ( $\sigma_{AE}$ ) for the sample to  $\sigma_{STD,CI}$  in quadrature. For example, our procedure applied to the  $^{13}\text{C}/\text{Unsub}$  ratio of methionine is depicted in Figure S3.4. Here, we plot the raw recovered ratios and associated error bars for each standard, the linear fit and its confidence intervals, and the predicted standard composition and associated error which we apply to our sample data.

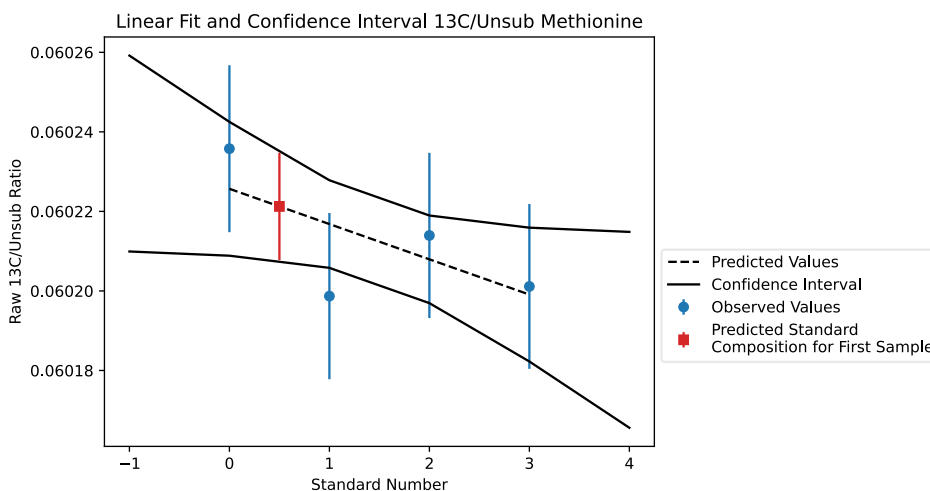


**Figure S3.4:** An example of the standardization procedure applied to  $^{13}\text{C}/\text{Unsub}$  in methionine. The blue circles are the reported  $^{13}\text{C}/\text{Unsub}$  ratios for each standard acquisition; the dashed line is the linear fit to these; and the solid lines are the associated confidence interval. The red square gives our reported standard value and error bar at the time of the first sample acquisition.

### S3.5 Failed D measurement of Acetone

While many of the isotopes of acetone were observed successfully, we consider the deuterium measurement a failure; we here discuss these results. Unlike the other measurements, the deuterium data do not track the shot noise limit; around 275 minutes, we see a sharp increase in the  $\sigma_{AE}$  and  $\frac{\sigma_{AE}}{\sigma_{SN}}$  ratio (Figure S3.5). As with the  $^{17}\text{O}$  peak, using the default FTStatistic setting results in the extraction of two closely related peaks; in this case, observations of two peaks are more common later in the measurement. Here, the lower mass peak better matches the theoretical mass of D (assuming the same mass error as the  $^{13}\text{C}$  peak, calculated as a moving average) and is present throughout the observation, so we assign this as the actual D peak. The higher mass peak does not match any

isotopologue associated with acetone; it has a mean distance of 0.23 mmu from the D peak, smaller than the 1.5 mmu for the H-adduct of unsubstituted acetone, and could represent an unidentified contaminant. As with the  $^{17}\text{O}$ , we apply a targeted extraction strategy to obtain only data from the D peak (Figure S3.5, center); however, in this case, the presence of the contaminant peak compromises our data quality. In scan-by-scan results from the observation (Figure S3.5, bottom), we see an increasing number of 0 scans later in the measurement, when the contaminant is more common; we interpret this as the D peak being lost due to the contaminant in these scans. Because of the large number of 0 scans (706 out of 33305 or 2.1%), as there is large apparent drift in the ratio across the measurement, and due to the sharp rise in precision of the observed ratio, we consider this observation to have failed. Additional efforts to identify and remove the contaminant could enable a successful D observation for this system.

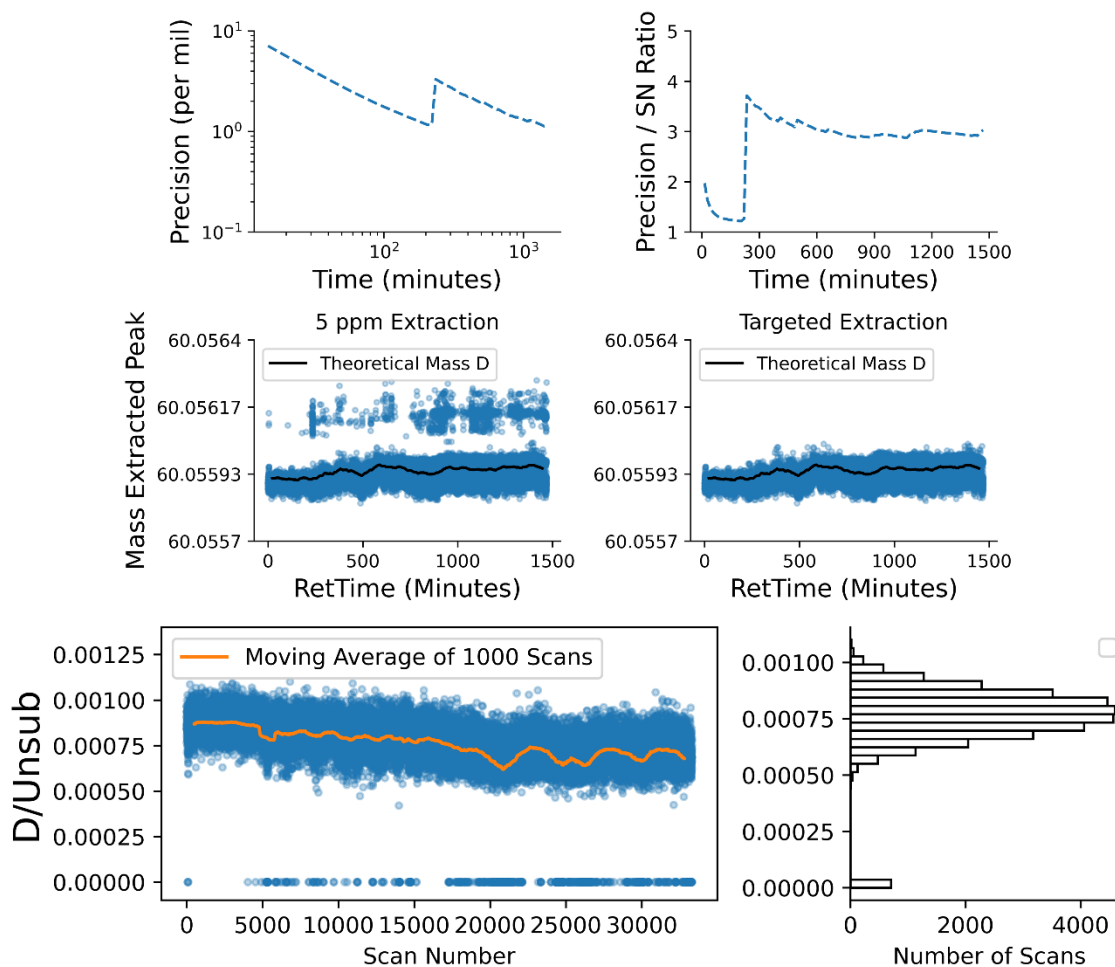


**Figure S3.5:** Analysis of the D measurement of acetone. Top: Precision and precision to shot noise ratio across the measurement. A sharp increase in precision is observed around  $\sim 275$  minutes into the measurement. Center: The observed mass by retention time for the D peak employing both 5 ppm and “targeted” FTStatistic procedures. There is a contaminant peak which becomes more common throughout the measurement, with the first increase in abundance around 275 minutes. We interpret this as the cause of our decrease in precision. Bottom: Scan-by-scan ratios and histogram for the D/Unsub ratio throughout the measurement for the targeted extraction. Despite targeting only the correct peak, we see an increasing number of 0 scans associated with the times where the contaminant is most common. We interpret this as evidence of the D peak being lost due to the contaminant, and thus not present in the spectrum. Because of the large number of 0 scans, long-term drift of the ratio, and observed increase in precision, we consider this observation a failure.

### S3.6. Culling Zero Scans of Deuterium in Methionine

When encountering zero scans for the observations of deuterium in methionine, we can proceed either by culling the zero scans or by including them with a value of  $N_{I0} = 0$  for

each; we find that culling introduces greater replicate-to-replicate variation into our results. We show the resulting data and sample standard comparisons from both methods in Figure S3.6, below; in the upper left plot, we also indicate the percentage of zero scans for each replicate. We find that the percentage of zero scans increases starting with the second sample replicate. We find that the percentage of zero scans increases starting with the second sample replicate, for unknown reason; we do not observe a shift in the average number of counts of deuterium. However, when we cull the zero scans, this increase in zero counts leads to an increase in the recovered isotope ratio, possibly because removing zero scans leads to an overestimate of the isotope ratio. This leads to an anomalously high sample standard comparison for the second bracket, where this shift occurs. No such behavior is observed when keeping all zero scans. For this reason, we employ the latter method. However, we note the drift present when culling zero scans is not beyond  $2\sigma$  error bars ( $\approx 7\%$ ) and do not recommend either method more generally.

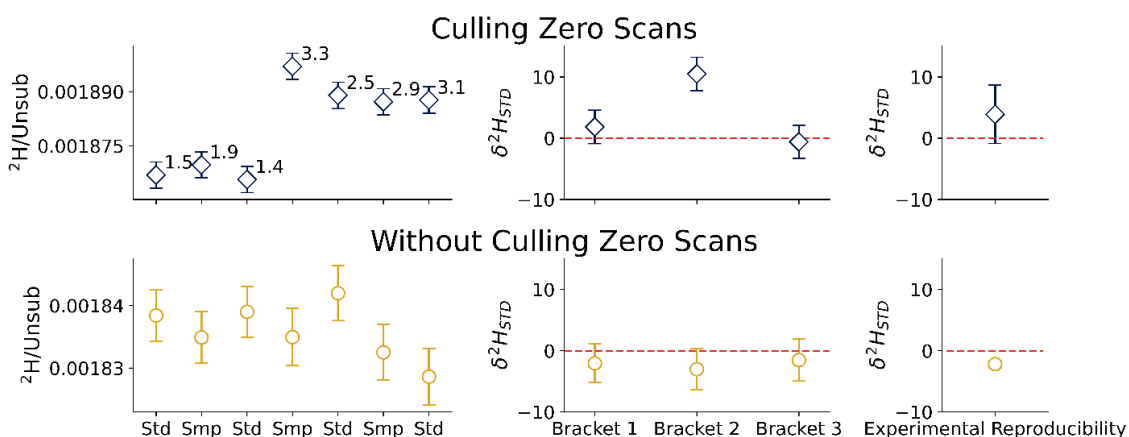


**Figure S3.6:** Two modes for dealing with zero scans in the methionine deuterium data. In the upper plot, we cull all zero scans; in the lower, we retain them and return an isotope ratio of 0. The percentage of zero scans for each replicate is shown in the upper left. We find that culling the zero scans leads to a shift in the recovered isotope ratio which is not present when they are retained. We attribute this effect to a shift in the number of zero scans in each observation, which increases on the second sample replicate. As culling zero scans results in a higher estimate of the isotope ratio, an increase in number of zero scans leads to a higher estimate of the ratio. We therefore use the data without culling zero scans; however, we note the observed drift is not beyond  $2\sigma$  error bars and this rule may not be applicable more generally.

## S3.7 Results From Perchlorate

Table S3.2: Results from Perchlorate Replicates 5e5<sup>a</sup>

	<i>Observed or Approximated Value</i>	<i>Average <math>\sigma_{AE}</math></i>	<i>Sample 1 and <math>\sigma_{PAE}</math></i>	<i>Sample 2 and <math>\sigma_{PAE}</math></i>	<i>Sample 3 and <math>\sigma_{PAE}</math></i>	<i>Average and <math>\sigma_{ER}</math></i>
$\delta^{37}Cl_{STD}$	0	0.09	-1.1 ± 0.6	0.7 ± 0.5	0.6 ± 0.6	0.0 ± 0.8
$\delta^{17}O_{STD}$	0	1.1	-0.3 ± 1.9	0.2 ± 1.6	2.3 ± 1.9	0.7 ± 1.1
$\delta^{18}O_{STD}$	0	0.5	-0.9 ± 0.9	1.1 ± 0.8	0.2 ± 0.9	0.1 ± 0.8
$\delta^{37}Cl^{17}O_{STL}$	0	1.9	-0.0 ± 2.2	3.0 ± 2.0	-3.7 ± 2.2	-0.3 ± 2.8
$\delta^{37}Cl^{18}O_{STL}$	0	0.8	-2.0 ± 1.6	2.7 ± 1.3	-0.5 ± 1.6	0.1 ± 1.9

a: All entries in per mil (‰)

Table S3.3: Results from Perchlorate Replicates 2e5\_S<sup>a</sup>

	<i>Observed or Approximated Value</i>	<i>Average <math>\sigma_{AE}</math></i>	<i>Sample 1 and <math>\sigma_{PAE}</math></i>	<i>Sample 2 and <math>\sigma_{PAE}</math></i>	<i>Sample 3 and <math>\sigma_{PAE}</math></i>	<i>Average and <math>\sigma_{ER}</math></i>
$\delta^{37}Cl_{STD}$	0	0.13	-0.2 ± 0.4	-0.9 ± 0.3	-0.8 ± 0.4	-0.6 ± 0.3
$\delta^{17}O_{STD}$	0	1.6	-3.8 ± 2.9	0.4 ± 2.4	-3.7 ± 2.9	-2.4 ± 1.9
$\delta^{18}O_{STD}$	0	0.7	-0.9 ± 0.9	0.2 ± 0.8	-0.2 ± 0.9	-0.3 ± 0.5
$\delta^{37}Cl^{17}O_{STD}^b$	0	4.7	7.7 ± 7.8	3.2 ± 6.7	11.7 ± 7.9	7.5 ± 3.5
$\delta^{37}Cl^{18}O_{STD}$	0	1.2	-1.9 ± 1.5	-0.3 ± 1.4	-2.1 ± 1.5	-1.4 ± 0.8

a: All entries in per mil (‰)

b: Rejected data due to high number (~20%) of zero scans

Table S3.4: Results from Perchlorate Replicates 2e5\_D<sup>a</sup>

	<i>Observed or Approximate d Value</i>	<i>Average <math>\sigma_{AE}</math></i>	<i>Sample 1 and <math>\sigma_{PAE}</math></i>	<i>Sample 2 and <math>\sigma_{PAE}</math></i>	<i>Sample 3 and <math>\sigma_{PAE}</math></i>	<i>Average and <math>\sigma_{ER}</math></i>
$\delta^{37}Cl_{STD}$	0	0.13	0.2 ± 0.6	-0.2 ± 0.4	0.2 ± 0.6	0.0 ± 0.2
$\delta^{17}O_{STD}$	0	1.6	0.6 ± 2.3	-0.2 ± 2.1	-0.3 ± 2.4	0.0 ± 0.4
$\delta^{18}O_{STD}$	0	0.7	0.1 ± 0.9	-0.2 ± 0.8	0.7 ± 0.9	0.2 ± 0.4
$\delta^{37}Cl^{17}O_{STD}^b$	0	4.7	1.9 ± 5.8	0.9 ± 5.3	-5.3 ± 5.8	-0.8 ± 3.2
$\delta^{37}Cl^{18}O_{STD}$	0	1.2	-0.6 ± 1.8	-0.1 ± 1.6	-0.6 ± 1.8	-0.4 ± 0.3

a: All entries in per mil (‰)

b: Rejected data due to high number (~20%) of zero scans

## OBSERVATIONS OF OVER 100 CONSTRAINTS ON METHIONINE'S ISOTOME

**Csernica, T.**, Session, A. L., and Eiler, J. M. High-dimensional isotomics part 2: Observations of over 100 constraints on methionine's isotome. *Chem. Geol.* 642, 121771. doi: 10.1016/j.chemgeo.2023.121771

### Abstract

The abundances of different isotopic forms of a compound, or isotopologues, will vary based on its physical and chemical history. The number of isotopologues increases combinatorically with the size of a molecule, and even small molecules such as amino acids have thousands of potentially observable isotopic variants. However, due to the analytical challenges of separating and observing isotopologues, only a few dimensions of isotopic diversity are routinely measured. Overcoming these challenges requires both an experimental method to observe many isotopic properties and a theoretical framework for interpreting these experiments. In Part 1, we presented such a theoretical framework; here, we demonstrate an experimental method, which we apply to methionine. Our approach uses a Q Exactive HF Orbitrap to perform several "M+N experiments," where a sample is ionized, a subset of its isotopologues with cardinal mass N daltons greater than the unsubstituted isotopologue is selected and fragmented, and the proportions of all detectable isotopic forms of those fragment ions are quantified. We perform M+1, M+2, M+3, and M+4 experiments of a methionine sample and standard where the sample has a 100 ‰ enrichment of  $^{13}\text{C}$  at the methyl carbon relative to the natural  $^{13}\text{C}$  abundance at that position in the standard, and is otherwise identical to the standard. We observe isotopic forms of 8 fragment ion species for each version of the M+N experiment. With the assistance of a forward model of expected mass spectra, we identify isotopic peaks for each fragment ion based on observed mass and abundance, screen these for data quality, and

quantify abundances for 146 unique isotopic peaks at precisions of  $\approx 0.3 - 3 \text{ ‰}$ . We present our direct observations and use them to reconstruct the concentrations of 19 individual singly, doubly, and triply-substituted isotopologues; doing so gives fewer constraints and broader error bars than working with the direct observations, but may be more interpretable for some applications. We also examine possibilities for measuring additional peaks, which are primarily limited by the detection limit of the Orbitrap-IRMS method. We then suggest some possible uses of our direct measurements for chemical forensics and hypothesis testing. Our results demonstrate the diversity of isotopic constraints currently observable and interpretable for organic molecules.

#### 4.1. Introduction

Natural compounds can exist in a variety of isotopic forms, or isotopologues, with varying number and location of isotopic substitutions. The chemical and physical properties of these isotopologues differ in subtle ways due to the presence of these substitutions; for example, they may have different absorption frequencies, diffusion rates, or chemical kinetics (Eiler, 2013). Moreover, the concentrations of these isotopologues in a given sample of a compound of interest will reflect several factors. These include: (1) inheritance from the mixture of isotopologues present in the substrates from which that compound was made; (2) chemical-kinetic and equilibrium isotope effects that preferentially discriminate between substrate isotopologues during synthesis; and (3) isotope effects acting on the compound of interest during any subsequent physical or chemical processing it might undergo (Eiler, 2013). These processes impart a unique isotopic fingerprint to that compound.

To frame our discussion, it is necessary to have a clear definition of isotopologue. For instance, “isotopologue” could be defined as a distinct isotopic stoichiometry (in which case  $^{14}\text{N}^{15}\text{N}^{16}\text{O}$  &  $^{15}\text{N}^{14}\text{N}^{16}\text{O}$  would be counted together as a single isotopologue) or distinguish based on the atomic locations of the isotopes in the molecular structure (in which case  $^{14}\text{N}^{15}\text{N}^{16}\text{O}$  &  $^{15}\text{N}^{14}\text{N}^{16}\text{O}$  would be counted as different isotopologues; some



authors have suggested the term ‘isotopocule’ for this purpose) (Toyoda et al., 2017). Both definitions have their limitations. If we do not consider location, then our concept of ‘isotopologue’ does not include site-specific information. However, if we always consider locations, then we introduce unhelpful complexity in applications where two or more location-specific isotopologues are not analytically distinguished, (e.g., treating  $^{14}\text{N}^{15}\text{N}^{16}\text{O}$  &  $^{15}\text{N}^{14}\text{N}^{16}\text{O}$  as different isotopologues for a mass spectrometric measurement that detects these two identical-mass species together). Therefore, we adopt a more flexible approach.

First, we split a molecule into individual ‘sites,’ each containing one or more atoms of the same element. Then, we define an isotopologue as ‘a version of a molecule with a specific set of isotopes at each site.’ This allows us to distinguish location when analytically relevant and ignore location otherwise (Csernica and Eiler, 2023). For example, if we only observe the intact  $\text{N}_2\text{O}$  molecule, we may define two sites: a nitrogen site with 2 atoms and an oxygen site with 1 atom. By this definition, there are then 9 isotopologues, which we may write in the form  $[^{14}\text{N}^{14}\text{N}, ^x\text{O}]$ ,  $[^{14}\text{N}^{15}\text{N}, ^x\text{O}]$ ,  $[^{15}\text{N}^{15}\text{N}, ^x\text{O}]$ , where sites are separated by commas and the substitutions at each site may occur at any positions within that site, and  $x = 16, 17, \text{ or } 18$ . If we instead observe fragments of  $\text{N}_2\text{O}$  which allow us to distinguish between nitrogen positions, we may define 2 separate nitrogen sites and have 12 isotopologues, of the form  $[^{14}\text{N}, ^{14}\text{N}, ^x\text{O}]$ ,  $[^{14}\text{N}, ^{15}\text{N}, ^x\text{O}]$ ,  $[^{15}\text{N}, ^{14}\text{N}, ^x\text{O}]$ , &  $[^{15}\text{N}, ^{15}\text{N}, ^x\text{O}]$ .

This flexible nomenclature allows us to tailor our description of a molecule to the problem of interest; when experiment can distinguish between atoms, our definition does so, and when experiment cannot, our definition does not. The cost savings offered by not tracking extraneous information for  $\text{N}_2\text{O}$  are small, but for small organic molecules like alanine ( $\approx 1,500$  isotopologues, defined with the sites in Csernica and Eiler 2023) or methionine ( $\approx 600,000$ , defined in the same), the system we describe here can decrease complexity by multiple orders of magnitude (Csernica and Eiler, 2023). We also note that our nomenclature makes it easy to extend to new scenarios, such as cases where one might wish to track atypical isotopes (e.g.,  $^3\text{H}$ ), where a user wants to treat different atoms of the same compound as different elements, or where a user may want to combine multiple

atoms into a single ‘superatom’ for ease of calculation (Roussis and Proulx, 2003; He et al., 2020). We use the term ‘isotome’ to refer to the concentrations of all isotopologues in a sample of a natural compound.

Despite the complexity of an isotome, most studies observe only a few dimensions of isotopic variation, which generally combine contributions from multiple isotopologues. For example, a common metric is the ratio of  $^{13}\text{C}$  to  $^{12}\text{C}$ , summing contributions from all carbons of a molecule; such measures fail to reflect information about the positional distribution of  $^{13}\text{C}$  across symmetrically non-equivalent carbon sites, multiple  $^{13}\text{C}$  substitutions, and correlations of  $^{13}\text{C}$  with isotopic substitutions of other elements. Recent advances in technology have begun to push back these limits, enabling observation of multiply-substituted (or ‘clumped’) isotopologues and isotopologues with substitutions at particular sites of a molecule (Eiler, 2007). Developing methods include nuclear magnetic resonance (NMR) spectroscopy, optical spectroscopy, and mass spectrometry, including Orbitrap isotope ratio mass spectrometry (Orbitrap-IRMS) (Caytan et al., 2007; Chaintreau et al., 2013; Prokhorov et al., 2019; Cesar et al., 2019; Chimiak et al., 2021). Improvements in analytical capabilities permit measurements which can contribute to a range of scientific questions, including the synthetic histories of amino acids and other organic molecules, paleo-temperatures, atmospheric budgets of  $\text{CO}_2$  and  $\text{O}_2$ , and the sources and sinks of petroleum hydrocarbons, among others (Abelson and Hoering, 1961; DeNiro and Epstein, 1977; Singleton and Thomas, 1995; Yeung et al., 2009, 2015; Eiler, 2011; Chimiak et al., 2021).

Orbitrap-IRMS, one of the developing technologies for these measurements, offers the ability to dramatically increase the number of constraints on the isotome for many compounds of interest. Orbitrap-IRMS has successfully been applied to a range of compounds, from organics like amino acids and fatty acids to oxyanions and metal oxides, and is sensitive enough for analysis of naturally occurring isotopologues for relatively small sample sizes ( $\approx$  tens of pmols) (Neubauer et al., 2020; Chimiak et al., 2021; Bills et al., 2021; Hilkert et al., 2021; Hoegg et al., 2021; Mueller et al., 2022a; Zeichner et al., 2022). It offers

high mass resolutions (upward of 1M has been demonstrated, although most applications use 60-240k), allowing many common nearly isobaric substitutions (e.g.,  $^{13}\text{C}$  and  $^{17}\text{O}$ ) to be resolved (Eiler et al., 2017; Denisov et al., 2021). It can be used to observe molecular fragments, permitting site-specific measurements where isotopic enrichment is localized to particular positions in a molecule (Eiler et al., 2017; Chimiak et al., 2021; Wilkes et al., 2022). Additionally, Orbitrap-IRMS is capable of observing rare isotopologues, including those with multiple substitutions (Neubauer et al., 2020; Hilkert et al., 2021). Combined, these capabilities permit the observation of a host of new isotopic constraints in numerous, chemically diverse compounds.

However, such observations are not straightforward: many isotopic constraints consist of rare, multiply-substituted isotopologues, and the specifics of Orbitrap-IRMS function dictate that observations of such isotopologues use unconventional experimental strategies. First, we note that Orbitrap-IRMS measurements are aggregates of many 'scans,' where each scan consists of a packet of ions which is injected into the Orbitrap and observed for some duration (typically  $\approx 0.1\text{-}500$  ms). The presence of too many ions in a single scan will cause deleterious space-charge effects, which will suppress the abundance and shift the location of low abundance peaks, preventing successful isotope ratio measurement (Eiler et al., 2017). Additionally, the Orbitrap has a limited dynamic range in intensity (i.e., the ratio of intensities between the least abundant peak that can be observed and the most abundant peak in a spectrum) of  $\approx 5000$  (Makarov et al., 2005, 2006b; Kaufmann and Walker, 2016). Therefore, the number of ions per scan must be limited. Simultaneously, the observed mass resolution ( $\frac{M}{\Delta M}$ ) will increase with scan duration. Therefore, long scan durations may be required to resolve some mass resolution problems. These constraints make it challenging to observe rare isotopologues at the same time as more common ones. For example, in a mass spectrum containing both the rare  $^{14}\text{N}^{17}\text{O}^{18}\text{O}^{16}\text{O}$  isotopologue of  $\text{NO}_3$  (abundance:  $\approx 4.5$  ppm) and the common unsubstituted isotopologue  $^{14}\text{N}^{16}\text{O}_3$  (abundance:  $\approx 990,000$  ppm), the limited ion capacity in each scan will be taken up by  $^{14}\text{N}^{16}\text{O}_3$ , and few or no ions of  $^{14}\text{N}^{17}\text{O}^{18}\text{O}^{16}\text{O}$  observed in any given scan;

because the scan rate is limited by the necessary mass resolution (e.g.,  $\approx 10,000$  to distinguish  $^{14}\text{N}^{17}\text{O}^{18}\text{O}^{16}\text{O}$  from  $^{15}\text{N}^{18}\text{O}_2^{16}\text{O}$ ), few ions of  $^{14}\text{N}^{17}\text{O}^{18}\text{O}^{16}\text{O}$  will be observed per unit time. To address this challenge, several authors have suggested a multi-stage experiment, where a quadrupole mass filter is used to exclude the common isotopologues and the ratio of two rare isotopologues is observed (i.e.,  $\frac{[^{14}\text{N}^{17}\text{O}^{18}\text{O}^{16}\text{O}]}{[^{15}\text{N}^{16}\text{O}_3]}$ , where  $^{15}\text{N}^{16}\text{O}_3$  has abundance  $\approx 3600$  ppm) (Eiler et al., 2017; Neubauer et al., 2020; Hilker et al., 2021). In this case, more ions of the rare isotopologue can be observed, enabling observation of less abundant peaks at higher precision. Data generated using this strategy can be combined with a separate observation of the ratio of more abundant rare isotope relative to the unsubstituted isotopologue (i.e.,  $\frac{[^{15}\text{N}^{16}\text{O}_3]}{[^{14}\text{N}^{16}\text{O}_3]}$ ) to obtain the enrichment of the less abundant one relative to the unsubstituted isotopologue (i.e.,  $\frac{[^{14}\text{N}^{17}\text{O}^{18}\text{O}^{16}\text{O}]}{[^{14}\text{N}^{16}\text{O}_3]}$ ). Applying a similar idea to the study of molecular fragments, Neubauer et al. have suggested the use of a ‘M+N’ experiment, a type of MS/MS experiment where a subset of the isotopologues of a compound with a cardinal mass “N” above the unsubstituted isotopologue are selected, fragmented, and observed (Neubauer et al., 2018). For example, a “M+1” experiment might include  $^{17}\text{O}$  and  $^{13}\text{C}$  substituted isotopologues, but not the unsubstituted (M0) isotopologue, of a compound containing both oxygen and carbon atoms. A M+N experiment finds the distribution of rare isotopologues relative to each other; when combined with an observation of the enrichment of one of the rare isotopologues relative to the M0 isotopologue, the enrichment of rare isotopologues from the M+N population relative to the M0 isotopologue may be calculated (Csernica and Eiler, 2023). Neubauer et al. presented results from a M+1 experiment, but did not explore the experimental challenges with higher order (N>1) experiments; moreover, at the time, there was no analytical algorithm for analyzing the data resulting from M+N experiments. We have since published such an algorithm and used it to interpret computed data, but did not yet apply it to data from an Orbitrap-IRMS experiment (Csernica and Eiler, 2023). Therefore, the limits of this experimental strategy and the interpretation of results remain unexplored.

Here, using the methionine isotome as a model, we explore the possibilities of Orbitrap-IRMS for high-dimensional isotopic measurements. We examine how many constraints may be observed and at what precisions, how they may be quantified and used, and how high-dimensional strategies can be extended and applied to new compounds. We selected methionine as a target compound because it has been previously used for M+1 experiments and has a range of accessible and well-understood fragment ions (Neubauer et al., 2018; Zhang et al., 2019). In total, our measurement strategy allows us to observe 146 constraints. We present results in two main modes: first, as direct observations of the isotopic composition of fragments of interest, and second as concentrations of individual isotopologues, calculated by combining several fragment observations. Then, using simulated methionine spectra, we explore ways to increase the number of peaks we can observe. Finally, we examine some possible use cases of our dataset, using it to test the plausibility of different fragmentation pathways and applying it to chemical forensics problems. Our results demonstrate the amount of information accessible by current techniques and should be broadly applicable to other molecular targets in geochemistry, biochemistry, and other applied science fields.

## **4.2. Methods**

### **4.2.1 The HPLC-modified sample introduction system**

We introduce and observe our analyte via reservoir injection, described in Chapter 3. Briefly, our system couples a Vanquish Horizon HPLC system (henceforth “Vanquish”) to a Q Exactive HF Mass Spectrometer (Thermo Fischer Scientific). The Vanquish has two pumps, labelled “A” and “B,” each of which can be connected to three reservoirs (pump A to reservoirs A1, A2, A3 and pump B to reservoirs B1, B2, B3). During operation, we may draw from one A and one B reservoir with some desired mixing ratio (e.g., 50% A1, 50% B2), introducing the mixture to the Q Exactive HF; flow rates give the combined flow of A & B, and both sample and standard were drawn from pump A. All experiments reported here

begin with a ‘priming’ step, where a 50/50 mixture of sample and solvent is introduced at 0.5 mL/minute for 8 minutes; this is done to fill the volume of all tubing with the analyte and prepare for analysis; a 50/50 mixture is used so that the priming step can be identical across methods, e.g., for a method that analyzes 100% sample or a method that analyzes 4% sample. After priming, we adjust the flow rate to 0.1 mL/minute for analysis (the lowest flow rate recommended for this system by the manufacturer, (personal communication)) and observe for 1 hour. Following analysis, we purge the system at a rate of 0.5 mL/minute for 20 minutes to prevent sample carryover. A representative set of standard and sample observation is given in Table 4.1. All of our observations consisted of a triplicate set of bracketed sample observations, in the order Standard 1/Sample 1/Standard 2/Sample 2/Standard 3/Sample 3/Standard 4, repeating the relevant sections of Table 4.1 as necessary.

**Table 4.1: A Representative Reservoir Injection Sample/Standard Comparison**

Time (minutes)	Flow (mL/min)	%B <sup>a</sup>	Pump A	Pump B	Description
0-8	0.5	50	A1: Standard	B2: Solvent	Prime standard
8-10	0.1	60	A1: Standard	B2: Solvent	Adjust flow
10-70	0.1	60	A1: Standard	B2: Solvent	Observe
70-90	0.5	0	A2: Solvent	B2: Solvent	Flush system
90-98	0.5	50	A3: Sample	B2: Solvent	Prime sample
98-100	0.1	30	A3: Sample	B2: Solvent	Adjust flow
100-160	0.1	30	A3: Sample	B2: Solvent	Observe
160-180	0.5	0	A2: Solvent	B2: Solvent	Flush system
<i>...Repeat standard &amp; sample injections as desired</i>					

a: %B is identical for all priming and flushing steps and varies in the observation step for both sample and standard based on experimental design. For each run, mixing ratios are selected to closely match observed TIC values for sample and standard.

#### 4.2.2. Experimental Conditions—M+N Experiments

Each M+N experiment consists of selection, fragmentation, and observation, and is most fundamentally defined by the selection window. For our Q Exactive HF instrument,

molecules are ionized in the source, pass through an advanced quadrupole system (AQS), a mass filter, collisionally fragmented in a higher-energy collisional dissociation (HCD) cell, and observed via Orbitrap. For each M+N experiment, the AQS is used to permit only methionine isotopologues with a cardinal mass increase of N over the unsubstituted methionine isotopologue into the HCD cell for fragmentation. The cardinal mass of positively ionized methionine,  $C_5H_{12}NO_2S^+$  which gains a hydrogen upon ionization, is 150, so, e.g., for a M+1 experiment, the mass window 150.5 – 151.5 is selected.

All experiments were undertaken with the following ion source parameters: sheath gas flow rate: 35 (arbitrary units); Aux gas flow rate: 10 (arbitrary units); sweep gas flow rate: 0 (arbitrary units); Spray voltage: 4.00 kV (positive ionization mode); Capillary temperature: 320 °C; S-lens RF level: 50 (arbitrary units); Aux gas heater temp: 40 °C. The mass spectrometer parameters, solute concentrations, and mixing ratios of A-pump to B-pump reservoirs for each experiment are shown in Table 4.2. New samples were prepared for each experiment at the nominal concentrations given in Table 4.2. Prior to each measurement, we signal balanced by introducing both sample ('Smp') and standard ('Std'), monitoring their total ion currents (TICs), and changing the mixing ratio of A sample (or standard) to B solvent to closely match TIC scores from each.

**Table 4.2: Experimental Conditions for M+N Observations**

	M+1	M+2	M+3	M+4
Reservoir Concentration ( $\mu$ M)	50	50	500	500
Mixing Ratio Std (%B)	60	58	50	50
Mixing Ratio Smp (%B)	30	50	0	50
Observed TIC Std (arbitrary units)	5.0E7	4.0E7	5.0E6	1.5E6
Observed TIC Smp (arbitrary units)	5.3E7	3.8E7	5.0E6	2.2E6
Isolation Range (m/z)	151.0 +/- 0.5	152.0 +/- 0.5	153.0 +/- 0.5	154.0 +/- 0.5
Normalized Collision Energy (NCE) (unitless)	60	60	50	40
Scan Range (m/z)	50.0-200.0	50.0-200.0	50.0-160.0	50.0-160.0

Mass Resolution at 200 m/z (M/ $\Delta$ M)	120,000	120,000	120,000	120,000
# Microscans	1	1	1	1
Automatic Gain Control (AGC) Setpoint	2e5	5e5	5e5	2e5
Maximum inject time (ms)	3,000	3,000	3,000	3,000
Sample Consumption ( $\mu$ Mol)	0.35	0.25	5	2.5

#### 4.2.3 Methionine Sample

We used a methionine with natural isotope abundance as a standard and the same methionine mixed with an artificially labeled methionine as a sample. In detail, we first acquired (1) a commercially available methionine with natural isotope abundances (Sigma Aldrich, 98% chemical purity) and (2) a  $^{13}\text{C}$ -methyl labelled methionine (Cambridge Isotope Laboratories, 99% label at methyl site and natural abundance elsewhere, 98% chemical purity). We set aside part of (1) as our standard. To create the sample, we first determined we needed  $\approx 0.11\%$  by mass of the  $^{13}\text{C}$ -methyl labelled methionine in the mixture to give an enrichment of  $\approx 100\text{‰}$  at the methyl site. We dissolved both the labelled methionine and the methionine standard in ultrapure water (Milli-Q IQ 7000 Purification) and mixed a combined solution in the corresponding proportions.

Both standard and sample have been analyzed previously. The standard was analyzed by Neubauer et al., and found to have  $\delta^{13}\text{C}_{\text{VPDB}} = -30.0 \pm 0.1\text{‰}$  (Neubauer et al., 2018). The sample was analyzed by Csernica et al., and found to have  $\delta^{13}\text{C}_{\text{VPDB}} = -11.0 \pm 0.1\text{‰}$  (Csernica et al., 2023). We computed that the sample is enriched in  $^{13}\text{C}$  by  $19.6 \pm 0.1\text{‰}$  vs the standard (differences in delta values are approximately but not precisely additive). Assuming the commercial labeled methionine has natural isotope abundances at all non-methyl sites, this difference in molecular average  $^{13}\text{C}/^{12}\text{C}$  ratio corresponds to a  $100.4 \pm 0.8\text{‰}$  enrichment at the methyl carbon relative to the standard (this calculation is available on the repository associated with this manuscript) (Csernica, 2023a).



Methionine solutions were made at a concentration of 50-500  $\mu\text{M}$  in a 70/30 mixture of LCMS-grade methanol (Fischer Scientific) and ultrapure water, with 0.1 % formic acid (Fischer Scientific) added to assist ionization.

#### 4.2.4 Observed Fragments of Methionine

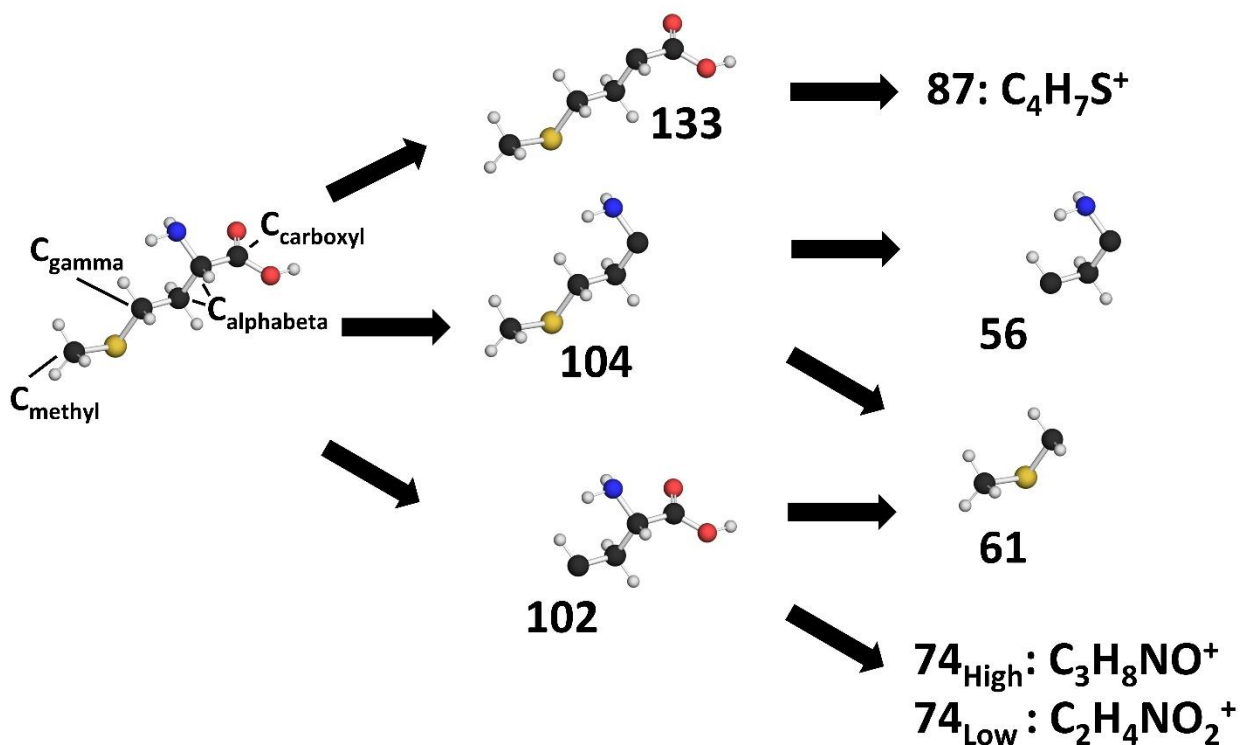


**Figure 4.1:** The methionine fragments observed in this work, named by the cardinal mass of the unsubstituted fragment.  $74_{\text{High}}$  and  $74_{\text{Low}}$  have the same cardinal mass, so these are distinguished by subscript;  $74_{\text{High}}$  has a higher isotopic mass. The fragments 133, 104, 102, 61, and 56 have been used previously in successful fragmentation studies of methionine and we are confident about which sites they sample, so these structures are depicted in the figure. We are less confident about structural assignment for fragments 87,  $74_{\text{High}}$ , and  $74_{\text{Low}}$ , so we only write their elemental composition. All fragments have been observed previously and have postulated fragmentation mechanisms, discussed by Zhang et al. (Zhang et al., 2019).

Each of our M+N experiments observes eight fragments of methionine, depicted in Figure 4.1, with fragmentation pathways adapted from Zheng et al. (Zhang et al., 2019). We name these by the cardinal mass of the unsubstituted version of that fragment; two have the same cardinal mass (74), so we distinguish based on which has higher and lower isotopic mass ( $74_{\text{High}}$  and  $74_{\text{Low}}$ ). We show structures for 5 of these fragments (133, 104, 102, 61, &

56); we are confident in our structural assignment for these, as they have been studied previously via a M+1 experiment. The remaining 3 (87, 74<sub>High</sub>, 74<sub>Low</sub>) have hypothesized structures but are less well studied, and so we do not specify any structures.

#### 4.2.5 Forward Modeling of Observed Mass Spectra

We use forward modeling of the methionine mass spectra for several purposes throughout our experiments. These include: 1) identification of relevant peaks; 2) standardization of sample data; 3) interpretation of the ‘completeness’ of our dataset; and 4) hypothesis testing to see how closely our data match the isotopic composition we expect. Here, we give a general overview of our forward modeling procedure.

In general, a forward model of the spectrum is a calculation of the abundance of each peak observed via each M+N experiment. We begin this calculation by defining a set of analytically distinguishable ‘sites,’ where a ‘site’ is a group of atoms of the same element (Table 4.3). The specific sites we use will depend on which fragments we are going to consider. In some cases, we will only use the fragments for which we have confident structural assignments (133, 104, 102, 61, and 56; see Figure 4.1). In other cases, we will use all fragments, and hypothesize structural assignments for the less well-known fragments (87, 74<sub>High</sub>, 74<sub>Low</sub>). When we are using the smaller set of fragments, we cannot distinguish between the alpha and beta carbons or the hydrogen attached to these carbons, so we define a combined ‘alphabeta’ site (e.g., C<sub>alphabeta</sub>) which includes all of these atoms. Additionally, the 74<sub>High</sub> fragment loses one oxygen, so we define two oxygen sites when considering the larger set of fragments. After defining the sites, we specify the isotopic composition, i.e., the concentration of each stable isotope, at each site. We use these isotopic compositions to compute concentrations of every isotopologue of methionine following a stochastic assumption; that is, the concentration of isotopologue  $a$  is the product of the site-specific concentrations of isotopes  $[x_i]$  at each site  $i$ :  $[a] = \prod_{i=1}^n [x]_i$ . For example, for N<sub>2</sub>O defined with sites N<sub>outer</sub>, N<sub>inner</sub>, O<sub>1</sub>, we have  $[^{14}\text{N}^{15}\text{N}^{16}\text{O}] = [^{14}\text{N}]_{\text{outer}} [^{15}\text{N}]_{\text{inner}} [^{16}\text{O}]_1$ .

With the concentration of every isotopologue in hand, we next simulate the spectrum by tracking every individual isotopologue through the M+N experiment. To do so, we first select only the isotopologues of interest for that M+N experiment. For example, in the M+4 experiment, we select only those isotopologues with a cardinal mass increase of 4 relative to the unsubstituted isotopologue. (In some cases, rather than calculating the concentrations of all isotopologues and then selecting the subset we need, we select first and only compute concentrations for these isotopologues). We then simulate the fragmentation of these isotopologues, determining which sites they lose and which they retain in each fragment. Based on which substitutions (if any) they retain, we determine where that isotopologue will appear in that fragment of that M+N experiment. For example, the M+4 isotopologue with substitutions of  $^{13}\text{C}_{\text{carboxyl}}^{18}\text{O}_{\text{carboxyl}}^2\text{H}_{\text{hydroxyl}}$  will lose all these substitutions when fragmented to form the 104 fragment, which loses the carboxyl group. Therefore, this isotopologue contributes to the observed unsubstituted (or ‘unsub’) peak of that fragment. We emphasize that the unsubstituted peak of a fragment from a M+N experiment is different from the unsubstituted isotopologue of the full molecule; the unsubstituted isotopologue is not included in a M+N experiment. By repeating this process for every isotopologue and combining the results, we obtain a forward model of the spectrum for a given input composition.

One use case of our forward modeling procedure is for peak identification in observed M+N spectra; we show an example in Figure 4.2. Here, we assign peaks of the 104 fragment of the M+4 experiment. On the top left, we depict three specific isotopologues from the M+4 population. We simulate the fragmentation process, losing the carboxyl group, and then determine which substitutions each isotopologue retains. By repeating the process for all M+4 isotopologues, we generate a simulated M+4 spectrum. We then compare our simulated spectrum to the observed spectrum for this experiment. Based on the location and abundance of each peak, we can determine the identity of the observed peaks. We have a few comments about the presentation in Figure 4.2. First, for ease of interpretation, we do not show peaks below an abundance threshold of  $1\text{e-}3$  relative to the

highest peak ( $^{34}\text{S}$ ) of the 104 fragment. Second, when reporting simulated masses, we offset each simulated peak by the mass error for that observation. We determine the mass error by comparing the observed mass of an abundant, easy-to-assign peak (e.g.,  $^{34}\text{S}$  or  $^{36}\text{S}$  for many M+4 fragments) to its computed mass, and shifting our simulated peaks accordingly. In some cases, for example the  $^{13}\text{C}^{34}\text{S}^{15}\text{N}$  peak, experimental mass resolution is insufficient to distinguish all predicted peaks. In this case, we do not include the unresolved peak in subsequent analysis. By repeating this process for fragments of each M+N experiment, we obtain a set of target peaks for extraction and analysis.

Because we use forward models for several different purposes, over the course of the study we computed such models for several different isotopic compositions of methionine. The compositions we use are given in Table 4.3. Here, the  $\delta$  value of each site is given relative to the reference frames VPDB (carbon), VSMOW (oxygen and hydrogen), CDT (sulfur), or AIR (nitrogen); we denote this ‘combined reference frame’ as ‘CRF.’ Unless noted otherwise, we use the hypothesized composition of our methionine standard, given in the “ $\delta_{\text{CRF,STD}}$ ” column. Here, several of the isotopic properties were constrained by Neubauer et al. 2018 (values in bold) (Neubauer et al., 2018). The  $^{33}\text{S}$  and  $^{36}\text{S}$  values were computed via mass scaling to those constraints ( $^{33}\text{S}$  scaled to  $^{34}\text{S}$ ,  $\lambda=0.515$ , i.e.,  $\delta^{33}\text{S} = 0.515 * \delta^{34}\text{S}$ ;  $^{36}\text{S}$  scaled to  $^{34}\text{S}$ ,  $\lambda=1.9$ ). Remaining values were set by assuming their value is identical to a common reference frame for that element ( $^{17}\text{O}$  vs VSMOW,  $^{15}\text{N}$  vs AIR,  $^2\text{H}$  vs VSMOW). We also employ forward models of the sample composition ( $\delta_{\text{CRF,SMP}}$ ), and, in section 4.3, a ‘perturbed’ version of the same. The perturbed values were drawn by specifying a normal distribution for each site centered around the values in the  $\delta_{\text{CRF,SMP}}$  column and with a standard deviation of 5 (or 20 for hydrogen sites). For sulfur and oxygen, we drew values for  $^{33}\text{S}$  and  $^{17}\text{O}$ , then set remaining values via mass scaling (for oxygen, we use  $\lambda=0.52$ ). While our hypothesized values for standard and sample are likely wrong in detail, especially for the sites which were not directly constrained, these errors are acceptable for the purposes of our forward models. In particular: for (1) peak identification and (3) determining the completeness of our dataset, our results are not sensitive to natural

abundance variation. For (2) standardization, we can obtain accurate sample/standard comparisons even with these errors in our hypothesized standard composition (Csernica and Eiler, 2023). And for (4) hypothesis testing, we are interested in the sample/standard comparison values. We discuss specific cases in more detail in the sections describing those results.

**Table 4.3: Assumed/Observed Isotopic Composition of Methionine Sample & Standard<sup>a</sup>**

Site	# Atoms	$\delta_{\text{CRF,STD}}$	$\delta_{\text{CRF,SMP}}$	$\delta_{\text{CRF,SMP,Perturb}}$
C <sub>methyl</sub>	1	<b>-53.9</b>	41.1	49.9
C <sub>gamma</sub>	1	<b>-23.7</b>	-23.7	-21.7
C <sub>alpha</sub>	1	<b>-24.0</b>	-24.0	-19.1
<i>C<sub>beta</sub></i>	<i>1</i>	<i><b>-24.0</b></i>	<i>-24.0</i>	<i>-12.8</i>
C <sub>carboxyl</sub>	1	<b>-24.3</b>	-24.3	-15.0
O <sub>carboxyl,retained</sub> ( <sup>17</sup> O/ <sup>18</sup> O)	1	0/0	0/0	0.1/0.2
<i>O<sub>carboxyl,lost</sub></i> ( <sup>17</sup> O/ <sup>18</sup> O)	<i>1</i>	<i>0/0</i>	<i>0/0</i>	<i>0.1/0.2</i>
S <sub>sulfur</sub> ( <sup>33</sup> S/ <sup>34</sup> S/ <sup>36</sup> S)	1	2.2/ <b>4.3</b> /8.2	2.2/4.3/8.2	1.5/2.8/5.4
N <sub>amine</sub>	1	0	0	-2.1
H <sub>methyl</sub>	3	0	0	8.2
H <sub>gamma</sub>	2	0	0	2.9
H <sub>alphabeta,retained</sub>	2	0	0	29.1
<i>H<sub>alphabeta,lost</sub></i>	<i>1</i>	<i>0</i>	<i>0</i>	<i>15.2</i>
H <sub>amine</sub>	2	0	0	2.4
H <sub>hydroxyl</sub>	1	0	0	8.9
H <sub>protonated</sub>	1	0	0	6.7

a: Sites of the standard which were constrained via direct observation by Neubauer et al. are indicated in bold; other the enrichment of other sites was assumed (Neubauer et al., 2018). These assumptions are likely incorrect but sufficient to return accurate sample/standard comparisons. For sites which are known, reported sample/standard comparisons can be reported in the combined 'CRF' reference frame, where enrichment of each isotope is given relative to an appropriate reference for that isotope (VPDB, VSMOW, AIR, or CDT). Sites in italics (*C<sub>beta</sub>*, *O<sub>carboxyl,lost</sub>*, *H<sub>alphabeta,lost</sub>*) are only used when considering the less well-known 87, 74<sub>High</sub>, and 74<sub>Low</sub> fragments; otherwise, they are combined with the sites directly above (e.g., to create a single C<sub>alphabeta</sub> site with 2 carbons).

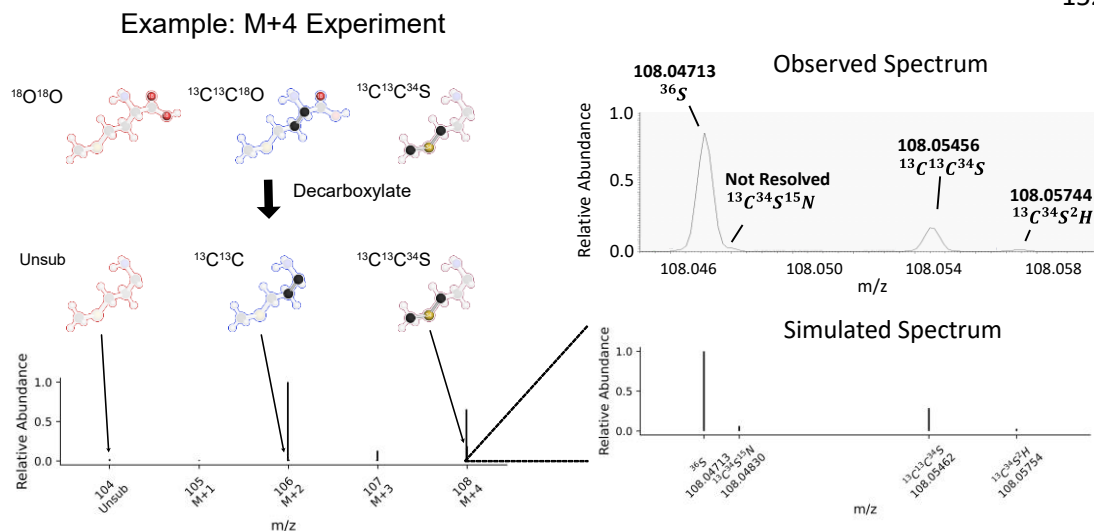


**Figure 4.2:** Our forward modeling procedure used for peak identification. We show three M+4 isotopologues of methionine and their corresponding chemical structures and isotopic substitutions upon loss of the carboxyl group in the 104 fragment. For example, the  $^{18}\text{O}^{18}\text{O}$  isotopologue loses both substitutions and becomes an unsubstituted fragment. By repeating this process for all M+4 isotopologues, we obtain a simulated methionine spectrum. We then compare this to the observed spectrum for this experiment and use the peak locations and abundances to assign peak identities. On the right, we expand the mass 108 region and compare the simulated spectrum to the spectrum we observe at the mass range. Simulated peaks with abundances relative to  $^{36}\text{S}$  of  $< 1\text{e-}3$  are not shown. The masses we report in our simulated spectrum were shifted by the observed mass error of the  $^{36}\text{S}$  peak. If the locations and abundance of an observed peak matches our simulated spectrum, they are assigned that isotopic identity. In some cases, as with the  $^{13}\text{C}^{34}\text{S}^{15}\text{N}$  peak, peaks are not sufficiently well resolved for observation. In this case, we do not analyze the unresolved peak.

#### 4.2.4 Quantification of Results

##### 4.2.4.1 Data Extraction & Quantification

We use the FTStatistic program (an unpublished, proprietary software provided by Thermo Fischer Scientific; a recently published software, IsoX, performs the same task (Hilkert et al., 2021)) to extract the intensity and associated noise from each peak of interest (as well as other details of each scan). These are then used to calculate the counts of each ion beam via

$$n_{IO} = \frac{S}{N} * \frac{C_N}{Z} * \left(\frac{R_N}{R}\right)^{\frac{1}{2}} * \mu^{\frac{1}{2}} \quad (4.1)$$

where  $n_{IO}$  gives the number of ions observed for that peak in that scan,  $S$  is the signal intensity,  $N$  is the peak noise,  $C_N$  is an empirical constant experimentally determined by

Makarov and Denisov and here taken to be 4.4 (Makarov and Denisov, 2009),  $R_N$  is the nominal mass resolution used to determine  $C_N$  (here 120,000),  $z$  is the charge on the ion, taken to be 1 in all cases,  $R$  is the nominal resolution of the scan, and  $\mu$  is the number of microscans used for that scan (1 for all data presented here). Data from each fragment is used to compute M+N relative abundances, or the abundance of each peak of a fragment relative to the abundances of all peaks of that fragment. For example, the 61 fragment of the M+1 experiment includes peaks with substitutions of “Unsub” (no substitutions),  $^{13}\text{C}$ ,  $^{33}\text{S}$ , and  $^2\text{H}$ ; writing  $n^i$  for the counts and  $\rho^i$  for the M+N relative abundance, we have

$$\rho_{61}^{13\text{C}} = \frac{n_{61}^{13\text{C}}}{n_{61}^{13\text{C}} + n_{61}^{33\text{S}} + n_{61}^{2\text{H}} + n_{61}^{\text{Unsub}}} \quad (4.2)$$

where the subscript indicates these correspond to the 61 fragment. We compute M+N relative abundances in each scan; reported values are the average value across all scans. We also report the relative standard error of this average, which we denote the ‘acquisition error,’ written  $\sigma_{\text{AE}}$ .

Following previous Orbitrap-IRMS work, we compare our recovered values to the shot noise limit for an acquisition (Eiler et al., 2017). The shot noise limit ( $\sigma_{\text{SN}}$ ) is the theoretical limit on precision based on how many ions have been observed (following eq (1)), and has been used as a gauge of data quality; typically, acquisitions with  $\frac{\sigma_{\text{AE}}}{\sigma_{\text{SN}}}$  values  $> 2$  are rejected (Eiler et al., 2017; Chimiak et al., 2021; Wilkes et al., 2022; Mueller et al., 2022a; Zeichner et al., 2022). For the example given in eq (2), let  $A = \mathcal{N}_{61}^{13\text{C}}$  and  $B = \mathcal{N}_{61}^{2\text{H}} + \mathcal{N}_{61}^{33\text{S}} + \mathcal{N}_{61}^{\text{Unsub}}$ , i.e., the sum of the counts of all other peaks. We may compute the shot noise limit as:

$$\sigma_{\text{SN}} = \frac{\mathcal{N}_B}{\mathcal{N}_A + \mathcal{N}_B} \sqrt{\frac{1}{\mathcal{N}_A} + \frac{1}{\mathcal{N}_B}}. \quad (4.3)$$

Note that this form differs from the shot noise formula used for more traditional isotope ratios of the form  $\frac{[\text{isotope } i]}{[\text{isotope } j]}$ ; we provide a derivation and more discussion in the supplement (S.1). For every observed peak, we calculate the corresponding shot noise limit, and reject

any data with  $\frac{\sigma_{AE}}{\sigma_{SN}} > 2$ . A plot of our recovered  $\frac{\sigma_{AE}}{\sigma_{SN}}$  values vs peak intensity is available in the supplement (Figure S4.1).

We make one additional comment about the  $C_N$  constant used in eq (1). The value of the  $C_N$  constant is not precisely known; the Denisov and Makarov experiment we rely on found values of both  $4.4 \pm 0.5$  and  $2.7 \pm 0.3$  (Makarov and Denisov, 2009). However, it is plausible that  $C_N$  varies, either with the abundance of the peak in question or with the abundance of all peaks. Eiler et al. previously observed nonlinearities in Orbitrap response with increasing ion loads; for example, injecting double the number of a particular ion caused its observed intensity to rise by  $< 2$  (see their Figure 7) (Eiler et al., 2017). Their experiment examined intensity, not intensity/noise (i.e., counts). However, it is plausible that the intensity/noise shows a similar nonlinearity, and therefore that  $C_N$  is function of intensity. To test for this effect, we plotted the average number of observed ion counts for each peak versus the theoretical abundance of that peak. Our results for each M+N experiment plot as a straight line, suggesting that these sorts of nonlinearities are not significant for our data (Figure S4.2).

We report M+N relative abundances rather than more traditional isotope ratios because the isotopologues constituting the unsubstituted ion beam differ radically across fragments. In a M+N experiment, no unsubstituted methionine isotopologues are fragmented; thus, when an unsubstituted fragment ion is observed, it results from a substituted methionine isotopologue which lost substitutions on fragmentation. For example, the unsubstituted peak of the 133 ion beam, which loses the  $N_{amine}$  and  $H_{amine}$  sites upon fragmentation, arises from M+1 isotopologues with a substitution at the  $N_{amine}$  or  $H_{amine}$  site. Therefore, the corresponding  $^{13}C/Unsub$  ratio, written in terms of sites (and treating alpha and beta carbons as a single site), is:

$$\frac{[^{13}C_{carboxyl}] + [^{13}C_{alphabet}] + [^{13}C_{gamma}] + [^{13}C_{methyl}]}{[^{15}N_{amine}] + [^2H_{amine}]} \quad (4.4)$$

Here, we write  $[^{13}C_{carboxyl}]$  for the concentration of the isotopologue with a single  $^{13}C$  substitution at the carboxyl position, and other concentrations are analogous. In contrast



to the 133, the unsubstituted peak of the 61 ion beam arises from M+1 isotopologues with a rare substitution at the C<sub>carboxyl</sub>, C<sub>alphabeta</sub>, N<sub>amine</sub>, O<sub>carboxyl</sub>, H<sub>amine</sub>, H<sub>hydroxyl</sub>, H<sub>alphabeta</sub>, or H<sub>protonated</sub> sites. The corresponding <sup>13</sup>C/Unsub ratio is

$$\frac{[^{13}\text{C}_{\text{gamma}}] + [^{13}\text{C}_{\text{methyl}}]}{[^{13}\text{C}_{\text{carboxyl}}] + [^{13}\text{C}_{\text{alphabeta}}] + [^{15}\text{N}_{\text{amine}}] + [^{17}\text{O}_{\text{carboxyl}}] + [^2\text{H}_{\text{amine}}] + [^2\text{H}_{\text{hydroxyl}}] + [^2\text{H}_{\text{alphabeta}}] + [^2\text{H}_{\text{protonated}}]} \quad (4.5)$$

Because these ratios have different denominators, it is difficult to compare them directly. In contrast, if we report both ratios relative to the sum of all M+1 Isotopologues, we have:

$$\frac{[^{13}\text{C}_{\text{carboxyl}}] + [^{13}\text{C}_{\text{alphabeta}}] + [^{13}\text{C}_{\text{gamma}}] + [^{13}\text{C}_{\text{methyl}}]}{[\text{All } M + 1 \text{ Isotopologues}]} \quad (4.6)$$

and

$$\frac{[^{13}\text{C}_{\text{gamma}}] + [^{13}\text{C}_{\text{methyl}}]}{[\text{All } M + 1 \text{ Isotopologues}]} \quad (4.7)$$

Here, the denominators are the same, and so we can add and subtract these quantities. This makes it easier to isolate and interpret the meaning of individual ion beams.

We make one additional comment about these M+N relative abundances. In some cases, we will not observe all M+1 isotopologues, preventing us from calculating them directly. For example, in the 104 fragment of the M+1 experiment, we do not report data for the <sup>2</sup>H substitution. In this case, we are intending to report quantities of the form:

$$\frac{[^{13}\text{C}]_{104}}{[^{15}\text{N}]_{104} + [^{33}\text{S}]_{104} + [^{13}\text{C}]_{104} + [^2\text{H}]_{104} + [\text{Unsub}]_{104}} \quad (4.8)$$

where the denominator includes all M+1 isotopologues. However, we instead observe quantities such as:

$$\frac{[^{13}\text{C}]_{104}}{[^{15}\text{N}]_{104} + [^{33}\text{S}]_{104} + [^{13}\text{C}]_{104} + [\text{Unsub}]_{104}} \quad (4.9)$$

Therefore, we may correct our observed values by applying an ‘observed abundance correction factor,’ in this case equal to:

$$O_{104} = \frac{[^{15}\text{N}]_{104} + [^{33}\text{S}]_{104} + [^{13}\text{C}]_{104} + [^2\text{H}]_{104} + [\text{Unsub}]_{104}}{[^{15}\text{N}]_{104} + [^{33}\text{S}]_{104} + [^{13}\text{C}]_{104} + [\text{Unsub}]_{104}} \quad (4.10)$$

While O values cannot be observed directly, they may be approximated using our forward model of standard composition: we will simulate the spectrum we expect to observe for our hypothesized standard composition and compute the relevant O value. To account for differences between our forward model and actual sample composition, we simulate O values as a distribution, centered around our computed value; we specify relative errors of 0.5 ‰ for the M+1 experiment and 1 ‰ otherwise, as there is more uncertainty in this factor when we observe fewer ion beams. We direct the reader to Chapter 2 for further discussion.

#### 4.2.4.2 Presentation of Results

We report our results in two ways: (1) ‘direct comparison’ mode (section 3.1), where the M+N relative abundance of each observed ion beam of the sample is compared to the standard; and (2) ‘isotopologue reconstruction’ mode, where these relative abundances are used to compute the abundances of individual isotopologues (section 3.2).

In ‘direct comparison’ mode, we compute delta values, in per mil, between the observed M+N relative abundances for the sample and predicted standard values at that timepoint. For example, for the  $^{13}\text{C}$  substitution of the 61 fragment, we compute:

$$\delta_{61,STD}^{13C} = 1000 * \left( \frac{\rho_{61,SMP}^{13C}}{\rho_{61,STD,pred}^{13C}} - 1 \right). \quad (4.11)$$

Here,

$$\rho_{61,SMP}^{13C} = \frac{1}{N} \sum_i^N \left( \frac{n_{61,SMP}^{13C}}{n_{61,SMP}^{13C} + n_{61,SMP}^{33S} + n_{61,SMP}^{2H} + n_{61,SMP}^{Unsub}} \right)_i, \quad (4.12)$$

i.e., the average M+N relative abundance of the quantity of interest across all N scans of the sample measurement. In contrast,  $\rho_{61,STD,pred}^{13C}$  is a predicted standard value from a linear regression across the average values of all four observed standards (hence the subscript, ‘pred,’ for predicted). We use this predicted standard value because our previous work using reservoir injection methods found isotope ratios vary systematically with acquisition number (equivalent to time, as each acquisition is the same length), making a

linear interpolation an effective method (Csernica et al., 2023). For each isotope, we obtain both  $\rho_{STD,pred}^i$ , a M+N relative abundance, and  $\sigma_{STD,pred,CI}^i$ , an associated confidence interval. We calculated propagated acquisition errors  $\sigma_{PAE}$  for the standardized measurement by adding  $\sigma_{AE}$  for the corresponding sample observation to  $\sigma_{STD,pred,CI}^i$  in quadrature, e.g.,:

$$\sigma_{PAE} = \sqrt{(\sigma_{STD,pred,CI}^i)^2 + (\sigma_{SMP,AE}^i)^2}. \quad (4.13)$$

When we present these results as a one number summary, e.g., in Figure 4.3, we compute average  $\delta$  and  $\sigma_{PAE}$  values from the 3 sample replicates. Note that for some Orbitrap-IRMS measurements, users have alternately reported ‘experimental reproducibilities’  $\sigma_{ER}$ , or the standard deviation of the computed  $\delta$  values across replicates (Mueller et al., 2022a; Zeichner et al., 2022). However, reporting standard deviations across 3 samples may understate our error bars for certain peaks (Csernica et al., 2023). We therefore elected to report average  $\sigma_{PAE}$  values. However, we do use experimental reproducibilities in our data screening (see section 2.7). Finally, we note that when calculating eq (11), any observed abundance correction factors would be applied to both sample and standard, and so cancel out; we therefore do not apply this correction.

In ‘isotopologue reconstruction mode,’ we combine information from multiple ion beams to compute the M+N relative abundances of individual isotopologues, then scale these using a ‘ $U^{M+N}$ ’ value to give site-specific or clumped isotope ratios. For this process, we only use fragments with confidently assigned structures (i.e., 56, 61, 102, 104, and 133). We here give an overview of our process; we direct the reader to our companion paper for additional discussion (Csernica and Eiler, 2023).

We begin by defining a “U-value” as the ratio between the sum of the concentrations of any set of isotopologues of a molecular and the concentration of the unsubstituted isotopologue of that same molecule. Specific types of U values (defined for methionine) include:

1) an isotopologue-specific U value, e.g.,  $U^{13C_{methyl}}$ , where the numerator is the isotopologue with a single heavy substitution at the  $^{13}C_{methyl}$  site:

$$U^{13C_{methyl}} = \frac{[^{13}C_{methyl}]}{[Unsubstituted\ Isotopologue]} \approx R_{methyl}^{13C}; \quad (4.14)$$

2) an element-specific U value, where the numerator includes all isotopologues with that heavy isotope substitution:

$$U^{13C} = \frac{[^{13}C_{methyl}] + [^{13}C_{\gamma}] + [^{13}C_{\alpha\beta}] + [^{13}C_{\text{carboxyl}}]}{[Unsubstituted\ Isotopologue]} \approx 5 * R^{13C} \quad (4.15)$$

where the coefficient 5 comes from the 5 carbon atoms included in the sum (note the combined alpha beta carbon site);

3) A  $U^{M+N}$  value, where the numerator includes all isotopologues with a cardinal mass increase of N relative to the unsubstituted isotopologue, e.g., for M+1

$$U^{M+1} = \frac{[All\ M + 1\ Isotopologues]}{[Unsubstituted\ Isotopologue]}. \quad (4.16)$$

In Part 1, we show that isotopologue-specific U values are approximately equal to the corresponding site-specific isotope ratios, multiplied by the number of atoms at that site; e.g.,  $U^{13C_{methyl}} \approx 1 * R_{methyl}^{13C}$  (an analogous statement holds for eq 15) (Csernica and Eiler, 2023). Because U values are written in terms of isotopologues rather than isotopes, they are more appropriate for mass spectrometry experiments which observe isotopologues.

We may use  $U^{M+N}$  values in combination with M+N relative abundances to calculate isotopologue-specific U values for many sites in a molecule. Intuitively, we can think of the M+N relative abundances as specifying the distribution of heavy isotopes within a population (e.g., the population of M+1 isotopologues), and the U value as scaling this distribution onto an absolute scale. For example, suppose we know  $\rho_{methyl}^{13C}$  and the  $U^{M+1}$  value for methionine. We may calculate  $U^{13C_{methyl}}$  ( $\approx R_{methyl}^{13C}$ ) via:

$$\rho_{methyl}^{13C} * U^{M+1} = \frac{[^{13}C_{methyl}]}{[All\ M + 1\ Isotopologues]} * \frac{[All\ M + 1\ Isotopologues]}{[Unsubstituted\ Isotopologue]} = U^{13C_{methyl}} \approx R_{methyl}^{13C}. \quad (4.17)$$

In our methionine experiment, we compute the  $U^{M+N}$  values in the following way. For  $U^{M+1}$ , we approximate  $U^{13C}$  using a previous EA-IRMS measurement of  $R^{13C}$  (though if these data had not been available this property could have been measured using the Orbitrap) (Neubauer et al., 2018; Csernica et al., 2023). Then we compute

$$U^{M+1} = \frac{U^{13C}}{\rho_{133}^{13C}} . \quad (4.18)$$

For  $U^{M+2}$ , we approximate  $U^{34S}$  using a previous EA-IRMS measurement of  $R^{34S}$  (Neubauer et al., 2018). Then we compute

$$U^{M+2} = \frac{U^{34S}}{\rho^{34S}} . \quad (4.19)$$

For  $U^{M+3}$ , we approximate  $U^{34S15N}$  using a previous EA-IRMS measurements of  $R^{34S}$ , assuming  $R^{15N}$  is equal to AIR (which is likely wrong, but sufficient for sample-standard comparison), and assuming a stochastic distribution of clumped isotopes for  $^{34S15N}$  (Neubauer et al., 2018; Csernica and Eiler, 2023). Then we compute:

$$U^{M+3} = \frac{U^{34S15N}}{\rho^{34S15N}} . \quad (4.20)$$

For  $U^{M+4}$ , we approximate  $U^{36S}$  using a previous EA-IRMS measurement of  $R^{34S}$  and assuming a mass law of 1.9 for the relationship between  $^{36S}$  and  $^{34S}$  (Neubauer et al., 2018). Then we compute:

$$U^{M+4} = \frac{U^{36S}}{\rho^{36S}} . \quad (4.21)$$

We note that the  $U^{M+N}$  values are identical for all fragments of a molecule; hence, we can constrain the  $U^{M+N}$  value using observations of one fragment and use this to constrain the other fragments. We standardize and propagate error via a Monte Carlo method, which includes experimental errors on each M+N relative abundance, errors in  $U^{M+N}$  values, and errors introduced by observed abundance correction factors (Csernica and Eiler, 2023).

We close this section with some additional comments about this strategy. We reiterate that the reason we use M+N relative abundances is to have a consistent

denominator across multiple observed fragments. If we observed a peak (or set of peaks) with consistent isotopologues across all fragments, we could use this rather than ‘all M+N isotopologues’ as our denominator. For example, if all fragments in the M+2 experiment retained the  $^{34}\text{S}$  substitution, it would be convenient to report ratios relative to  $^{34}\text{S}$ , e.g.,  $\frac{^{13}\text{C}_{133}}{^{34}\text{S}_{133}}$ ,  $\frac{^{15}\text{N}_{104}}{^{34}\text{S}_{104}}$ , and  $\frac{^{13}\text{C}_{61}}{^{34}\text{S}_{61}}$ . We could use these to compute site-specific ratios relative to  $^{34}\text{S}$ , e.g.,  $\frac{[^{13}\text{C}_{methyl}]}{[^{34}\text{S}]}$ . These quantities could be scaled using  $U^{34\text{S}} = \frac{[^{34}\text{S}]}{[U_{sub}]}$  to compute the corresponding U values, e.g.,  $U^{13\text{C}_{methyl}} = \frac{[^{13}\text{C}_{methyl}]}{[U_{sub}]} \approx R_{methyl}^{13\text{C}}$ . Our choice to use “M+N relative abundances” and “ $U^{M+N}$ ” values was made based on the difficulty of finding a smaller set of peaks which was consistent across all fragments. And, the “ $U^{M+N}$ ” present a general approach that will be applicable in all future applications of the methods we present. However, experiments on different compounds with different sets of fragments may present opportunities for more intuitive and convenient alternatives; in some cases, it may allow users to bypass the ‘observed abundance’ correction entirely.

#### 4.2.5 Controls on Precision

As discussed above, the precision of our measurements is similar to the shot noise limit for the number of ions observed in each ratio, and therefore the number of ions observed across a measurement. The number of ions observed across a measurement is controlled by the number of ions observed in each scan as well as the duration of each scan; it is especially affected by the AGC (automatic gain control) target and resolution setpoints for each measurement (Table 4.2). Precision across different fragments is also affected by their relative abundances, which is controlled by the fragmentation energy, given as a normalized collision energy (NCE). We discuss each of these parameters in turn.

#### 4.2.5.1 AGC (Automatic Gain Control) Target

The AGC target controls the target number of ions to permit in a single scan. A higher number is desirable as it increases the number of ions per scan and therefore improves the precision of an isotope ratio for a given measurement duration. However, space-charge effects, i.e., effects on ion trajectories caused by the presence of charge in the Orbitrap, become more pronounced when more ions are present, and so too high a AGC target may compromise a measurement (Kharchenko et al., 2012; Eiler et al., 2017; Kaufmann and Walker, 2018; Grinfeld et al., 2019). Of particular interest here is the coalescence (or peak merging) effect, which causes closely spaced peaks (e.g., within 20 ppm) to merge, especially when one of the peaks is substantially more abundant (e.g., a factor of 100) larger than the other peak. Setting the correct AGC target is therefore a tradeoff between faster measurement time and avoiding space-charge effects.

#### 4.2.5.2 Resolution

The resolution refers to the nominal mass resolution  $\frac{\Delta M}{M}$  of the Orbitrap at  $m/z = 200$ ; mass resolution varies with  $m/z$  as  $(m/z)^{-1/2}$ , and so resolution will be higher than the setpoint for lower  $m/z$  and lower for higher  $m/z$  (Makarov, 2000; Eiler et al., 2017). Scan time varies inversely with resolution, and so higher resolution will result in a longer measurement. Higher resolution also results in more pronounced space charge effects (Kaufmann and Walker, 2018; Hofmann et al., 2020). As with the AGC target there is a tradeoff between resolution of many different isotopic peaks and rapid/effective measurements.

#### 4.2.5.3 NCE (Normalized Collision Energy)

The collision energy used to fragment methionine results in different relative abundances of the fragment ions, with higher mass fragments (133, 104) more abundant at lower collision energies and lower mass fragments (61, 56) more abundant at higher

collision energies. The precision with which the isotopic composition of each fragment can be measured can therefore be tuned by varying the collision energy.

Our measurement strategy used a resolution of 120,000 and then tuned NCE and AGC to optimize the number of peaks observed simultaneously with precisions of  $< \approx 3\%$  for each M+N measurement (Table 4.2). A more targeted approach, e.g., a study solely of the isotopic composition of the 61 fragment, may tune these differently to expedite measurement.

#### *4.2.6 Data quality tests*

Due to the large number of mass spectrometric peaks observed over the course of the several M+N experiments we use in this study, we implemented an automated screening procedure to confirm accurate assignment and observation of each extracted peak. These included tests for peak location, to confirm isotopic identity, and tests for 'zero scans,' 'shot noise,' and 'experimental reproducibility,' to ensure data quality, including the identification of measurements compromised by nearly isobaric contaminants.

##### *4.2.6.1 Peak Location*

We first test that each extracted peak is in the correct location in the mass spectrum (i.e., the correct m/z ratio), relative to the most intense peak of that molecular or fragment stoichiometry, to a tolerance of 2.5 ppm, relative. We choose to use a relative error rather than an absolute error in m/z ratio because, while the absolute mass error in the Orbitrap changes from day to day (and is typically on the order of a few ppm, relative)(Olsen et al., 2005; Eiler et al., 2017), we find that the relative mass error is consistent across peaks of the same fragment. For example, if the  $^{13}\text{C}$  peak of the 61 fragment has an absolute error of 1 ppm on Tuesday and 2 ppm on Friday, the D,  $^{33}\text{S}$ , and Unsub peaks of the same fragment will have an absolute error of  $\approx 1$  ppm on Tuesday and  $\approx 2$  ppm on Friday, and so the relative mass error between the D and  $^{13}\text{C}$  peaks will be constant. In some cases, when



a low abundance peak is closely adjacent to a more abundant peak, space-charge effects may shift the position of the less abundant peak, increasing the relative mass error; this is also called a ‘coalescence’ effect (Gorshkov et al., 2012; Eiler et al., 2017; Hofmann et al., 2020). We find a 2.5 ppm threshold is sufficiently large to allow observation of peaks with minor but consistent shifts due to coalescence, while sufficiently small to reject incorrect peaks or peaks experiencing greater coalescence.

#### 4.2.6.2 Acquisition Error to Shot Noise Ratio

As discussed above (section 4.2.5), previous work has suggested that  $\frac{\sigma_{AE}}{\sigma_{SN}}$  ratios  $> 2$  indicate poor data quality. We therefore reject peaks where this ratio is greater than 2 (Eiler et al., 2017).

#### 4.2.6.3 Zero Scans

If we fail to observe an expected ion beam in 0.1% or more of all scans, we reject it as not sufficiently abundant for reliable observation. For ion beams we accept with a nonzero number of zero scans we calculate ratios including all zero scans, specifying a value of 0 ions observed for such scans. Across all ion beams which passed this test, a total of 7 substitutions had some number of zero scans; the most affected observation was the third standard replicate of  $^{13}\text{C}$  in the  $74_{\text{High}}$  fragment of the M+4 experiment, for which 11 out of 13667 (0.08%) scans are zero scans.

#### 4.2.6.4 Experimental Reproducibility

For each observed ion beam, we compute the experimental reproducibility  $\sigma_{ER}$  as the standard deviation of the standardized  $\delta$  values across all three samples. Typically, these are similar to the  $\sigma_{PAE}$  values reported for individual sample deltas. If the  $\sigma_{ER}$  are more than three times the size of the average  $\sigma_{PAE}$  values for a measurement, we conclude that

the observation drifted beyond our ability to standardize (due to nearly isobaric contaminants (see below), coalescence effects, or otherwise) and reject that peak.

#### *4.2.6.5 Nearly Isobaric Contaminants*

We close this section with some comments on the presence of nearly isobaric contaminants, i.e., contaminant peaks, originating from compounds other than methionine, with masses overlapping the methionine peaks. For example, if we observe the  $^{36}\text{S}$  peak of the 104 fragment of the M+4 experiment at  $m/z$  108.04713, and there is an unidentified contaminant peak at  $m/z = 108.04718$ , it may negatively affect our isotopic measurement; this will be especially detrimental if the contaminant differs in abundance between sample and standard. First, we note that the mass filtering of the M+N experiment helps to minimize such contamination, as only parent molecules with  $m/z$  in a range of 1 are fragmented and observed. For example, a nearly isobaric contaminant peak in the M+1 experiment must correspond to a parent molecule with  $m/z$  between 150.5-151.5; this parent molecule must then fragment at an energy of  $\text{NCE} = 60$  (unitless) to form a peak which is sufficiently close to the methionine peak to not be resolved at our experimental resolution ( $>120,000$ ). Second, previous analysis of such contaminants suggests they will result in drift in the isotope ratio measurements (e.g., Csernica et al. 2023, Appendix Figure 5) (Csernica et al., 2023). We therefore rely on our drift tests, both within acquisitions ('acquisition error to shot noise ratio') and between acquisitions ('experimental reproducibility') to identify anomalous data resulting from such contaminants.

#### *4.2.7 Data and Figure Availability*

Data, including .RAW files from our Orbitrap-IRMS experiments and .csv files generated by FTStatistic, is available on the Caltech data repository (T. Csernica, 2023a). Code for our data processing and the generation of Figures 4.2-4.7 is publicly available (Csernica, 2023a). In some cases, plots were further modified and/or joined using Affinity

Designer. Figure 4.1 was generated using PyMol and Microsoft Powerpoint, and Figure 4.2 includes instrument screenshots and images generated using PyMol.

## 4.3 Results and Discussion

### 4.3.1 Summary of Results

Across all measurements, we report 146 M+N relative abundances as constraints on the methionine isotome. Typical precisions are in the range of 0.3 – 3 ‰, and our dataset includes M+N relative abundances for peaks that correspond to isotopologues with absolute concentrations (i.e., as fractions of all molecules) as low as  $\approx 1e-6$  (see Supplemental Figure S4.3). Some of our M+N relative abundances constrain the same property (e.g.,  $\rho_{104}^{15N}$  and  $\rho_{56}^{15N}$  both correspond to the M+1 relative abundance of  $^{15}N$ , or the abundance of M+1 isotopologues with a  $^{15}N$  substitution, which does not vary across fragment); when we account for such redundancies, we report 124 *unique* M+N relative abundances.

### 4.3.2 Direct Comparison

The most straightforward way to present our results is to directly compare each observed constraint in the sample to the standard; that is, in the form  $\delta_{STD}^i = 1000 * \left( \frac{\rho_{SMP}^i}{\rho_{STD}^i} - 1 \right)$  (see eq (11)). These ‘direct comparisons’ are shown in Figure 4.3, as a heatmap showing the enrichment or depletion of sample (i.e,  $^{13}C$ -spiked methyl) with respect to standard for each ion beam. The size of each circle represents the experimental error for this constraint, and the color indicates the enrichment or depletion.

Some features of this plot can be understood based on our knowledge of the sample. For example, in the M+1 map, we see an increase in the abundance of either the  $^{13}C$  peak for fragments which retain the methyl carbon (133, 104, 61) or the unsubstituted peak for those which lose it (102, 56) (our results suggest that the mass 87 fragment ion

retains the methyl carbon site and  $74_{\text{High}}$  &  $74_{\text{Low}}$  lose it; we develop this argument further in section 3.5). Moreover, the size of this increase is more pronounced when this methyl site contributes relatively more to the observed fragment. For example, compare the results from the 102, unsub peak and the 133,  $^{13}\text{C}$  of the M+1 experiment. Both include the  $^{13}\text{C}_{\text{methyl}}$  carbon and are enriched in sample relative to the standard. However, the size of the increase is greater for the 102, unsub peak because the  $^{13}\text{C}_{\text{methyl}}$  contributes relatively more to the 102, unsub peak. Quantitatively, the 102, unsub peak is formed by isotopologues containing either  $^{33}\text{S}$ ,  $^{13}\text{C}_{\text{methyl}}$ , or  $^2\text{H}_{\text{methyl}}$  substitutions, and has a M+N relative abundance of  $\approx 0.285$ . In contrast, the  $^{13}\text{C}$  ion beam of 133 is formed by isotopologues with a  $^{13}\text{C}$  at any site of methionine, and has a M+N relative abundance of  $\approx 0.821$ . The  $^{13}\text{C}_{\text{methyl}}$  site with a M+N relative abundance of  $\approx 0.164$ , contributes  $\approx 58\%$  of the signal for the 102, unsub peak, but only 20% of the 133,  $^{13}\text{C}$  peak. Therefore, the size of the increase is smaller for the 133,  $^{13}\text{C}$  case. It also allows us to see a perhaps counterintuitive implication of working in M+N relative abundance space: although the abundances of most substitutions in the sample are unchanged relative to the standard (e.g., they have the same  $^{15}\text{N}$  abundance), the M+N relative abundances of these may change. For example, for the M+1 experiment,  $\rho^{15\text{N}}$  is less abundant in the sample because  $\rho^{13\text{C}}$  has increased, even while the  $^{15}\text{N}$  composition of the sample and standard are the same. For M+N experiments where  $N > 1$ , we caution against intuitive interpretations of contrasts between sample and standard; while these can be understood through clearly defined relationships between isotope proportions in the parent molecule and  $p^i$  values of fragment ions, the interpretation is indirect. For example, the increase of  $^{15}\text{N}$  in the 56 fragment of the M+2 experiment stems from the increase in  $^{13}\text{C}_{\text{methyl}}^{15}\text{N}$  in the sample; in the 56 fragment, the methyl carbon is lost, so the  $^{15}\text{N}$  beam of the mass 56 fragment is higher in abundance. Because there are many peaks and their interpretations are indirect, we prefer to use forward modeling to interpret these results; we discuss this further in section 3.5.

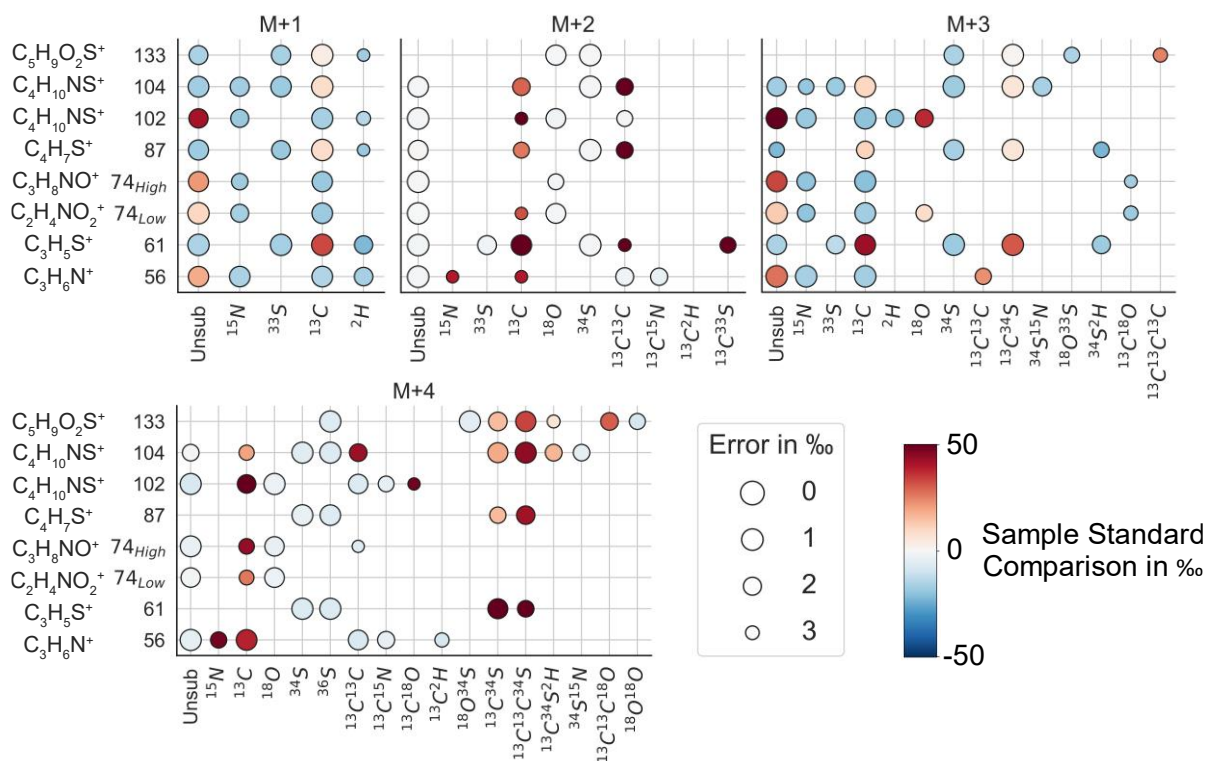


**Figure 4.3:** A direct sample-standard comparison of 100.4 ‰ methyl-labeled versus unlabeled methionine.

Each constraint in ‘direct comparison’ mode has the form  $\delta_{STD}^i = 1000 * \left( \frac{\rho_{SMP}^i}{\rho_{STD}^i} - 1 \right)$  (see eq (11)). The structure of each fragment is annotated next to the row for that entry. The presence of the methyl group can be traced intuitively through the M+1 data, where fragments retaining the methyl are enriched in  $^{13}\text{C}$  in the sample relative to the standard. The size of this increase is larger for fragments where the methyl contributed relatively more. For example, note that  $^{13}\text{C}_{\text{methyl}}$  has a M+N relative abundance around  $\approx 0.164$ . The 102, Unsub peak includes the  $^{13}\text{C}_{\text{methyl}}$  isotopologue, as the methyl group is lost in this fragment. The peak has a total M+N relative abundance of  $\approx 0.285$  and  $^{13}\text{C}_{\text{methyl}}$  contributes  $\approx 58\%$  of the signal. Therefore, the observed shift in delta value is large. In contrast, the 133,  $^{13}\text{C}$  peak, includes  $^{13}\text{C}_{\text{methyl}}$  and has a total M+N relative abundance of  $\approx 0.821$ . Therefore,  $^{13}\text{C}_{\text{methyl}}$  contributes only  $\approx 20\%$  of the signal. Hence, the size of the observed shift in delta value is smaller for the 133  $^{13}\text{C}$  peak than the 102, Unsub peak. We caution against intuitive interpretation for M+2 and higher measurements; while it is possible to quantitatively interpret such data, many of the effects are indirect and better interpreted in the context of a forward model relating molecular isotopic composition to mass spectrum.

#### 4.3.2 Isotopologue-specific Reconstruction

We also present a reconstruction of the abundances of specific isotopologues constrained via our measurements (Figure 4.4). Here, each data point is given as a delta value comparing isotopologue specific U values of the sample to the standard (i.e.,  $\delta_{STD}^i = 1000 * \left( \frac{U_{SMP}^i}{U_{STD}^i} - 1 \right)$ ). Note that these results rely on a detailed knowledge of methionine

fragmentation, and so we only use five fragments (133, 104, 102, 61, and 56) and do not distinguish between alpha and beta positions (see Table 4.3). The U values are calculated by scaling the M+N relative abundance ( $\rho$ ) of that isotopologue using the corresponding  $U^{M+N}$  values. In some cases, the  $\rho$  values arise from a single observation. For example,  $\rho_{M+2}^{13Cmethyl13Cgamma} = \rho_{61,M+2}^{13C13C}$ , the observed M+N relative abundance of  $^{13}C^{13}C$  in the 61 fragment of the M+2 experiment. In other cases, they arise from linear combinations of multiple peaks. For example,  $\rho_{M+2}^{13Cmethyl13Calpha} = \rho_{104,M+2}^{13C13C} - \rho_{61,M+2}^{13C13C} - \rho_{56,M+2}^{13C13C}$ . Additionally, isotopologues which are used to calculate the  $U^{M+N}$  values ( $^{13}C$  in M+1,  $^{34}S$  in M+2,  $^{34}S^{15}N$  in M+3, and  $^{36}S$  in M+4) deserve special comment, and are indicated with underlines in Figure 4.4. When we calculate the  $U^{M+N}$  value, e.g., via  $U^{M+1} = \frac{U^{13C}}{\rho^{13C}}$ , we include knowledge of the associated U value measurement ( $U^{13C}$ ,  $U^{34S}$ ,  $U^{34S^{15}N}$ , or  $U^{36S}$ ) in our computation. For example, our EA-IRMS measurements of  $^{13}C$  in the sample and standard found a difference of  $19.6 \pm 0.1$  ‰ between sample and standard. This information is included in our calculation of  $U^{M+1}$ . We then use this  $U^{M+1}$  to calculate the site-specific carbon results, e.g.,  $U^{13Cmethyl} = U^{M+1} \rho^{13Cmethyl}$ . Therefore, the site-specific carbon results must give a methionine which has an enrichment, across all carbons, of  $19.6 \pm 0.1$  ‰ relative to the standard. For  $N > 1$ , because the U values used ( $U^{34S}$ ,  $U^{34S^{15}N}$ , or  $U^{36S}$ ) corresponds to a single isotopologue, our reported values and errors are equal to the those for the U value. Because we did not explicitly measure  $U^{34S}$ ,  $U^{34S^{15}N}$ , and  $U^{36S}$ , but rather assumed they were identical to the standard, we do not count these isotopologues as constrained by our model, and say we report 19 rather than 22 values. However, because we do observe the corresponding  $\rho$  values, we could use a different isotopologue to compute  $U^{M+N}$  and report results for these isotopologues. For example, we could use  $U^{18O}$  to compute  $U^{M+2}$ , and then use this  $U^{M+2}$  to report a result for  $U^{34S}$ . For this reason, we still report results for  $^{34}S$ ,  $^{34}S^{15}N$ , and  $^{36}S$  in our plot. Finally, we omit three isotopologues constrained via our algorithm: these are (with corresponding values and errors):  $^{17}O_{carboxyl}$  ( $11 \pm 31$  ‰),  $^2H_{hydroxyl}$  ( $-51 \pm 160$  ‰), and  $^2H_{protonated}$  ( $98 \pm 85$  ‰).

‰). For  $^{17}\text{O}_{\text{carboxyl}}$ , the abundance is only constrained via closure; we have no direct observations of  $^{17}\text{O}$  in the M+1 spectrum, but the M+N relative abundance of  $^{17}\text{O}_{\text{carboxyl}}$  is still constrained by the fact that the M+N abundance of all isotopologues must sum to 1. Because we lack a direct constraint and because the error bars obtained via closure are exceptionally large for this isotope, we do not consider this isotopologue to be meaningfully constrained. Additionally, the two hydrogen sites are exchangeable in solution, and we do not anticipate meaningful isotopic information from these observations. Therefore, we do not include any of these isotopologues.

Compared to ‘direct comparison’ mode, ‘isotopologue reconstruction’ mode offers fewer constraints and broader error bars. However, it puts the data in a form that may be easier to understand and interpret. The resulting errors combine error from many sources, including: (1) error on the U value used to compute  $U^{M+N}$ ; (2) error on the  $\rho$  value used to compute  $U^{M+N}$ ; (3) error from any  $\rho$  values used to compute the isotopologue-specific  $\rho$  values; (4) additional error from the observed abundance correction factors. The error bars ( $1\sigma$ ) for each isotopologue differ widely due to the different individual measurements used to constrain each. For example,  $^{13}\text{C}_{\text{methyl}}^{13}\text{C}_{\text{alphabeta}}$  includes results from three fragment observations (104, 61, and 56), while  $^{13}\text{C}_{\text{methyl}}^{13}\text{C}_{\text{gamma}}$  only includes one (61); therefore,  $^{13}\text{C}_{\text{methyl}}^{13}\text{C}_{\text{alphabeta}}$  has broader error bars. Our observations overestimate the isotopic enrichment for both  $^{13}\text{C}_{\text{methyl}}^{13}\text{C}_{\text{gamma}}$  and  $^{13}\text{C}_{\text{methyl}}^{13}\text{C}_{\text{gamma}}^{34}\text{S}$ , which we suspect is due to a scale expansion, similar to effects observed previously for Orbitrap measurements, (Hilkert et al., 2021) although it may reflect a real enrichment of clumped isotopologues containing the  $^{13}\text{C}_{\text{methyl}}^{13}\text{C}_{\text{gamma}}$  bond. Of the clumped isotopologues we report data for, the  $^{13}\text{C}_{\text{methyl}}^{13}\text{C}_{\text{gamma}}^{34}\text{S}$  includes atoms which share a bond, and therefore may experience more significant thermodynamic effects, while the others do not. Finally, we note that many of the errors we report in Figure 4.4 are correlated and should not be considered independent. For example, values for  $^{13}\text{C}_{\text{methyl}}$  and  $^{13}\text{C}_{\text{gamma}}$  have a correlation coefficient of  $\approx -0.88$ . These correlations arise from the dependence of each recovered value on the  $U^{M+N}$  scaling constant, the coupled nature of

M+N relative abundance space (i.e., because the sum of all M+N relative abundances in a given fragment is 1, an increase in the M+N relative abundance of one peak requires a decrease in the M+N relative abundance of others), and from the common ion beams used to constrain each value. For example,  $^{13}\text{C}_{\text{methyl}}$  may be calculated using  $\rho_{133,M+1}^{13\text{C}} - \rho_{102,M+1}^{13\text{C}}$  while  $^{13}\text{C}_{\text{gamma}}$  may be calculated using  $\rho_{61,13\text{C}}^{13\text{C}} - (\rho_{133,M+1}^{13\text{C}} - \rho_{102,M+1}^{13\text{C}})$ ; the two are inversely related based on the content of  $(\rho_{133,M+1}^{13\text{C}} - \rho_{102,M+1}^{13\text{C}})$ . We provide correlation coefficients for all isotopologues we constrain in the supplement (Figure S4.4).

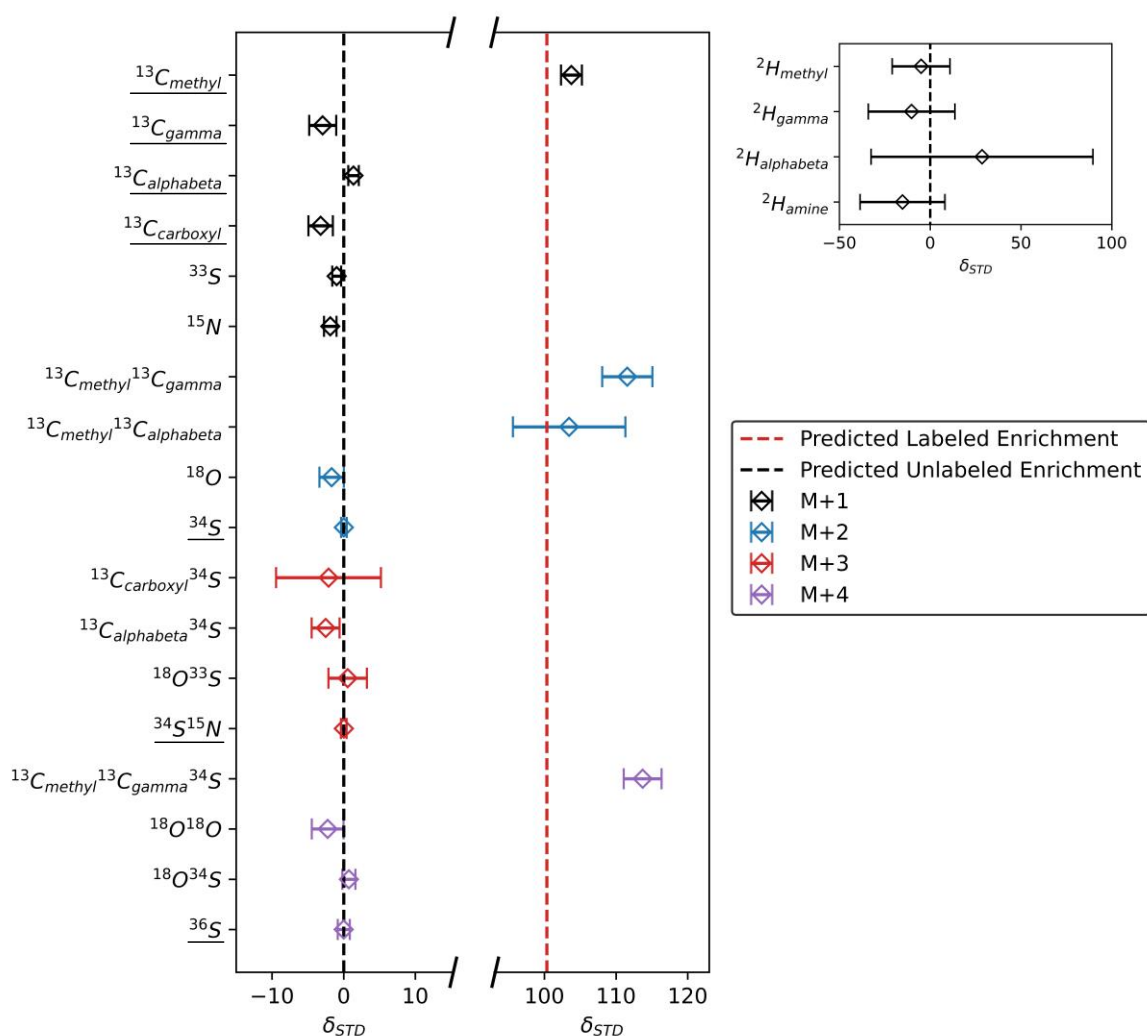


**Figure 4.4:** Reconstructed site-specific and clumped sample standard comparisons for isotopologues which our observations constrain explicitly. Results are presented as delta value comparisons of U values for sample and standard, i.e., for isotopologue  $i$ ,  $\delta_{STD}^i = 1000 * \left( \frac{U_{SMP}^i}{U_{STD}^i} - 1 \right)$ . Isotopologues which are used to calculate



the  $U^{M+N}$  values used in the computation of the  $U^i$  values are indicated with underlines. Our observed error bars are broader for isotopologues which combine observations from many fragments. While these results give fewer constraints with broader error bars than the direct observations, they may be easier to rationalize and interpret in the context of physical and chemical properties.

### 4.3.3 Completeness of Isotopologue Reconstruction

A central question of our investigation into high dimensional isotomics is: how many dimensions of isotopic complexity are measurable, and how close does the experiment we present here get to that limit? We first address this question by quantifying the completeness of our observations for both ‘direct observation’ and ‘isotopologue reconstruction’ modes of measurement (Figure 4.5). Here, the ‘direct observation’ plot uses all 8 fragments, while the ‘isotopologue reconstruction’ mode only uses the 5 fragments we can confidently assign to sites in the parent molecule structure.

For ‘direct comparison’ mode (Figure 4.5, top), we show the number of ion beams for which we report data versus the theoretical maximum number, assuming we quantified every substitution of every observable fragment. As the order of the  $M+N$  experiment increases, the fraction of recovered beams declines, to a recovery rate of  $\approx 10\%$  for the  $M+4$  experiment (we discuss ways to improve this recovery rate in section 4.2).

In ‘isotopologue reconstruction’ mode, we present three measures of the completeness of our observations: the number of ‘observed’ isotopologues (i.e., those for which we report a comparison in Figure 4.4), the number of ‘plausibly observed’ isotopologues (i.e., those for which we could report a comparison assuming that we observed all possible ion beams) and the number of ‘unobservable isotopologues’ (i.e., those which exist but could not be constrained by any combination of the observed ion beams). The  $M+1$  experiment observes every singly-substituted isotopologue, in part because we defined our isotopologues based on their distinguishability in the  $M+1$  experiment. However, the fraction of observed isotopologues decreases precipitously for higher order ( $M+2$ ,  $M+3$ ,  $M+4$ ) experiments. This decline occurs principally because these experiments measure fragment ions that contain two or more rare isotope substitutions

that are spread across some larger number of atomic sites; thus, several structurally non-equivalent isotopologues contribute to the measured fragments.

At this point, it is worth emphasizing that our presentation methods—'direct comparison' mode and 'isotopologue reconstruction' mode—are two extremes. When we show data in 'isotopologue reconstruction' mode, we are presenting either individual constraints or linear combinations of constraints which give a unique expression for a single isotopologue. For example,  $^{13}\text{C}_{\text{methyl}}^{13}\text{C}_{\text{gamma}}$  is uniquely constrained by the measurement of  $^{13}\text{C}^{13}\text{C}$  in the 61 fragment of the M+2 experiment, while  $^{13}\text{C}_{\text{methyl}}^{13}\text{C}_{\text{alphabeta}}$  results from the linear combination  $\rho_{104,M+2}^{13\text{C}^{13}\text{C}} - \rho_{61,M+2}^{13\text{C}^{13}\text{C}} - \rho_{56,M+2}^{13\text{C}^{13}\text{C}}$ . In some cases, our data may be used to report intuitive sums of isotopologues which do not correspond to a single isotopologue and so do not appear in Figure 4.5. For example, the linear combination  $^{13}\text{C}_{\text{carboxyl}}^{13}\text{C}_{\text{alphabeta}} + ^{13}\text{C}_{\text{carboxyl}}^{13}\text{C}_{\text{gamma}}$  is constrained via  $\rho_{102,M+2}^{13\text{C}^{13}\text{C}} - \rho_{56,M+2}^{13\text{C}^{13}\text{C}}$ . We note that this is simply a more complex version of an established practice of reporting sums of isotopologues in molecular mass spectrometry; for example, the current literature reports the  $\Delta_{47}$  value in  $\text{CO}_2$  ( $^{13}\text{C}^{18}\text{O}^{16}\text{O} + ^{12}\text{C}^{18}\text{O}^{17}\text{O} + ^{13}\text{C}^{17}\text{O}^{17}\text{O}$ ) relative to their stochastic distribution (Eiler and Schauble, 2004; Eiler, 2011). We also note that the quantities which we eventually report as 'isotopologues' may vary based on our definition of the sites of the molecule. For example, in generating the bottom row of Figure 4.5, we treat the alpha and beta carbons and alpha and beta hydrogens as combined sites, as they are not analytically distinguishable via our measurement; hence, in the M+1 experiment, we report constrained  $\text{C}_{\text{alphabeta}}$  and  $\text{H}_{\text{alphabeta}}$  isotopologues. If we instead treated them as distinct, we would report observing 11 of 15 isotopologues, 'failing' to constrain  $\text{C}_{\text{alpha}}$ ,  $\text{C}_{\text{beta}}$ ,  $\text{H}_{\text{alpha}}$ , and  $\text{H}_{\text{beta}}$ . However, the combined versions of these,  $\text{C}_{\text{alpha}} + \text{C}_{\text{beta}}$  and  $\text{H}_{\text{alpha}} + \text{H}_{\text{beta}}$ , remain constrained. In this context, our results shown in Figures 4.4 and 4.5 for isotopologue reconstruction mode are a conservative estimate of the more intuitively understandable properties which we observe (see the supplement, section S.4 for further discussion).

We conclude that it is often useful to present results of M+1 experiments in ‘isotopologue reconstruction’ mode as individual isotopologues, but that results of higher order experiments may be more usefully presented via ‘direct observation’ mode or as linear combinations of these which constrain groups of isotopologues with similar properties. For this reason, it is important to understand how different isotopic compositions map onto the observed composition space; we address this question further below, in section 3.5.

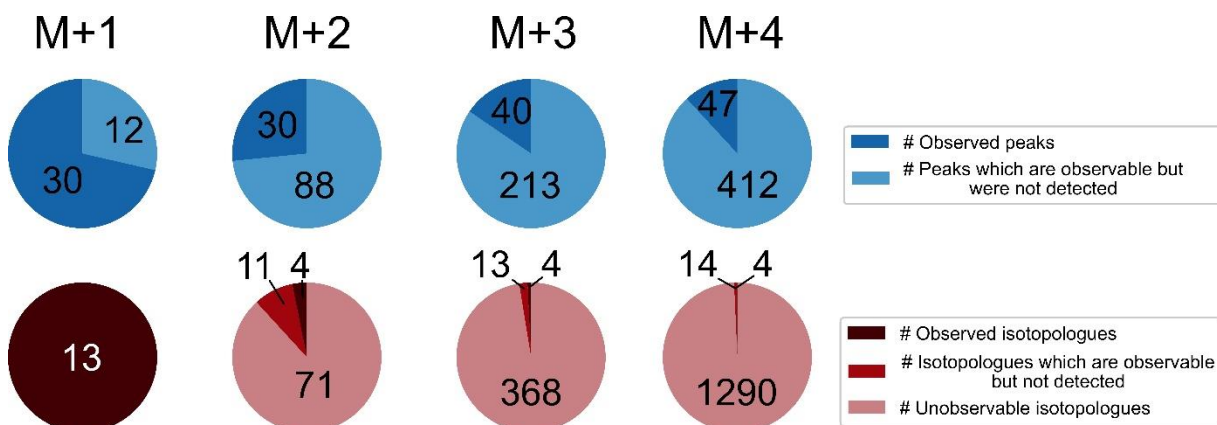


**Figure 4.5:** Completeness of observation for the M+N experiments presented here. Top: The number of ion beams we observe relative to the possible number of ion beams we could have observed across these 8 fragments of methionine, assuming perfect resolution and abundance sensitivity. Bottom: The number of individual isotopologues we constrain in ‘isotopologue-reconstruction’ mode, relative to both the number of isotopologues we could constrain assuming observation of all ion beams, and the total number of isotopologues for that population. These results vary based on the sites (and therefore isotopologues) we define for methionine, and do not capture linear combinations of the measured constraints which are readily interpretable but do not correspond to individual isotopologues (e.g.,  $^{13}\text{C}_{\text{carboxyl}}^{13}\text{C}_{\text{alphabeta}} + ^{13}\text{C}_{\text{carboxyl}}^{13}\text{C}_{\text{gamma}}$ ). Note the isotopologue-specific results are computed using only the 5 fragments for which we have more confident structures. Especially for higher-order experiments, the number of isotopologues we may observe is small relative to the isotopologues present, and most fruitful interpretation will occur in terms of more complex data products.

#### 4.3.3 Feasibility of Usefully Measuring Additional Dimensions

With an understanding of how many dimensions are theoretically observable, we next examine the practical concerns regarding their observation by simulating the number of observable ion beams under a range of conditions (Figure 4.6). We focus on two main factors affecting the number of observable beams: 1) the Orbitrap’s ability to resolve between nearly isobaric peaks, and 2) the Orbitrap’s ability to detect low abundance ions.

Our treatment of abundance limits requires some discussion, as there are two related but distinct issues: First, there is 2a) the dynamic range of ion beam intensities that can be simultaneously observed the Orbitrap, i.e., the ratio of the intensity of the least abundant peak relative to the intensity of the most abundant peak in a spectrum,  $\left(\frac{S_{least\ abundant}}{S_{most\ abundant}}\right)$ , where S is signal intensity, as defined above. In typical use cases, the dynamic range of an Orbitrap is  $> 1:5000$  ( $2e-4$ ) (Makarov et al., 2006a, b; Kaufmann and Walker, 2016; Bills et al., 2021). Second, there is 2b) the detection limit, or the concentration of the lowest ion-count ion beam of a M+N experiment that can be observed, expressed as a fraction of all ions of all isotopologues observed in that M+N experiment, or  $\left(\frac{\left(\frac{S}{N}\right)_{least\ abundant}}{\sum\left(\frac{S}{N}\right)}\right)$ . (Murray et al., 2013) The detection limit will be set by the smallest number of counts (calculated by multiplying the signal to noise ratio by several quantities which are constant throughout an experiment, eq (1)) required for observation; this has been previously estimated as  $\approx 30$  (Olsen et al., 2005), but following eq (1), we find a value of  $\approx 20$  (Csernica et al., 2023). Across all fragments and peaks of methionine for which we present data, we observe  $\approx 40,000$  ions per scan in the M+1 and M+4 experiments (AGC =  $2e5$ ) and  $\approx 65,000-70,000$  ions per scan in the M+2 and M+3 experiments (AGC =  $5e5$ ). Using our value of  $\approx 20$  counts per scan for observation, we estimate detection limits of  $\approx 5e-4$  ( $2e5$ ) and  $\approx 3e-4$  ( $5e5$ ) for the AGC settings we use here. As we do not include either contaminant peaks or methionine peaks which we excluded from our analysis due to poor data quality, the actual values of ions per scan are larger, and so our estimates of the detection limit are upper bounds.

Recently, Bills et al. have demonstrated improvements in both dynamic range and detection limit by employing an external data acquisition system (Bills et al., 2021). Their system employs absorption mode (aFT) rather than the typical enhanced mode (eFT) with a noise thresholding step; this change increases the accessible dynamic range to at least  $5e-5$ . Additionally, they process data by coadding many transients (microscans); the default software permits 10 microscans, while they demonstrate as many as 10,000. (We note that processing in eFT mode with “service mode” access enables  $>10$  microscans with the

default software). The signal to noise ratio will increase as the square root of the number of microscans; our data have  $\approx 10,000$  individual transients, so a factor of  $\approx 100$  increase in the detection limit to values of  $\approx 5e-6$  or  $\approx 3e-6$  are plausible (Eiler et al., 2017).

In cases of such low detection limits, we believe that the dynamic range will not be limiting, for the following reason: in our experiments, our largest observed ion beam has  $< 13,000$  counts per scan (M+1, M+3, M+4) or  $\approx 25,000$  counts per scan (M+2). Observing a single ion in such a scan gives a ratio of S/N values of  $\frac{1}{25000} \approx 4e-5$  in the most limiting case. While this is different than an intensity ratio, we find that relative S/N ratios and relative intensity ratios are similar, and conclude a dynamic range of  $\approx 4e-5$  would be sufficient to observe a peak with a single ion in a scan. We assume that if the dynamic range is not limiting in an individual scan, it will not be limiting in coadded scans. As our requisite dynamic range  $\approx 4e-5$  is near the demonstrated limit of  $5e-5$ , we proceed by considering only the detection limit.

Our results are shown in Figure 4.6, depicting the number of observable ion beams for various M+N experiments under a range of resolutions and detection limits. We include four detection limits; these are: '4e-4,' similar to the values for our experiments; '1e-4,' corresponding to a small improvement; '1e-5,' another order of magnitude improvement; and '5e-6,' a plausibly achievable increase by coadding 10,000 transients. Our resolution values give the resolution setpoint of the mass spectrometer at  $m/z = 200$ . Actual Orbitrap resolution scales as the inverse square root of the  $m/z$  ratio, and so is higher for lower masses, including methionine fragments, which we account for in these simulations (e.g., a setpoint of 120k at 200  $m/z$  gives an actual resolution of  $\sqrt{2} * 120,000 \approx 170,000$  at 100  $m/z$ ). Our experimental results for the M+1, M+3, and M+4 experiment are similar to those in the '120k, 4e-4' column; for the M+2 experiment, our results place us in '120k' row with a detection limit between 4e-4 and 1e-4. In all cases, we see that improvements to the detection limit generally offer better returns than improvements to resolution. For the higher order M+N experiments, even a small improvement to detection limit yields substantial gains; going from 4e-4 to 1e-4 leads to a  $>50\%$  increase in the number of

observed peaks. The best avenue for improving high-dimensional measurements is to improve our ability to observe low abundance peaks. Future experiments in this vein therefore should explore coadding multiple transients as a way to increase the number of observable peaks. We make one additional comment about the absolute abundance of these peaks. Assuming useful ion yield of  $10^{-5}$  (our results have values of  $10^{-6}$  to  $10^{-9}$ , in part because of the high flow rates used for reservoir injection, but  $10^{-5}$  is plausible for Orbitrap-IRMS) (Eiler et al., 2017) and 1  $\mu$ Mol of sample, only peaks with abundances relative to their isotopologue population of greater than  $2.7e-6$  (M+1),  $3.7e-6$  (M+2),  $6.1e-5$  (M+3), and  $5.1e-4$  (M+4), (i.e., peaks above that detection limit in Figure 4.6), will yield 1 million observable ions, sufficient for precisions of  $\approx 1\%$ . Therefore, it may not be possible to take advantage of all observable peaks at this high precision without using sample sizes larger than 1  $\mu$ Mol or improving useful ion yield.

We close this section with some additional comments on the scope of our simulation. First, we do not evaluate the additional ion beams which may be observed by tuning the heights of fragments differently via a change in fragmentation energy. For example, under our experimental conditions, the M+1 experiment has a fragmentation energy (NCE) of 60 (unitless), causing the 56 and 61 fragments to be most abundant. At a lower fragmentation energy, e.g., 10, the 133 fragment is more abundant. By varying the fragmentation energy, more peaks may be observed, even if other measurement conditions are unchanged; our figure therefore underestimates the number of observable peaks. Second, we do not analyze possible  $MS^n$  strategies which perform multiple cycles of isolation and fragmentation. In our experiment, we mass select a single population of isotopologues, then observe all fragments of that population; hence, the detection limit is set by the abundance of a particular peak relative to all peaks observed for that population. On an appropriately configured platform (i.e., one capable of  $MS^n$  analysis where  $n$  is 3 or more), a user could perform an additional mass selection step for a fragment of interest, allowing more peaks of that fragment to be observed, and improving on the recoveries indicated here (albeit, at the cost of not observing as many fragments simultaneously).

Third, we do not account for space-charge or transient decay effects which may influence the ion beams. Space-charge effects such as coalescence may cause closely adjacent peaks to merge, especially when a large number of ions are present in the Orbitrap (i.e., when using a higher AGC target), decreasing the number of observable ion beams (Grinfeld et al., 2019). Transient decay effects refer to the tendency of low-abundance ion beams to decay more rapidly than higher abundance ones, suppressing their measured intensity, especially at higher resolutions (Hofmann et al., 2020). This may cause some low abundance ion beams to not be observed, again decreasing the number of observable ion beams. Because of these limitations, our figure is not intended to be the final word on number of observed peaks, but rather a first-order approximation of how adjustments in mass resolution and detection limit can increase the amount of data constrained by an experiment.

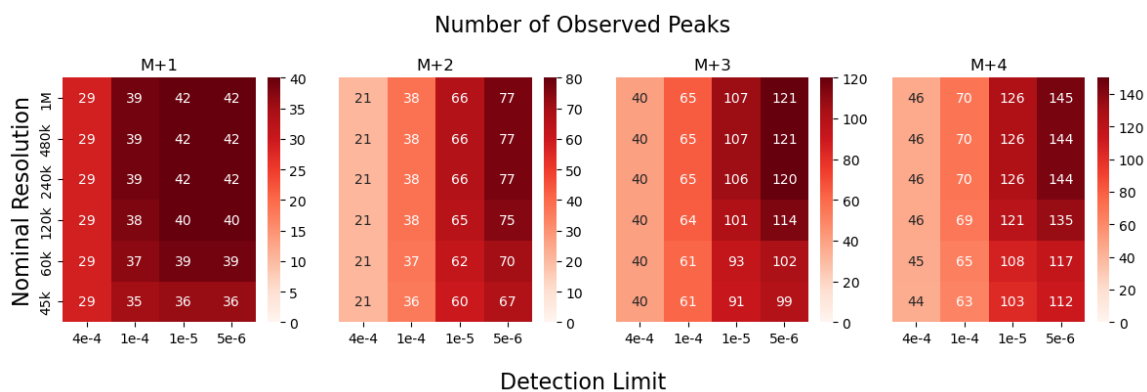


**Figure 4.6:** Simulated numbers of observed peaks in M+N experiments at a range of mass resolutions and detection limits. Simulations include all 8 fragments as well as the full molecule. A peak is considered ‘observable’ if it is not so close in mass that it merges with a more intense peak at the target resolution and has an abundance relative to all simulated peaks greater than the detection limit. Our experimental results are similar to the 120k, 4e-4 box for all experiments except M+2; this is in the 120k row with a detection limit between 4e-4 and 1e-4. Substantial gains in the number of peaks observed are possible with small increases in detection limit, which can be achieved by coadding multiple transients.

#### 4.3.4 Hypothesis Testing

We now turn to the question of how to use our measured constraints to evaluate different hypotheses, focusing on data interpretations that use the directly observed composition space of our methods (i.e., intensity ratios of ion peaks, rather than calculated proportions of isotopologues). Here, we rely on forward modeling of the sample-standard

comparison to determine how closely an observed isotopic fingerprint matches a hypothesized contrast between the sample and standard isotomes. We first simulate measurements of both sample and standard using hypothesized isotomes. We then compare the observed (OBS) and simulated (SIM) sample-standard comparisons for each ion beam, e.g.,  $\delta_{56,OBSvsSIM}^{15N} = 1000 * \left( \frac{R_{56,STD,OBS}^{15N}}{R_{56,STD,SIM}^{15N}} - 1 \right)$  (where  $R_{56,STD,SIM}^{15N} = \frac{\rho_{56,SMP,SIM}^{15N}}{\rho_{56,STD,SIM}^{15N}}$ ).

Explicitly written out, the terms of the fraction are as follows. For the observed dataset:

$$R_{56,STD,OBS}^{15N} = \frac{\frac{1}{N} \sum_i \left[ \left( \frac{n_{56,i}^{15N}}{n_{56,i}^{15N} + n_{56,i}^{2H} + n_{56,i}^{13C} + n_{56,i}^{Unsub}} \right)_{SMP,OBS} \right]}{\rho_{56,STD,pred}^{15N}} \quad (4.22)$$

where  $n_{56,i}^{15N}$  gives the counts observed for the  $^{15N}$  peak of the 56 fragment in scan  $i$ , and an average is taken across all  $N$  scans of the sample. The standard value  $\rho_{56,STD,pred}^{15N}$  is the predicted value of the standard at the timepoint of that sample observation, computed via a linear fit to the four observed standard replicates (see section 2.5). And for the simulated dataset:

$$R_{56,STD,SIM}^{15N} = \frac{\left( \frac{[^{15N}]_{56}}{[^{15N}]_{56} + [^2H]_{56} + [^{13C}]_{56} + [Unsub]_{56}} \right)_{SMP}}{\left( \frac{[^{15N}]_{56}}{[^{15N}]_{56} + [^2H]_{56} + [^{13C}]_{56} + [Unsub]_{56}} \right)_{STD}} \quad (4.23)$$

Where  $[^{15N}]_{56}$  gives the concentration of the  $^{15N}$  peak in the 56 fragment. For the simulation, we do not simulate  $N$  scans and then average across them, but only simulate the abundance of each peak. Note that for this comparison, we are not using  $U^{M+N}$  values or observed abundance correction factors. In this case, if the observed and simulated datasets match exactly, the resulting  $\delta_{56,OBSvsSIM}^{15N}$  will have a value of 0.

To demonstrate this approach in practice, we begin with a simple use case: testing the fragmentation geometries of the 87 fragment of methionine to determine whether or not it contains the methyl carbon, using our experimental measurements that compare  $^{13C}$ -labeled to unlabeled methionine. We proceed by calculating different simulated datasets for both cases and then comparing; results are plotted in Figure 4.7A. We quantify the fit



by calculating weighted root mean square errors (WRMSE) for each case, where the weights are equal to  $\left(\frac{1}{\sigma_{PAE}}\right)^2$  for each observation (favoring observations with smaller error bars). We see substantially better agreement with the results if the 87 includes the methyl carbon (WRMSE = 4.41) compared to if it loses it (WRMSE = 45.01), suggesting that the 87 fragment is formed via decarboxylation of the 133 fragment (Figure 4.2) without significant recombination.

We next expand on this idea, to a use case that involves higher dimensionality measurements (i.e., combining data for multiple fragment ions). To do so, we compute the OBS vs SIM comparison for our experimental data (neglecting the 87, 74<sub>High</sub>, and 74<sub>Low</sub> ion beams, but including all five confidently assigned ion beams) using both 1) our computed methionine composition (Table 4.3) and 2) a perturbed version of the same. To compute (2), we drew delta values for each site from a normal distribution centered around the delta value in (1) with a standard deviation of 5 ‰ for C, N, O and S isotope ratios and 20 ‰ for hydrogen isotope ratios. We present results from this test in two ways. First, in Figure 4.7B, we compare the squared values of  $\frac{\delta_{SIM}^{OBS}}{\sigma_{PAE}}$  for each variable and final WRMSE values, of 4.5 (computed) and 9.8 (perturbed) (due to the large number of variables, the squared variables are easier to visualize and closely related to the reported WRMSE values). The x-axis gives a somewhat arbitrary ‘variable number,’ where variables are numbered by M+N experiment (hence low variable numbers correspond to M+1 and high variable numbers correspond to M+4). We observe a large spike in the observed dataset for M+4, fragment 61,  $^{13}\text{C}^{13}\text{C}^{34}\text{S}$ ; this is closely related to the value for the  $^{13}\text{C}_{\text{methyl}}^{13}\text{C}_{\text{gamma}}^{34}\text{S}$  isotopologue reported in Figure 4.4 and may be the result of a scale expansion which is not adequately corrected for by a single standard. The resulting WRMSE value gives us a one-number summary which can indicate how well different hypotheses fit our data. Second, in Figure 4.7C, we provide global maps of the values of  $\delta_{SIM}^{OBS}$  at each observed position for both methionine compositions. Here, each point is a single  $\delta_{SIM}^{OBS}$ , with the size of the point indicating the error bar and the color indicating the value. In both cases, larger deviations

in  $\delta_{SIM}^{OBS}$  are concentrated among observations with lower M+N relative abundances as these are observed with larger error bars. As with Figure 4.3, we caution against too intuitive an interpretation, as the isotopologues each experiment samples and the coupled nature of M+N relative abundance space makes the drivers of individual shifts nonobvious. However, we suggest that these visualizations can complement the one-number summary approach of Figure 4.7B by demonstrating which ion beams are most relevant for distinguishing between competing hypotheses, aiding experimental design by indicating which peaks are most important to measure. We anticipate developments will go beyond our WRMSE approach to test hypotheses, incorporating more advanced methods to account for our error bars and M+N relative abundances; our intention here is to present an example of one style of hypothesis testing, not a definitive algorithm for doing so. This broader style of hypothesis testing is applicable to many problems in chemical forensics, such as food authentication, the identification of human remains, or determining the sources of drugs and chemical weapons (Ehleringer et al., 2000; Primrose et al., 2010; Bartelink et al., 2014; Cerling et al., 2016).

We have one final comment to make about Figure 4.7B. A possible criticism of high-dimensional isotomics is that measuring such a high number of dimensions is not useful, because observation of a small subset set of features should be sufficient to distinguish forensically. While this may be true in some cases, we note that (1) observing a larger number of dimensions may allow one to distinguish between compounds more rapidly, (2) our high-dimensional methods demonstrate the options available for study, but do not require that all dimensions be observed in every case, and (3) it may not be obvious, a priori, which of the many observable features of the mass spectrum will offer the greatest potential for forensic discrimination.

For instance, we note that the deviation between our prediction and the perturbed methionine was larger for the M+3 and M+4 than the M+1, implying the (possibly counter-intuitive) conclusion that M+3 and M+4 results are more useful for distinguishing samples than the M+1 (Figure 4.7B). This is a natural consequence of the nature of combined

substitutions. Consider two samples, A and B, where A is heavier in  $^{13}\text{C}$  by 10‰ at two different carbon positions, and the two are otherwise identical. Their  $^{13}\text{C}^{13}\text{C}$  content will differ by  $\approx 20\%$  (precisely, 21 ‰) relative to *each other*, assuming no clumped isotope effects. Therefore, observing the combined  $^{13}\text{C}^{13}\text{C}$  content relative to each other will give a larger signal than observing either carbon individually. If the precision of the  $^{13}\text{C}^{13}\text{C}$  measurement is comparable (and in our case, it is) it is better to target  $^{13}\text{C}^{13}\text{C}$  than  $^{13}\text{C}$ . If the  $^{13}\text{C}$  content of A and B differed in opposite directions, it could have the inverse effect, such that  $^{13}\text{C}$  was a larger signal than  $^{13}\text{C}^{13}\text{C}$ . However, at least for this instance, we find that observing combined substitutions leads to many larger signals. Further, we emphasize that this principle is statistical, and therefore applies even for atoms which are nonadjacent and would be expected to exhibit minor (or no) clumped isotope effects. For example, it holds for the carboxyl and methyl carbons of methionine, although they are on opposite sides of the molecule. Because of this effect, if one is designing a measurement to distinguish two compounds and only wishes to measure a small set of features, the best features to study may be unconventional and arise from higher order M+N experiments, like those we describe here.

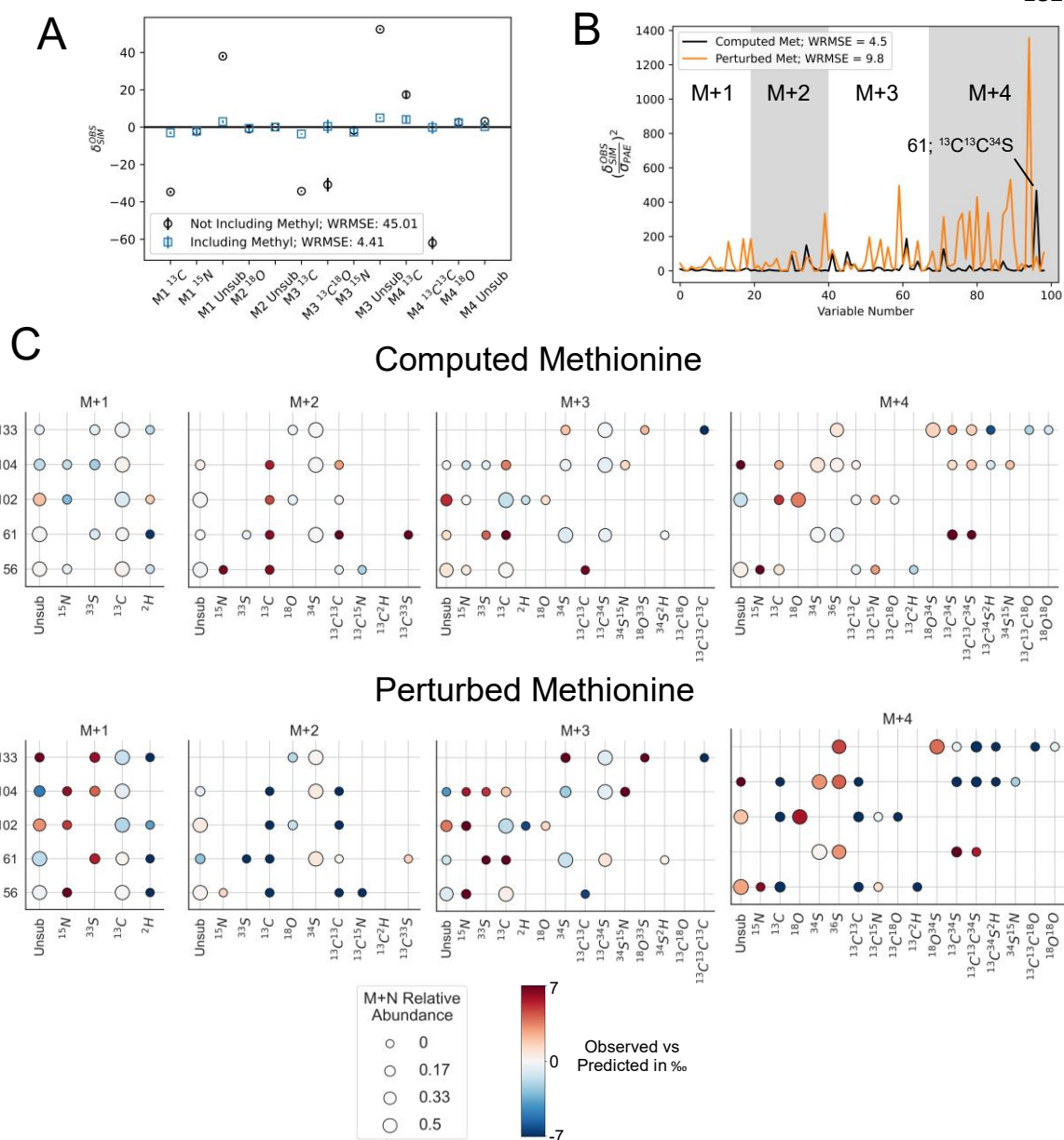


**Figure 4.7:** A: A simple case of hypothesis testing applied to the structural interpretation of the 87 fragment of methionine. Black circles show the  $\delta_{SIM}^{OBS}$  values computed assuming the fragment does not include the methyl group; blue squares show the same assuming it does include the methyl group. Inclusion of the methyl group is a superior fit to the experimental data. B: Squared values of  $\frac{\delta_{SIM}^{OBS}}{\sigma_{PAE}}$  from a hypothesis test that compares observed M+N data and two hypothesized methionine isotopic structures; one computed (Table 4.2) and one where every site is perturbed by drawing from a normal distribution with  $\sigma = 5$  per mil ( $\sigma=20$  for hydrogen sites), centered around the computed value. C: Data from the same hypothesis test as B, now plotted as individual points to allow visualization of where deviations occur. These plots complement the one-number summary calculated via WRMSE.

#### 4.3.5 Future Prospects

Our results suggest several directions for future work in high-dimensional isotomics. The central questions here are: given the increase in complexity and technical difficulty for this measurement strategy, where are such measurements useful and preferable to simpler isotopic measurements? What problems can they contribute to? And what needs to be done to make measurements of this sort more routine? We first emphasize that, while our results were presented together, there are four distinct M+N measurements shown here with a range of complexities. The M+1 experiment involves 13 isotopologues and 26 observed peaks, and the relationships between isotopologue abundances and peak intensities is analytically solvable; in contrast, the M+4 experiment involves dozens of observed peaks corresponding to over 1000 isotopologues, and nearly all peaks represent combinations of contributions from multiple isotopologues. The use cases and potential applications of these measurements differ notably. The M+1 experiment offers a more rapid method for obtaining site-specific information which has been observed by NMR or via Orbitrap-IRMS but using different, and generally more time consuming, experimental designs. In contrast, higher order M+N experiments constrain previously unobserved isotopic dimensions, including clumped isotopologues localized to individual positions within a molecule, or more esoteric M+N relative abundances which are not directly interpretable as individual isotopologues (i.e., measured signals always combine contributions from multiple isotopologues). The observed values can nevertheless be predicted, modeled, and understood as properties of the molecule. To move these observations from curiosity to application, we must build an understanding of how these dimensions are affected by physical and chemical processes and what precisions are necessary for effective observation.

Building this understanding is a difficult task, but here we offer a few comments as to how to proceed. First, while the effects of many processes on the multiply-substituted versions of a molecule are currently unknown, we anticipate that these will be observable; we discuss an example of mixing in Part 1, and there is theoretical justification for

equilibration, diffusion, and photochemical effects, among others (Eiler, 2007, 2013; Csernica and Eiler, 2023). With more properties available for study, more theoretical work must be done to understand which should be targeted. Second, we note that not all questions require that every possible dimension be used. For example, consider a scenario like that of alanine observed from the Murchison meteorite, where one carbon (alpha) has a large enrichment relative to the other carbons (Chimiak et al. find values of  $142 \text{ ‰} \pm 20$  for the alpha,  $-29 \pm 10 \text{ ‰}$  for the carboxyl, and  $-36 \pm 20 \text{ ‰}$  for the methyl, all relative to VPDB) (Chimiak et al., 2021). In a measurement designed to observe such enrichment, targets may be (1) site-specific observations of the enrichment at the positions of interest or (2) combinatorial isotope effects arising from the differences between carbon composition between multiple positions (e.g., a measurement of  $^{13}\text{C}^{13}\text{C}$  clumping between alpha and carboxyl and/or alpha and methyl carbons; both are  $\approx -7 \text{ ‰}$  for this system, assuming it follows the stochastic assumption) (Mueller et al., 2022b). Here, the  $^{13}\text{C}$  and  $^{13}\text{C}^{13}\text{C}$  data will be most relevant, while  $^{15}\text{N}$ ,  $^2\text{H}$ ,  $^{18}\text{O}$ ,  $^{13}\text{C}^{15}\text{N}$ , or  $^{13}\text{C}^{18}\text{O}$  are less so. In these scenarios, our work demonstrates the full palette of options available for study (such as  $^{13}\text{C}^{13}\text{C}$  clumping at particular positions of a molecule); it does not legislate that all dimensions be studied. Taking advantage of some aspects of high dimensional measurements therefore may be less daunting than it seems, requiring an understanding of only a few previously unobserved targets. Third, we believe that automation will be crucial to the implementation of these techniques. Every step our data processing—the identification of target peaks, optimization of measurement conditions, screening for peak quality, extraction of data, and presentation—is automatable (indeed, publicly available code included with this manuscript accomplishes many of these functions) (Csernica, 2023a). If these steps can be automated and integrated with Orbitrap-IRMS workflows, they can more easily be applied to high dimensional targets. For example, if the software is sufficiently general, a user analyzing alanine could observe the site-specific enrichment, then switch modes to observe  $^{13}\text{C}^{13}\text{C}$  clumping with minimal effort. Current software tools

should consider the diversity of data products available, with an eye towards facilitating high dimensional observations in the future.

#### **4.3.4 Conclusion**

Our high-dimensional observations of the isotome of methionine demonstrate the amount of isotopic information available via current techniques for organic molecules and suggest several avenues for their widespread application. Mass selection and fragmentation via 'M+N' experiments can sample many different subsets of the isotopic forms of a compound, resulting in many unique observations of its isotome. These data can be used directly to define a unique mass spectrometric fingerprint for that sample. Alternatively, it can be used to reconstruct the abundances of individual isotopologues, which may be more effective for interpreting certain isotope effects. Our strategy is immediately applicable to current problems in chemical forensics, where the large number of observations will help distinguish between different versions of the same compound with measurable isotopic structures. Applications in new or poorly understood environments require more theoretical and experimental work to become mature; we expect automation to make these observations more routine, enabling high-dimensional isotomics to contribute to a range of scientific questions.

#### **Acknowledgements**

We thank Cajetan Neubauer, Gabriella Weiss, Elliott Mueller, Guannan Dong, Elise Wilkes, Laura Chimiak, Nivedita Thiagarajan, Sarah Zeichner, and Renée Wang for their helpful discussion on the content of this manuscript. We also thank Fenfang Wu for the assistance with the EA-IRMS measurements. Finally, we thank Max Lloyd, Guannan Dong, Peter Martin, and Sarah Zeichner for their contributions to the data processing scripts used in this article. We additionally thank Huiming Bao and the Orbitrap-MS team at ICIER,

Nanjing University, Shuhei Ono, and one anonymous reviewer for insightful and constructive comments on the content of this manuscript.

This work was supported by the Simons Foundation, Award Number 626103 and DOE-BES funding to JME.



### S4.1. Comments on Shot Noise

#### S.4.1 Derivation of the shot noise formula for M+N relative abundances

Here, we derive eq (3), giving the shot noise limit for M+N relative abundances. We begin from the equation for propagation of error into a function of two variables (Taylor, 1997):

$$\sigma_f^2 = \left(\frac{\partial f}{\partial A}\right)^2 \sigma_A^2 + \left(\frac{\partial f}{\partial B}\right)^2 \sigma_B^2 + 2 \left(\frac{\partial f}{\partial A}\right) \left(\frac{\partial f}{\partial B}\right) \sigma_{AB} \quad (S4.1)$$

where our function is

$$f = \frac{A}{A+B}. \quad (S4.2)$$

Here,  $f$  gives the M+N relative abundance in scan  $i$ ,  $A$  gives the counts of the isotope of interest in that scan, and  $B$  gives the counts of all other isotopes used to calculate that M+N relative abundance. For example, if we observe  $^{13}\text{C}$ ,  $^2\text{H}$ ,  $^{33}\text{S}$ , and Unsub, and report the M+N relative abundance of  $^{13}\text{C}$ , then  $A = n^{13\text{C}}$  and  $B = n^{2\text{H}} + n^{33\text{S}} + n^{\text{Unsub}}$ , where  $n$  is the number of counts for that isotope. Then,  $\sigma_A$ ,  $\sigma_B$ , and  $\sigma_f$  are the respective standard deviations and  $\sigma_{AB}$  the covariance of  $A$  and  $B$ .

We begin by evaluating the derivatives:

$$\frac{\partial f}{\partial A} = \frac{B}{(A+B)^2}; \quad \frac{\partial f}{\partial B} = -\frac{A}{(A+B)^2}. \quad (S4.3)$$

Substituting, we have

$$\sigma_f^2 = \frac{B^2}{(A+B)^4} \sigma_A^2 + \frac{A^2}{(A+B)^4} \sigma_B^2 - \frac{2AB}{(A+B)^4} \sigma_{AB}. \quad (S4.4)$$

Multiply both sides by  $\frac{1}{f^2} = \frac{(A+B)^2}{A^2}$  and rearrange:

$$\frac{\sigma_f^2}{f^2} = \frac{1}{(A+B)^2} * \left( \frac{B^2}{A^2} \sigma_A^2 + \sigma_B^2 - 2 \frac{B}{A} \sigma_{AB} \right). \quad (S4.5)$$

Taking the square root gives:

$$\frac{\sigma_f}{f} = \frac{1}{(A+B)} \sqrt{\left( \frac{B^2}{A^2} \sigma_A^2 + \sigma_B^2 - 2 \frac{B}{A} \sigma_{AB} \right)}. \quad (S4.6)$$

Finally, multiplying the right-hand side by  $\frac{B}{B}$  yields:

$$\frac{\sigma_f}{f} = \frac{B}{(A+B)} \sqrt{\left(\frac{\sigma_A}{A}\right)^2 + \left(\frac{\sigma_B}{B}\right)^2 - 2\frac{B}{A}\sigma_{AB}} \quad (\text{S4.7})$$

and, assuming negligible covariance:

$$\frac{\sigma_f}{f} = \frac{B}{(A+B)} \sqrt{\left(\frac{\sigma_A}{A}\right)^2 + \left(\frac{\sigma_B}{B}\right)^2}. \quad (\text{S4.8})$$

In equation S.8, A, B, and f in S.8 correspond to the expectation values for these quantities in a single scan. We next interpret them in terms of the sum of ions observed across all scans. We write  $\mathcal{N}_A$  for the total number of counts of ion beam A and N for the total number of scans. For the first term, we have:

$$\frac{B}{A+B} = \frac{N}{N} \left( \frac{B}{A+B} \right) = \frac{\mathcal{N}_B}{\mathcal{N}_A + \mathcal{N}_B}. \quad (\text{S4.9})$$

For the second, we note that at the shot noise limit, the mean and variance (e.g.,  $\sigma_A^2$ ) are identical. Therefore

$$\left(\frac{\sigma_A}{A}\right)^2 = \frac{A}{A^2} = \frac{1}{A} \quad (\text{S4.10})$$

and likewise for B. Substituting and pulling out a factor of N, we have:

$$\sqrt{\left(\frac{\sigma_A}{A}\right)^2 + \left(\frac{\sigma_B}{B}\right)^2} = \sqrt{\frac{1}{A} + \frac{1}{B}} = \sqrt{\frac{N}{NA} + \frac{N}{NB}} = \sqrt{N} \sqrt{\frac{1}{\mathcal{N}_A} + \frac{1}{\mathcal{N}_B}}. \quad (\text{S4.11})$$

Putting this together, we obtain:

$$\sigma_{SN} = \frac{\sigma_f}{f\sqrt{N}} = \frac{\mathcal{N}_B}{\mathcal{N}_A + \mathcal{N}_B} \sqrt{\frac{1}{\mathcal{N}_A} + \frac{1}{\mathcal{N}_B}}. \quad (\text{S4.12})$$

An expression for the relative standard error of f in terms of the counts of A and B.

### S4.1.2 Acquisition Error to Shot Noise Ratios

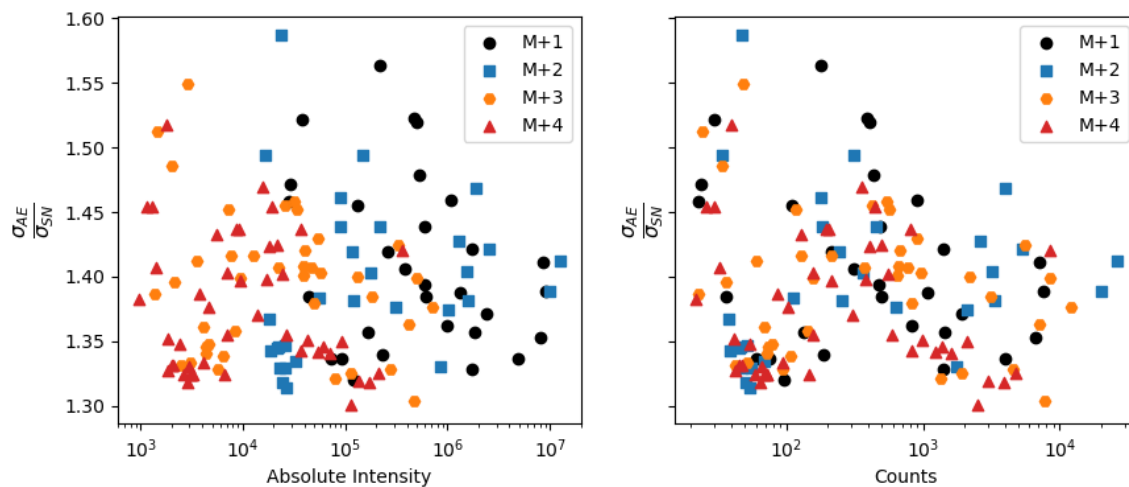


**Figure S4.1:** The observed  $\frac{\sigma_{AE}}{\sigma_{SN}}$  ratios for each peak we report data for vs their corresponding average absolute intensities and average number of counts per scan. Any peaks with values  $>2$  are rejected as having poor data quality, following Eiler et al. 2017.

### S4.1.3 Observed counts per scan vs predicted abundance

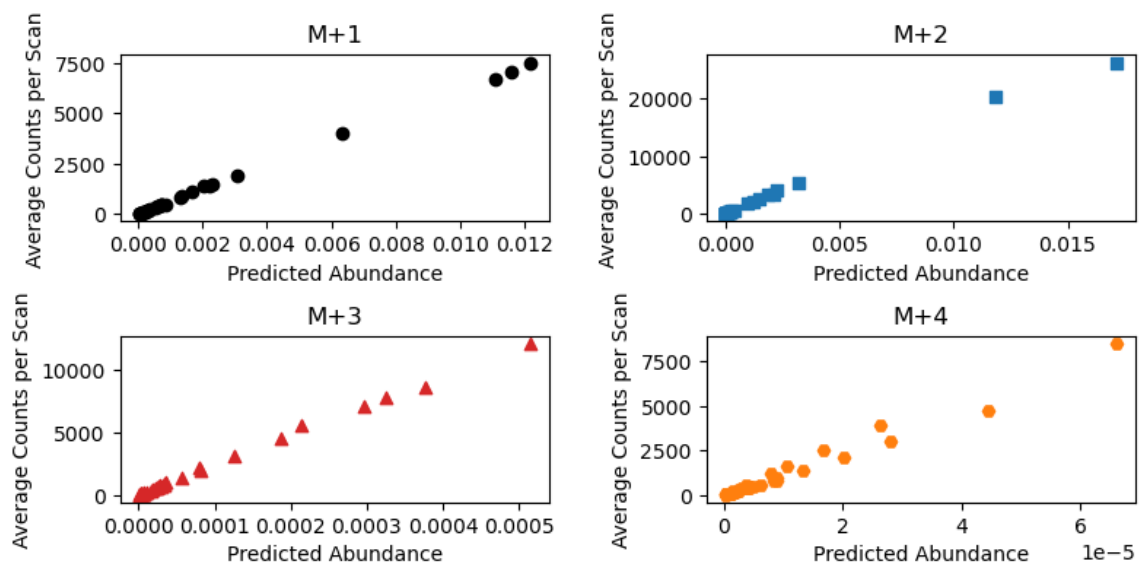


**Figure S4.2:** The average number of counts per scan for each reported peak vs their predicted abundance, calculated via forward model. If nonlinearities like those observed by Eiler et al., 2017 are significant, we would expect logarithmic behavior with increasing intensity. Instead, each experiment plots along a line ( $R^2 > 0.98$  for each experiment), suggesting the response of the Orbitrap in our experiment is roughly linear.

## S4.2 Comparison to the 'With M0' Measurement

In the introduction, we discuss the benefits of the M+N experiments we perform here compared to a 'with M0' experimental strategy which includes the unsubstituted isotopologue; here we quantify some of those benefits.

First, we examine the gains in precision ( $\sigma_{AE}$ ) from the M+1 experiment relative to the with M0 experiment (Figure S4.2A). To do so, we performed a 'with M0' observation of the methionine standard and compared it to the results of a M+1 experiment. For each, we injected a 50  $\mu$ M solution of our methionine standard using a Fusion 101 (Chemyx, Inc.) syringe pump at a flow rate of 10  $\mu$ L/minute; the gas flow settings were sheath gas flow rate = 10 and aux gas flow rate = 0, and otherwise identical to those in the main text. We then performed both a M+1 experiment (following the settings on Table 4.2), and a 'with M0,' which used an isolation mass range of  $150.5 \pm 1$  and was otherwise identical to Table 4.2. We performed a 30 minute acquisition for each experiment. We extracted M+N relative abundances for the M+1 data or corresponding isotope ratios (i.e.,  $^{13}\text{C}/\text{Unsub}$ ) for the with M0 data. In Figure S4.2A, we plot the corresponding precisions for these values in both experiments. Each data point corresponds to an isotope of interest for one of the 8 methionine fragments observed. First, we note that many peaks which we extracted and observed for the M+1 experiment were not observed via the with M0 experiment; this includes all of the  $^{15}\text{N}$  and  $^2\text{H}$  data, and the majority of the  $^{33}\text{S}$ . Second, those isotopes which we do extract for the with M0 experiment have substantially worse precisions than for the M+1 experiment, by a factor of  $\approx 6$ . Because precision scales with the square root of experimental duration, this corresponds to  $\approx 36$  times longer to obtain the same precision using the with M0 strategy.

We note that Figure S4.2A may overstate the benefits of the M+1 experiment somewhat, due to the effects of space-charge effects on the M+1 experimental strategy. Space charge effects such as coalescence are at their worst when there is a small peak closely adjacent to a much larger peak. In a with M0 experiment, the largest peak is M0, which is  $\approx 1$  amu away from the substituted peaks. In contrast, in a M+1 experiment, the

largest peak may be, e.g., a  $^{13}\text{C}$  peak which lies close to other substituted peaks, such as  $^2\text{H}$ . Therefore, M+1 experiments may require lower ion loads for successful measurement, mitigating their advantages somewhat. Both experiments we present here were performed at AGC 2e5. Mueller et al. report with M0 measurements of acetate at AGC = 1e6; if this could be adopted generally, it would lead a factor of  $\approx 5$  time decrease for the with M0. In this case, the M+1 experiment would still be faster by a factor of  $\approx 7$ . However, we note this analysis is general, and may vary case to case.

Second, we examine the range of concentrations of peaks recovered via our with M0 experiment vs our M+N, in Figure S4.2B. Here, each observed peak is plotted vs the concentration of the sum of isotopologues contributing to that peak. Each experiment spans concentrations of  $\approx 2$ -3 orders of magnitude (controlled by the detection limit; see section 3.4). The with M0 experiment is dominated by the unsubstituted peak, preventing observation of peaks with lower concentrations. By shifting to the M+N strategy, we are able to observe peaks with a much lower range of concentrations. For our experiments, we reach concentrations as low as  $10^{-6}$ .

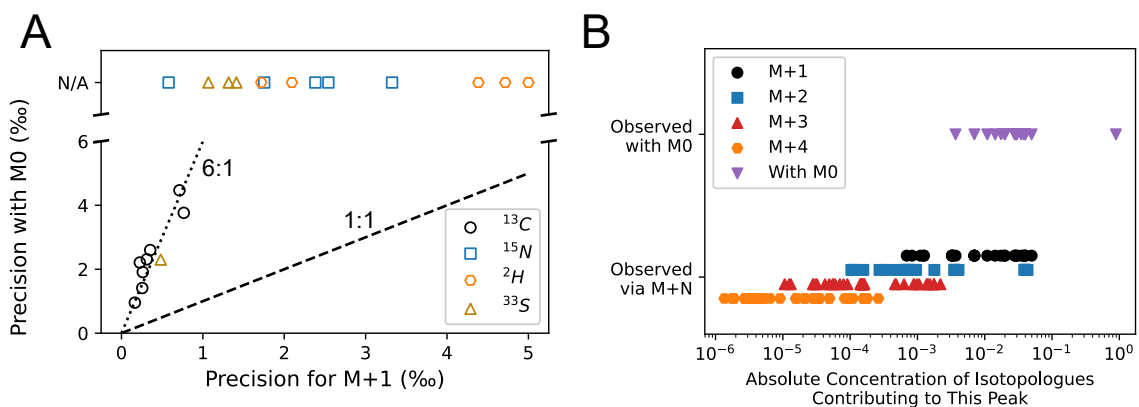


**Figure S4.3:** The benefits of the M+N experimental strategy relative to the with M0 approach. A: A comparison of the precisions (acquisition errors) obtained via the M+1 experiment vs the with M0 experiment. Each marker denotes an observed peak (e.g., the  $^{13}\text{C}$  peak in the 133 fragment). The x-axis gives the recovered precision of the M+N relative abundance of that peak, while the y-axis gives the recovered precision of the isotope ratio (e.g.,  $^{13}\text{C}/\text{Unsub}$ ) associated with that peak. The M+1 experiment allows more peaks to be seen and has precisions which are better by a factor of  $\approx 6$ . B: The absolute concentrations of the isotopologues contributing to each peak of each experiment. Data points are calculated by summing up the concentrations of each isotopologue contributing to each observed peak. Each experiment spans  $\approx 2$ -3 orders of magnitude. The 'with M0' experiment is dominated by the unsubstituted isotopologue (far right). Higher order M+N experiments permit lower abundance peaks to be observed.

### S4.3: Correlation Coefficients Between Isotopologue-Specific Values

In the text, we note that the error bars reported for our isotopologue-specific reconstructions in Figure 4.4 are correlated; in Figure S4.4, we plot the corresponding correlation matrices. For example, if we perform the Monte Carlo algorithm 1000 times, we obtain 1000 values for each isotopologue-specific delta. The mean and standard deviations of these 1000 values for each individual isotopologue are plotted in Figure 4.4. For every pair of isotopologues, A and B, we calculate the Pearson correlation coefficient for the same sets of 1000 values. Negative numbers indicate that two values are negatively correlated; e.g.,  $^{13}\text{C}_{\text{methyl}}$  and  $^{13}\text{C}_{\text{gamma}}$  have a correlation coefficient of -0.88, so higher values of  $^{13}\text{C}_{\text{methyl}}$  correspond to lower values of  $^{13}\text{C}_{\text{gamma}}$ . We here show results for the first sample replicate of each M+N experiment, which are representative.

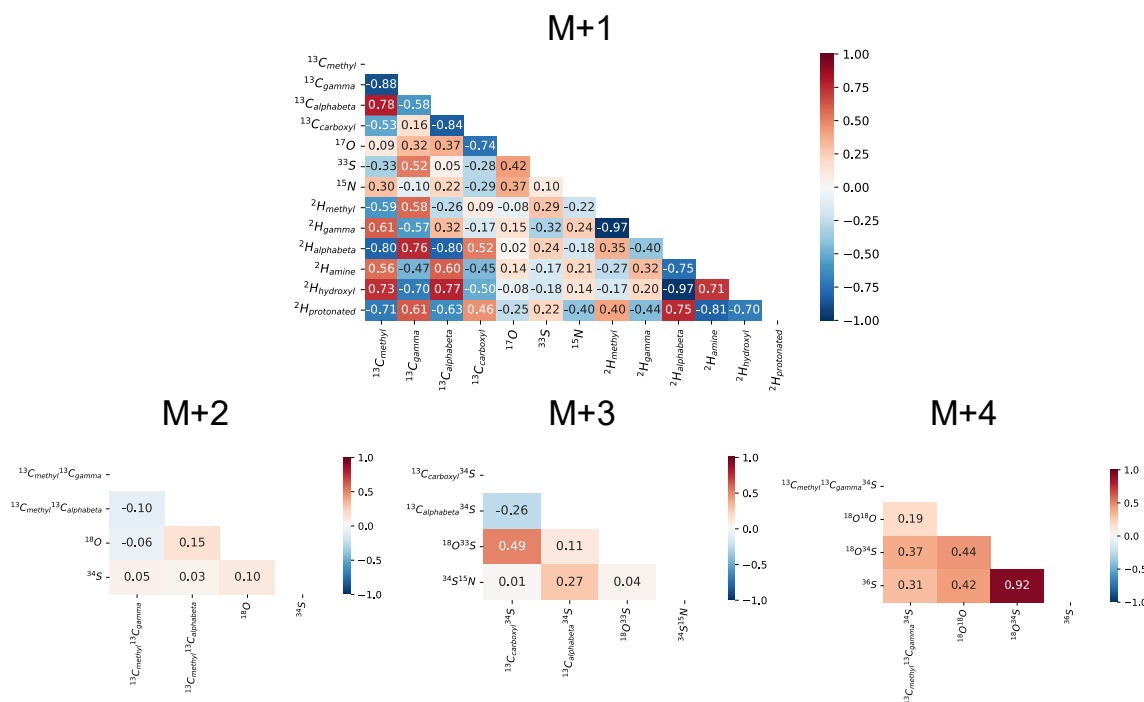


**Figure S4.4:** Correlation coefficients for isotopologue-specific reconstructions for each M+N experiment. Positively correlated values have correlation coefficients > 0 and negatively correlated values have correlation coefficients < 0.

#### S4.4: Calculation of Linear Combinations of Directly Measured Constraints

In the main text, we allude to the possibility of reporting data products consisting of linear combinations of observed constraints. As an example, consider the  $^{13}\text{C}^{13}\text{C}$  substitution observed via the M+2 experiment. We may construct the following matrix consisting of our observations. Here, the columns give individual  $^{13}\text{C}^{13}\text{C}$  substituted isotopologues (computed treating alpha and beta as distinct sites) the column labels give one letter abbreviations for the carbons involved: a = alpha, b = beta, c = carboxyl, g = gamma, m = methyl; e.g., column 'm,g' =  $^{13}\text{C}_{\text{methyl}}^{13}\text{C}_{\text{gamma}}$ . The row labels give the fragment of interest; an isotopologue has a value of 1 if it is observed in that column, and 0 otherwise.

$$\begin{array}{c}
 \begin{array}{ccccccccccc}
 m, g & b, c & a, b & g, c & g, b & g, a & a, c & m, a & m, c & m, b
 \end{array} \\
 \begin{array}{c}
 f_{133} \\
 f_{104} \\
 f_{102} \\
 f_{61} \\
 f_{56}
 \end{array}
 \begin{pmatrix}
 1 & 1 & 1 & 1 & 1 & 1 & 1 & 1 & 1 & 1 \\
 1 & 0 & 1 & 0 & 1 & 1 & 0 & 1 & 0 & 1 \\
 0 & 1 & 1 & 1 & 1 & 1 & 1 & 0 & 0 & 0 \\
 1 & 0 & 0 & 0 & 0 & 0 & 0 & 0 & 0 & 0 \\
 0 & 0 & 1 & 0 & 1 & 1 & 0 & 0 & 0 & 0
 \end{pmatrix}
 \end{array}$$

By inspection, we observe the following:

- 1) Fragment 61 constrains  $^{13}\text{C}_{\text{methyl}}^{13}\text{C}_{\text{gamma}}$  uniquely.
- 2)  $^{13}\text{C}_{\text{methyl}}^{13}\text{C}_{\text{alpha}} + ^{13}\text{C}_{\text{methyl}}^{13}\text{C}_{\text{beta}}$  may be computed from  $f_{104} - f_{61} - f_{56}$ .
- 3)  $^{13}\text{C}_{\text{methyl}}^{13}\text{C}_{\text{carboxyl}}$  may be calculated via  $f_{133} - f_{104} - f_{102} + f_{56}$  (note we did not observe  $f_{133,^{13}\text{C}^{13}\text{C}}$ , and so do not report this isotopologue).
- 4)  $^{13}\text{C}_{\text{carboxyl}}^{13}\text{C}_{\text{alpha}} + ^{13}\text{C}_{\text{carboxyl}}^{13}\text{C}_{\text{beta}} + ^{13}\text{C}_{\text{carboxyl}}^{13}\text{C}_{\text{gamma}}$  may be calculated via  $f_{102} - f_{56}$ .
- 5)  $^{13}\text{C}_{\text{alpha}}^{13}\text{C}_{\text{beta}} + ^{13}\text{C}_{\text{alpha}}^{13}\text{C}_{\text{gamma}} + ^{13}\text{C}_{\text{beta}}^{13}\text{C}_{\text{gamma}}$  is directly obtained via  $f_{56}$ .

Determining how and which data products to report is challenging, because 1) one must decide which linear combinations (perhaps those involving less than a certain number of isotopologues?) are most important and 2) have a method for computing such linear combinations. Regarding (2), while the Gauss-Jordan reduction employed will reveal all



uniquely constrained isotopologues, it will not necessarily find all linear combinations of interest.

Nevertheless, we can report many linear combinations; in Figure S4.5, we present an analogous Figure to Figure 4.5, showing the proportion of isotopologues which may be reported either individually or as combinations of small numbers of isotopologues for each M+N experiment, assuming a perfect measurement. The results here were calculated for fragments 133, 104, 102, 61, and 56, and defining separate sites for the alpha and beta carbons and hydrogens. Rather than performing a single Gauss-Jordan reduction on the entire matrix, we pulled out submatrices for each substitution, performed a GJ-elimination on these, and compiled all of the linear combinations consisting of individual isotopologues or groups of 2, 3, or 4 isotopologues (e.g.,  $^{13}\text{C}_{\text{carboxyl}}^{13}\text{C}_{\text{alpha}} + ^{13}\text{C}_{\text{carboxyl}}^{13}\text{C}_{\text{beta}} + ^{13}\text{C}_{\text{carboxyl}}^{13}\text{C}_{\text{gamma}}$  is a group of 3). We found applying GJ elimination to these submatrices found more such combinations than GJ elimination of the entire matrix. In the M+1 case, we observe 11 of a total 15 isotopologues individually, and two sets ( $\text{C}_{\text{alpha}} + \text{C}_{\text{beta}}$  and  $\text{H}_{\text{alpha}} + \text{H}_{\text{beta}}$ ) as sums of two isotopologues. For the M+2 experiment, many (almost half) of isotopologues are constrained in such small groups, while for M+3 and M+4, the results primarily consist of more complex data products.

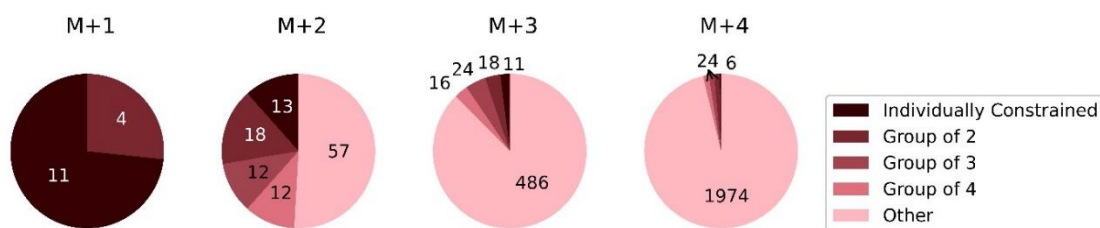


**Figure S4.5:** Sets of isotopologues constrained via a M+N dataset which observes all possible ion beams, treating the alpha and beta sites as distinct. The number of isotopologues which we constrain individually (analogous to those shown in Figure 4.5) are plotted as dark wedges; then, there are successive wedges for groups of small numbers of isotopologues (e.g.,  $^{13}\text{C}_{\text{carboxyl}}^{13}\text{C}_{\text{alpha}} + ^{13}\text{C}_{\text{carboxyl}}^{13}\text{C}_{\text{beta}} + ^{13}\text{C}_{\text{carboxyl}}^{13}\text{C}_{\text{gamma}}$  is a group of 3).

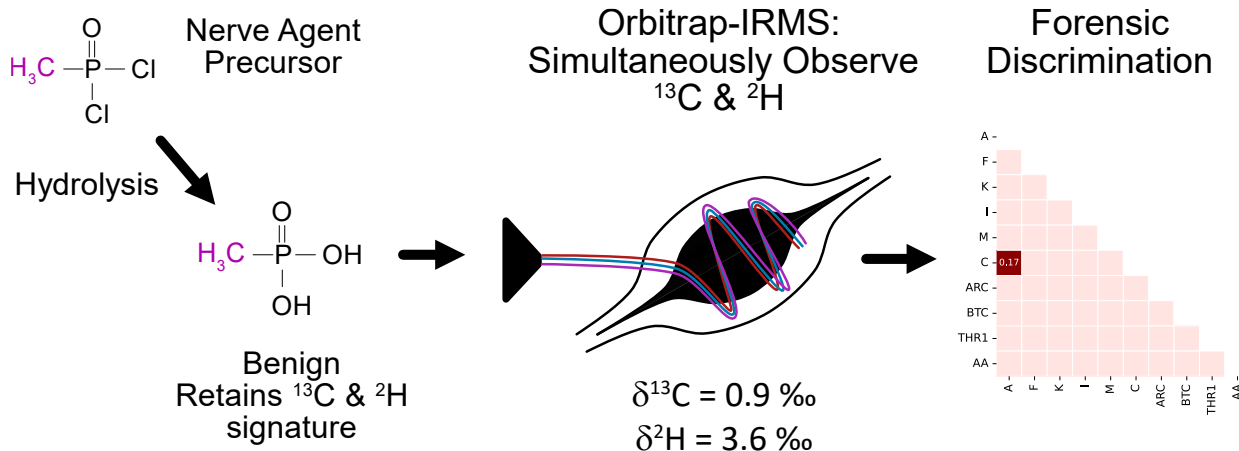
*Chapter 5*SIMULTANEOUS OBSERVATION OF  $^2\text{H}$  AND  $^{13}\text{C}$  ENRICHMENT OF METHYL PHOSPHONIC ACID VIA ORBITRAP-IRMS WITH APPLICATIONS TO NERVE AGENT FORENSICS

Under review as Csernica, T., Moran, J. J., Fraga, C. G., and Eiler, J. M. Simultaneous observation of  $^2\text{H}$  and  $^{13}\text{C}$  enrichment of methyl phosphonic acid via Orbitrap-IRMS with applications to nerve agent forensics.

**Abstract**

Quantification of the stable isotopes within a compound aids forensic investigations as it provides a fingerprint which can determine that compound's source substrates, synthetic route, and possible mechanisms of degradation. Previous stable isotope studies have explored  $^{13}\text{C}$  and  $^2\text{H}$  measurements of the sarin gas precursors methylphosphonic dichloride (DC) and methylphosphonic difluoride (DF) as forensic signatures. However, these measurements required different sample preparations and measurement techniques. Orbitrap-IRMS is a developing technique which can characterize multiple stable isotopes simultaneously. Here, we apply Orbitrap-IRMS to simultaneously observe the  $^{13}\text{C}$  and  $^2\text{H}$  content of methylphosphonic acid (MPA), the hydrolysis product of DC and DF, which can be used as a proxy for the isotopic content of DC and DF. Our method requires twenty minute analyses and consumes  $\approx 60$  nmol of sample, with precisions of  $\approx 0.9$  ‰ ( $^{13}\text{C}$ ) and  $\approx 3.6$  ‰ ( $^2\text{H}$ ). We apply our method to both commercially acquired MPA and MPA obtained from the hydrolysis of commercially acquired DC. We validate our methods via comparison to elemental-analyzer isotope ratio mass spectrometry (EA-IRMS). The combined  $^{13}\text{C}$  and  $^2\text{H}$  measurement creates a more robust forensic tool than either isotope individually. Our results demonstrate the viability of Orbitrap-IRMS for chemical forensic measurements.

## Graphical Abstract



## 5.1 Introduction

Sarin is a highly toxic, odorless, and colorless liquid, and has been prepared for use as a chemical weapon since its discovery in 1938. The use of sarin has been confirmed on several occasions, including during the Iran-Iraq War, in the Tokyo subway attacks in 1995, and during the Syrian Civil War (Black et al., 1994; Okumura et al., 1996, Anon, 2017). In the Syrian case, sarin is believed to have been deployed as a binary weapon; here, methyl phosphonic difluoride (DF) and isopropanol (IPA) (in addition to additives, such as hexamine) are loaded into two separate compartments of the same munition, and the two are mixed either just before or after firing (Smart, 1997; Pita and Domingo, 2014, Anon, 2017). Large stockpiles of precursor compounds have been discovered, including 581 metric tons of DF in Syria in 2014 (Anon, 2014). DF can in turn be synthesized from methyl phosphonic dichloride (DC); this synthetic route was employed to create the sarin used in Tokyo, and has also been performed by the United States (Tu, 2007; Danzig et al., 2012; U.S. Army, 2016). Because of the danger posed by these weapons, it is important to be able to trace the origins of sarin, DF, and DC, which will help identify the groups creating these compounds and their synthetic methods.

There are several techniques used to determine the origins of chemical weapons, depending on the accessibility of both the synthesis site and the weapons themselves. In

some cases, as in the Tokyo attacks, access to the production site and descriptions of the synthesis from the perpetrators were available (Tu, 2007). More commonly, investigators will only have access to an attack site, and will rely on environmental samples, attempting to observe decomposition products or other compounds of interest (e.g., additives used in a synthesis) (Secretary-General, 2013; Pita and Domingo, 2014). Such techniques can be complemented by measurements of the 'impurity profile' of a compound, or contaminants which are a byproduct of (but not directly implicated in) its synthesis (Hoggard et al., 2010; Fraga et al., 2011; Höjer Holmgren et al., 2021; Lu et al., 2021b). Beyond these, the abundances of stable isotopes of a compound (e.g.,  $^{13}\text{C}$ ,  $^{15}\text{N}$ , or  $^2\text{H}$ ) can be indicative of both the synthetic route and specific reagent stocks (i.e., batches) used (Benson et al., 2006; Lock and Meier-Augenstein, 2008; Howa et al., 2014; Gentile et al., 2015; Chesson et al., 2016; Moran et al., 2018; Vanninen et al., 2020; Lu et al., 2021a; Meier, 2023). Stable isotopes are an appealing tool because the stable isotope content of a compound can be inherited by its degradation products (possibly modulated by predictable isotope effects associated with degradation) (Howa et al., 2014; Moran et al., 2018; Lu et al., 2021a; Meier, 2023).

While there are many synthetic routes for sarin production, common to these pathways is the conservation of a methyl group transferred from DC to DF to the final sarin product. The isotopic content of this methyl group will reflect that in DC and is typically derived from industrial methanol. The synthetic route used for commercial DC production (Hoggard et al., 2010; Fraga et al., 2010), similar to that used to produce the sarin used in the Tokyo subway attack (Tu, 2007), is depicted in Figure 5.1. It begins with the production of trimethyl phosphite (TMP) and methyl chloride. The methyl group of each likely comes from industrial methanol (some methyl chloride is also produced from methane, but this is less common than methanol) (Holbrook, 2003; Rossberg et al., 2006; Moran et al., 2018). These compounds then react to form DMMP via a Michaelis-Arbuzov reaction (Bhattacharya and Thyagarajan, 1981; Kostoudi and Pampalakis, 2022). The reaction of TMP and methyl chloride has been studied previously and found to have a kinetic isotope effect which lowers the  $^{13}\text{C}$  content of DMMP relative to the methanol source (Eiler et al., 2014).

The methyl group of DMMP comes from methyl chloride, but during the reaction it is possible for the methyl group of TMP to regenerate  $\text{CH}_3\text{Cl}$ , and so the product DMMP (and therefore DC) may sample both pools (Figure 5.1, inset) (Moran et al., 2018).

Both the carbon and hydrogen isotope composition of the methyl group have been characterized, albeit by separate techniques. Meier characterized the hydrogen isotope ratios of DC, DF, and sarin via a site-specific natural isotopic fractionation by nuclear magnetic resonance (SNIF-NMR) technique. They found only small differences between the  $^2\text{H}$  content of DC stocks from different suppliers ( $\approx 20$  ‰) with precisions of  $\approx 5$ -15 ‰ (calculations of ‰ from ppm our own), and determined there was no significant difference in the  $^2\text{H}$  content of DC and DF synthesized from that DC via  $\text{NaF/SbF}_3$  (Meier, 2023). Separately, two of us have developed a method for observing the  $^{13}\text{C}$  content of DC and DF (Moran et al., 2018). Our method first hydrolyzes these compounds to the relatively benign methyl phosphonic acid (MPA) (Figure 5.1). MPA is then observed via elemental analysis-isotope ratio mass spectrometry (EA-IRMS), with precisions of 0.1-0.5 ‰. In that study, we discovered the existence of three distinct clusters of commercial DC based on  $\delta^{13}\text{C}$  content. The SNIF-NMR technique uses  $\approx 1$  mmol of each analyte, while the EA-IRMS method requires  $\approx 1$   $\mu\text{mol}$ . These techniques require different sample preparations and measure two different compounds.

Orbitrap isotope ratio mass spectrometry (Orbitrap-IRMS) is a rapidly growing technique, with the capability to simultaneously observe multiple rare isotopes (e.g.,  $^{13}\text{C}$  and  $^2\text{H}$ ) of target compounds, and may be an effective method for chemical forensics (Eiler et al., 2017). It has been applied to a range of compounds, such as amino acids, oxyanions, and metal oxides, and can characterize rare isotopes including  $^{13}\text{C}$ ,  $^{15}\text{N}$ ,  $^2\text{H}$ ,  $^{34}\text{S}$ ,  $^{37}\text{Cl}$ ,  $^{86}\text{Sr}$ , and  $^{87}\text{Sr}$ , among others (Neubauer et al., 2018, 2020; Chimiak et al., 2021; Bills et al., 2021; Hilker et al., 2021; Wilkes et al., 2022; Mueller et al., 2022a; Zeichner et al., 2022; Weiss et al., 2023). Orbitrap-IRMS is particularly appealing due to the high mass resolution (as high as  $\frac{\Delta M}{M} \approx 2 \times 10^6$  has been demonstrated) (Denisov et al., 2021), small sample requirements (as small as tens of pmols), (Zeichner et al., 2022) and the flexibility of isotopic targets,

including many multiply-substituted (or “clumped”) isotopologues (Neubauer et al., 2020; Hilkert et al., 2021). Moreover, it can be interfaced with liquid or gas chromatography and applied to the study of molecular fragments, allowing compound- and position-specific isotope measurements (Chimiak et al., 2021; Zeichner et al., 2022; Weiss et al., 2023).

In this study, we apply Orbitrap-IRMS to simultaneously observe the  $^{13}\text{C}$  and  $^2\text{H}$  content of MPA. Our method is applicable to small sample sizes ( $\approx 60$  nmol) with minimal sample preparation and yields precisions of  $\approx 0.9$  ‰ ( $^{13}\text{C}$ ) and  $\approx 3.6$  ‰ ( $^2\text{H}$ ). We apply this technique to six MPA samples obtained via the hydrolysis of DC and previously analyzed by Moran et al., as well as four commercially available MPA samples (Moran et al., 2018). We compare our results to observations of  $\delta^{13}\text{C}$  and  $\delta^2\text{H}$  via traditional EA-IRMS. We find that the  $^2\text{H}$  data provides meaningful additional information for distinguishing hydrolyzed DC samples. Our results suggest that Orbitrap-IRMS is an effective tool for the forensic analysis of DC and DF and should be considered more broadly as a technique for chemical forensics.

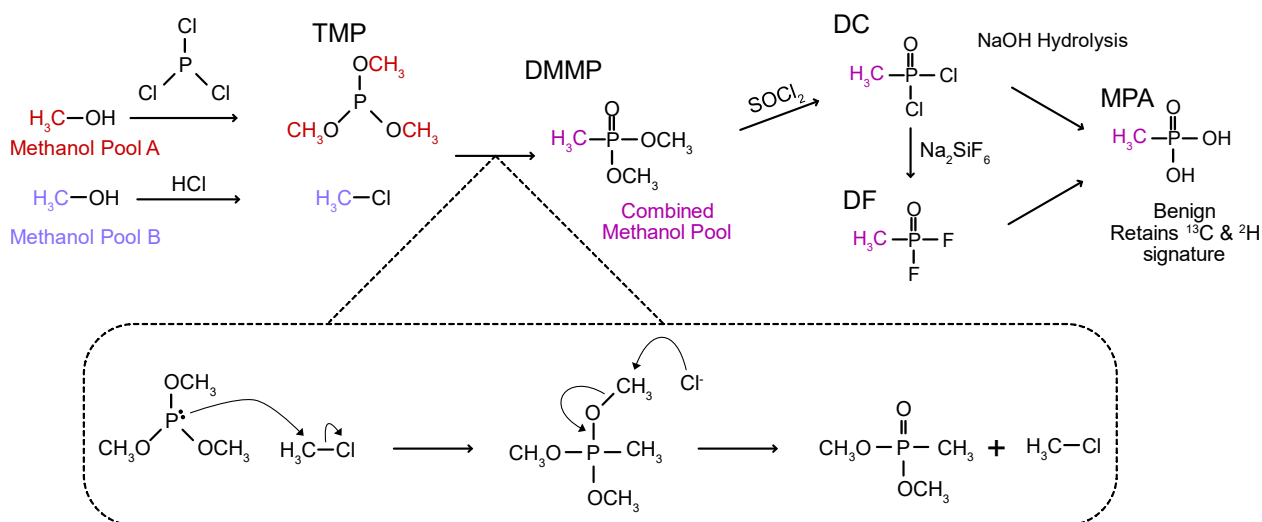


**Figure 5.1:** A depiction of the compounds of interest in our study (adapted from (Moran et al., 2018)). Two potential methanol sources affect the final composition of the methyl group of MPA. Methanol pool A is used to generate trimethyl phosphite (TMP) while pool B is used to generate methyl chloride; the two react to form dimethyl phosphonate (DMMP), the source of commercial DC. In the reaction of methyl chloride and TMP, the methoxy carbons may regenerate methyl chloride (see inset). This methyl chloride can also react with TMP, causing DMMP to sample a combination of pools A and B. The methyl group present in DMMP is then sampled in DC, DF, and MPA.

## 5.2 Materials & Methods

### 5.2.1 Methyl Phosphonic Acid Samples

We acquired five methyl phosphonic acid samples from commercial suppliers, all >98% purity, from the following sources: 1) SIG = Sigma Aldrich (Source: MKCL9585); 2) BTC = Beantown Chemical (Lot 50010821); 3) ARC = Arcos Organics (Lot A0405505); 4) THR1 = Thermo Fischer Scientific (Lot 10227190); 5) THR2 = Thermo Fischer Scientific (via Alfa Aesar) (Lot 10219934) (Table 5.1). We adopted the SIG sample as our in-house standard.

We additionally analyzed six methyl phosphonic acid samples which have previously been measured for  $\delta^{13}\text{C}_{\text{VPDB}}$  by two of us, detailed in Moran et al., 2018 (Table 5.1) (Moran et al., 2018). These samples were made by hydrolyzing commercially acquired DC stocks using 9.1% NaOH. In the previous publication, they were given identifiers A, F, K, I, M, and C, and are referred to by the same name here. Each of these six samples consisted of approximately 53 % NaCl, 44 % MPA, and 3% NaOH, by weight percent. The concentration of MPA in solutions made from these stocks is not precisely known, as the amount of MPA may vary if the sample composition differed from our estimates (e.g., had a larger amount of NaOH). Therefore, we report their concentrations as  $\mu\text{g}/\text{mL}$  of the combined sample, and give the approximate concentration of MPA in parentheses, e.g., “a solution of 150  $\mu\text{g}/\text{mL}$  (est. 50  $\mu\text{M}$  MPA).”

**Table 5.1: MPA Sources**

DC Samples				
	Method	Manufacture Location	Manufacture Date	Analysis Date (if manufacturing date not available)
A	DC Hydrolysis	Canada	June 2004	---
F	DC Hydrolysis	USA	December 2007	---
K	DC Hydrolysis	USA	August 2012	---
I	DC Hydrolysis	UK	May 2007	---
M	DC Hydrolysis	---	---	---
C	DC Hydrolysis	USA	June 2004	---

MPA Samples				
	Method	Manufacture Location	Manufacture Date	Analysis Date (if manufacturing date not available)
SIG	Proprietary	Milwaukee WI, USA	April 16, 2020	---
ARC	Proprietary	France	---	Feb 11, 2019
BTC <sup>a</sup>	Proprietary	France	---	---
THR1	Proprietary	France	---	March 26, 2020
THR2 <sup>b</sup>	Proprietary	France	---	Feb 7, 2019

a: Bean Town Chemical acquired this sample from a separate manufacturer.

b: Ordered from Alfa Aesar, which was acquired by Thermo Fischer in 2015.

### 5.2.2 Other Chemicals

Sodium chloride (>99%) and formic acid were acquired from Fischer Scientific.

### 5.2.3 EA-IRMS analysis- $\delta^{13}C$

We analyzed the  $\delta^{13}C_{VPDB}$  content of both our MPA samples and standards using an EA IsoLink combustion elemental analyzer system interfaced to a Delta V Plus isotope ratio mass spectrometer (EA-IRMS, Thermo Fischer Scientific). For this system, samples are prepared by weighing an appropriate amount of material ( $\approx 20 \mu\text{g}$  carbon) into tin capsules, combusting these at 1020 °C using tungsten oxide as an oxidizer and performing carrier-gas isotope ratio mass spectrometry on the resulting CO<sub>2</sub>. Our reporting of these results on the VPDB scale was calibrated by comparison to in-house standards; these were: (1) methionine (nominally -33.52 ‰ vs VPDB); (2) Glycine (-45.72 ‰ vs VPDB); (3) glucose (-10.99 ‰ vs VPDB).

### 5.2.4 EA-IRMS analysis- $\delta^2H$

The  $\delta^2H_{VSMOW}$  content of our MPA samples was analyzed by the Center for Stable Isotopes (CSI) at the University of New Mexico (UNM) using the protocols described by Sharp et al. (Sharp et al., 2001). The CSI analysis used Temperature Conversion IRMS, using



a Thermo Fisher Scientific TC-EA device, coupled to a Thermo Fisher Scientific Delta V Plus isotope ratio mass spectrometer via a ConFlo IV interface. Samples were prepared by weighing material corresponding to  $\approx 10$   $\mu\text{g}$  of hydrogen in silver capsules. These then experienced high-temperature reduction at 1400  $^{\circ}\text{C}$ , and the resulting  $\text{H}_2$  gas was measured for  $\delta^2\text{H}$  values. The results were calibrated vs the VSMOW scale using the following international standards: V-SMOW (0 ‰), GISP (-189.7 ‰), NBS22 (-117.2 ‰), and USGS 77 (-75.9 ‰). V-SMOW, GISP and NBS22 standards were purchased pre-packed in silver tubes from USGS Reston Stable Isotope Laboratory.

#### *5.2.5 Orbitrap-IRMS: Analytes and TIC Effects*

Methylphosphonic acid was dissolved in a solution of 50/50 acetonitrile (LC-MS grade, Sigma Aldrich) and ultrapure water (Milli-Q IQ 7000 Purification) with 0.1 % formic acid (Sigma Aldrich) by volume. For the commercial samples, we used 150  $\mu\text{M}$  of both sample and standard.

Each of our hydrolyzed samples includes a significant and possibly variable amount of both NaCl and MPA. We therefore explored the effect of both concentration and NaCl content on recovered isotope ratios. We found that the presence of NaCl suppresses ionization of MPA, resulting in lower observed total ion currents (TIC). Simultaneously, greater concentrations of MPA lead to greater TICs. Observed isotope ratios vary with TIC, regardless of whether it is a salt or concentration effect. We found that if TICs of sample and standard differed from one another by  $<1\text{e}7$ , or  $\approx 10\%$  for a typical acquisition, they did not induce errors beyond our measurement precisions (specifically, a linear fit to our calibration causes an error of 0.8 ‰ for  $^{13}\text{C}$  and 1.9 ‰ for  $^2\text{H}$  for a TIC difference of  $1\text{e}7$ ). Therefore, when measuring the hydrolyzed samples, we began with concentrations of  $\approx 15$   $\mu\text{g}/\text{mL}$  (samples;  $\approx 70$   $\mu\text{M}$  of MPA, assuming  $\approx 44\%$  of each sample is MPA) and  $\approx 70$   $\mu\text{M}$  of standard and modified concentrations of each to balance observed total ion currents (TIC). For all hydrolyzed samples, our mean sample and standard TICs were within  $1\text{e}7$ , except for

MPA M where the difference was  $1.3e7$ . We provide a detailed discussion of these issues in the supplement (section S.1).

#### *5.2.6 Orbitrap-IRMS: Standardization*

Our Orbitrap-IRMS measurements make use of sample-standard bracketing. Isotope ratios observed via Orbitrap-IRMS will be biased away from the true isotope ratio due to various processes which preferentially select for one isotope versus another throughout the measurement process (e.g., during ionization, transmission, or observation) (Eiler et al., 2017). We collectively refer to the isotope ratio changes associated with these processes as ‘instrumental fractionation.’ We assume that observations of the same compound at the same instrumental conditions and at similar times (i.e., directly before or after one another) will experience similar instrumental fractionations, so by comparing our sample observations to a standard observed by the same methods, equipment and instrument conditions directly before or after, we can determine the sample isotope enrichment relative to the standard (Eiler et al., 2017). We therefore alternate observations of our samples with an in-house standard (SIG), and compute results relative to that standard. Each observation consists of a sequence of acquisitions: ‘Standard/Sample/Standard/Sample/Standard/Sample/Standard.’ Each acquisition has a duration of 20 minutes, for  $\approx 140$  minutes for the entire sequence. We standardize by performing a linear fit to all 4 standards (vs their acquisition numbers) and calculate the enrichment of the samples relative to this fit (see *Orbitrap-IRMS: Calculation of Results and Error Measures*, below).

#### *5.2.7 Orbitrap-IRMS: Introduction and Observation*

Our experimental conditions are summarized in Table 5.2; we here provide more detail regarding the operation of Orbitrap-IRMS and parameters of interest.

Samples were injected from a Fusion 101 (Chemyx Inc.) syringe pump using a 500  $\mu\text{L}$  syringe (Hamilton Robotics) to a Q Exactive HF mass spectrometer (Thermo Fischer

Scientific) via a HESI-II Probe (Thermo Fischer Scientific). Our analyses used a flow rate of 20  $\mu\text{L}/\text{minute}$  with a 32-gauge needle insert to the HESI-II Probe. The HESI-II probe generates ions via electrospray ionization which may then be introduced to the mass spectrometer. We operated in negative mode and produced the anion  $\text{CH}_4\text{O}_3\text{P}^-$ .

After being generated, ions are filtered using an Advanced Quadrupole Selector (AQS) system which permits only ions with a target range of masses ('scan range'). Setting a narrow scan range to remove contaminants is necessary for reproducible isotope ratio measurements, as the presence of large contaminant peaks (generally, totaling >20% of the intensity of the monoisotopic peak of the sample compound) result in instrumental biases which prevent accurate sample standard comparison (Hofmann et al., 2020). We use a scan range of 92.5-99.5  $m/z$  for all acquisitions except those associated with MPA C. In MPA C, we observed a contaminant around  $m/z = 92.925$  with a height of  $\approx 20\%$  of the unsubstituted peak. We therefore used a scan range of 93.5-99.5 for all acquisitions (sample and standard) associated with MPA C.

Following the AQS, the ions are injected to and observed in the Orbitrap. These observations take place as a series of microscans, where each microscan is a discrete observation of the current (or transient) induced by a packet of ions. Applying a Fourier transform to this transient results in the reported spectrum. Several transients can be coadded prior to applying the Fourier transform, which increases the signal of low abundance peaks by the square root of the number of microscans. The resulting spectrum obtained via Fourier transform is called a scan. Here, we acquired scans consisting of 10 each microscans to aid observation of the low abundance  $^2\text{H}$  peak (Eiler et al., 2017; Bills et al., 2021).

For our observations, Orbitrap-IRMS accuracy and precision is primarily a function of the automatic gain control target (AGC target) and the mass resolution, both of which limit the number of ions that can be observed in a fixed period of time. The AGC target determines the amount of charge permitted into the Orbitrap for each scan. The amount of charge in each scan must be roughly constant, as variations in the number of ions

observed per scan will change the instrumental biases in the isotope ratios of interest and lead to uncontrolled variations in measured isotope ratios (Eiler et al., 2017; Hofmann et al., 2020). Additionally, permitting too many ions into the Orbitrap results in deleterious space-charge effects, such as ‘coalescence,’ causing close-lying peaks to merge and suppressing the intensity of low abundance peaks; the AGC target must be sufficiently low to minimize these effects (Eiler et al., 2017; Hofmann et al., 2020). The mass resolution is determined by the duration of each scan and increases with higher scan lengths. It is set via a single number, giving the nominal resolution at  $m/z = 200$ , but experimental resolution scales as  $\left(\frac{m}{z}\right)^{-\frac{1}{2}}$ , and so is better than the setpoint by a factor of  $\approx\sqrt{2}$  for the peaks we observe. Here, we use an AGC target of  $5e5$  and a resolution setpoint of 120,000 (sufficient to resolve  $^{13}\text{C}$  and  $^{17}\text{O}$  at the masses of interest). We observe five isotopologues:  $^{12}\text{C}^1\text{H}_4^{16}\text{O}_3^{31}\text{P}^-$ ,  $^{13}\text{C}^1\text{H}_4^{16}\text{O}_3^{31}\text{P}^-$ ,  $^{12}\text{C}^2\text{H}_1^1\text{H}_3^{16}\text{O}_3^{31}\text{P}^-$ ,  $^{12}\text{C}^1\text{H}_4^{17}\text{O}_1^{16}\text{O}_2^{31}\text{P}^-$ , and  $^{12}\text{C}^1\text{H}_4^{18}\text{O}_1^{16}\text{O}_2^{31}\text{P}^-$ ; we refer to these as ‘Unsub’ (unsubstituted),  $^{13}\text{C}$ ,  $^2\text{H}$ ,  $^{17}\text{O}$ , and  $^{18}\text{O}$ , respectively.

**Table 5.2: Experimental Conditions**

Measurement Duration (minutes)	20
Typical $\sigma_{\text{AE}}$ : $^{13}\text{C}$ (‰)	0.7
Typical $\sigma_{\text{AE}}$ : $^2\text{H}$ (‰)	3.3
Concentration	Variable <sup>a</sup>
Solvent	50/50 Acetonitrile/Water
Additive	0.1 % Formic Acid
Flow Rate ( $\mu\text{L}/\text{minute}$ )	20
Needle	High Flow
Scan range ( $m/z$ )	92.5-99.5 <sup>b</sup>
Resolution at 200 $m/z$ $\left(\frac{\Delta M}{M}\right)$	120,000
Microscans (#)	10
AGC Target (unitless)	$5e5$
Max IT time (ms)	1000
Polarity ( $\pm$ )	(-)
Sheath gas flow rate (arbitrary)	5
Aux gas flow rate (arbitrary)	0
Sweep gas flow rate (arbitrary)	0
Spray voltage (kV)	3.00
Capillary temp ( $^{\circ}\text{C}$ )	320

S-lens RF level (arbitrary)	50
Aux gas heater temp (°C)	0
Sample Consumption (nmol)	≈60

a: see 'Analytes and TIC effects'

b: except MPA C, which used 93.5-99.5 (see introduction and observation)

### 5.2.8 Orbitrap-IRMS: Data Analysis

Ion intensities were extracted from instrument-generated RAW files using FTStatistic, a proprietary software provided by Thermo Fischer Scientific. For each scan, ion intensities and noise were extracted for each identified isotopic peak (Unsub, <sup>13</sup>C, <sup>2</sup>H, <sup>17</sup>O, and <sup>18</sup>O), and the associated ion counts were calculated via

$$N_{IO} = \frac{S}{N} * \frac{C_N}{z} * \left(\frac{R_N}{R}\right)^{\frac{1}{2}} * \mu^{\frac{1}{2}}. \quad (5.1)$$

Here,  $N_{IO}$  is the number of observed ions per scan,  $S$  is the ion intensity,  $N$  is the peak noise,  $C_N$  is an empirical constant measured by Denisov and Makarov and here taken to be 4.4,  $z$  is the charge (1 in all cases presented here),  $R_N$  is a reference resolution used in the experiment which determined  $C_N$  and equal to 120,000,  $R$  is the mass resolution actually defined for the measurement in question, and  $\mu$  is the number of microscans (Eiler et al., 2017).

### 5.2.9 Orbitrap-IRMS: Calculation of Results and Error Measures

We use the obtained  $N_{IO}$  to calculate results as follows. First, for an individual acquisition of a given isotope ratio  $i$ , we calculate isotope ratio for each scan,  $j$ , and present the average isotope ratio across all  $N$  scans:

$$R^i = \frac{1}{N} \sum_{j=1}^N R_j^i = \frac{1}{N} \sum_{j=1}^N \frac{N_{IO,j}(\text{isotope } i)}{N_{IO,j}(\text{unsubstituted isotopologue})}. \quad (5.2)$$

We also present the acquisition error,  $\sigma_{AE}$ , for this ratio as the standard error of  $R_j^i$  across all  $N$  scans:

$$\sigma_{AE} = \frac{STDEV(R_j^i)}{\sqrt{N}}. \quad (5.3)$$

This error is given in per mil (‰).

Next, for each sample acquisition, we compute the enrichment of each isotope ratio relative to the standards, as a delta value. To do so, we take a linear fit of each of the recorded isotope ratios for the standard as functions of order in the sample-standard bracketing sequence, use that fitted line to predict the standard ratio at the timepoint where the sample was observed, and then standardize to this prediction. That is, we report:

$$\delta_{STD}^i = 1000 * \left( \frac{R_{SMP}^i}{R_{STD,pred}^i} - 1 \right). \quad (5.4)$$

We also compute the associated confidence interval for our predicted standard ratio,  $\sigma_{STD,CI}$ . We use this to calculate a ‘propagated acquisition error,’ giving the error on that single sample acquisition:

$$\sigma_{PAE} = \sqrt{\sigma_{AE}^2 + \sigma_{STD,CI}^2}. \quad (5.5)$$

We present the average of all three delta values,  $\delta_{STD,AVG}^i$  as a one number summary. If we reject any sample files (see ‘data quality tests’) we do not calculate an associated  $\delta_{STD}^i$  value, and our  $\delta_{STD,AVG}^i$  will reflect only two acquisitions. If we reject any standard files, we do not use those values in our linear regression.

Finally, we calculate the error of the entire method, or ‘methodological reproducibility’ ( $\sigma_{MR}$ ), as follows. First, we compile the residuals ( $\delta_{STD}^i - \delta_{STD,AVG}^i$ ) for each replicate. Then, we report  $\sigma_{MR}$  as the standard deviation of all residuals for each isotope ratio ( $^{13}\text{C}$ ,  $^2\text{H}$ ). These residuals do not significantly differ from a normal distribution ( $n = 29$ ,  $p = 0.28$  for carbon,  $n = 29$ ,  $p = 0.81$  for hydrogen, using the Shapiro-Wilkes test implemented in the scipy.stats python package). We report  $\sigma_{MR} = 0.9$  for  $^{13}\text{C}$  and  $\sigma_{MR} = 3.6$  for  $^2\text{H}$ , similar to our average  $\sigma_{PAE}$  (0.9 for  $^{13}\text{C}$ , 3.9 for  $^2\text{H}$ ). When combining results of  $n$  measurements, we report the according standard errors for that number of acquisitions, i.e.,  $\frac{\sigma_{MR}}{\sqrt{n}}$ . In most cases (unless we reject a sample measurement), we have three sample measurements, and so report errors of 0.5 ‰ ( $^{13}\text{C}$ ) and 2.1 ‰ ( $^2\text{H}$ ) across the measurement

sequence (although we note there is a possibility for tic effects beyond this range for  $^{13}\text{C}$ ; see *Orbitrap-IRMS: Analyte and TIC effects*).

Our Orbitrap-IRMS results show a scale compression relative to the EA-IRMS data; we therefore perform a linear correction for this effect (see *Results & Discussion*). In all cases, this correction does not influence our interpretation.

#### 5.2.10 Orbitrap-IRMS: Data Quality Tests

We performed four tests to ensure data quality. First, we evaluate the stability of ion loading into the Orbitrap across a measurement; as we note above (in “Introduction and Observation”), the number of ions must be tightly controlled for reproducible isotope ratio measurement. The target amount of charge per scan is set by the AGC target, and recorded as TIC\*IT, the product of TIC (the total ion current) and IT (the injection time, or the amount of time required to accumulate ions for that scan). For a typical observation, TIC\*IT has a relative standard deviation of <5%. We reject any observation with a TIC\*IT value having a relative standard deviation of >10%. Second, we evaluate the  $\frac{\sigma_{AE}}{\sigma_{SN}}$  or ‘acquisition error to shot noise’ ratio for each recovered isotope ratio. The shot noise limit represents the maximum precision (i.e., smallest uncertainty) we could have obtained for that measurement under the approximation of the number of ions we observed:

$$\sigma_{SN} = \sqrt{\frac{1}{\sum_{j=1}^N N_{IO,j} (\text{isotope } i)} + \frac{1}{\sum_{j=1}^N N_{IO,j} (\text{unsub})}}. \quad (5.6)$$

Previous work has suggested that  $\frac{\sigma_{AE}}{\sigma_{SN}}$  ratios >2 are diagnostic of poor quality data, so we reject any such data (Eiler et al., 2017). Third, we check the number of ‘zero scans’ in each acquisition, where a ‘zero scan’ is defined as a scan where a peak of interest (e.g., the  $^2\text{H}$  bearing ion beam) is not detected (e.g., due to low abundance). We reject data with any zero scans present. Finally, we check the ‘internal stability’ of each isotope ratio within an acquisition to evaluate the presence of intra-measurement drift, using a z-score method described previously (Csernica et al., 2023).

Our dataset includes 66 total acquisitions. For the  $^{13}\text{C}/\text{Unsub}$  and  $^2\text{H}/\text{Unsub}$  data we reject 2 which fail our TIC\*IT test. However, a total of 8 acquisitions of  $^{18}\text{O}/\text{Unsub}$  and 7 acquisitions of  $^{17}\text{O}/\text{Unsub}$  fail at least one test, mainly due to internal stability (if only the oxygen data failed this test, we treated the  $^{13}\text{C}/\text{Unsub}$  and  $^2\text{H}/\text{Unsub}$  data as normal). This lack of stability may be due to oxygen isotope exchange during the ionization process, which has been observed previously (Kostyukevich et al., 2015). We also note that two of the three oxygens in the hydrolyzed samples come from the hydrolyzed step. While the third may contain useful information, more work would need to be done to verify it does not exchange at any point. We found these analytical problems and uncertainties in interpretation sufficiently large to not interrogate the oxygen isotope results in detail.

#### 5.2.11 Forensic Discrimination

We attempted to discriminate between samples by performing pairwise ANOVA tests (using *scipy.stats.f\_oneway*) between each pair of samples using the values from the 3 sample replicates. We performed these tests for both  $^{13}\text{C}$  and  $^2\text{H}$  data individually using  $p < 0.05$  as a threshold. We also evaluated using both variables together, combining results from both  $^{13}\text{C}$  and  $^2\text{H}$  and using  $p < 0.025$  to avoid the multiple comparisons problem (a Bonferonni correction). In this case, if either variable distinguished the samples at  $p < 0.025$ , we consider them forensically resolved.

#### 5.2.12 Data and Figure Availability

Our observed .RAW files from Orbitrap-IRMS measurements are available on the Caltech data repository (T. Csernica, 2024). Our data processing code and scripts to generate all figures except Fig 1 are available on a zenodo repository (Csernica, 2024). In some cases, the outputs of these scripts were modified using Affinity Designer. Figure 5.1 was created using Affinity Designer.



## 5.3 Results & Discussion

### 5.3.1 Recovered Isotopic Values

First, we show representative results (from sample ‘A’) from our  $^{13}\text{C}$  and  $^2\text{H}$  observations via Orbitrap-IRMS (Figure 5.2). Each sample observation was made in triplicate, each of which was bracketed by two standard measurements, and so yields a series of acquisitions that includes 7 distinct observations of each isotopologue; these observed values are plotted on the left of Figure 5.2 ( $^{13}\text{C}/\text{Unsub}$  error bars are smaller than the size of the points). We then standardize and propagate error via bracketing (see “Data Analysis”) and report the enrichment of each sample versus the standards. In this case, our reported error bars are ‘propagated acquisition errors’ ( $\sigma_{\text{PAE}}$ ). Finally, we report the average of all three acquisitions and estimated standard errors (methodological reproducibilities divided by the square root of the number of acquisitions, here  $\frac{\sigma_{\text{MR}}}{\sqrt{3}}$ ).

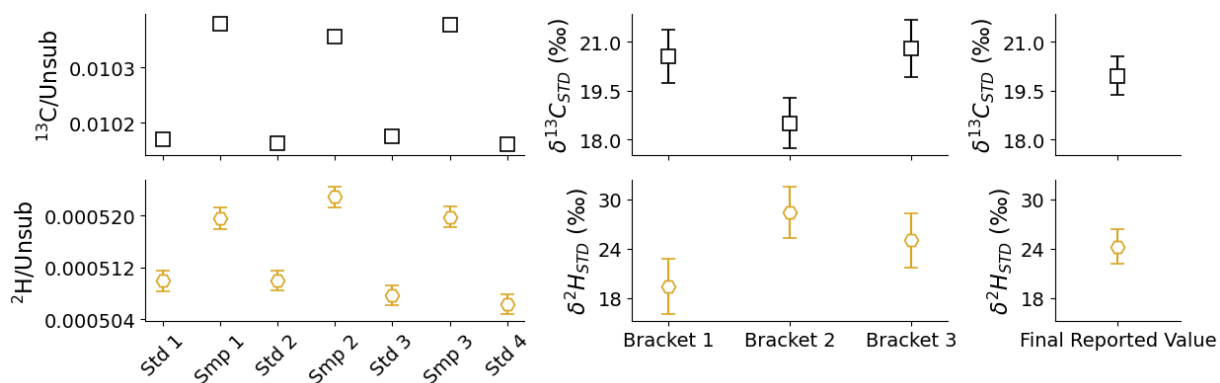


**Figure 5.2:** Representative results from an Orbitrap-IRMS measurement. Left: The raw observed isotope ratio of each sample/standard. If error bars are not shown, they are smaller than the size of the points. Center: Standardized isotope ratios for each sample replicate and associated  $\sigma_{\text{PAE}}$  values. Right: Mean of the three standardized isotope ratios and associated standard error estimates.

We next compare our results for  $^{13}\text{C}$  and  $^2\text{H}$  versus the values recovered from established EA-IRMS techniques (Figure 5.3). We note that EA-IRMS and Orbitrap-IRMS measure subtly different information and discuss each isotope individually.

First, we examine the  $^{13}\text{C}$  results. Here, the EA-IRMS measures the total  $^{13}\text{C}/^{12}\text{C}$  ratio of all carbon present in each sample. In contrast, Orbitrap-IRMS measures the ratio between the  $^{13}\text{C}$  substituted and  $^{12}\text{C}$  anions of MPA ( $^{13}\text{C}^1\text{H}_4^{16}\text{O}_3^{31}\text{P}^- / ^{12}\text{C}^1\text{H}_4^{16}\text{O}_3^{31}\text{P}^-$ ). We

interpret each measurement as giving the  $\frac{^{13}\text{C}}{^{12}\text{C}}$  ratio of the sample, making the approximation  $\frac{^{13}\text{C}^1\text{H}_4^{16}\text{O}_3^{31}\text{P}^-}{^{12}\text{C}^1\text{H}_4^{16}\text{O}_3^{31}\text{P}^-} \approx \frac{^{13}\text{C}}{^{12}\text{C}}$ . This assumption holds exactly assuming a stochastic distribution of clumped isotopologues, and causes minor errors (<0.1 ‰) for clumped isotope anomalies (i.e., departures from random proportions of multiply substituted isotopologues) of <10 ‰ (Csernica and Eiler, 2023).

The  $^2\text{H}$  data require a more involved interpretation, because there is a greater difference between the observable quantities in the two measurements. Here, the TC-EA-IRMS pyrolyzes the sample and measures the D/H ratio of the resulting  $\text{H}_2$ , which includes all hydrogen in the sample (3 methyl hydrogen, 2 hydroxyl, contributions from NaOH for the hydrolyzed samples, and any additional hydrogen, such as from residual water). In contrast, Orbitrap-IRMS observes the isotopologue ratio  $^{12}\text{C}^2\text{H}_1^1\text{H}_3^{16}\text{O}_3^{31}\text{P}^- / ^{12}\text{C}^1\text{H}_4^{16}\text{O}_3^{31}\text{P}^-$ , including only four hydrogens (3 methyl hydrogen, 1 hydroxyl). In both cases, only the D content of the methyl group is of forensic value. The hydroxyl hydrogen likely equilibrates with an environmental pool (e.g., solvents; atmospheric water vapor) and so is expected to have a similar isotope composition for both sample and standard, assuming the two are handled in the same ways using the same reagents and in the same environments. For the Orbitrap-IRMS measurement, the environmental pool is the polar solvent used to dissolve both sample and standard. For the TC-EA-IRMS measurement, this is the water vapor in the sample storage and laboratory environments (atmospheric moisture in New Mexico when the samples were analyzed in August 2023). Additionally, our results from the TC-EA-IRMS are reported relative to VSMOW, while those from Orbitrap-IRMS are reported relative to our in-house SIG standard.

We have addressed these issues in the following way. First, we chose to report our  $^2\text{H}$  results for both TC-EA-IRMS and Orbitrap-IRMS relative to the SIG standard, rather than vs VSMOW. Doing so puts our results in a common reference frame, without requiring assumptions about the composition of a putative equilibrated pool of hydroxyl hydrogens, as would be necessary to report Orbitrap-IRMS results vs VSMOW. Second, we chose to

report all  $^2\text{H}$  results as the enrichment of the methyl group only, as this is the quantity we are most interested in. To do so, we applied a scaling constant to each measurement, with a value of 5/3 for the EA-IRMS (scaling a measurement of 5 hydrogens to 3 hydrogens) and 4/3 for the Orbitrap-IRMS (scaling a measurement of 4 hydrogens to 3 hydrogens). For example, for the Orbitrap-IRMS data, we report  $\delta_{methyl,SIG}^{2H} = \frac{4}{3} * \delta_{Orbitrap,SIG}^{2H}$ , where  $\delta_{Orbitrap,SIG}^{2H}$  is the observed value from the Orbitrap measurement. We comment that the precise value of these scaling constants may differ based on the D content of the equilibrating pool. If, for example, the solvent pool in the Orbitrap measurement, and thus the hydroxyl hydrogen, had no deuterium, the sample standard comparison would be uncompromised; i.e.,  $\delta_{methyl,SIG}^{2H} \approx \delta_{Orbitrap,SIG}^{2H}$ . Conversely, if the solvent pool were pure deuterium, then changes in  $\delta_{methyl,SIG}^{2H}$  would result in very small observed differences in  $\delta_{Orbitrap,SIG}^{2H}$ . Similar issues exist for interpreting EA-IRMS data. However, assuming natural abundances of the equilibrating pools, the differences will be slight and not affect our ability to distinguish between samples; therefore, we neglect this issue in the analysis presented in the main text and reserve a more detailed and quantitative discussion of this problem for the supplement.

Our results are plotted in Figure 5.3. We observe a scale compression for the Orbitrap-IRMS data relative to the EA-IRMS data for both  $^{13}\text{C}$  and  $^2\text{H}$ . Similar scale compressions have been observed previously for Orbitrap-IRMS, and can be addressed via a linear correction (Hilkert et al., 2021). For each set of results, we plot our best fit line ( $R^2 = 0.992$  for  $^{13}\text{C}$ , 0.997 for  $^2\text{H}$ ) and give RMSD values (2.45 ‰ for  $^{13}\text{C}$  and 20.54 ‰ for  $^2\text{H}$ ). Despite the presence of the scale compressions, our precisions are sufficient to reveal the range of natural abundance variation in our samples.

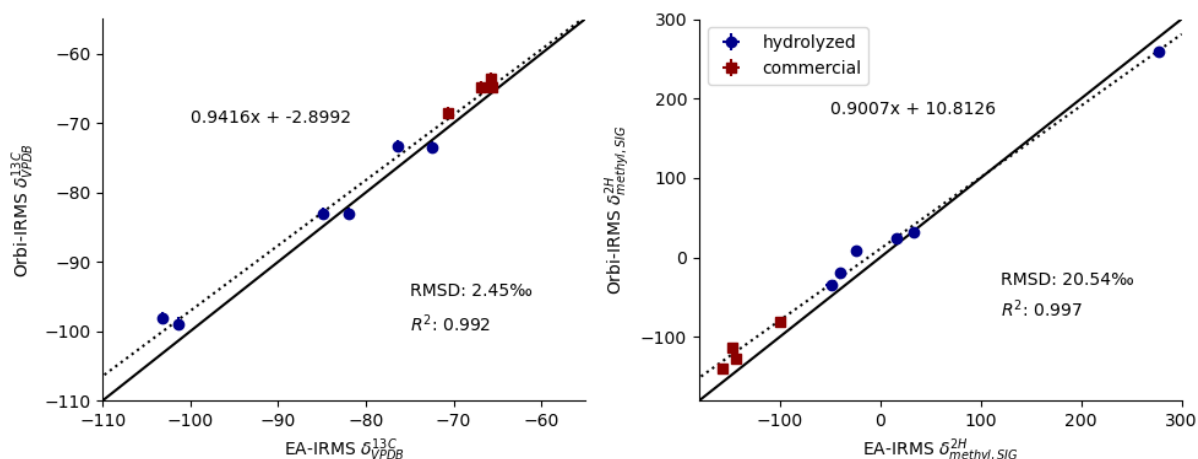


**Figure 5.3:** Linearity of our recovered  $^{13}\text{C}$  and  $^2\text{H}$  values, obtained via EA-IRMS or Orbitrap-IRMS. In both cases, we observe a scale compression for the Orbitrap-IRMS measurement. Our linearity results show  $R^2$  values of 0.992 ( $^{13}\text{C}$ ) and 0.997 ( $^2\text{H}$ ). RMSD values are calculated between the EA-IRMS and Orbitrap-IRMS results. Dotted lines represent our linear fits, while the solid black line is the 1:1 line.

### 5.3.2 Interpretation of $\delta$ Values

We next explore our observed isotopic enrichment, via a crossplot of our Orbitrap-IRMS results, corrected for scale compression, for  $\text{d}^{13}\text{C}$  and  $\text{d}^2\text{H}$  (Figure 5.4). We additionally show our result for the SIG standard; note that we did not recover an independent Orbitrap-IRMS  $\delta^{13}\text{C}_{\text{VPDB}}$  value for this sample, and the plotted  $\text{d}^{13}\text{C}$  value comes from EA-IRMS. We compare these to a range of literature values for the isotopic content of our precursors, industrial methanol and methyl chloride, compiled in Table 5.3; we note the final precursor value will represent some mixture of these two pools (Figure 5.1). To place this hydrogen result in the  $\delta^2\text{H}_{\text{methyl,SIG}}$  reference frame used in our plot, we must approximate the value of  $\delta^2\text{H}_{\text{methyl,VSMOW}}$  for our SIG sample. For this sample, our TC-EA-IRMS measurement found a value of  $\delta^2\text{H}_{\text{VSMOW}} = -159.4 \pm 2.6$  ‰. Assuming the two hydroxyl hydrogens in this MPA sample equilibrated with New Mexico air in August, previously measured to have  $\delta^2\text{H}_{\text{VSMOW}} = -120 \pm 20$  ‰ (Strong, 2012), and assuming no equilibrium fractionation between these groups and water vapor (but see Wang et al. (Wang et al., 2009)), we calculate  $\delta^2\text{H}_{\text{methyl,VSMOW}} \approx -185 \pm 15$  ‰ for our SIG sample. With this constraint, our precursors have a range of  $\delta^{13}\text{C}_{\text{VPDB}} \approx -25$  to  $-60$  ‰,  $\delta^2\text{H}_{\text{VSMOW}} \approx -100$  to  $-180$  ‰, and  $\delta^2\text{H}_{\text{methyl,SIG}}$  of  $\approx -10$  to  $130$  ‰. We indicate this precursor range with a red box in Figure 5.4.

In Figure 5.4, we also examine possible isotope effects on the synthetic routes to MPA. We assume the synthetic route shown in Figure 5.1 for the hydrolyzed samples. However, specific information about the commercially acquired MPA samples was proprietary. Shao et al. claim MPA is generally prepared from DMMP by chlorination and hydrolysis, (i.e., also following Figure 5.1), but do not provide a citation to support this suggestion (Shao et al., 2015). Alternatively, Toy et al. have published a method for producing MPA via hydrolysis of chloromethyl phosphonic dichloride ( $\text{ClCH}_2\text{PCl}_2$ ), which was itself made from chloromethyl phosphonic dichloride ( $\text{ClCH}_2\text{POCl}_2$ ); the authors do not report a synthesis for  $\text{ClCH}_2\text{POCl}_2$  (Uhing et al., 1961; Toy et al., 1963). We choose to analyze only the route in Figure 5.1 in detail, but note alternative routes may be used for the commercial MPA.

The key step along this pathway is the Michaelis-Arbuzov reaction used to synthesize DMMP from TMP and methyl chloride, shown in the Figure 5.1 inset. This has previously been observed to have a carbon isotope effect of  $\approx -38\text{‰}$  at the methyl carbon, although full details of this measurement were not provided (Eiler et al., 2014). To our knowledge, no hydrogen isotope measurements exist for either this specific reaction or for Michaelis-Arbuzov reactions more generally. The literature for Michaelis-Arbuzov reactions suggest a  $\text{S}_{\text{N}}2$  mechanism for both steps (Bhattacharya and Thyagarajan, 1981; Kostoudi and Pampalakis, 2022), while a previous study of TMP and methyl iodide suggests the first step is rate determining (Mccortney, 1986). Studies of  $\text{S}_{\text{N}}2$  reactions with methyl chloride using other nucleophiles suggest an inverse ( $\frac{k_{\text{H}}}{k_{\text{D}}} < 1$ , where  $k_{\text{H}}$  and  $k_{\text{D}}$  are the rate constants for methyl chloride with hydrogen or deuterium) isotope effect on the order of  $\approx 100\text{‰}$  (Poirier et al., 1994; Westaway, 2007). However, there is the possibility that the phosphonium intermediate could be stabilized by hyperconjugation via the C-H bond of the methyl group (Barbosa et al., 2005), leading to a normal ( $\frac{k_{\text{H}}}{k_{\text{D}}} > 1$ ) stable isotope effect, also on the order of  $\approx 100\text{‰}$  (Anslyn and Dougherty, 2006). We do not offer a specific hypothesis and suggest that more robust measurement of both the carbon and deuterium isotope

effects in this reaction are a good target for future study. Later steps do not directly involve the methyl group, and we hypothesize no isotope effects after the synthesis of DMMP. We comment that the previous studies did not observe significant isotope effects for several reactions on related compounds that did not involve the methyl group, including for  $^{13}\text{C}$  during the hydrolysis of DC or DF to MPA (Moran et al., 2018) and for  $^2\text{H}$  during the reaction of DC to DF, DF to sarin, and DC to di-isopropyl methylphosphonate (Meier, 2023).

With this context, we next examine the observed isotopic values. Our results are generally  $\delta^{13}\text{C}$  and  $\delta^2\text{H}$ -deplete relative to the industrial materials, consistent with  $\delta^{13}\text{C}$  fractionation during the formation of DMMP and a normal  $^2\text{H}$  kinetic isotope effect (KIE). For the hydrolyzed DC samples, we find a range of  $\approx 80$  ‰ in  $\delta^2\text{H}_{\text{methyl,SIG}}$ , plus an outlier enriched by  $\approx 250$  ‰ compared to the others; this range is much larger than the 20 ‰ variation in the  $^2\text{H}$  of 6 commercial DC samples observed by Meier (Meier, 2023). The pairs M&K and A&C, with similar  $^{13}\text{C}$ , also have similar  $^2\text{H}$  content, while samples F&I, which also have similar  $^{13}\text{C}$ , are clearly distinguished by their  $^2\text{H}$  enrichment. Three of our commercial samples (THR, THR2, and BTC) are similar in both  $\delta^{13}\text{C}_{\text{VPDB}}$  and  $\delta^2\text{H}_{\text{methyl,SIG}}$ . ARC also has similar values but is clearly distinct from this group. In contrast, our SIG standard differs substantially from the remaining commercial samples, appearing more similar to hydrolyzed samples M and K.

Previously, Moran et al. found the three clusters of  $\delta^{13}\text{C}$  content in the hydrolyzed samples were correlated with manufacture date (F&I, A&C, M&K; see Table 5.1) (Moran et al., 2018). They hypothesized that this was because all of the DMMP used to synthesize those DC samples came from the same manufacturer, who cycled through precursor pools (methanol, TMP, methyl chloride) with distinct isotopic content (Hoggard et al., 2010; Fraga et al., 2010; Moran et al., 2018). If this were the case, and as we assume no significant isotope effects following the production of DMMP, we anticipate  $\delta^2\text{H}$  would vary in a similar manner. Of the hydrolyzed samples with similar  $\delta^{13}\text{C}$  content, samples A&C also have similar  $\delta^2\text{H}$  content; while the manufacture date of M is not known, its  $\delta^2\text{H}$  content is similar to sample K, supporting this hypothesis. However, samples F&I show a  $\approx 300$  ‰ difference

in  $\delta^2\text{H}$ , despite a similar date of manufacture and  $\delta^{13}\text{C}$  content. The higher  $^2\text{H}$  content of MPA F is consistent with a DMMP synthesis with an inverse KIE; however, given that the DMMP likely originated from the same source, and that no other DMMP samples show this enrichment, we find this explanation unlikely (Moran et al., 2018). If we assume F&I began with similar isotopic content, there may have been a process encountered by sample F to enrich  $\delta^2\text{H}$  while leaving  $\delta^{13}\text{C}$  unchanged. For example, there may be an exchange process for the methyl hydrogen in DMMP or DC via tautomerization of the phosphoryl group, which occurs under conditions encountered only by precursors to MPA F (Mastryukova and Kabachnik, 1991; Schimmelmann et al., 2006; Janesko et al., 2015). Future work should explore the possibility of exchange to aid interpretation of  $^2\text{H}$  signatures.

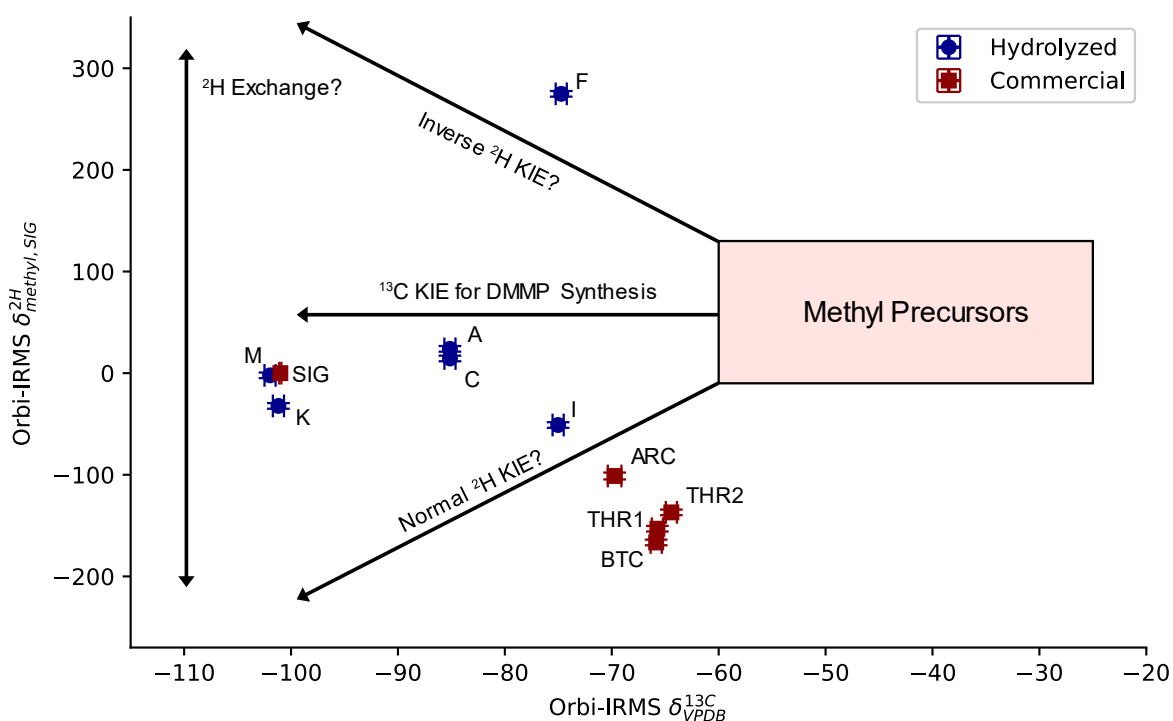


**Figure 5.4:** A crossplot of our observed  $\delta^2\text{H}$  &  $\delta^{13}\text{C}$  values. The  $\delta^2\text{H}$  data are given as our computed composition for the methyl hydrogen relative to our sigma standard (all 5 hydrogens of this standard had an enrichment of  $\delta^2\text{H}_{\text{VSMOW}} = -159.4 \pm 2.6$ ), while the  $\delta^{13}\text{C}$  data are given relative to VPDB. We additionally plot the sigma standard for reference; in this case, we use the  $\delta^{13}\text{C}$  data from EA-IRMS and stipulate  $\delta^{2\text{H}}_{\text{methyl,SIG}} = 0$ . Plausible precursor (MeOH,  $\text{CH}_3\text{Cl}$ ) values for  $^{13}\text{C}$  and  $^2\text{H}$  are indicated in the box. The Michaelis-Abruzov reaction used to synthesize DMMP has been studied previously and observed to have a substantial  $^{13}\text{C}$  KIE; the  $^2\text{H}$  KIE has not been studied, and could be either inverse or normal.

**Table 5.3: Isotopic Composition of Source Compounds**

	$\delta^{13}\text{C}_{\text{VPDB}}$ (‰)	$\delta^2\text{H}_{\text{VSMOW}}$ (‰)	Reference
<b>MeOH</b>	$-25.40 \pm 0.3$	-167 to -170	(Lloyd et al., 2021)
<b>MeOH</b>	-46.2	-	(Londry et al., 2008)
<b>MeOH</b>	38.9 to -39.9	-	(Krzycki et al., 1987)
<b>MeOH</b>	-41.1 to -43.0	-	(Tagami and Uchida, 2008)
<b>CH<sub>3</sub>Cl</b>	-	$-117.1 \pm 4.7$	(Greule et al., 2012)
<b>CH<sub>3</sub>Cl</b>	-58.03 -58.77	-	(Holt et al., 1997)
<b>CH<sub>3</sub>Cl</b>	$-32.84 \pm 0.06$	$-140.1 \pm 1.0$	(Keppler et al., 2020; Hartmann et al., 2023)
<b>CH<sub>3</sub>Cl</b>	$-45 \pm 15^a$	$-127 \pm 20^a$	(Hartmann et al., 2023)

a: These data are mean and standard deviation of two industrial CH<sub>3</sub>Cl standards.

### 5.3.3 Efficacy of Chemical Forensics

Finally, we examine the efficacy of our methods for forensic discrimination of the sources of MPA samples. In Figure 5.5, we present the results of pairwise ANOVA comparisons between each set of three sample replicates (again, corrected for scale compression). We first show the results for  $\delta^{13}\text{C}_{\text{STD}}$  and  $\delta^2\text{H}_{\text{STD}}$ , testing the null hypothesis that they were drawn from the same distribution at a significance level of  $p < 0.05$ . We then show results for the combined tests, testing at a significance level of  $p < 0.025$  to avoid the multiple comparisons problem (a Bonferroni correction). We depict a pairwise comparison in dark red and write the p-value if we fail to reject the null hypothesis. For the combined test, we show the lower of the two p-values. We find that  $\delta^2\text{H}$  is significantly better than  $\delta^{13}\text{C}$  at distinguishing samples; the  $\delta^2\text{H}$  fail to reject the null hypothesis for two pairs, while the  $\delta^{13}\text{C}$  fail for six. The combined test offers a minor improvement to the  $\delta^2\text{H}$ , enabling discrimination between samples K&I. While the  $\delta^2\text{H}$  data are sufficient to distinguish most of our dataset, we note the  $\delta^{13}\text{C}$  adds important contextual information—for example, samples F&I span the entire range of  $\delta^2\text{H}$ , but their similarity in  $\delta^{13}\text{C}$  (and manufacture date) suggests a link between the two which would not be revealed by  $\delta^2\text{H}$  alone. We conclude



that the combined measurement gives us additional power to interpret the origins of these samples compared to either technique individually.

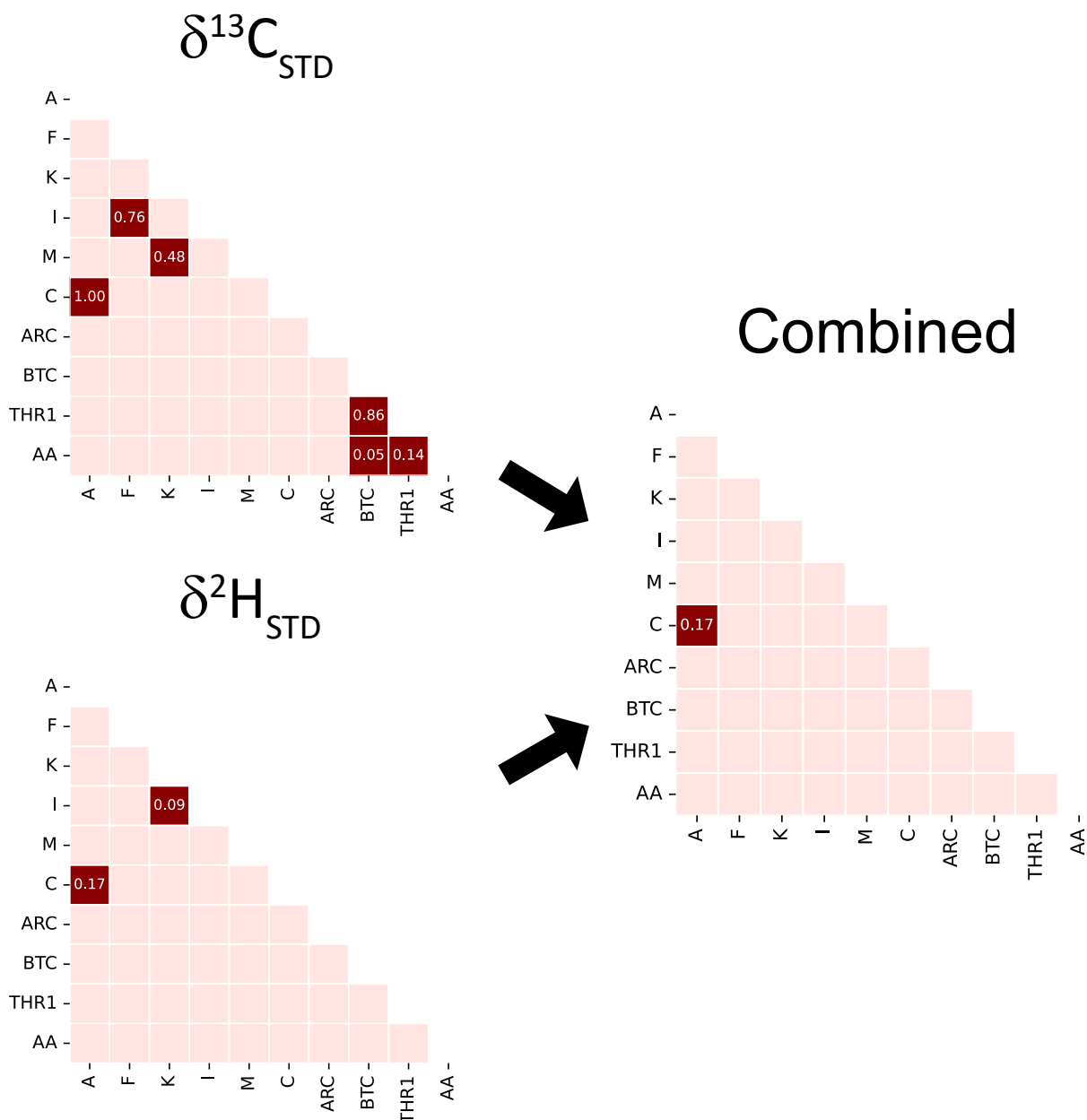


**Figure 5.5:** Using isotopic data as a chemical forensics tool. Replicates from each sample are compared pairwise with all other samples using ANOVA. Samples that significantly differ from each other for either  $\text{d}^{13}\text{C}$ ,  $\text{d}^2\text{H}$ , or both, are filled in with their p values indicated. We use a threshold of  $p < 0.05$  for each variable individually, and a Bonferroni corrected  $p < 0.025$  for their combination. Using  $\text{d}^{13}\text{C}$  alone fails to distinguish between 6 samples, while  $\text{d}^2\text{H}$  fails to distinguish only 2. The combined diagnostic distinguishes all samples except A & C.

#### 5.3.4 Comparison between Orbitrap-IRMS, EA-IRMS, and SNIF-NMR

Thus far, three different techniques have been demonstrated to measure the stable isotopes of compounds related to sarin. Compared to Orbitrap-IRMS, SNIF-NMR requires larger sample sizes (Meier uses mmol) (Meier, 2023), and has only been applied to  $^2\text{H}$ . However, this technique can achieve similar precisions to Orbitrap-IRMS and can observe site-specific content without any chemical manipulation. Either EA-IRMS or Orbitrap-IRMS can observe both  $^{13}\text{C}$  and  $^2\text{H}$ . Orbitrap-IRMS observes  $^{13}\text{C}$  and  $^2\text{H}$  simultaneously, while EA-IRMS must make separate measurements; moreover, the sample consumption for Orbitrap-IRMS ( $\approx 60$  nmol) is significantly lower than that for EA-IRMS, which requires  $\approx 4$   $\mu\text{mol}$  total ( $\approx 1.5$   $\mu\text{mol}$  for carbon and  $\approx 2.5$   $\mu\text{mol}$  for hydrogen). Orbitrap-IRMS is also more specific, both because it observes MPA directly (avoiding any residual hydrogen in the sample) and because the signal of the methyl hydrogens is diluted by only one hydroxyl hydrogen for Orbitrap-IRMS compared to two for EA-IRMS. While the error bars for  $^{13}\text{C}$  via Orbitrap-IRMS are greater than those for EA-IRMS ( $\approx 1$  ‰ for  $^{13}\text{C}$  vs  $\approx 0.1$  ‰), the size of the separation we observe between groups of MPA is significantly larger ( $\approx 10$  ‰), so this does not impair our ability to forensically discriminate between stocks. Moreover, it is possible further developments in Orbitrap IRMS methods could result in higher precisions (see below). We conclude that in most cases, Orbitrap-IRMS is a superior technique, principally due to lower sample size and logistical simplicity; however, in cases where a significant amount of material is available and the differences in  $^{13}\text{C}$  are minor ( $\approx 1$  ‰), EA-IRMS measurements of  $^{13}\text{C}$  combined with observations of  $^2\text{H}$  via another technique will be more effective.

#### 5.3.5 Possible Improvements to Orbitrap-IRMS

We recommend three avenues for possible improvements to our Orbitrap-IRMS design. First, the flow rate used for our system was 20  $\mu\text{L}/\text{minute}$  and used a 32-gauge ‘high-flow’ spray needle. Some users have made Orbitrap-IRMS measurements using a 34-gauge ‘low flow’ needle, and employed flow rates as low as 3  $\mu\text{L}/\text{minute}$  (Neubauer et al., 2020; Hilkert et al., 2021). If we applied lower flow methods, we could reduce sample

consumption by almost an order of magnitude. Second, we selected a mass resolution of 120,000, to separate  $^{13}\text{C}$  from  $^{17}\text{O}$ . However, we do not use the  $^{17}\text{O}$  data, and a lower mass resolution may still permit accurate measurement of  $^{13}\text{C}$ . We explored both possibilities in a measurement sequence with a 10  $\mu\text{L}/\text{minute}$  flow rate and a resolution of 45,000, but found this low resolution resulted in data artifacts for the  $^2\text{H}$  data (possibly related to data processing; see the supplement, S.3). However, there remains a significant amount of parameter space (AGC values, resolutions, flow rates) to explore, and more rapid forensic assignment may be possible. Finally, improvements in precision might be achieved by simply increasing integration duration per acquisition and/or the number of acquisitions per sequence of sample/standard comparisons.

### 5.3.6 Future Directions

We suggest three additional avenues for exploration. First, EA-IRMS measurements can constrain the hydrogen isotope compositions of methyl hydrogen, via a two-point calibration where the sample is equilibrated with two known, distinct hydrogen pools prior to measurement (Sauer et al., 2009). This could provide reference standards that permit us to report Orbitrap IRMS measurements of  $\delta^2\text{H}$  on the VSMOW scale (particularly when combined with Orbitrap measurements using two or more solvents that differ in  $\delta^2\text{H}$ , letting us correct accurately for the contribution of hydroxyl hydrogens). Future work should develop these methods, especially for applications which rely on more detailed interpretation of  $\delta^2\text{H}$ .

Second, the clumped isotope content ( $^{13}\text{C}^2\text{H}$ ,  $^2\text{H}^2\text{H}$ ) of the methyl group of MPA may provide additional information for forensic discrimination. The clumped isotopes of MPA can plausibly be observed via Orbitrap-IRMS, as they are of similar abundances to clumped isotopes observed previously (Neubauer et al., 2020; Hilker et al., 2021; Csernica et al., 2023). Alternatively, the methane from methylphosphonic acid may be released microbially allowing it to be studied with sector mass spectrometry (Daughton et al., 1979; Stolper et al., 2014). Indeed, Taenzer et al. have performed such an experiment to study the composition of microbially-produced methane (L. Taenzer et al., 2020; Lina Taenzer et al.,

2020). Their study was designed to observe the resulting methane rather than the MPA pool, and used a large excess of MPA; with some modification, such that the MPA is converted quantitatively, this strategy may be applicable to clumped isotopes of MPA.

Third, MPA has scientific relevance beyond chemical weapons, as a possible contributor to the global methane cycle (Weber et al., 2019). In particular, MPA has been suggested as a solution to the ‘marine methane paradox,’ or the production of methane in aerobic environments where traditional biogenic methanogenesis pathways are not active (Karl et al., 2008; Metcalf et al., 2012). The demethylation of MPA or its polysaccharide esters offers an explanation for methanogenesis in these environments (Repeta et al., 2016). The carbon isotope fractionation imparted by this process has been studied and found to be minor ( $\approx 1.3\%$ ) (Taenzer et al., 2020). Moreover, the  $\delta^{13}\text{C}$  composition of MPA will vary based on the dominant microbial producers of MPA, and thus will be useful for studying the sources of marine methane in more detail. However, in part due to the low abundance of MPA in marine environments, its  $\delta^{13}\text{C}$  content has not been observed directly. Because of the low sample requirements ( $\approx 60$  nmol) of our method, it may be a useful technique for studying this aspect of the methane cycle in more detail.

#### 5.4 Conclusions

Our Orbitrap-IRMS method simultaneously observes the  $\delta^{13}\text{C}$  and  $\delta^2\text{H}$  content of MPA samples. The combination of these two observations results in a more robust forensic tool for distinguishing between and interpreting the origin of MPA samples. Our technique can be applied to hydrolyzed DC or DF, and therefore used for forensic studies of these chemical weapon precursors. Compared to EA-IRMS, Orbitrap-IRMS is superior in that it can measure  $\delta^2\text{H}$  and  $\delta^{13}\text{C}$  simultaneously, is compound-specific (measuring only MPA rather than the bulk solid), and has greater specificity (diluting the methyl hydrogens of interest with only one hydroxyl hydrogen rather than two). However, EA-IRMS shows better precision for  $\delta^{13}\text{C}$ . Future work should evaluate the effect of different synthetic processes on the observed isotope ratios in more detail and observe MPA samples from other

environments. Our results demonstrate the efficacy of Orbitrap-IRMS as a technique for chemical forensics and suggest this method should be applied more broadly.

### **Acknowledgements**

We would like to thank Alex Sessions for the use of laboratory space. A special thanks to Hannah Dion-Kirschner, as well as Fenfang Wu and Elliott Mueller, for their assistance with  $^{13}\text{C}$  EA-IRMS measurements. We additionally thank Viorel Atudorei for assistance with  $^2\text{H}$  EA-IRMS measurements, and Nils Kuhlbusch for discussion regarding the low-resolution dataset. Finally, we thank Sarah Zeichner, Max Lloyd, Peter Martin, and Guannan Dong for development of data processing scripts.

### **Funding**

This work was supported by US Department of Energy [grant number DE-SC0016561].

## Supplementary Material for Chapter 5

### S5.1: Concentration and Salt Effects

In this section, we analyze the effect of both variable MPA concentration and variable NaCl concentration on observed isotope ratios. We were particularly concerned about the hydrolyzed samples, which consisted of a mixture of NaCl, MPA, and NaOH. The amount of NaOH should be minor (~3 weight percent), and in a solution of 150  $\mu\text{g/mL}$ , has a concentration two orders of magnitude lower than formic acid; we therefore do not consider this relevant.

We analyzed three sets of samples to investigate NaCl and MPA concentration. First, we evaluated the effect of MPA concentration by preparing solutions of MPA using the SIG standard at 25, 100, 150, 250, and 500  $\mu\text{M}$ . Second, we evaluated the effect of NaCl concentration by preparing five samples with 100  $\mu\text{M}$  of MPA, adding sufficient NaCl to have ratios of NaCl:MPA (by mass) of 0, 0.6, 1.2, 1.8, and 2.4 (the hydrolyzed samples have ratios  $\approx 1.2$ ). Third, we tested the effect of NaCl and MPA increasing in tandem at a constant NaCl:MPA ratio of 1.2, preparing MPA solutions of 25, 100, 150, 250, and 500  $\mu\text{M}$ , with the corresponding amount of NaCl.

For each set, we observed all 5 samples in sequence under the same conditions as the manuscript. We recorded the tics and both  $^{13}\text{C}/^{12}\text{C}$  and  $^2\text{H}/^1\text{H}$  isotope ratios. We plot the tics for each set in Figure S5.1, finding an increase with concentration of MPA, a decrease with concentration of NaCl, and an increase when both are increased simultaneously. For the isotope ratios, we computed delta values where the reference is the mean of all 5 isotope ratios associated with that sample set, e.g.,  $\delta_{AVG}^i = 1000 * \left( \frac{R^i}{\sum_{i=1}^5 R^i} - 1 \right)$  where  $i$  represents a specific sample. Note that the reference average is different for each sample set. In figure S5.2, we plot the observed tic values vs observed isotope ratios for each sample set. Error bars are  $1\sigma$  standard deviations (tic) or acquisition errors ( $\sigma_{AE}$ , isotope ratios). In all cases, we observed that isotope ratios were inversely

related with tic and had effects of similar magnitudes. Our results suggest that the important parameter regarding the observed isotope ratios is not concentration or NaCl, but rather the observed tic; therefore, it may be appropriate to perform sample standard comparisons of analytes with different concentrations of NaCl or MPA, if their tics were similar.

To confirm this, we performed a bracketed standardized measurement (Std/Smp/Std) where the standard was 100  $\mu\text{M}$  MPA with no NaCl and the sample had 250  $\mu\text{M}$  of MPA and a NaCl:MPn ratio of 1.2. Mean tic values were  $6.2 \times 10^7$ ,  $5.6 \times 10^7$ , and  $5.6 \times 10^7$  for the three injections, respectively, and we recovered standardized values of  $\delta^{13}\text{C}_{\text{STD}} = 0.93 \pm 1.12$  for carbon and  $2.4 \pm 5.2$  for hydrogen. We conclude that the important parameter with respect to concentration and matrix effects is not the precise concentration or NaCl content, but the TIC resulting from their combination. Therefore, for the hydrolyzed samples, we adjusted concentrations attempting to match the TIC values of sample and standard. We give these values in Table S5.1.

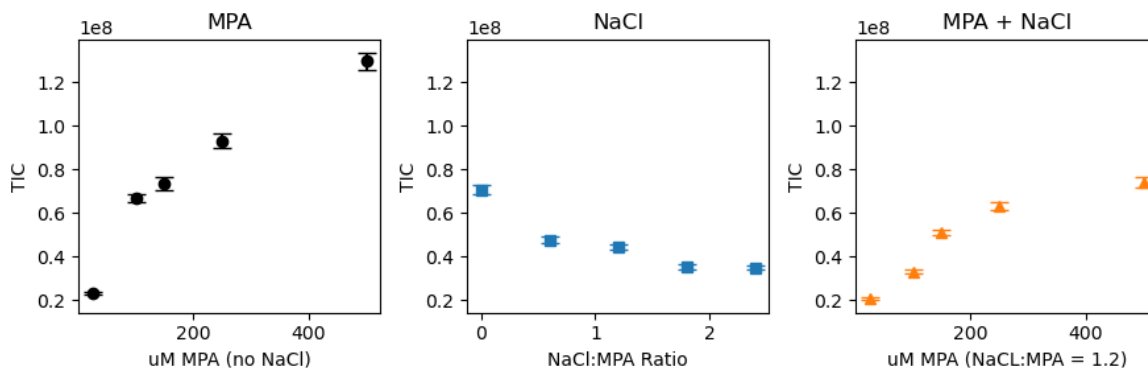


**Figure S5.1:** The observed tic (mean  $\pm 1\sigma$ ) versus the parameter of interest for each dataset. We observe an increase of tic with concentration of MPA, a decrease with concentration of NaCl, and a smaller increase with an increase in both simultaneously.

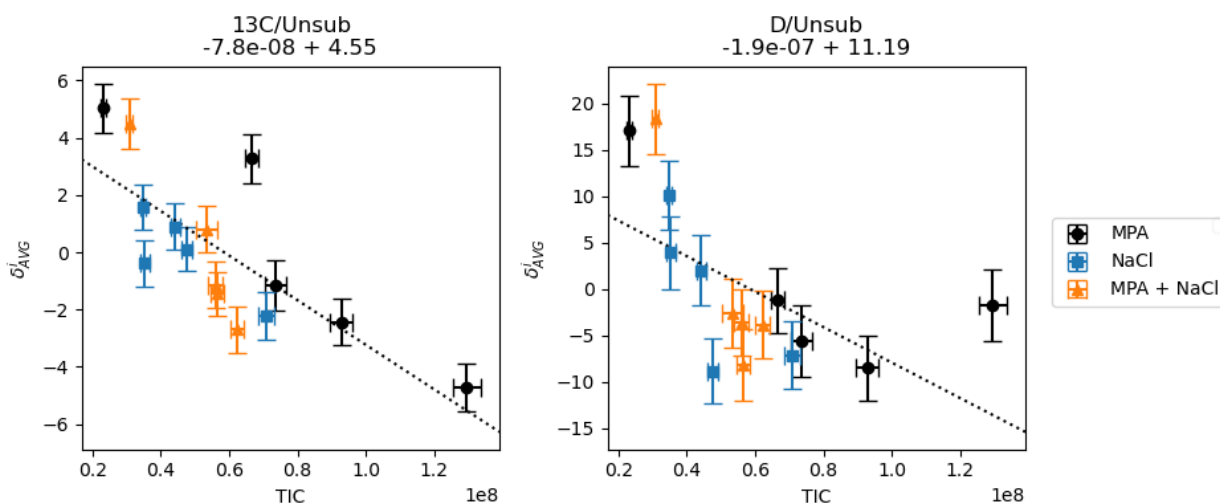


**Figure S5.2:** The effect of observed tic versus recovered isotope ratios for both  $^{13}\text{C}/\text{Unsub}$  and  $^2\text{H}/\text{Unsub}$ . For each variable (MPA concentration, NaCl concentration, and both simultaneously), we see an inverse effect with observed isotope ratio with varying tic. The magnitude of the effect is similar for each case and correlates with the observed tic. Therefore, for standardization, the important parameter is the tic.

**Table S5.1 Concentrations and Average TIC scores of hydrolyzed samples**

	Standard Concentration ( $\mu\text{M}$ )	Sample Concentration $\mu\text{g}/\text{mL}$ (est. $\mu\text{M}$ )	Standard TIC	Sample TIC
MPA A	100	45 (205)	1.42e8	1.50e8
MPA F	100	45 (205)	1.35e8	1.43e8
MPA K	70	30 (135)	1.28e8	1.24e8
MPA I	70	15 (70)	1.23e8	1.22e8
MPA M	70	45 (205)	9.6e7	1.09e8
MPA C	100	45 (205)	6.1e7	5.9e7

## S.2 Effects of Deuterium Equilibration

In the text, we discuss the importance of the exchangeable  $^2\text{H}$  values on our Orbitrap-IRMS results, and consequently our ability to perform chemical forensics using those data. Here, we discuss this issue in more detail.

First, we justify why we employ a scaling constant (here, denoted  $k_{ORBI}$ ) to calculate enrichment at the methyl site, via  $\delta_{methyl,SIG}^{2H} = k_{ORBI} * \delta_{Orbitrap,SIG}^{2H}$ . To derive this constant, first note that the actual quantity we observe in the Orbitrap is:

$$\frac{3 * [^2\text{H}]_{methyl} + [^2\text{H}]_{hydroxyl}}{[Unsub]} \quad (\text{S5.1})$$



where we write  $[^2H]_{methyl}$  to give the concentration of the isotopologue with a  $^2H$  substitution at the methyl site and the abundant isotope at all other sites (e.g.,  $^{12}C^2H_1^1H_3^{16}O_3^-$ ), and likewise for  $[^2H]_{hydroxyl}$ , while [Unsub] refers to the unsubstituted isotopologue. When making a sample standard comparison, we compute:

$$\frac{\left(\frac{3 * [^2H]_{methyl} + [^2H]_{hydroxyl}}{[Unsub]}\right)_{SMP}}{\left(\frac{3 * [^2H]_{methyl} + [^2H]_{hydroxyl}}{[Unsub]}\right)_{STD}} \approx \frac{4 * R_{SMP}^{Orbi}}{4 * R_{STD}^{Orbi}} = \frac{R_{SMP}^{Orbi}}{R_{STD}^{Orbi}}. \quad (S5.2)$$

The ratio between observed isotope ratios for the sample and the standard. We are making an approximation here: delta values normally use ratios of isotopes, e.g.,  $R = \frac{[^2H]}{[^1H]}$ , while we are observing a ratio of isotopologues, e.g.,  $\frac{[^{12}C^2H_1^1H_3^{16}H_3]}{[^{12}C^1H_4^{16}H_3]}$ ; the two are approximately equal, and exactly equal if there is a stochastic distribution of isotopes across isotopologues. We direct the reader to Csernica and Eiler 2023 for a more detailed discussion. We then present results as a  $\delta$  value:

$$\delta_{STD}^{2H} = 1000 * \left( \frac{R_{SMP}^{Orbi}}{R_{STD}^{Orbi}} - 1 \right). \quad (S5.3)$$

We will now show that there is a constant relationship between  $\delta_{methyl,SIG}^{2H}$  and  $\delta_{Orbitrap,SIG}^{2H}$ . We define and expand this relationship, and set it equal to k:

$$k_{ORBI} = \frac{\delta_{Met,STD}^{2H}}{\delta_{OrbiSTD}^{2H}} \approx \frac{\frac{\left(\frac{3 * [^2H]_{methyl}}{[Unsub]}\right)_{SMP} - 1}{\left(\frac{3 * [^2H]_{methyl}}{[Unsub]}\right)_{STD}}}{\frac{\left(\frac{3 * [^2H]_{methyl} + [^2H]_{hydroxyl}}{[Unsub]}\right)_{SMP} - 1}{\left(\frac{3 * [^2H]_{methyl} + [^2H]_{hydroxyl}}{[Unsub]}\right)_{STD}}}. \quad (S5.4)$$

Here, the numerator is the delta value for the methyl site only, and the denominator is our observation, and the approximation is again due to the stochastic assumption. If we assume [Unsub] is roughly constant between sample and standard, we may write:

$$\frac{\left(\frac{3 * [^2H]_{methyl}}{[Unsub]}\right)_{SMP} - 1}{\left(\frac{3 * [^2H]_{methyl}}{[Unsub]}\right)_{STD}} \approx \frac{\frac{[^2H]_{methylSMP}}{[^2H]_{methylSTD}} - 1}{\frac{3 * [^2H]_{methyl} + [^2H]_{hydroxyl}}{3 * [^2H]_{methyl} + [^2H]_{hydroxyl}} - 1} \cdot \frac{\left(\frac{3 * [^2H]_{methyl} + [^2H]_{hydroxyl}}{[Unsub]}\right)_{SMP} - 1}{\left(\frac{3 * [^2H]_{methyl} + [^2H]_{hydroxyl}}{[Unsub]}\right)_{STD}} \quad (S5.5)$$

Now, we write  $a = [^2H]_{methylSMP}$ ,  $b = [^2H]_{methylSTD}$ , and  $c = [^2H]_{hydroxyl}$ . Note that we are assuming  $c$  is identical between sample and standard. We have:

$$\frac{\frac{[^2H]_{methylSMP}}{[^2H]_{methylSTD}} - 1}{\frac{3 * [^2H]_{methyl} + [^2H]_{hydroxyl}}{3 * [^2H]_{methyl} + [^2H]_{hydroxyl}} - 1} = \frac{\frac{a}{b} - 1}{\frac{3a + c}{3b + c} - 1} = \frac{\frac{a - b}{b}}{\frac{3a - 3b}{3b + c}} \quad (S5.6)$$

We simplify:

$$\frac{\frac{a - b}{b}}{\frac{3a - 3b}{3b + c}} = \frac{\frac{1}{b}}{\frac{3}{3b + c}} = \frac{3b + c}{3b} = 1 + \frac{c}{3b} \quad (S5.7)$$

or:

$$k_{ORBI} = \frac{\delta_{Met,STD}^{2H}}{\delta_{OrbiSTD}^{2H}} \approx 1 + \frac{[^2H]_{hydroxyl}}{3 * [^2H]_{methylSTD}} \quad (S5.8)$$

When  $[^2H]_{hydroxyl} = [^2H]_{methylSTD}$ , the  $k_{ORBI} \approx \frac{4}{3}$ , the approximation we use in the main text. We note that  $k$  does not depend on the sample composition, only the standard and the equilibrating solvent pool. A similar analysis applies to EA-IRMS, with  $k_{EA} \approx 1 + \frac{2 * [^2H]_{hydroxyl}}{3 * [^2H]_{methylSTD}}$ .

We next explore how these scaling constants vary, and the effect they have on our results. We assume that the hydroxyl hydrogens have  $^2H$  content equal to the pool they are equilibrating with, omitting equilibrium isotope fractionation. For the Orbitrap experiments, this pool is the Milli Q water used as solvent; this was not measured in association with our experiments but is used as an internal standard for other  $^2H$

measurements in our laboratory, with typical values of  $-80 \pm 10 \text{‰}$ ; we here use an estimate of  $-80 \text{‰}$ . For the EA-IRMS experiments, the deuterium enrichment of water vapor in New Mexico has been measured previously, and found to have a value of  $\approx -120 \pm 20 \text{‰}$  in August; we therefore estimate a value of  $-120 \text{‰}$  (Strong, 2012). Applying this assumption to our EA-IRMS measurement of the SIG standard ( $\delta^{2H}_{VSMOW} = 159.4 \pm 2.6$ ) implies its methyl group has  $\delta^{2H}_{VSMOW} \approx -186 \text{‰}$ . The corresponding scaling constants are  $k_{EA} = 1.72$  and  $k_{ORBI} = 1.38$ . We present data calculated using these scaling constants in Figure S5.3, left, and results in a similar fit to that in the manuscript. We additionally show a comparison between our raw EA-IRMS and Orbitrap-IRMS data (i.e., without a scaling constant), the least processed version of our results. These are shown in Figure S5.3, right. In all cases, we note that our treatment of the scaling constant does not significantly impact our ability for forensic discrimination.

The associated calculations are presented in full in the github repository associated with this chapter.

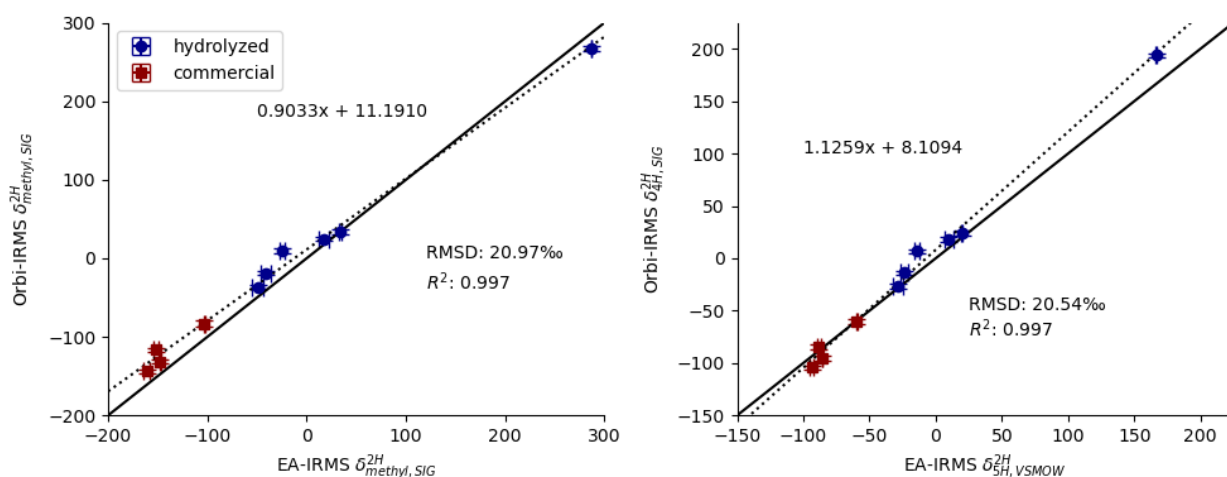


**Figure S5.3:** Hydrogen data calculated with different scaling constants. Left: Our  $^2H$  results calculated using scaling constants of  $k_{ORBI} = 1.38$  and  $k_{EA} = 1.72$ . These values result in a similar fit to that presented in the main text. Right: Our  $^2H$  results calculated using no scaling constant for either dataset; these are just the raw data we report. In this case, we observe a scale expansion, which is expected as the Orbitrap data include 4 hydrogens and the EA-IRMS include 5 hydrogens.

### S5.3 Data Artifacts For Low Resolution Dataset

We attempted a 'low resolution' optimization of our method, with several modifications, in order to improve on the measurement time; however, the resulting measurements showed poor data quality for  $^2\text{H}$ . These measurements were performed in August 2022, and differed from those in the manuscript as follows. First, we used a 34-gauge 'low flow' needle and a flow rate of 10  $\mu\text{L}/\text{minute}$ . Second, we set several different mass spectrometry parameters to different settings, specifically: scan range = 93.5-99.5 for all samples, resolution = 45k, microscans = 1, AGC target = 1e6, sheath gas flow rate = 10. All other parameters were as in the manuscript. Third, each measurement had a duration of  $\approx 4.5$  minutes. Because of the higher AGC target and lower resolution, these shorter duration measurements had propagated acquisition errors similar to (slightly larger than) data in the manuscript, with typical  $\sigma_{\text{PAE}}$  values of  $\approx 1$  ‰ ( $^{13}\text{C}$ ) and  $\approx 5.5$  ‰ ( $^2\text{H}$ ).

Using these conditions, we characterized the 6 hydrolyzed MPA samples relative to the SIG standard. Our results for  $^{13}\text{C}$  and  $^2\text{H}$  relative to our EA-IRMS data are shown below, in Figure S5.4. In this case, the error bars for the Orbitrap-IRMS data are standard deviations of the three  $\delta^2\text{H}$  values rather than methodological reproducibilities. Our  $^{13}\text{C}$  data are of a similar quality to that from the 120k dataset, with a lower RMSD of 2.01 ‰. In contrast, the  $^2\text{H}$  data, while relatively linear, are depleted relative to the accepted values, with a RMSD of 55.9 ‰.

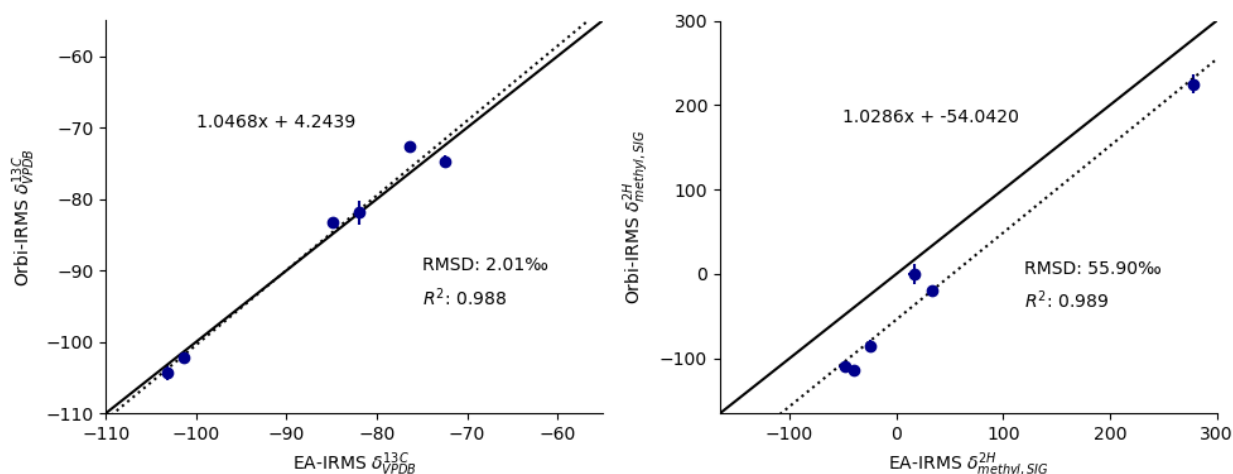


**Figure S5.4:** Linear fits for the  $^{13}\text{C}$  and  $^2\text{H}$  data obtained via our ‘low resolution’ 45k method. Our results for  $^{13}\text{C}$  are similarly accurate to the 120k dataset, but the  $^2\text{H}$  results show a much larger deviation from the EA-IRMS values.

When we investigated our  $^2\text{H}$  data, we observed systematic differences that may have impaired our ability to standardize. In particular, in the samples but not the standards, we observed bimodal distributions for the mass difference between the  $^2\text{H}$  and unsubstituted peak, coupled with deviations in the number of observed counts for the deuterium beam; in both cases, more counts of  $^2\text{H}$  are associated with smaller mass differences. In Figure S5.5, we show representative results for both the standard (SIG) and sample (any hydrolyzed sample). We hypothesize that this arises from the differing treatments used in data processing for Orbitrap peaks with low S/N vs high (and see especially (Kuhlbusch et al., 2023)); in this case, repeating the measurement with a higher number of microscans would likely resolve the issue. However, it could also arise from space-charge effects, or due to the interference of the  $^2\text{H}$  peak with a close-lying contaminant which is present in the hydrolyzed samples but not the standard. If accurate measurements can be made at this resolution, they will lead to a faster method.

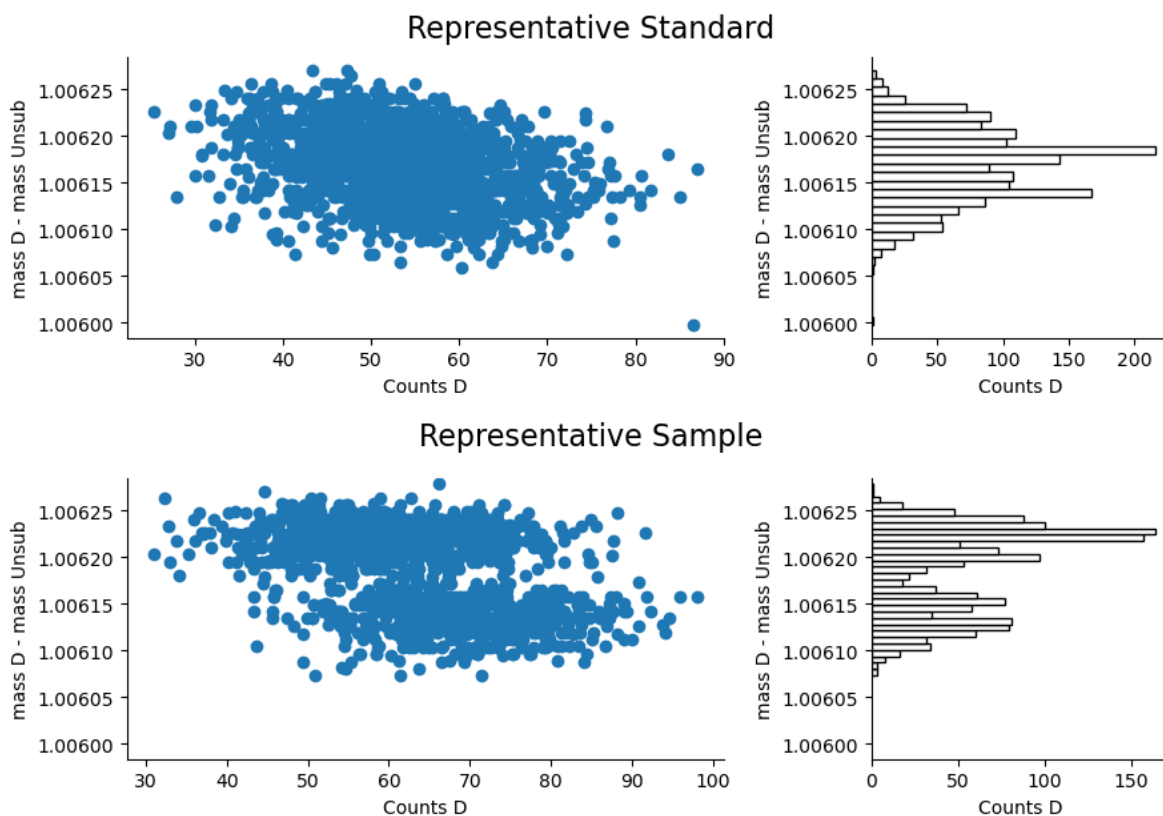


**Figure S5.5:** Data artifacts associated with the  $^2\text{H}$  observations for the low-resolution dataset. In these plots, the x-axis is the number of 'counts' of deuterium ions (calculated via eq (1)) and the y-axis is the mass difference between the deuterium peak and the unsubstituted peak. Each point corresponds to a single scan. In both datasets, higher counts of D are correlated with smaller mass differences. However, in our standard data, we observe a histogram with a single peak, while the sample data show a bimodal distribution of mass differences.

## ISOTOPIC SIGNATURE OF A PREBIOTIC ADENINE SYNTHESIS AND CONSEQUENCES FOR METEORITIC NUCLEOBASES

### **Abstract**

Purines have been detected on carbonaceous chondrites with abundances of 1s-100s of ppb. The synthesis mechanism for these compounds remains unknown. The isotopic signatures of these compounds, especially their site-specific isotopic structures, can reveal their formation history because different pathways will result in distinct fingerprints. However, interpreting this information requires a detailed understanding of the isotope effects along different synthesis pathways. Here, we develop an Orbitrap-IRMS method to probe the site-specific isotopic structure of adenine and use it to examine adenine formed via an abiotic synthesis beginning from formamide and cyanide. Our method allows us to characterize the enrichment in  $\delta^{13}\text{C}$  and  $\delta^{15}\text{N}$  of adenine in both the full molecule and nine fragments formed via collisional dissociation. By combining data from the three of these fragments with the most well-understood fragmentation mechanisms (119, 109, and 94), we can compute the enrichment at C-6, C-2, N-1, N<sup>6</sup>, and the combinations (C-4, C-5, C-8) and (N-3, N-7, N-9). The remaining fragments still provide useful data, but our understanding of which sites they sample is insufficient to constrain individual positions. For the abiotic synthesis, we find that a two-hour reaction of cyanide in formamide at 165 °C results in product adenine which is depleted in  $\delta^{13}\text{C}_{\text{VPDB}}$  relative to its precursors by  $32.4 \pm 1.1$  ‰. The depletion occurs at C-2 and the combination (C-4, C-5, C-8), and possibly at C-6. We then analyze the formation pathways of this adenine to determine possible causes of the isotopic signature. The adenine is formed via two competing pathways which incorporate different proportions of formamide and cyanide; only the first has been studied in detail via DFT, and isotope effects from this pathway are likely to arise during the ring closing steps. We conclude by exploring the observed isotope

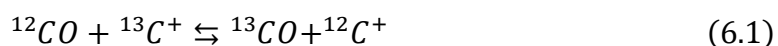
enrichment of meteoritic xanthine, the only extraterrestrial nucleobase yet characterized isotopically, in the context of a proposed reaction mechanism which branches off from our adenine synthesis. We find the most likely explanations are 1) the xanthine was formed from an isotopically heavy precursor, such as formamide derived from the  $^{13}\text{C}$ -enriched interstellar CO pool, or 2) the observed xanthine is a highly degraded residue. Our analysis allows us to make first order predictions of the  $\delta^{13}\text{C}_{\text{VPDB}}$  content of 9 other nucleobases (hypoxanthine, guanine, adenine, purine, 2-aminopurine, 8-aminopurine, 2,8-diaminopurine, 2,6-diaminopurine, and 6,8-diaminopurine). Our network contributes to debates about the origin of meteoritic formamide and will inform future isotopic measurements of these compounds.

## 6.1 Introduction

Organic compounds including amino acids, sugars, and nucleobases are abundant in carbonaceous chondrites (Sephton, 2002; Martins, 2011; Callahan et al., 2011; S. Burton et al., 2012); these molecules have formed abiotically, raising questions about their formation mechanisms. To help address this question, laboratory studies of reactions beginning with plausibly available precursors have been performed (Benner et al., 2012; Sutherland, 2016). These investigations have identified certain classes of reaction which yield some or all of these products abiotically. For example, the Formose reaction results in sugars, Strecker chemistry can form amino acids, and the polymerization of hydrogen cyanide yields nucleobases. However, for each class of compound, there are multiple viable mechanisms; e.g., amino acids can also be formed via irradiation of ices (Bernstein et al., 2002), while irradiation of formamide results in nucleobases (Barks et al., 2010). Tying an observed compound to a particular formation mechanism is therefore challenging. The concentrations of different types of compounds, as well as the conditions of a specific carbonaceous chondrite's parent body, are useful tools for distinguishing between pathways, but are generally insufficient to gain a complete picture (Elsila et al., 2016).



The stable isotope compositions of these extraterrestrial organics are an additional tool that can help reveal the history of these compounds. Different synthesis pathways will sample different pools and impart different isotope effects, resulting in distinct isotopic fingerprints. Stable isotope compositions are especially tempting in the extraterrestrial context because the precursor pools have relatively large differences. Previous studies have suggested that meteorite organics sample at least two carbon pools: a ‘reduced’ carbon pool (i.e., CH<sub>x</sub>) and a CO-derived pool. In the interstellar medium, heavy carbon is preferentially partitioned into the CO pool, due to the reaction:



which favors the <sup>13</sup>CO isotopologue due to its lower zero-point energy. This signature is large: previous results suggest  $\delta^{13}\text{C}_{\text{VPDB}} = 162 \pm 20 \text{ ‰}$  for the CO pool and  $\delta^{13}\text{C}_{\text{VPDB}} = -36 \pm 20 \text{ ‰}$  for the reduced carbon pool, a difference of  $\approx 200 \text{ ‰}$  (Chimiak et al., 2021). In contrast, measurements of specific extraterrestrial compounds (‘compound-specific isotope analysis,’ or CSIA) can have precisions of 1-10 ‰ (Martins et al., 2008; Elsila et al., 2012). CSIA measurements average across all positions in a molecule, and the associated isotopic signatures can remain ambiguous, especially if multiple formation mechanisms are active or these have substantial isotope effects, or if there are changes due to secondary alteration or degradation. These can be strengthened by measurements of the isotopic enrichment at individual atoms of a molecule (‘site-specific isotope analysis,’ or SSIA) as well as an understanding of the site-specific isotope effects along possible reaction pathways.

Previous CSIA and SSIA measurements have been used to develop a working hypothesis for the origins of meteoritic compounds, with a special focus on the Murchison meteorite, a CM2 chondrite (Figure 6.1) (Burton et al., 2012; Elsila et al., 2012; Chimiak et al., 2021; Zeichner et al., 2023a, b; Chimiak and Eiler, 2024). In this scheme, the CO pool serves as the origin of the carbonyl carbon in the aldehydes, while remaining aldehyde carbons come from the reduced carbon pool. These aldehydes then act as precursors for several classes of compounds: they may undergo Strecker chemistry (react with NH<sub>3</sub>, then

HCN, followed by hydrolysis) to form  $\alpha$ -amino acids; they may be oxidized to  $\alpha$ -carboxylic acids; or they may undergo reductive amination to create amines. Branches from this network focused on the chemistry of nitriles, especially  $\alpha,\beta$ -unsaturated nitriles and oxonitriles. The  $\alpha,\beta$ -unsaturated nitriles may be isotopically light at all positions or may incorporate some heavy carbon, while the oxonitriles sample the CO pool at carbonyl carbons and the reduced carbon pool elsewhere (Elsila et al., 2012; Zeichner et al., 2023b; Chimiak and Eiler, 2024).  $\beta$ -amino acids may originate from either  $\alpha,\beta$ -unsaturated nitriles via the Michael addition of ammonia or oxonitriles via reduction of imines formed from Strecker chemistry. Each type of nitrile can also form dicarboxylic amino acids, such as aspartic acid. To do so, the  $\alpha,\beta$ -unsaturated nitriles may be aminated by  $\text{NH}_3$ , while the oxonitriles again undergo Strecker chemistry. At every step of the process, carboxyl carbons can exchange with carbonate, resulting in  $^{13}\text{C}$  enrichment at those positions.

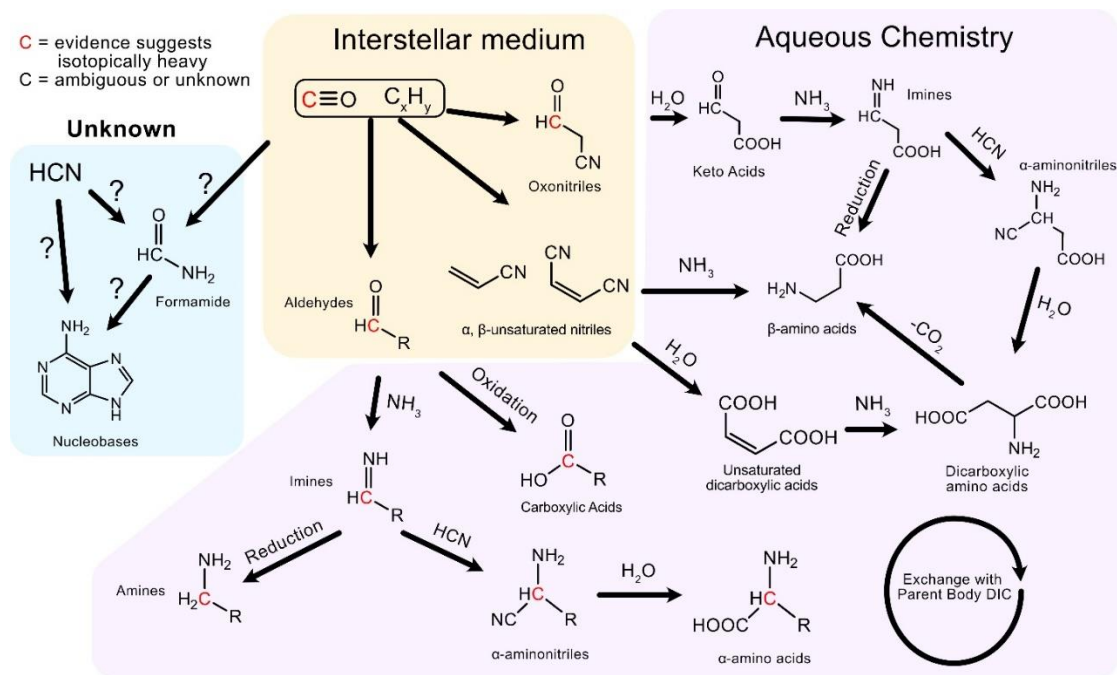


**Figure 6.1:** A reaction network of some meteorite organics which have had their isotopic content observed previously. Major isotopic signatures originate in the interstellar medium with the preferential partitioning of  $^{13}\text{C}$  into the CO pool (red) and away from the reduced carbon pool ( $\text{C}_x\text{H}_y$ ). Further reactions in the ISM lead to a variety of precursors, including aldehydes, nitriles, and oxonitriles. On the parent body, these then undergo a variety of aqueous reactions resulting in the organic compounds observed on meteorites.

Nucleobases may be formed as an offshoot of this network, likely incorporating combination of cyanide and formamide as precursors; however, this part of the network has not been explored in detail.

Cyanide is a key precursor in this network; it has also been identified as a key source of nucleobases (Figure 6.1). The polymerization of HCN at a range of temperatures (as low as  $-78\text{ }^{\circ}\text{C}$ , given decades to react) results in the formation of purines, pyrimidines, and some amino acids, such as glycine and aspartic acid (Ferris et al., 1978; Levy et al., 2000; Miyakawa et al., 2002). Alternatively, a palette of nucleobases can be formed by heating of formamide and cyanide to  $\approx 140\text{ }^{\circ}\text{C}$ , possibly in the presence of catalysts such as meteorite powder (Hudson et al., 2012; Saladino et al., 2012, 2018; Rotelli et al., 2016). Extraterrestrial nucleobases have been detected on CM2 chondrites, including Murchison, and over a dozen have now been identified (Martins et al., 2008; Callahan et al., 2011; Koga et al., 2024). Based on the abundances of meteoritic purines and these laboratory studies, networks for the synthesis of these compounds have been proposed (Burton et al., 2012; Koga et al., 2024). Connecting these syntheses with the isotopic network developed by previous authors would result in a more complete understanding of the synthesis pathways active on meteorites. Thus far only one measurement of the isotopic content of nucleobases has been made (Martins et al., 2008), while the isotope effects along the path to nucleobases have not been studied.

This study attempts to contribute to isotopic investigations of the organic reaction network active on meteorites by characterizing the isotope effects associated with an abiotic synthesis of adenine and interpreting these results in the context of proposed meteorite syntheses. Our work includes several datasets and interprets the results of multiple sets of older studies; we summarize our main points as follows. First, we designed an Orbitrap-IRMS method to observe adenine, including both its molecular-average isotope enrichment and site-specific structure. The molecular-average measurement is straightforward and allows us to observe  $^{13}\text{C}$  and  $^{15}\text{N}$  simultaneously. Computing the site-specific structure requires 1) a measurement of the isotopic enrichment of several fragments of adenine and 2) an understanding of which positions these fragments sample.

While (1) is feasible, and we can observe isotopic information for 9 fragments, (2) is more challenging, as nearly every adenine fragment can be formed by multiple mechanisms. To understand the fragmentation, we relied on a study of adenine fragmentation which investigated several adenines, each labeled at one of the 5 nitrogen positions, as well as one labeled at the C-2 carbon (Nelson and McCloskey, 1992). We supplemented these results with our own study of an adenine labeled at the C-8 position. Based on these results, we identified three of the nine fragments which had simple fragmentation mechanisms and used these data to compute site-specific enrichments for several positions, including C-6, C-2, N-1, and N<sup>6</sup>. These three fragments were not able to distinguish between (C-4, C-5, C-8) and (N-3, N-7, N-9) and instead constrained the sum of these positions. The remaining fragments could be formed via a diversity of pathways and were less well constrained given our results, so we did not use these for site-specific reconstruction.

With this method in hand, we next performed an abiotic synthesis of adenine by heating cyanide in formamide. This synthesis has been previously studied via experimental ((Hudson et al., 2012; Liu et al., 2020)) and computational ((Wang et al., 2013c, b, a; Slavova and Enchev, 2020)) methods. We then measured the isotopic content of adenine resulting from this reaction via our Orbitrap-IRMS method. While we obtained site-specific results, their interpretation was challenging as we do not have an adenine standard with known intramolecular isotopic content. By assuming that no carbon atom of the standard differs by >20 ‰ from the molecular average value, our results suggest that depletion occurs at the C-2 and (C-4, C-5, C-8) sites, and plausibly the C-6 site. We then explored previous computational studies to attempt to identify possible sources (i.e., individual elementary steps) which are the source of the signature. While some possibilities are identified, the uncertainties regarding mechanism and standard composition make it difficult to draw firm conclusions.

Our third objective was to interpret previously observed isotopic signatures for meteoritic nucleobases in the light of previous isotopic studies of meteoritic syntheses (Figure 6.1) and our adenine results. In this context, the most important observation is that

the only meteoritic purine with observed isotopic content (xanthine,  $\delta^{13}\text{C}_{\text{VPDB}} = 37.7 \pm 1.6$  ‰; (Martins et al., 2008)) is significantly enriched relative to the meteoritic cyanide (closer to the reduced carbon pool;  $\delta^{13}\text{C}_{\text{VPDB}} \approx -7 \pm 10$  ‰; (Chimiak et al., 2021)). We explore possible routes for xanthine's observed signature, concluding the most likely causes are either 1) it incorporates formamide derived from the isotopically enriched CO pool or 2) it represents a highly degraded residue from xanthine originally sourced from the cyanide pool. We then make testable predictions of the isotopic content of other meteoritic purines assuming heavy CO-derived carbon is incorporated to varying extents.

## 6.2 Materials & Methods

### 6.2.1 Materials

Potassium cyanide, magnesium chloride, ammonium formate, and formamide were acquired from Sigma Aldrich. An adenine standard (98% purity) was acquired from VWR. A labeled adenine ( $8\text{-}^{13}\text{C}$ , 95%; may contain up to 7%  $2\text{-}^{13}\text{C}$ ; chemical purity >98%) was acquired from Cambridge Isotope Laboratories. We refer to these as the "VWR" and "CIL" adenine, respectively.

### 6.2.2 Adenine Synthesis and Purification

30 mg of potassium cyanide and 22 mg of magnesium chloride were added to 1 mL of 3.5 mol % of ammonium formate in formamide and heated at 165 °C for 0.5-4 hours. The resulting mixture consisted of a supernatant and a solid residue; only the supernatant was investigated further. The supernatant was taken and the solvent evaporated at 1 torr and 80 °C; then, 3 mL of deionized water were added, and the mixture filtered using Celite® S. 100  $\mu\text{L}$  of sample was then loaded onto an Agilent 1200 HPLC system with a C18 column. The mobile phase consisted of (A) 25 mM ammonium acetate and (B) 90/10 methanol/acetonitrile and was introduced at a rate of 3.600 mL/min with a linear gradient of 5% B, 0 min, to 10% B, 12 min; 10% B was maintained until 17 minutes. Peaks of interest were collected manually, with an emphasis on collecting the entirety of every peak to

prevent column fractionation. Fractions were either a) concentrated and analyzed with an Agilent 1290 UHPLC-MS system, to identify major components, or b) evaporated to dryness at room temperature and 1 torr to obtain solid samples for Orbitrap-IRMS. A typical adenine fraction contained  $\approx 300$   $\mu\text{g}$  of material.

### *6.2.3 Spiked adenine standard*

We prepared an artificially enriched adenine standard by mixing the CIL adenine with the VWR adenine at a ratio of 9:1 (approximately  $\approx 10$  % of all C-8 carbon is  $^{13}\text{C}$ ). We refer to this as the SPK standard.

### *6.2.4 EA-IRMS Measurements*

Selected analytes had their  $\delta^{13}\text{C}_{\text{PDB}}$  and  $\delta^{15}\text{N}_{\text{AIR}}$  measured on an EA IsoLink™ combustion elemental analyzer system interfaced to a Delta V Plus isotope ratio mass spectrometer (EA-IRMS, Thermo Fischer Scientific). Samples were prepared by weighing an appropriate amount of material (corresponding to  $\approx 20$   $\mu\text{g}$  of carbon or  $\approx 50$   $\mu\text{g}$  of nitrogen) into tin capsules. These were then combusted at 1020 °C using tungsten oxide as an oxidizer. For carbon, the resulting  $\text{CO}_2$  was analyzed for its  $^{13}\text{C}/^{12}\text{C}$  ratio. For nitrogen, the combustion products were then reduced at 650 °C using copper, and the resulting  $\text{N}_2$  was analyzed for its  $^{15}\text{N}/^{14}\text{N}$  ratio. Formamide is a liquid at room temperature with a high boiling point (210 °C); rather than weighing formamide, we calculated the corresponding volume (density = 1.13 g/mL) and placed this into a capsule immediately prior to measurement.

### *6.2.5 Orbitrap-IRMS Analytes and Sample Introduction*

We prepared the adenine standards (i.e., the VWR standard or the SPK standard) by dissolving 1 mg of adenine in 100 mL of 50/50 acetonitrile/water with 0.1 % (by volume) formic acid as an additive. These were then diluted to concentrations of 75  $\mu\text{M}$ . Adenine obtained from preparatory HPLC was prepared at the same concentrations, assuming  $\approx 300$   $\mu\text{g}$  of adenine per run. The dissolved analytes were injected onto a Q Exactive HF Mass

Spectrometer (Thermo Fisher Scientific) with a HESI-II Probe (Thermo Fisher Scientific) using a Fusion 101 (Chemyx Inc.) syringe pump and a 500  $\mu\text{L}$  syringe (Hamilton Robotics). Our analyses used a flow rate of 5  $\mu\text{L}/\text{minute}$ .

### 6.2.6 Orbitrap-IRMS Mass Spectrometry

We performed three sets of Orbitrap-IRMS measurements. First, we made a ‘molecular-average’ measurement, which observed the intact molecule. Second, we performed a ‘fragmentation’ experiment, which observed adenine’s fragments. Third, we performed a ‘M+1’ experiment, which first mass selected the isotopologues of adenine with a cardinal mass increase of 1 relative to the unsubstituted isotopologue, then fragmented and observed these. We develop the theory surrounding the ‘M+1’ experiment in more detail in Chapter 2. Throughout each, we used the same mass spectrometry parameters. These are: AGC Target: 2e5 (unitless) Max IT time: 1000 ms; Polarity: positive; sheath gas flow rate: 5 (arbitrary units) Aux gas flow rate: 0 (arbitrary units) Sweep gas flow rate: 0 (arbitrary units) Spray voltage: 4.5 kV, S lens RF level: 50 (arbitrary); Capillary temperature: 320  $^{\circ}\text{C}$ .

Specific settings which differed are as follows. For the molecular average measurements, we isolated a mass window of 50-150 (m/z) and observed the  $^{12}\text{C}_5^{14}\text{N}_5^1\text{H}_6^+$  ion at cardinal mass 136 and its substituted variants  $^{13}\text{C}_1^{12}\text{C}_4^{14}\text{N}_5^1\text{H}_6^+$  and  $^{12}\text{C}_4^{15}\text{N}_1^{14}\text{N}_4^1\text{H}_6^+$  at cardinal mass 137. For the ‘fragmentation’ measurements, we first isolated a mass window of 135.5-137.5 m/z, then fragmented these ions in the HCD cell at a normalized collision energy of 140 (arbitrary units). Nine fragments were detected, at cardinal masses 119 ( $\text{C}_5\text{N}_4\text{H}_3^+$ ), 109 ( $\text{C}_4\text{N}_4\text{H}_5^+$ ), 94 ( $\text{C}_4\text{N}_3\text{H}_4^+$ ), 92 ( $\text{C}_4\text{N}_3\text{H}_2^+$ ), 82 ( $\text{C}_3\text{N}_3\text{H}_4^+$ ), 77 ( $\text{C}_4\text{N}_2\text{H}^+$ ), 67 ( $\text{C}_3\text{N}_2\text{H}_3^+$ ), 65 ( $\text{C}_3\text{N}_2\text{H}^+$ ), and 55 ( $\text{C}_2\text{N}_2\text{H}_3^+$ ). All fragments were measured simultaneously. The M+1 measurements were identical to the fragmentation measurements, except that we isolated ions in the mass window of 136.5-137.5 m/z (i.e., only those adenine isotopologues with a single rare  $^{13}\text{C}$ ,  $^{15}\text{N}$ , or  $^2\text{H}$  substitution) and used a resolution of 60,000.

### 6.2.7 Analytes Observed and Measurement Order

We present measurements which occurred on two different days: November 11, 2019, and September 24, 2021. The 2019 measurements examined adenine synthesized from cyanide and formamide (see 6.2.2) and were performed on a Q Exactive HF at the Caltech Proteome Exploration Laboratory. The measurement sequence included both molecular average ('MA') and M+1 measurements and occurred in the order: Standard (MA)/Standard (M+1)/Sample (MA)/Sample (M+1)/Sample (M+1)/Standard (MA)/Standard (M+1). Note that two acquisitions occurred for the sample M+1 measurement. The molecular average acquisitions were 15 minutes each, while the M+1 measurements were 30 minutes each, except for the final standard acquisition, which was 20 minutes. The 2021 measurements examined the SPK adenine (see 6.2.3) and were performed on the Q Exactive HF in the Eiler laboratory at Caltech. These measurements followed the 'fragmentation' parameters and occurred in the order Standard/Sample/Standard/Sample/Standard/Sample/Standard; these acquisitions were 20 minutes each.

### 6.2.8 Data Analysis

The ion intensities and noise associated with each isotopic peak were extracted from .RAW files generated by the instrument using the IsoX software. These were used to calculate ion counts using:

$$N_{IO} = \left(\frac{S}{N}\right) * \left(\frac{C_N}{z}\right) * \left(\frac{R_N}{R}\right)^{\frac{1}{2}} * \mu^{\frac{1}{2}} \quad (6.2)$$

where  $N_{IO}$  is the number of ions observed for that peak in that scan,  $S$  is the peak intensity,  $N$  is the peak noise,  $C_N$  is a reference constant, here taken to be 4.4 (see (Eiler et al., 2017)),  $z$  is the charge,  $R_N$  is a reference resolution used to determine  $C_N$  (here 120,000),  $R$  is the instrument resolution, and  $\mu$  is the number of microscans.

We then calculated either isotope ratios (for the 'molecular average' and 'fragmentation' measurements) or M+1 relative abundances (for the M+1 measurements;



see Chapter 2) as follows. When reporting isotope ratios, we computed the ratio of the  $^{13}\text{C}$ ,  $^{15}\text{N}$ , or  $^2\text{H}$  substituted isotopologues of the ion relative to the unsubstituted isotopologue of the same ion. To do so, we first computed the ratios of  $N_{IO}$  in each scan to compute corresponding isotope ratios for each scan. For example, for the  $^{13}\text{C}/\text{Unsub}$  ratio calculated for the molecular average adenine measurement, the relevant peaks were  $^{12}\text{C}_5^{15}\text{N}_5^1\text{H}_6^+$  and  $^{13}\text{C}_1^{12}\text{C}_4^{15}\text{N}_5^1\text{H}_6^+$ ; for each scan  $i$ , we calculated  $R_i^{13\text{C}} = \frac{N_{IO}({}^{13}\text{C}_1{}^{12}\text{C}_4{}^{14}\text{N}_5{}^1\text{H}_6^+)}{N_{IO}({}^{12}\text{C}_5{}^{14}\text{N}_5{}^1\text{H}_6^+)}$ . We reported the average of the  $R_i^{13\text{C}}$  values across the whole acquisition and their relative standard error, which we call the acquisition error,  $\sigma_{\text{AE}}$ . When reporting M+1 relative abundances, we computed the ratio of the  $^{13}\text{C}$ ,  $^{15}\text{N}$ ,  $^2\text{H}$ , or Unsub isotopologues of the ion relative to the sum of all observed peaks for that ion. That is, the ' $^{13}\text{C}$  M+1 relative abundance' ( $\rho^{13\text{C}} = \frac{[{}^{13}\text{C}]}{[{}^{13}\text{C}] + [{}^2\text{H}] + [{}^{15}\text{N}] + [\text{Unsub}]}$ ) was computed scan-by-scan as

$$\rho_i^{13\text{C}} = \frac{N_{IO}({}^{13}\text{C}_1{}^{12}\text{C}_4{}^{14}\text{N}_5{}^1\text{H}_6^+)}{N_{IO}({}^{12}\text{C}_5{}^{15}\text{N}_5{}^1\text{H}_6^+) + N_{IO}({}^{13}\text{C}_1{}^{12}\text{C}_4{}^{15}\text{N}_5{}^1\text{H}_6^+) + N_{IO}({}^{12}\text{C}_5{}^{15}\text{N}_1{}^{14}\text{N}_4{}^1\text{H}_6^+) + N_{IO}({}^{12}\text{C}_5{}^{15}\text{N}_5{}^2\text{H}_1{}^1\text{H}_5^+)}. \quad (6.3)$$

We then reported the average  $\rho^{13\text{C}}$  value across all scans and its relative standard error, which we call the acquisition error,  $\sigma_{\text{AE}}$ .

### 6.2.9 Shot Noise Limit

For each observed ratio or M+1 relative abundance, we estimate the corresponding shot noise limit  $\sigma_{\text{SN}}$ , or the maximum achievable precision given the number of ions observed, as follows. For isotope ratios, we compute:

$$\sigma_{\text{SN}} = \sqrt{\frac{1}{\sum N_{IO, \text{beam } 1}} + \frac{1}{\sum N_{IO, \text{beam } 2}}} \quad (6.4)$$

for the two ion beams used to compute the ratio. For M+1 relative abundances, we compute:

$$\sigma_{\text{SN}} = \frac{N_{IO, \text{all other beams}}}{\sum N_{IO, \text{beam } 1} + \sum N_{IO, \text{all other beams}}} \sqrt{\frac{1}{\sum N_{IO, \text{beam } 1}} + \frac{1}{\sum N_{IO, \text{all other beams}}}}. \quad (6.5)$$

We derive eq (6.5) in the supplement to Chapter 4.

### 6.2.10 Standardization

We computed standardized isotope ratios as follows. We began by taking the average (isotope ratio or M+1 relative abundance) of all sample and all standard acquisitions. We then reported the enrichment of the average sample relative to the average standard as a delta value; for isotope ratios:

$$\delta^{13C} = 1000 * \left( \frac{R_{SMP,AVG}^{13C}}{R_{STD,AVG}^{13C}} - 1 \right) \quad (6.6)$$

and for M+1 relative abundances:

$$\delta^{13C} = 1000 * \left( \frac{\rho_{SMP,AVG}^{13C}}{\rho_{STD,AVG}^{13C}} - 1 \right). \quad (6.7)$$

To propagate error bars, we first find the average acquisition errors for sample and standard, then add these in quadrature. That is:

$$\sigma_{PAE} = \sqrt{(\sigma_{AE,SMP,AVG})^2 + (\sigma_{AE,STD,AVG})^2}. \quad (6.8)$$

Our error treatment is simpler than that used elsewhere in this thesis; we adopt it here because of the smaller number of data (1-2 sample observations and 2 standard observations for M+1 and molecular average measurements) for each observation. For the fragmentation data, with 4 standard and 3 sample acquisitions, we find no significant differences between this approach and that used in previous chapters.

### 6.2.11 Data Quality Tests

To ensure data quality, we apply three data quality tests to each observed peak. First, we check that the acquisition error to shot noise ratio ( $\frac{\sigma_{AE}}{\sigma_{SN}}$ ) of all observed data is less than 2, as higher values have been associated with poor quality data (Eiler et al., 2017). Second, we examine all data for zero scans, where a 'zero scan' is a scan in which that peak is not observed; we reject any peaks where >1% of all scans are zero scans. Third, we test for 'peak drift' to confirm that each peak is in its expected location; deviations from the expected location may occur due to misidentification of a peak (e.g., because of the

presence of a contaminant) or due to shifts in peak location due to coalescence (Eiler et al., 2017; Hofmann et al., 2020). To do so, for each peak (e.g., the  $^{13}\text{C}$  peak of the 119 fragment) we select a close-lying reference peak (e.g., the Unsub peak of the 119 fragment), and compute the observed mass difference between the two. We also compute the theoretical mass difference between the two. If the observed and computed mass differences differ by more than 2 ppm, then we reject the observation. These tests cause us to reject the  $^2\text{H}$  peaks for all observed fragments.

#### 6.2.12 Analysis of spiked adenine fragmentation

Our 2021 dataset examined the fragmentation of C-8 spiked adenine in order to determine which fragments sampled this carbon. We note that the CIL adenine had up to a 7% contribution from C-2; we therefore performed two calculations: one assuming the CIL standard had a 7% label at the C-2 carbon, and a second assuming no labelling. We present the case where the 7% label was present; the case without a label is a straightforward simplification of this calculation.

First, we describe the system. In each case, our observations consist of the standardized isotope ratios observed for each fragment (see 6.2.10), which were used to compute the  $^{13}\text{C}$  concentration for each fragment,  $x_{obs,frag}$ . We can express the observed fragment concentration as a function of the site concentrations and the contributions of each site to the observed fragment. That is:

$$x_{obs,frag} = \sum_i k_i x_i \quad (6.9)$$

across all sites  $i$ , where  $n_c$  is the number of carbons in that fragment and  $k_i$  is the relative contribution of that site to that fragment. For example, consider a  $\text{C}_2$  fragment which is formed via two pathways, one containing  $\text{C}_2$  and  $\text{C}_8$ , and the other containing  $\text{C}_2$  and  $\text{C}_5$ , in equal proportions: then in eq (6.9),  $k_2 = 1$ , and  $k_8 = k_5 = 0.5$ . Returning to the general expression, we assume that, in the VWR standard, every site had the same concentration of  $^{13}\text{C}$  (defined as  $x_{unlab}$ ); then:

$$x_{obs,frag} = (k_{C4} + k_{C5} + k_{C6})x_{unlab} + k_{C2}x_{C2} + k_{C8}x_{C8} \quad (6.10)$$

Where

$$x_{C2} = (1 - y)x_{unlab} + 0.07y \quad (6.11)$$

$$x_{C8} = (1 - y)x_{unlab} + 0.95y \quad (6.12)$$

and  $y$  is the mixing ratio of our Cambridge Isotope Laboratory standard. We calculated  $y$  using the 119 fragment, which retains all five carbons ( $k_i = 1$  for all  $i$ ); therefore:

$$y = \frac{5x_{obs,119} - 5x_{unlab}}{1.02 - 2x_{unlab}} \quad (6.13)$$

With the mixing ratio constrained, we next tested possible values of  $k_2$  and  $k_8$  for each fragment. Beginning with:

$$x_{obs,frag} = (n_c - k_{C2} - k_{C8})x_{unlab} + k_{C2}x_{C2} + k_{C8}x_{C8}, \quad (6.14)$$

we rearrange:

$$x_{obs,frag} = k_{C2}(x_{C2} - x_{unlab}) + k_{C8}(x_{C8} - x_{unlab}) + n_c x_{unlab} \quad (6.15)$$

and solve for  $k_{C8}$ :

$$k_{C8} = \frac{x_{obs,frag} - n_c x_{unlab} - (x_{C2} - x_{unlab})k_{C2}}{(x_{C8} - x_{unlab})}. \quad (6.16)$$

Here,  $x_{obs,frag}$  is observed directly,  $n_c$  is known from fragment stoichiometry,  $x_{unlab}$  is assumed based on the molecular average content of the VWR adenine, and  $x_{C2}$  and  $x_{C8}$  are constrained based on our calculation of the mixing ratio and our assumptions about the amount of label at the C-2 and C-8 carbons in the CIL standard. Values for  $k_{C2}$  were taken from a previous study of adenine's collisional fragmentation (see Table 6.1; we also used these values in our site-specific reconstruction) (Nelson and McCloskey, 1992).

### 6.2.13 Site-Specific Reconstruction

We attempted to calculate site-specific enrichments from our M+1 data using the methods developed in Chapter 2. To do so, we defined a matrix giving the relative contributions of each site to each fragment, then used this to calculate M+1 relative abundances for each site from the fragment observations. Our input data include 1) a labelling study for collisional fragmentation of adenine which introduced a  $^{15}\text{N}$  label at each

nitrogen (individually) and separately a  $^{13}\text{C}$  label at C-2 (a total of 6 labelled adenines; (Nelson and McCloskey, 1992)); and 2) our labelling study using a  $^{13}\text{C}$  label at C-8. We discuss (2) below (6.3.1); as we must employ these results to describe our treatment of fragmentation, we include them here. We also direct the reader to two studies regarding the fragmentation pathways of adenine; however, because these did not experimentally probe the branching ratios, they do not provide further information for our analysis (Kamel and Munson, 2004; Giacomozzi et al., 2019).

Based on the results of these experiments, we divided the fragments into two groups: 'simple' fragments, where the losses come from easily interpretable processes (119, 109, & 94), and 'complex' fragments, which are formed from many possible routes (92, 82, 77, 67, 65, & 55) (Figure 6.2). We first examine the simple fragments. The 94 fragment ( $\text{M}^+ - \text{NH}_2\text{CN}$ ) is accompanied by the loss of N-1 and  $\text{N}^6$ ; we assert that the lost carbon comes entirely from C-6. The 119 fragment ( $\text{M}^+ - \text{NH}_3$ ) loses either the exocyclic  $\text{N}^6$  or N-1, with a minor contribution from N-9. For the 109 fragment ( $\text{M}^+ - \text{HCN}$ ) the primary loss route ( $\approx 90\%$ ) is due to the loss of N-1 and C-2, with a minor loss of  $\text{N}^6$  (4%) and N-9 (6%). We assume that the  $\text{N}^6$  pathway loses C-6 —  $\text{N}^6$ . Our labelling study with C-8 reveals a small amount of C-8 loss ( $\approx 5\%$ ), so we assume that N-9 — C-8 are lost together along the other minor pathway. Next, we consider the complex fragments; these may be formed by multiple neutral losses and exhibit complicated branching ratios, sampling every carbon and nitrogen to variable extents (typically  $>5\%$  and  $<90\%$ ). As an example, we show the 92 fragment ( $\text{M}^+ - \text{NH}_3 - \text{HCN}$ ) (Figure 6.2). This samples the following sites: N-1 (44%), N-3 (52%),  $\text{N}^6$  (29%), N-7 (86%), N-9 (83%), C-2 (50%), and C-8 (82%). It can be formed via the loss of HCN from the 119 fragment ( $\text{M}^+ - \text{NH}_3$ ) or the loss of  $\text{NH}_3$  from the 94 fragment ( $\text{M}^+ - \text{HCN}$ ). Both the 119 and 94 fragments form product ions with multiple structures, and each one of these structures can break down in multiple ways to form product ions with  $m/z = 92$ . In Figure 6.2, we show some possible routes to the 92 fragment for each of the major ( $>10\%$ ) structures formed in the 119 fragments.

**Table 6.1: Fragment Contributions Used to Compute Site-specific Structure**

Site Names	Element	Number Atoms	Fragment 119	Fragment 109	Fragment 94
C-2	C	1	1	0.1	1
C-458	C	3	1	0.98	1
C-6	C	1	1	0.96	0
N-1	N	1	0.455	0.1	0
N-6	N	1	0.575	0.96	0
N379	N	3	0.99	0.98	1
H-all	H	6	3/6	5/6	4/6

Because of this greater complexity, we calculated site-specific results using only the simple fragments (119, 109, and 94). We defined the following sites, where a site is group of analytically indistinguishable atoms: C-2, C-6, C-458, N-1, N-6, N-379, and H-all. We assigned the relative contribution of each site to each fragment in Table 6.2. Then we used this data to construct a matrix, taking the M+1 relative abundances of the sites to the M+1 relative abundances of the fragments:

$$\begin{pmatrix} 1 & 1 & 1 & 0 & 0 & 0 & 0 \\ 0 & 0 & 0 & 0 & 0 & 1 & 0 \\ 0 & 0 & 0 & 1 & 1 & 0 & 0.5 \\ 0.1 & 0.96 & 0.98 & 0 & 0 & 0 & 0 \\ 0 & 0 & 0 & 0.1 & 0.96 & 0.98 & 0 \\ 0.9 & 0.04 & 0.02 & 0.9 & 0.04 & 0.02 & 0.167 \\ 1 & 0 & 1 & 0 & 0 & 0 & 0 \\ 0 & 0 & 0 & 0 & 0 & 1 & 0 \\ 0 & 1 & 0 & 1 & 1 & 0 & 0.333 \end{pmatrix} \begin{pmatrix} \rho_{C2}^{13C} \\ \rho_{C6}^{13C} \\ \rho_{C458}^{13C} \\ \rho_{N1}^{15N} \\ \rho_{N6}^{15N} \\ \rho_{N379}^{15N} \\ \rho_{Hall}^{2H} \end{pmatrix} = \begin{pmatrix} \rho_{119}^{13C} \\ \rho_{119}^{15N} \\ \rho_{119}^{Unsub} \\ \rho_{109}^{13C} \\ \rho_{109}^{15N} \\ \rho_{109}^{Unsub} \\ \rho_{94}^{13C} \\ \rho_{94}^{15N} \\ \rho_{94}^{Unsub} \end{pmatrix}.$$

Inverting and solving this matrix allows us to calculate the M+1 relative abundances of each site.

With the M+1 relative abundances in hand, we next calculate the site-specific enrichments. We first calculate the  $U^{M+1}$  value, using the molecular-average Orbitrap-IRMS measurement and the  $\rho_{119}^{13C}$  value (which samples all 5 carbons):

$$U^{M+1} \approx 5 * \frac{R^{13C}}{\rho_{119}^{13C}}. \quad (6.16)$$

We then apply this  $U^{M+1}$  value to each of our site-specific  $M+N$  relative abundances to calculate the site-specific enrichments; for example, for  $N^6$ :

$$R_{N^6}^{15N} = U^{M+1} * \rho_{N^6}^{15N} \quad (6.17)$$

We report our results as delta values giving the enrichment or depletion of the sample relative to the standard for each site. Because we do not know the site-specific composition of the standard in any reference frame, we cannot interpret these results in any other reference frame (e.g., VPDB, AIR).

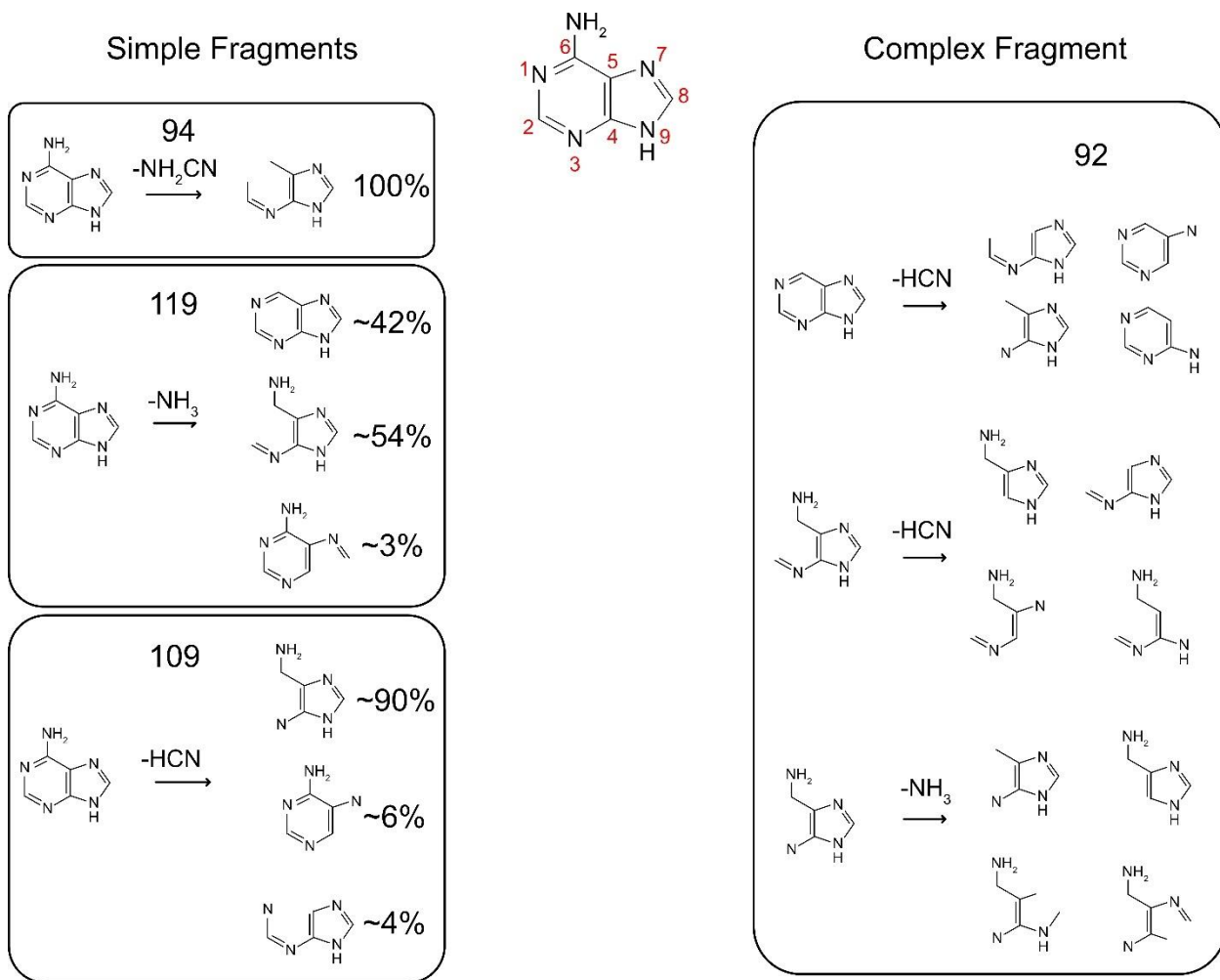


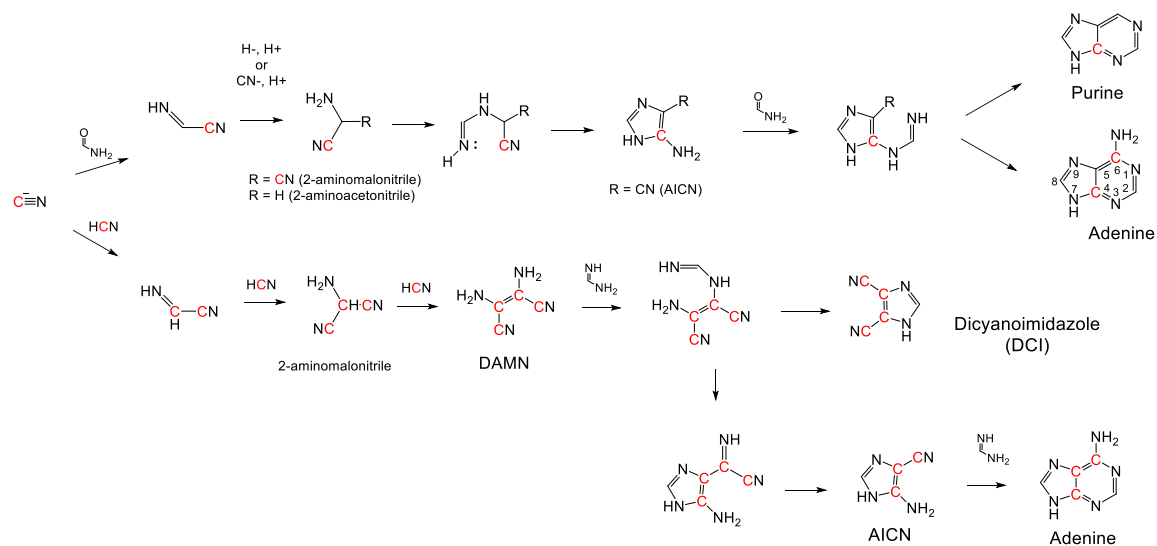
**Figure 6.2:** Branching ratios along the pathways to adenine fragments. We distinguish between ‘simple’ fragments, where the fragment is formed primarily via one pathway, and ‘complex’ pathways, which form by multiple neutral losses and many distinct pathways. On the left are fragmentation pathways for the ‘simple’ fragments, while on the right is a representative example of a ‘complex’ fragment.

#### 6.2.14: Analysis of the Reaction Pathway

We analyzed the mechanism for the formation of adenine from cyanide and formamide to examine possible sources of the isotopic signature. There is evidence for multiple reaction mechanisms: what we label the “formamide” reaction mechanism (as it is more active with greater amounts of formamide), implementing 3 formamide carbons and 2 cyanide carbons; and a “DAMN” mechanism, proceeding through a diaminomalonitrile (DAMN) intermediate, which includes 2 formamide carbons and 3 cyanide carbons (Scheme 6.1) (Hudson et al., 2012). We note that dicyanoimidazole (DCI), another major product of the reaction, is likely formed as a branch of the DAMN route, while purine is a side product of the formamide route (Liu et al., 2020). Previous studies indicate that, under the conditions used here, the formamide route is dominant, but there is a significant contribution from the DAMN route, and the relative amounts of adenine formed via each pathway have not been quantified (see especially the supplement to (Hudson et al., 2012)). Each route forms the intermediate 4-aminoimidazole-5-carbonitrile (AICN). Two sets of studies have explored the “formamide” reaction mechanism via DFT: first a series of a studies by Wang et al., which explored routes from formamide to purine and adenine using formamide as a catalytic solvent, and second, a study by Slavova and Enchev which revisited this mechanism as well as routes to other nucleobases (Wang et al., 2013c, b, a; Slavova and Enchev, 2020). We also direct the reader to a study by Šponer et al., which explored the synthesis of adenine in formamide by way of a pyrimidine intermediate, and differs from our working mechanism (Šponer et al., 2012). No study has included the use of  $Mg^{2+}$ , as in our experiment. While the DAMN route has been investigated, this mechanism occurs in many contexts and the details are significantly different from our experiment. For example, these studies explore a route where photochemistry is used to convert DAMN to AICN and the reaction takes place in aqueous solvent, or consider the pathway in interstellar space (Glaser et al., 2007; Roy et al., 2007). To our knowledge, no computational study of the formation of adenine from the DAMN pathway in formamide has been performed. Given the significant impact on the energetics



of the solvent, as well as our addition of  $Mg^{2+}$ , we do not analyze this route in detail.



**Scheme 6.1:** Possible mechanisms active in our formamide synthesis. The top route has been identified as the dominant source of adenine based on previous labelling experiments (Hudson et al., 2012), but there is a minor contribution from the competing “DAMN” route, below. DCI, a major product, has been identified as a side product of the DAMN pathway (Liu et al., 2020).

Along these pathways, isotopic effects can occur as either equilibrium isotope effects (EIEs) or kinetic isotope effects (KIEs). EIEs occur due to the lowering of vibrational energies due to bonds with heavy elements; therefore, heavy isotopes are likely to favor bonds with heavy elements. These may occur during reversible steps. In contrast, KIEs act during irreversible steps due to differences in the activation energy for the reaction between heavy and light isotopes and have the strongest effects on atoms which are involved in bond formation or destruction. We therefore explored the energetics of the reaction to determine which steps are reversible and irreversible and which types of isotope effects are likely to occur. To do so, we compiled the energetics from previous computational studies ((Wang et al., 2013c, b, a; Slavova and Enchev, 2020)), then approximated rates of each elementary step via an Eyring-Polyani treatment. That is, we assumed the rate constants  $k$  were:

$$k = \frac{\kappa k_b T}{h} e^{-\frac{\Delta G^\ddagger}{RT}} \quad (6.18)$$

where  $\kappa$  is the transmission function (here set to 1),  $k_b$  is the Boltzmann constant,  $T$  is temperature (here 438 K),  $h$  is Planck's constant,  $\Delta G^\ddagger$  is the activation energy for the reaction, and  $R$  is the universal gas constant. We computed rates for both forward and reverse reactions. We chose to treat reactions with activation energies of  $< 31$  kcal/mol as permitted, as these had half-lives of  $< 5$  minutes under our reaction conditions. With this treatment, if a forward elementary step were permitted while the back reaction was not, we identified it as a possible source of a KIE; otherwise, we identified it as a source of equilibrium fractionation.

When different compounds were in equilibrium with each other, we estimated the magnitudes of equilibrium effects as follows. First, we note that equilibrium fractionation can be estimated using the reduced partition function ratios,  $\beta$ , for heavy and light substitutions. For a single substitution, and under the harmonic approximation:

$$\beta = \left(\frac{Q_1}{Q_2}\right) = \prod_i \frac{v_{1i}}{v_{2i}} * \frac{e^{-\frac{u_{1i}}{2}}}{e^{-\frac{u_{2i}}{2}}} * \frac{1 - e^{-\frac{u_{1i}}{2}}}{e^{-\frac{u_{2i}}{2}}} \quad (6.19)$$

where  $u_{ni} = \frac{hv_{ni}}{k_B T}$ ,  $h$  is Planck's constant,  $k_B$  is the Boltzmann constant, and  $v_{ni}$  is the harmonic vibrational frequency in  $s^{-1}$  of the  $i$ th vibrational mode; the product is across all  $i$  vibrational modes of the molecule (Urey, 1947; Bigeleisen et al., 1973; Rustad, 2009; Liu et al., 2010). The equilibrium fractionation for substitution between two compounds,  $j$  and  $k$ , is then:

$$\alpha_{j/k} = \frac{\beta_j}{\beta_k}. \quad (6.20)$$

Calculating the  $\beta$  factors explicitly requires electronic structure calculations which are beyond the scope of this study; however, we can gain some insight by using a 'bond additivity' approach, first proposed by Galimov which has been shown yield similar results (Galimov, 1985; Rustad, 2009). Galimov's approach assumes that 1)  $\beta$  factors will be dominated by the local bonding environment of an atom and 2) effects are driven by the type of bond (e.g., C-C, C-N, or C=C) and are similar for the same types of bonds in different

molecules. Under these assumptions, the  $\beta$  factor for atom  $i$  in a molecule can be approximated as:

$$\beta_i = 1 + \sum_m L_m \quad (6.21)$$

where  $L_m$  is a constant based on the type of bond and the sum is taken across all bonds to atom  $i$ . For example, for the carbon in formamide:

$$\beta_C = 1 + L_{C=O} + L_{C-N} + L_{C-H}. \quad (6.22)$$

This approach allowed us to calculate  $\beta$  factors, and therefore equilibrium fractionations, for compounds which equilibrated with each other. Our  $L_m$  values were taken from Galimov, 1985.

## 6.3 Results

### 6.3.1 Fragmentation of Labelled Adenine

For the SPK adenine, we found a mixing ratio of 7.9% (i.e., the sample consisted of 7.9% CIL adenine and 92.1 % VWR adenine). Results for the amount of C-8 label retained assuming no label and a 7% label at C-2 are presented in Table 6.2. Errors induced by our acquisition errors on each beam are  $<0.01$  and significantly smaller than those due to the uncertain abundance at the C-2 site.

**Table 6.2: Analysis of Labeled Fragments**

Fragment m/z	Amount C-8 retained: No label at C-2	Amounts C-8 retained: label at C-2
<b>119 (M<sup>+</sup> - NH<sub>3</sub>)</b>	<b>1</b>	<b>1</b>
<b>109 (M<sup>+</sup> - HCN)</b>	<b>0.90</b>	<b>0.95</b>
<b>94 (M<sup>+</sup> - NH<sub>2</sub>CN)</b>	<b>1</b>	<b>1</b>
92 (M <sup>+</sup> - NH <sub>3</sub> - HCN)	0.80	0.82
82	0.24	0.25
77	0.46	0.44
67	0.89	0.93
65	0.17	0.15
55	0.06	0.06

### 6.3.2 Preparatory HPLC

HPLC traces from formamide syntheses at 165 °C from 30 minutes – 4 hours are displayed in Figure 6.3. Our primary products were adenine, purine, and dicyanoimidazole (DCI), in line with previous results (Hudson et al., 2012; Liu et al., 2020). DCI is likely formed as a side-product of the DAMN pathway (Scheme 6.1) (Liu et al., 2020). The adenine signal remained constant throughout the time series, while DCI signals decreased, and purine signals increased with increasing reaction time. 7 mg of adenine was obtained for the 2-hour reaction, corresponding to 17 % yield from cyanide.

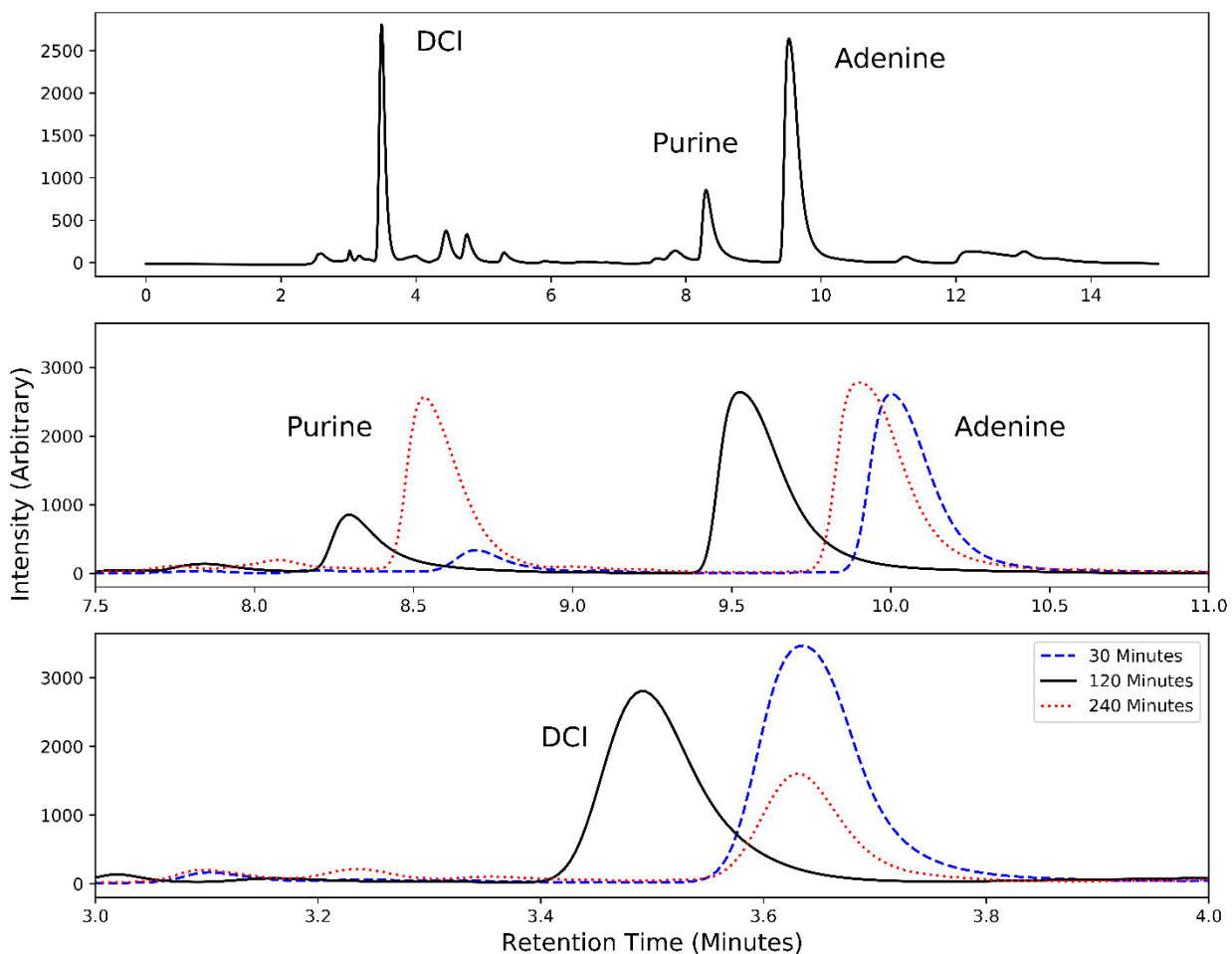


**Figure 6.3:** HPLC traces of 100  $\mu\text{L}$  of extracted product, corresponding to  $\sim 300 \mu\text{g}$  of adenine. The top panel shows the full time series for the 2-hour reaction, while the middle and bottom panel zoom in on major products and show differences with different reaction times. The identity of the three major products, DCI, purine and adenine are consistent across all measured timescales.

### 6.3.2 Molecular-Average Isotope Data

The molecular-average isotope enrichment of our precursors (constrained via EA-IRMS) and our synthesized adenine (constrained via Orbitrap-IRMS) are presented in Table 6.2. We also include the calculated composition of our product adenine assuming that no isotope effects were experienced during the synthesis and that only the “formamide” route was active (i.e., the weighted average of 3 formamide and 2 cyanide carbons). However, our other major product, DCI, has been identified as a side product of the DAMN pathway (Liu et al., 2020); we comment that the branch point could occur prior to the production of DAMN, during the formation of 2-aminomalonitrile, which is present on both routes. Our experiment does not distinguish between adenine synthesized by the DAMN and the formamide pathway and we cannot rule out the possibility of a significant contribution from the DAMN route. Future work must investigate the branching between these pathways under the presence of variable quantities of cyanide. We find that the recovered adenine has a  $\delta^{13}\text{C}_{\text{PDB}} = -55.8 \pm 0.8 \text{ ‰}$ , or  $32.4 \pm 1.1 \text{ ‰}$  less than the predicted value based on our precursor composition assuming production from 2 cyanide and 3 formamide carbons. A greater contribution from the DAMN pathway would make our estimate of the KIE slightly larger (by  $\approx 3 \text{ ‰}$  if all adenine was produced along this route).

**Table 6.2: Molecular-Average Data for Precursors and Synthesized Compounds**

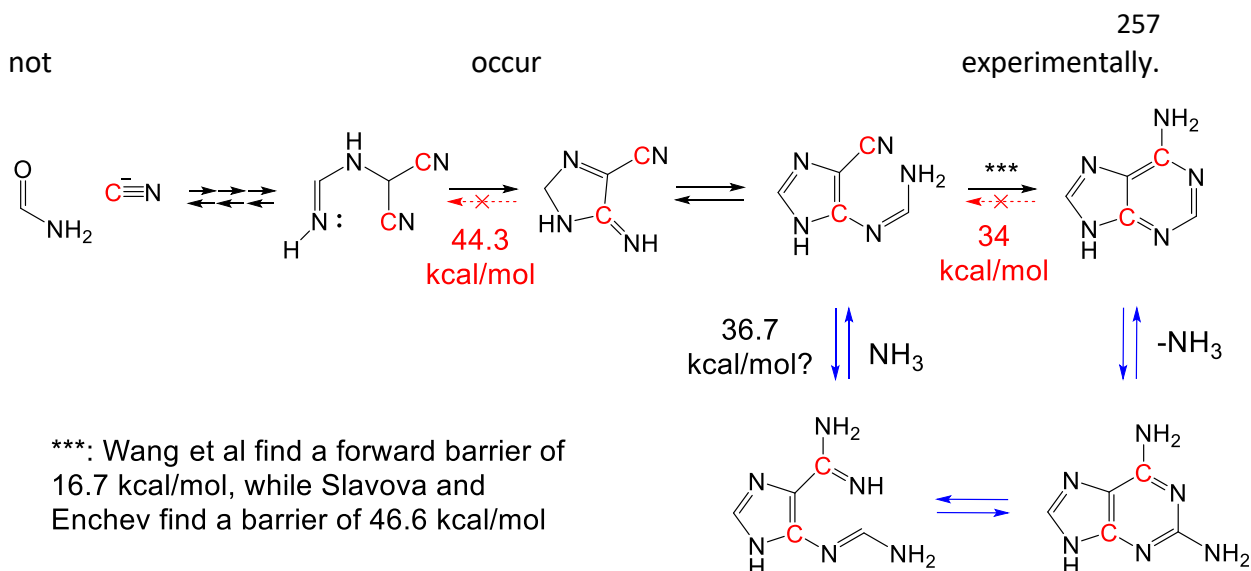
<b>Compound</b>	<b><math>\delta^{13}\text{C}_{\text{PDB}}</math></b>	<b><math>\delta^{15}\text{N}_{\text{AIR}}</math></b>
<b>VWR Adenine Standard</b>	-9.8	-4.2
<b>Formamide</b>	-29.5	---
<b>Cyanide</b>	-14.7	1.0
<b>Calculated Synthetic Adenine absent KIEs<sup>a</sup></b>	-23.6	---
<b>Synthesized adenine (2 hour reaction)</b>	$-55.8 \pm 0.8$	$-25.6 \pm 1.2$

Errors are  $\pm 0.2 \text{ ‰}$  (vs PDB or AIR) unless indicated otherwise.

a: Calculated value assuming no kinetic fractionation, e.g., values averaged across cyanide and formamide inputs, and that there was no contribution from the DAMN pathway.

### 6.3.3: Analysis of the Reaction Pathway

Our Eyring-Polanyi treatment of previously compiled energetics identified three steps on the route to adenine which may be irreversible: the reaction of cyanide with water to form formamide, the closure of the 5-membered ring, and the closure of the 6-membered ring. First, we consider the reaction between formamide and cyanide. Wang et al. predict the dehydration of formamide to cyanide has an activation energy of 26.1 kcal/mol, while the reverse reaction (cyanide + H<sub>2</sub>O → formamide) has an activation energy of >35 kcal/mol and is disallowed over the course of our study (Wang et al., 2013c, b, a). Results from Hudson et al. are consistent with the back reaction not occurring, in that an experiment with labelled cyanide and unlabeled formamide did not result in any labeling on the C-2 and C-8 (formamide derived) carbons of adenine (Hudson et al., 2012). However, the low activation energy for the forward reaction suggests that some cyanide may be provided by formamide. A labelling experiment performed by Hudson et al. under similar conditions, with <sup>13</sup>C-labeled cyanide and unlabeled formamide, can reveal the dynamics here: if the formamide were a source of unlabeled cyanide, we would anticipate the formation of some unlabeled adenine. Mass spectrometric results were not provided for adenine synthesized during this reaction but were for purine synthesized in the same mixture. The purine samples one cyanide and four formamide carbons, and no unlabeled purine was observed, suggesting that the contribution of formamide to the cyanide pool was negligible. The lack of such contribution demonstrates the limitations of our kinetic model—while our Eyring-Polanyi model suggests rapid formamide dehydration, this does



**Scheme 6.2:** Energetics of the formamide pathway to adenine. Literature studies differ on the energetics of the 6-membered ring closure; (Wang et al., 2013c, b, a) find a modest barrier, while (Slavova and Enchev, 2020) find a severe one. Slavova and Enchev hypothesize an alternative mechanism, via  $\text{NH}_3$ , but we note the energetics remain unfavorable according to our Eyring-Polyani treatment.

Next, we examine the ring closing reactions (Scheme 6.2). For the five-membered ring closure, both Wang et al. and Slavova and Enchev find a significant barrier to back reaction, of 44.3 kcal/mol and 46.8 kcal/mol, respectively (Wang et al., 2013c, b, a; Slavova and Enchev, 2020). However, the studies find different dynamics for the 6-membered ring closure. In the Wang et al. study, this occurs with a barrier of 16.2 kcal/mol, while the reverse reaction has a barrier of 34 kcal/mol ( $t_{1/2} \approx 100$  minutes under our conditions). However, the Slavova and Enchev study finds a significantly higher activation energy of 46.6 kcal/mol for the same reaction; their mechanism differs slightly in that their mechanism uses formimidic acid to catalyze the ring closure while Wang et al. use formamide. We also note the Wang et al. study proceeds through several transition states, whereas the Slavova and Enchev occurs in a single step. If the activation energy is 46.6 kcal/mol, the ring closure would not occur in any significant amount over the timescale of our study. Slavova and Enchev suggest an alternative mechanism where the 6-membered ring closure occurs between C-2 and N-1, with an activation energy of 36.7 kcal/mol; the reverse reaction is also feasible (23.2 kcal/mol) (Scheme 2). With their modified mechanism, the reaction would proceed slowly (36.7 kcal/mol implies  $t_{1/2} \approx 43$  hours at 165 °C). In either case, kinetic

isotope effects are likely to affect the C-4 carbon during the closure of the 5-membered ring; depending on mechanism, they may also affect the C-6 carbon during the closure of the 6-membered ring.

We then examined the equilibrium fractionation for key compounds which were formed reversibly. In Figure 6.4, we show major compounds which will exist in equilibrium, based on our analysis of the energetics, and the associated  $\beta$  factors; we additionally report the enrichment or depletion in ‰ vs the source carbon (formamide or cyanide). We report these results for both the final product adenine, and the final intermediate which is in equilibrium (via many elementary steps) with each source of carbon. For example, the first irreversible step is the closing of the 5-membered ring, at which point 4 carbons have been incorporated; we report results for all four carbons in this intermediate. We find that equilibrium effects can lead to depletion of up to 15 ‰ at the formamide-derived C-2 and C-8 carbons; they can also cause enrichment of  $\approx$ 40–80 ‰ at the cyanide-derived C-4 and C-6. Given our observation that the product adenine is depleted at all carbons (or all except the C-6), we suggest that equilibrium effects for cyanide do not play a substantial role in the observed signature.

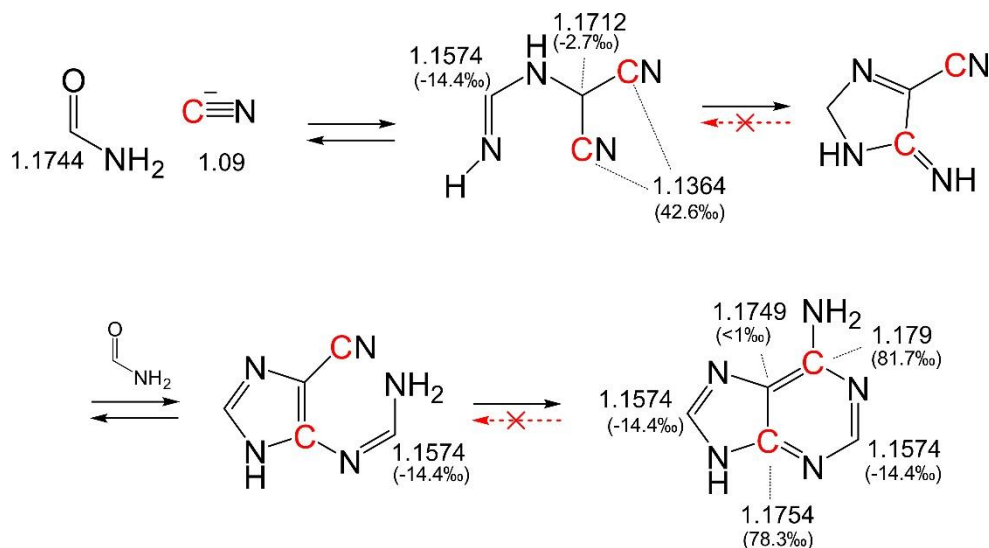


**Figure 6.4:** Reduced partition function ratios ( $\beta$  factors) for major intermediates and the product adenine. Enrichments or depletions vs the source of each carbon along this route are reported in ‰.  $\beta$  factors were obtained via the bond additivity approach proposed by Galimov (Galimov, 1985).



### 6.3.4 Orbitrap-IRMS Fragmentation Data

Our Orbitrap-IRMS fragmentation data are presented in Table 6.3 and visualized in Figure 6.5. In each case, the values we give are delta values comparing the M+N relative abundances of each observed ion beam. First, we comment that main trend we observe is depletion of the  $^{13}\text{C}$  ion beam coupled with increases in the M+N relative abundance of  $^{15}\text{N}$ . We emphasize that this need not correspond to an enrichment of  $^{15}\text{N}$  in the sample—because all M+N relative abundances must sum to 1, a decrease in the  $^{13}\text{C}$  content will be accompanied by an increase in the M+N relative abundance of  $^{15}\text{N}$ . Second, we note that if the adenine sample and standard contained no site-specific variation, we would observe (within error) identical values for the M+N relative abundances of  $^{13}\text{C}$  and  $^{15}\text{N}$  across all fragments, as the relative enrichment of these isotopes would not depend on which sites they sample. (The Unsub M+N relative abundance would continue to change in variable amounts, based on the proportion of C, N, and H contributing to that beam). We do observe substantial variation between fragments, suggesting that at least one of our sample or standard exhibit site-specific variation in both C and N.

**Table 6.3: Delta comparisons for fragmentation data**

	<b><math>^{13}\text{C}</math></b>	<b><math>^{15}\text{N}</math></b>	<b>Unsub</b>
<b>119</b>	-9.7 (0.1)	30.8 (0.4)	22.3 (0.9)
<b>109</b>	-7.7 (0.8)	30.7 (2.0)	-5.8 (2.0)
<b>94</b>	-16.9 (0.5)	36.9 (1.5)	22.9 (-1.1)
<b>92</b>	-11.2 (0.1)	31.3 (0.4)	8.3 (0.3)
<b>82</b>	-3.8 (1.0)	27.7 (2.2)	-5.3 (1.1)
<b>77</b>	-20.3 (0.4)	21.0 (1.5)	36.9 (0.8)
<b>67</b>	-20.1 (0.2)	28.9 (0.8)	14.4 (0.2)
<b>65</b>	-12.3 (0.2)	22.2 (0.6)	7.5 (0.2)
<b>55</b>	-10.2 (0.6)	22.7 (1.3)	2.1 (0.3)

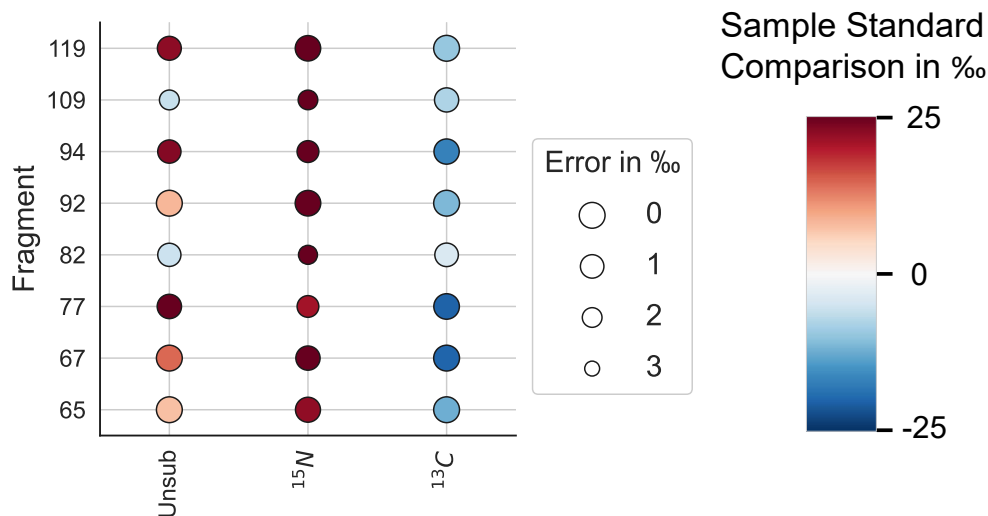


**Figure 6.5** Recovered fragment-specific comparisons for adenine synthesized from a 2-hour reaction of cyanide and formamide. Values are delta values giving the comparison between M+1 relative abundances for each isotope in each fragment. The <sup>15</sup>N values are heavily enriched relative to the standard, but we note this can be an artifact of M+1 relative abundance space; the decrease in <sup>13</sup>C will induce an increase in the M+1 relative abundance of <sup>15</sup>N even with no change in <sup>15</sup>N content.

### 6.3.5 Site-specific reconstruction

Our recovered values and error bars for the site-specific comparison between sample and standard ( $\delta_{STD}$ ) are shown in Table 6.4. The abundances of N-1 and N<sup>6</sup> are correlated and we constrain their combined abundance more precisely, listed in Table 6.4 as combined (N-1, N<sup>6</sup>). We also list the origin of each carbon or nitrogen, assuming that no adenine was produced via the DAMN pathway. If the DAMN pathway were active, then C-4 and N-9 are also cyanide derived. Our lack of knowledge of the composition of the standard (VWR) makes it difficult to interpret our results in terms of an absolute reference frame (VPDB). For example, if there is variation in the site-specific enrichment of the VWR standard, it would manifest as significant variation in our  $\delta_{STD}$  values even if the adenine sample does not show any heterogeneity. Simultaneously, variation in the VWR standard could amplify or mask variation in our product adenine. For example, suppose the  $\delta^{13}C_{VPDB}$  of C-6 in the standard was  $\approx -30$  ‰ while  $\delta^{13}C_{VPDB}$  of C-4 was  $\approx 10$  ‰, while all other sites were the molecular average value of  $-9.8$  ‰; this scenario is plausible based on our molecular average measurement. In this case, although our results show a large difference

between C-6 and C-4 for  $\delta_{\text{STD}}$  values, the two would have equivalent  $\delta^{13}\text{C}_{\text{VPDB}}$  values of  $\approx -45$  ‰. To address this problem, we calculated a plausible range of  $\delta^{13}\text{C}_{\text{VPDB}}$  values for each site assuming that each site of the VWR standard differed from the molecular average value of  $-9.8$  ‰ by no more than  $20$  ‰ (i.e., each carbon had  $\delta^{13}\text{C}_{\text{VPDB}}$  between  $-30$  and  $10$  ‰). We note that variation in one site demands compensating variation in others; i.e., if one site is depleted relative to the molecular average value by  $20$  ‰, then the combination of the other sites must be enriched by an average of  $\approx 5$  ‰ to yield our observed molecular average value. Based on these estimates, we suggest a range of plausible isotope effects for each site. We find that C-2 and the combined (C-4, C-5, C-8) sites both experience significant depletions ( $>15$ ‰ versus their precursors) during the synthesis. In contrast, C-6 may experience either no depletion or a depletion of up to  $30$  ‰.

**Table 6.4: Site-specific Reconstruction**

Site	$\delta_{\text{STD}}$	Range of $\delta_{\text{VPDB}}$	Plausible Isotope Effect Range	Origin
C-2	$-54.3 \pm 3.3$	-44.3 to -84.3	-15 to -55 ‰	Formamide
(C-4, C-5, C-8)	$-55 \pm 1.5$	-45 to -85	-25 to -65 ‰	C-4: Cyanide. C-5/C-6: Formamide
C-6	$-15.1 \pm 2.0$	-5 to -45	10 to -30 ‰	Cyanide
N-1	$-18.8 \pm 11.2$	-3 to -43	-	Formamide
N-6	$-21.8 \pm 9.1$	-7 to -47	-	Cyanide
(N-1, N-6)	$-21.1 \pm 4.4$		-	---
(N-3, N-7, N-9)	$-3.3 \pm 1.5$		-	N-3: Cyanide. N-7/N-9: Formamide
H-all	$11.8 \pm 34$		-	---

## 6.4 Discussion

### 6.4.1 Analysis of the Reaction Pathway

Our results show a net isotope effect of  $32.4 \pm 1.1$  ‰ in the  $\delta^{13}\text{C}$  for the product adenine; we now explore some possible causes of this depletion. We first note that the adenine is part of a complex reaction network with many side pathways. While we only

quantified the yield of adenine from cyanide (17%), previous results for the yield of DCI (21 %) (Liu et al., 2020) and purine (3%) (Hudson et al., 2012) suggest that only a minority of the cyanide is accounted for (Figure 6.6). The remaining >50 % may form either minor products (some of which may be visible on the HPLC data, Figure 6.3 as peaks which were not analyzed in detail), form larger compounds which constitute the insoluble residue (likely poly hydrogen cyanide (Cataldo et al., 2010; Ruiz-Bermejo et al., 2021)), or remain present in solution. All yields from formamide are minor,  $\approx 1\%$ . Based on our observation that DCI and adenine abundance do not increase following 30 minutes of reaction (Figure 6.3), and based on the low abundance of minor products, we hypothesize the remaining >50 % of cyanide is primarily in the residue. Future work should determine both how much cyanide ends up in the residue, as well as the relative proportions of cyanide and formamide in this polymer.

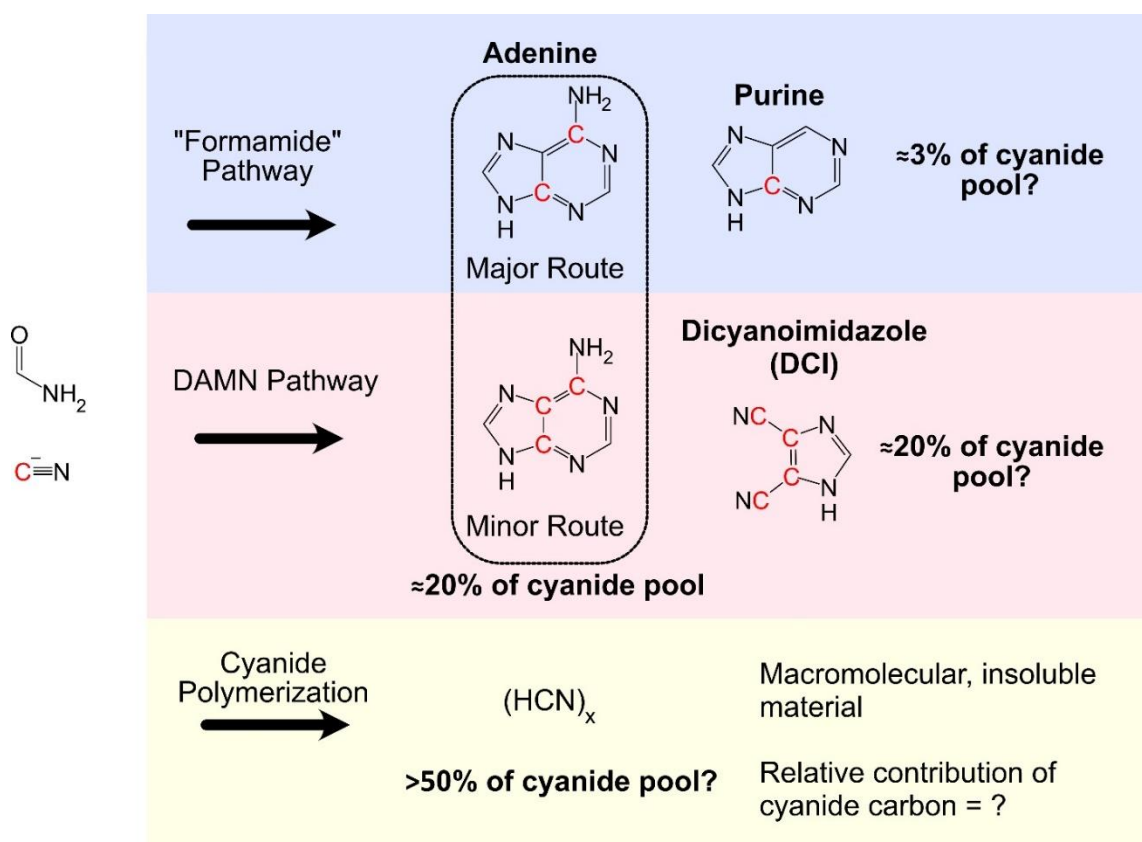


**Figure 6.6:** Routing of cyanide during our formamide synthesis. Primary products include adenine and DCI, while purine is a minor product; together, these account for <50 % of the cyanide. The remaining cyanide could partition into either minor soluble products or the insoluble residue.

Because we lack knowledge about most products formed via the reaction (Figure 6.6) and many details about the energetics are unknown, interpretation of our site-specific results is challenging; nevertheless, we can draw some tentative conclusions, as follows. First, we note that if adenine were formed via the formamide route only, with the energetics constrained by Wang et al. and our working assumption about the kinetics, we would anticipate KIEs at C-4 and C-6, and EIEs which may cause depletion of  $\approx 15$  ‰ (vs formamide) at C-2 and C-8, and enrichment of 40-80 ‰ (vs cyanide) on C-6 and C-4. KIEs for other ring closing reactions are in the range of 20-50 ‰, which we can use as a working estimate (Singleton and Thomas, 1995; Keating et al., 1999; Singleton et al., 1999; Singleton and Szymanski, 1999). If all these effects were active, we would anticipate anything from a small depletion to a large enrichment on C-6 and C-4 (-10 to 60 ‰) and modest depletions ( $\approx -15$  ‰) on C-2 and C-8. However, these effects are insufficient to account for our observed molecular average change. While they can explain our observations for the C-6 and C-2 carbons, if we assert effects of -10 ‰ for C-6 and -15 ‰ for C-4, the remaining carbons must have an average depletion of  $\approx -47$  ‰; compatible with our measurements, but difficult to justify theoretically. For these reasons, we believe our description of the kinetics is incomplete, or that a substantial amount of adenine is formed via alternative pathways (e.g., DAMN) with distinct isotope effects. Finally, we comment that the isotope effects associated with the other pathways, e.g. cyanide polymerization, can have a substantial impact on our results. For example, if we assume each pathway is operating continuously, and the cyanide polymer preferentially incorporates heavy cyanide, then it will cause the cyanide pool to gradually become depleted during the reaction, causing adenine carbons originating from cyanide to appear isotopically light.

## 6.4.2 Geochemical interpretation

### 6.4.2.1 Precursor values in the Extraterrestrial Context

We next explore implications for meteoritic purines. We begin with the precursor pools. If the adenine observed on meteorites was formed via the mechanism investigated here, it would sample two primary pools of carbon and nitrogen: cyanide and formamide. The  $\delta^{13}\text{C}_{\text{VPDB}}$  of meteoritic cyanide has been investigated previously for the Murchison meteorite, and found to have a value of  $-7 \pm 10 \text{ ‰}$  based on the isotopic content of alanine hypothesized to form from this cyanide (Chimiak et al., 2021). The  $\delta^{15}\text{N}_{\text{AIR}}$  of cyanide on Murchison has also been investigated and found to have a value of  $\approx 6 \pm 5 \text{ ‰}$ , by analysis of the HCN released from salts following the addition of phosphoric acid (Pizzarello, 2014). However, the author of that study notes that this value is significantly depleted relative to other water-soluble compounds found in meteorites, which typically have  $\delta^{15}\text{N}_{\text{AIR}}$  values of  $\approx 50$  to  $450 \text{ ‰}$ , and cautions that the observed HCN may not reflect the HCN pool used in early organic syntheses.

The formamide source is less well constrained; its isotopic content and abundance on CM2 chondrites have not been determined. Formamide has been detected in the interstellar medium and observed on comets, and was plausibly present on asteroid parent bodies (Biver et al., 2014; Goesmann et al., 2015; López-Sepulcre et al., 2019). Measurements of the  $^{13}\text{C}/^{12}\text{C}$  ratio of interstellar formamide have been made, albeit only close to the galactic center. The resulting values (e.g.,  $25 \pm 8$ ,  $\delta^{13}\text{C}_{\text{PDB}} = 2600_{-900}^{+1700}$ ) have, for our purposes, broad error bars; they are also typical of  $^{12}\text{C}/^{13}\text{C}$  values near the galactic center, and are not instructive for our purposes (Gardner et al., 1980; Langer and Penzias, 1990; Halfen et al., 2017). The  $^{15}\text{N}$  isotopologue of formamide has only been tentatively detected (Coutens et al., 2016; Belloche et al., 2017).

We can sketch out some hypotheses surrounding the isotopic content of formamide based on its formation mechanism. Here, the key question is: does formamide arise from

the  $^{13}\text{C}$ -deplete reduced carbon pool (likely the origin of meteoritic CN) or does it come from the  $^{13}\text{C}$ -enriched CO pool? With this framing, we examine three hypothesized pathways to formamide: gas phase chemistry, grain-surface chemistry, and cyanide hydrolysis (each reviewed in (López-Sepulcre et al., 2019)). In the gas-phase, there are direct routes from the CO pool (e.g.,  $\text{NH}_2 + \text{H}_2\text{CO} \rightarrow \text{NH}_2\text{CHO}$ ) as well as routes through cyanide (e.g.,  $\text{CN}^+ + \text{H}_2\text{O} \rightarrow \text{HNCO}^+ + \text{H}$ , followed by  $\text{HNCO} + \text{HCO}^+ \rightarrow \text{H}_2\text{NCO}^+ + \text{CO}$ , and subsequent protonation of  $\text{H}_2\text{NCO}$ ). Similarly, on grain surfaces, multiple pathways are plausible—the carbon containing compound can originate from the CO pool (e.g., CO itself (Fedoseev et al., 2016)) or the reduced carbon pool (e.g., HCN (Gerakines et al., 2004)). In contrast, if formamide were formed via cyanide hydrolysis on the asteroid parent body, it would sample the same carbon pool as CN. The cyanide hydrolysis scenario is therefore more restrictive than the others in terms of isotopic content.

#### 6.4.1.2 Nucleobases Observed on Meteorites

No direct measurements of the isotopic content of meteoritic adenine have been made. However, the  $\delta^{13}\text{C}_{\text{VPDB}}$  content of two nucleobases, xanthine ( $\delta^{13}\text{C}_{\text{VPDB}} = 37.7 \pm 1.6$  ‰) and uracil ( $\delta^{13}\text{C}_{\text{VPDB}} = 44.5 \pm 2.3$  ‰), has been measured. Adenine and xanthine are both purines, and it is plausible that the two are related by common intermediates. For example, the AICN intermediate identified along the formamide route to adenine has been observed to form xanthine when heated in the presence of urea (Shaw, 1950; Sanchez et al., 1968). We do not observe xanthine, nor is it observed under reaction conditions like those we employ (i.e., heating formamide with or without cyanide and in the presence of various catalysts, such as powdered Murchison meteorite) (Saladino et al., 2011, 2012, 2018; Hudson et al., 2012; Yadav et al., 2020); however, theoretical mechanisms of xanthine formation from formamide have been proposed (Jeilani et al., 2014; Slavova and Enchev, 2020). Indeed, a proposed network for purine synthesis on carbonaceous chondrite parent bodies suggests that a combined synthesis of xanthine and adenine occurred, with key intermediates (5-aminoimidazole-4-carboxamide (AICA), 5-aminoimidazole-4-carbonitrile

(AICN), and 5-aminoimidazole-4-carboxamide (AICAI)) formed from cyanide and other cyanide-derived compounds such as cyanogen, formamide, formamidine, and urea (Koga et al., 2024).

If we assume this hypothesized network were active, the most interesting question is: what is the source of xanthine's observed enrichment in  $\delta^{13}\text{C}_{\text{VPDB}}$ ? If all of xanthine's carbons originated from the reduced carbon pool and/or cyanide, and there were no significant isotope effects due to degradation, it is difficult to explain the observed enrichment; the mechanism must include an inverse isotope effect (i.e.,  $k_{13}/k_{12} > 1$ ) with a magnitude sufficient to enrich the molecular-average carbon signature of xanthine by  $\approx 40$  ‰ (i.e., an effect of  $\approx 200$  ‰ at a single carbon, 100 ‰ at two carbons, etc.), which we consider implausible. We therefore evaluated alternative scenarios that would result in this enrichment.

We first analyzed the mechanisms for purine formation on meteorite parent bodies proposed by Koga et al., to determine the possible sources of xanthine's carbons; we also included the other nucleobases identified in their network (Figure 6.7). The main distinction in Figure 6.7 is between the "formamide" route (i.e., the dominant pathway studied here) and the "cyanide" route (i.e., the DAMN pathway and other routes beginning with cyanide), as these both can lead to the palette of nucleobases observed on Murchison but have distinct carbon reservoirs. For each mechanism, we track each carbon atom through the final nucleobase, and assign it to the formamide pool, the cyanide pool, or as ambiguous if it is from a third source (e.g., urea). Typically, these 'third source' carbons can be indirectly derived from formamide or cyanide (e.g., urea, formamidine, cyanogen) (Saladino et al., 2012; Slavova and Enchev, 2020; Koga et al., 2024). We then compiled the resulting isotope signatures of each nucleobase, prior to any isotope effects in the synthesis, under three scenarios: 1) all carbon coming from the isotopically light reduced carbon pool (either because it is derived from cyanide, or has a distinct formation mechanism which is also isotopically light); 2) isotopically heavy formamide and isotopically light cyanide, with 2a) 'ambiguous' carbons isotopically enriched (e.g., formamide derived) and 2b) 'ambiguous'



carbons isotopically deplete (e.g., cyanide derived). For simplicity, we estimate the ‘isotopically light’ pool to have  $\delta^{13}\text{C}_{\text{VPDB}} \approx 0 \text{‰}$ , and the ‘isotopically enriched’ pool to have  $\delta^{13}\text{C}_{\text{VPDB}} \approx 150 \text{‰}$ . We compile these predictions in Table 6.5.

There is a significant uncertainty here, as the isotope effects associated with the synthesis of the other nucleobases have not been studied. If the reaction mechanism proceeded analogously to our synthesis (i.e., a combination of the “formamide” and “DAMN” mechanism with formamide solvent), then because AICN is a common intermediate, we can use our adenine results as a first-order estimate. Based on the energetics discussed in 6.4.1, we anticipate that AICN will also be deplete relative to the starting materials, by no more than the net effect observed for the net reaction (i.e.,  $\leq 32.4 \text{‰}$ ). Some reaction pathways (e.g., to guanine) may have greater isotope effects than observed for adenine, especially with their distinct mechanisms for the closure of the 6-membered ring. Based on the fact that typical ring-closing KIEs are in the range of 20-50 ‰ for the carbon involved in bond formation (i.e., 4-10‰ for the molecular-average isotope signature of a compound with 5-carbons, assuming the ring closing step involves one carbon and one nitrogen), we suggest a range of net isotope effects of 0-50 ‰ (molecular-average) for each nucleobase (Singleton and Thomas, 1995; Keating et al., 1999; Singleton et al., 1999; Singleton and Szymanski, 1999). In any case, we note the most important aspect of our hypothesis is that isotope effects associated with the syntheses will cause the products to be deplete relative to their starting materials.

These synthesis methods offer a plausible route to the observed isotopic signature of xanthine: it was formed via a pool of isotopically enriched formamide and isotopically deplete cyanide; the additional carbon was provided by urea derived from those precursors and could have been enriched or depleted; and the entire reaction was accompanied by a net isotope effect of  $\approx 0\text{-}50 \text{‰}$ . For example, it may have been formed via light cyanide, light urea, and heavy formamide, with a net isotope effect of 20 ‰; this predicts a final  $\delta^{13}\text{C}_{\text{VPDB}}$  of  $\approx 40 \text{‰}$ , similar to the observed 37.7 ‰. Looking at other nucleobases, this scenario suggests the  $\delta^{13}\text{C}_{\text{VPDB}}$  of adenine is  $\approx 30\text{-}60 \text{‰}$  (60-90 ‰ based on precursors, with an

isotope effect of  $\approx 30$  ‰), while guanine and hypoxanthine should lie in a similar range. The most diagnostic target for confirming or rejecting this scenario may be purine; there is only one synthesis route (via formamide) which samples 4 formamide carbons, and purine should therefore be highly enriched, with  $\delta^{13}\text{C}_{\text{VPDB}} \approx 100$  ‰. In this case, we can also conclude that the formamide used in the parent body syntheses was derived from a CO-based source, rather than provided by cyanide hydrolysis.

However, the hypothesis that all the source carbon is light and cyanide-derived may still be plausible if the observed xanthine is a highly degraded residue (e.g., due to destruction of xanthine via photochemistry or hydrolysis). We here examine the hydrolysis case in detail. The extent of breakdown due to hydrolysis is unknown; nucleobases were protected somewhat from these destructive processes by their environment (Levy and Miller, 1998; Zaia, 2012; Baú et al., 2020; Koga et al., 2024); however, the hydrolysis lifetimes of the bases alone are sufficiently short (e.g., xanthine has a half-life of  $10^4$  years at pH 7 and 25 °C) for degradation to be a factor. A typical isotope effect for a carbon atom undergoing hydrolysis is  $\approx 30$ -70 ‰ (Marlier and O'Leary, 1990; Marlier et al., 1999; Masbou et al., 2018); or of the order  $\approx 10$  ‰ for the molecular-average isotope signature of xanthine. If we assume that that 1) the hydrolysis occurred from a static pool of xanthine, and 2) the breakdown products did not react to form more xanthine, we can model its isotope signature as a Rayleigh fractionation process (Sharp, 2017). In this case:

$$\frac{R}{R_i} = F^{\alpha-1} \quad (6.22)$$

where  $R$  is the observed isotope ratio,  $R_i$  is the initial isotope ratio,  $F$  is the fraction remaining, and  $\alpha$  is the (molecular-average) fractionation factor. Written as delta values:

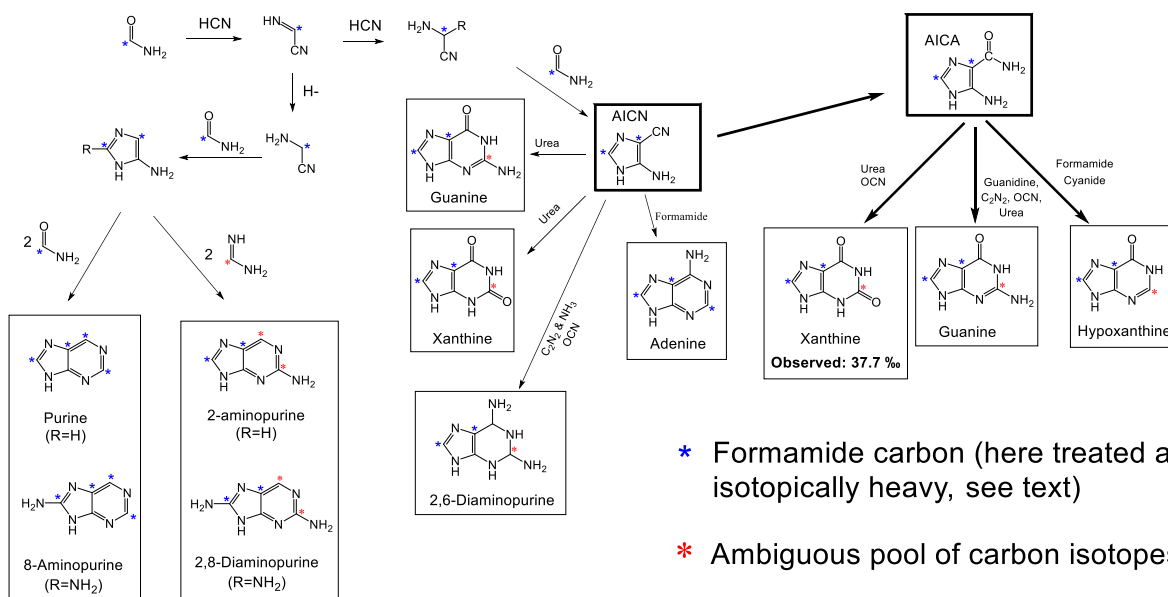
$$\delta = [\delta_i + 1000]F^{(\alpha-1)} - 1000 \quad (6.23)$$

where  $\delta$  is the observed delta value and  $\delta_i$  is the initial pool. If  $\delta_i = 0$  ‰ (the upper limit, assuming production from cyanide carbon only), and assuming a large fractionation of 20 ‰ for the whole molecule ( $\alpha = 0.980$ ), then  $\approx 85\%$  of the xanthine must be degraded to account for the observed  $\delta^{13}\text{C}_{\text{VPDB}} = 37.7$  ‰. Smaller fractionations, or  $\delta_i$  values  $< 0$  ‰ (i.e.,

because of a KIE associated with Xanthine's formation) require more extensive breakdown. Similar arguments apply to other breakdown scenarios, such as photochemical destruction. In these cases, a significant amount of degradation products may have accumulated, and will have  $\delta^{13}\text{C}_{\text{VPDB}}$  values which are depleted relative to xanthine.

We emphasize that our analysis is limited by assumptions (1) and (2). Simply permitting additional xanthine to be formed with  $\delta^{13}\text{C}_{\text{VPDB}} \leq 0 \text{ ‰}$  will not alter our analysis; in this case, even more extensive breakdown is required. However, it is plausible that the nucleobases form a more complex network which interconvert. Adenine hydrolyzes to hypoxanthine, which in turn hydrolyzes to AICA and can then serve as a precursor for other nucleobases; similarly, guanine hydrolyzes to xanthine, while 2,6-diaminopurine hydrolyzes to guanine, xanthine, and isoguanine (Levy and Miller, 1998). To our knowledge, no detailed study of the breakdown products of xanthine hydrolysis has been performed; Levy and Miller note no UV-absorbing products from the hydrolysis of xanthine (Levy and Miller, 1998). While there is no straightforward explanation to enrich xanthine using such a network (and we note most purines will have similar preferences for  $^{13}\text{C}$  based on equilibrium considerations; see 6.2.14), we cannot rule out this scenario. Further studies of the degradation of both xanthine and other purines, as well as the corresponding isotope effects, should be performed to evaluate the hypothesis that the observed xanthine is a breakdown residue.

## "Formamide" Route



## "Cyanide" Route

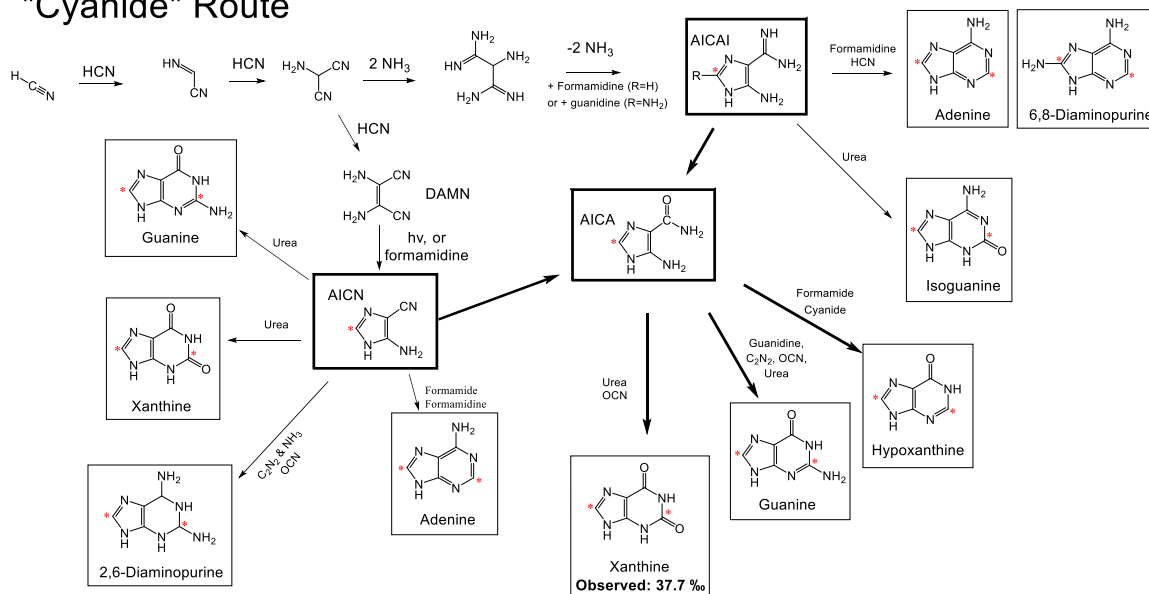


**Figure 6.7:** Tracing the sources of carbon along different routes to the nucleobases observed on CM2 chondrites. The "formamide" route is active with higher quantities of formamide, which we assume is due to a distinct, isotopically enriched source. In contrast, the "cyanide" route includes multiple pathways beginning from cyanide, including the DAMN route examined above; some of this carbon comes from formamide. Due to the lower quantities of formamide used, we permit this to come either exogenously or from cyanide hydrolysis.

**Table 6.5: Predicted  $\delta^{13}\text{C}_{\text{VPDB}}$  values for various synthesis pathways<sup>a</sup>**

	All reduced carbons ( $\delta^{13}\text{C}_{\text{VPDB}}$ , ‰)	Heavy formamide, light ambiguous ( $\delta^{13}\text{C}_{\text{VPDB}}$ , ‰)	Heavy formamide, heavy ambiguous ( $\delta^{13}\text{C}_{\text{VPDB}}$ , ‰)	Plausible KIEs ( $\delta^{13}\text{C}_{\text{VPDB}}$ , ‰)
Adenine	0	90 (FA) 0 (CN)	90 (FA) 60 (CN)	30-35
Purine (FA Only)	0	120	120	0-50
Hypoxanthine	0	60 (FA) 0 (CN)	90 (FA) 60 (CN)	0-50
Xanthine	0	60 (FA) 0 (CN)	90 (FA) 60 (CN)	0-50
Guanine	0	60 (FA) 0 (CN)	90 (FA) 60 (CN)	0-50
Isoguanine (CN Only)	0	0	60	0-50
2,6-Diaminopurine	0	60 (FA) 0 (CN)	90 (FA) 60 (CN)	0-50
2-Aminopurine (FA Only)	0	60	120	0-50
6,8-Diaminopurine (CN Only)	0	0	60	0-50
8-Aminopurine (FA Only)	0	120	120	0-50
2,8-Diaminopurine (FA Only)	0	60	120	0-50

a: "FA" = formamide route. "CN" = cyanide route.

#### 6.4.3 Limitations and Future Directions

There are four main limitations to our study. First, the utility of our fragmentation data for site-specific reconstruction is limited by our lack of knowledge regarding the branching ratios for 6 of the 9 observed adenine fragments (55, 65, 67, 77, 82, & 92). If these can be constrained by experiment, they may be sufficient to permit a reconstruction of the isotopic content at every available site. Second, our knowledge of the partitioning of

cyanide carbon between different products is speculative, with significant consequences for our interpretation. Future experiments must examine this information in more detail, obtaining more precise yields as well as  $\delta^{13}\text{C}_{\text{VPDB}}$  values of the DCI, purine, and adenine under a range of reaction conditions. We also recommend further labelling experiments to explore the insoluble residue as well as tests for residual cyanide present in solution (e.g., via precipitation with silver chloride), to further elucidate this routing. Third, our description of kinetic and equilibrium isotope effects along the path to adenine is limited by 1) the lack of reduced partition function ratios for intermediates and 2) lack of energetic information regarding the DAMN pathway in formamide. Additional modeling studies are necessary to help interpret the isotope effects along these pathways. Fourth, the adenine standard we use (VWR) has an unknown intramolecular isotope composition, which hampers our ability to interpret site-specific results. Previous works have characterized isotopic standards via NMR (Neubauer et al., 2018). It is tempting to apply a similar approach for adenine; however, we note that the poor solubility of adenine in common NMR solvents makes it difficult to dissolve sufficient material (10s of mgs) for a NMR analysis (Jézéquel et al., 2017). Adenine has greater solubility in ionic liquids, and this may be a successful strategy for characterizing a standard (Ghoshdastidar et al., 2016).

Despite these limitations, our analysis of the meteorite reaction network makes two statements which can immediately inform investigation. First, if the reaction network described in Koga et al. is responsible for xanthine discovered on Murchison, then the isotopically enriched xanthine observed by Martins et al. likely either 1) incorporated a significant amount of carbon from an isotopically enriched, CO derived pool (via formamide?), or 2) represents a residue of a highly degraded product. Second, subject to the mechanisms in that network, the  $\delta^{13}\text{C}_{\text{VPDB}}$  content of almost a dozen purine nucleobases can be predicted. Measurements of the isotopic content of other meteoritic purines as well as possible breakdown products are necessary to distinguish between these scenarios.

## 6.5 Conclusion

Our isotopic measurement demonstrates that the  $\delta^{13}\text{C}_{\text{VPDB}}$  of adenine synthesized via the heating of cyanide in formamide is depleted relative to its precursors. This depletion is likely due to kinetic isotope effects associated with its synthesis; however, because of the uncertainties involved with site-specific measurement, and because the adenine is formed via multiple pathways, we cannot definitively assign these effects to certain elementary reactions. Indeed, it is plausible that the product adenine incorporates several isotope effects from several different steps, resulting in a depletion at every carbon. Our results are useful in the context of meteoritic purines because adenine and the other purines, including xanthine, may share AICN as a common intermediate. Therefore, we suggest that other nucleobases are also depleted relative to the precursors. Because the only  $\delta^{13}\text{C}_{\text{VPDB}}$  observed for a meteoritic purine (xanthine,  $\delta^{13}\text{C}_{\text{VPDB}} = 37.7 \text{ ‰}$ ) is enriched relative to the meteoritic cyanide pool ( $\delta^{13}\text{C}_{\text{VPDB}} = -7 \pm 10 \text{ ‰}$ ), our results suggest that either 1) this xanthine was not formed from meteoritic cyanide alone, but sampled an enriched carbon source, possibly formamide, formed from the enriched interstellar CO pool, or 2) the xanthine is a highly degraded residue. We describe plausible enrichments of other purines based on different carbon sources, which can be used to interpret future measurements of meteoritic purines.

## 6.6 Acknowledgements

A special thanks to Elle Chimiak; this work would not have been started without their support. We would like to thank Sarah Zeichner, Elliott Mueller, Gabriella Weiss, Caj Neubauer, and Elise Wilkes for discussions regarding interstellar chemistry, meteoritics, and mass spectrometry. Max Lloyd, Sarah Zeichner, Max Lloyd, Guannan Dong, and Peter Martin contributed to data processing scripts used in this work. We are grateful to Spiros Garbis, Annie Moradian, and Ting-Yu Wang for their assistance at the Caltech Proteome Exploration Laboratory. Finally, we thank Alex Sessions for the use of laboratory space.

## BIBLIOGRAPHY

- Abelson, P. H., and Hoering, T. C. (1961) Carbon isotope fractionation in formation of amino acids by photosynthetic organisms. *Proc. Natl. Acad. Sci. U. S. A.* **47**, 623–632.
- Adnew, G. A., Hofmann, M. E. G., Paul, D., Laskar, A., Surma, J., Albrecht, N., Pack, A., Schwieters, J., Koren, G., Peters, W., and Röckmann, T. (2019) Determination of the triple oxygen and carbon isotopic composition of CO<sub>2</sub> from atomic ion fragments formed in the ion source of the 253 Ultra high-resolution isotope ratio mass spectrometer. *Rapid Commun. Mass Spectrom.* **33**, 1363–1380.
- Anon (2017) Seventh report of the organisation for the prohibition of chemical weapons-united nations joint investigative mechanism (S/2017/904) [EN/AR] - Syrian Arab Republic | ReliefWeb.
- Anon (2014) U.S. Completes Destruction of Sarin Precursors from Syria on the Cape Ray. *OPCW*.
- Anslyn, E. V., and Dougherty, D. A. (2006) *Modern Physical Organic Chemistry*., University Science Books, Sausalito, CA.
- Barbosa, A. C. P., Borges, I., and Lin, W. O. (2005) An ab initio study of the structure and methyl rotational barriers of methylphosphonic dihalides. *J. Mol. Struct. THEOCHEM* **718**, 105–109.
- Barks, H. L., Buckley, R., Grieves, G. A., Di Mauro, E., Hud, N. V., and Orlando, T. M. (2010) Guanine, adenine, and hypoxanthine production in UV-irradiated formamide solutions: Relaxation of the requirements for prebiotic purine nucleobase formation. *Chembiochem Eur. J. Chem. Biol.* **11**, 1240–1243.
- Bartelink, E. J., Berg, G. E., Beasley, M. M., and Chesson, L. A. (2014) Application of stable isotope forensics for predicting region of origin of human remains from past wars and conflicts. *Ann. Anthropol. Pract.* **38**, 124–136.
- Belloche, A., Meshcheryakov, A. A., Garrod, R. T., Ilyushin, V. V., Alekseev, E. A., Motiyenko, R. A., Margulès, L., Müller, H. S. P., and Menten, K. M. (2017) Rotational spectroscopy, tentative interstellar detection, and chemical modeling of N-methylformamide. *Astron. Astrophys.* **601**, A49.
- Benner, S. A., Kim, H.-J., and Carrigan, M. A. (2012) Asphalt, water, and the prebiotic synthesis of ribose, ribonucleosides, and RNA. *Acc. Chem. Res.* **45**, 2025–2034.
- Benson, S., Lennard, C., Maynard, P., and Roux, C. (2006) Forensic applications of isotope ratio mass spectrometry—A review. *Forensic Sci. Int.* **157**, 1–22.



- Bernstein, M. P., Dworkin, J. P., Sandford, S. A., Cooper, G. W., and Allamandola, L. J. (2002) Racemic amino acids from the ultraviolet photolysis of interstellar ice analogues. *Nature* **416**, 401–403.
- Bhattacharya, A. K., and Thyagarajan, G. (1981) Michaelis-Arbuzov rearrangement. *Chem. Rev.* **81**, 415–430.
- Bigeleisen, J., Lee, M. W., and Mandel, F. (1973) Equilibrium isotope effects. *Annu Rev Phys Chem V 24 Pp 407-440*.
- Bills, J. R., Nagornov, K. O., Kozhinov, A. N., Williams, T. J., Tsybin, Y. O., and Marcus, R. K. (2021) Improved uranium isotope ratio analysis in liquid sampling–atmospheric pressure glow discharge/orbitrap FTMS coupling through the use of an external data acquisition system. *J. Am. Soc. Mass Spectrom.* **32**, 1224–1236.
- Biver, N., Bockelée-Morvan, D., Debout, V., Crovisier, J., Boissier, J., Lis, D. C., Russo, N. D., Moreno, R., Colom, P., Paubert, G., Vervack, R., and Weaver, H. A. (2014) Complex organic molecules in comets C/2012 F6 (Lemmon) and C/2013 R1 (Lovejoy): Detection of ethylene glycol and formamide. *Astron. Astrophys.* **566**, L5.
- Black, R. M., Clarke, R. J., Read, R. W., and Reid, M. T. J. (1994) Application of gas chromatography-mass spectrometry and gas chromatography-tandem mass spectrometry to the analysis of chemical warfare samples, found to contain residues of the nerve agent sarin, sulphur mustard and their degradation products. *J. Chromatogr. A* **662**, 301–321.
- Blázquez-García, A., Conde, A., Mori, U., and Lozano, J. A. (2021) A review on outlier/anomaly detection in time series data. *ACM Comput. Surv.* **54**, 56:1-56:33.
- Böcker, S., Letzel, M. C., Lipták, Z., and Pervukhin, A. (2009) SIRIUS: Decomposing isotope patterns for metabolite identification†. *Bioinformatics* **25**, 218–224.
- Braei, M., and Wagner, S. (2020) Anomaly detection in univariate time-series: A survey on the state-of-the-art. arXiv: 2004.00433v1 [cs.LG]
- Brand, W. A., Assonov, S. S., and Coplen, T. B. (2010) Correction for the 17O interference in  $\delta(13C)$  measurements when analyzing CO<sub>2</sub> with stable isotope mass spectrometry (IUPAC Technical Report). *Pure Appl. Chem.* **82**, 1719–1733.
- Brownawell, M. L., and San Filippo, J. (1982) Simulation of chemical instrumentation. II: A program for the synthesis of mass spectral isotopic abundances. *J. Chem. Educ.* **59**, 663.
- Bubas, A. R., Perez, E., Metzler, L. J., Rissler, S. D., and Van Stipdonk, M. J. (2021) Collision-induced dissociation of [UO<sub>2</sub>(NO<sub>3</sub>)<sub>3</sub>]<sup>-</sup> and [UO<sub>2</sub>(NO<sub>3</sub>)<sub>2</sub>(O<sub>2</sub>)]<sup>-</sup> and reactions of product ions with H<sub>2</sub>O and O<sub>2</sub>. *J. Mass Spectrom.* **56**, e4705.
- Callahan, M. P., Smith, K. E., Cleaves, H. J., Ruzicka, J., Stern, J. C., Glavin, D. P., House, C. H., and Dworkin, J. P. (2011) Carbonaceous meteorites contain a wide range of extraterrestrial nucleobases. *Proc. Natl. Acad. Sci.* **108**, 13995–13998.

- Caytan, E., Eliot P. Botosoa, Virginie Silvestre, Richard J. Robins, Serge, A., and Remaud, G. S. (2007) Accurate quantitative  $^{13}\text{C}$  NMR spectroscopy: repeatability over time of site-specific  $^{13}\text{C}$  isotope ratio determination. *Anal Chem* **79**, 8266–8269.
- Cerling, T. E., Barnette, J. E., Bowen, G. J., Chesson, L. A., Ehleringer, J. R., Remien, C. H., Shea, P., Tipple, B. J., and West, J. B. (2016) Forensic stable isotope biogeochemistry. *Annu. Rev. Earth Planet. Sci.* **44**, 175–206.
- Cesar, J., Eiler, J., Dallas, B., Chimiak, L., and Grice, K. (2019) Isotope heterogeneity in ethyltoluenes from Australian condensates, and their stable carbon site-specific isotope analysis. *Org. Geochem.* **135**, 32–37.
- Chaintreau, A., Fieber, W., Sommer, H., Gilbert, A., Yamada, K., Yoshida, N., Pagelot, A., Moskau, D., Moreno, A., Schleucher, J., Reniero, F., Holland, M., Guillou, C., Silvestre, V., Akoka, S., and Remaud, G. S. (2013) Site-specific  $^{13}\text{C}$  content by quantitative isotopic  $^{13}\text{C}$  Nuclear Magnetic Resonance spectrometry: A pilot inter-laboratory study. *Anal. Chim. Acta* **788**, 108–113.
- Chesson, L. A., Howa, J. D., Lott, M. J., and Ehleringer, J. R. (2016) Development of a methodological framework for applying isotope ratio mass spectrometry to explosive components. *Forensic Chem.* **2**, 9–14.
- Chimiak, L., and Eiler, J. (2024) Prebiotic synthesis on meteorite parent bodies: Insights from hydrogen and carbon isotope models. *Chem. Geol.* **644**, 121828.
- Chimiak, L., Elsila, J. E., Dallas, B., Dworkin, J. P., Aponte, J. C., Sessions, A. L., and Eiler, J. M. (2021) Carbon isotope evidence for the substrates and mechanisms of prebiotic synthesis in the early solar system. *Geochim. Cosmochim. Acta* **292**, 188–202.
- Clayton, R. N. (2008) Oxygen isotopes in the early solar system — A historical perspective. *Rev. Mineral. Geochem.* **68**, 5–14.
- Coplen, T. B. (2011) Guidelines and recommended terms for expression of stable-isotope-ratio and gas-ratio measurement results. *Rapid Commun. Mass Spectrom.* **25**, 2538–2560.
- Coutens, A., Jørgensen, J. K., Wiel, M. H. D. van der, Müller, H. S. P., Lykke, J. M., Bjerke, P., Bourke, T. L., Calcutt, H., Drozdovskaya, M. N., Favre, C., Fayolle, E. C., Garrod, R. T., Jacobsen, S. K., Ligterink, N. F. W., Öberg, K. I., Persson, M. V., Dishoeck, E. F. van, and Wampfler, S. F. (2016) The ALMA-PILS survey: First detections of deuterated formamide and deuterated isocyanic acid in the interstellar medium. *Astron. Astrophys.* **590**, L6.
- Csernica (2023b) Csernica/Experimental\_Isotomics: Revisions. <https://doi.org/10.5281/zenodo.8281012>.
- Csernica (2024) Csernica/MPA-Forensics: Initial Release. DOI: 10.5281/zenodo.10614297
- Csernica (2023b) Csernica/Reservoir-Injection: Initial Zenodo Release. <https://doi.org/10.5281/zenodo.7765053>,

- Csernica, T. (2023a) RAW and csv files for “High-dimensional isotomics, part 2: Observations of over 100 constraints on methionine’s isotome.” <https://doi.org/10.22002/4WXPS-84P41>.
- Csernica, T. (2024) RAW and FTStatistic extracted files for methylphosphonic acid forensics. <https://doi.org/10.22002/8v0dd-nxh68>.
- Csernica, T. (2023b) RAW, isox, and txt files associated with accuracy and precision of ESI-Orbitrap-IRMS observations of hours to tens of hours via reservoir injection. <https://doi.org/10.22002/qw1m6-1w831>.
- Csernica, T., Bhattacharjee, S., and Eiler, J. (2023) Accuracy and precision of ESI-Orbitrap-IRMS observations of hours to tens of hours via reservoir injection. *Int. J. Mass Spectrom.* **490**, 117084.
- Csernica, T., and Eiler, J. M. (2023) High-dimensional isotomics, part 1: A mathematical framework for isotomics. *Chem. Geol.* **617**, 121235.
- Danzig, R., Sageman, M., Leighton, T., Hough, L., Yuki, H., Kotani, R., and Hosford, Z. M. (2012) *Aum Shinrikyo: Insights Into How Terrorists Develop Biological and Chemical Weapons*. 2nd ed., Center for a New American Security. n. p.
- Daughton, C. G., Cook, A. M., and Alexander, M. (1979) Biodegradation of phosphonate toxicants yields methane or ethane on cleavage of the C-P bond. *FEMS Microbiol. Lett.* **5**, 91–93.
- DeNiro, M. J., and Epstein, S. (1977) Mechanism of carbon isotope fractionation associated with lipid synthesis. *Science* **197**, 261–263.
- Denisov, E., Damoc, E., and Makarov, A. (2021) Exploring frontiers of Orbitrap performance for long transients. *Int. J. Mass Spectrom.* **466**, 116607.
- Douglas, P. M. J., Stolper, D. A., Eiler, J. M., Sessions, A. L., Lawson, M., Shuai, Y., Bishop, A., Podlaha, O. G., Ferreira, A. A., Santos Neto, E. V., Niemann, M., Steen, A. S., Huang, L., Chimiak, L., Valentine, D. L., Fiebig, J., Luhmann, A. J., Seyfried, W. E., Etiope, G., Schoell, M., Inskip, W. P., Moran, J. J., and Kitchen, N. (2017) Methane clumped isotopes: Progress and potential for a new isotopic tracer. *Org. Geochem.* **113**, 262–282.
- Dührkop, K., Fleischauer, M., Ludwig, M., Aksenov, A. A., Melnik, A. V., Meusel, M., Dorrestein, P. C., Rousu, J., and Böcker, S. (2019) SIRIUS 4: A rapid tool for turning tandem mass spectra into metabolite structure information. *Nat. Methods* **16**, 299–302.
- Eagle, R. A., Schauble, E. A., Tripathi, A. K., Tütken, T., Hulbert, R. C., and Eiler, J. M. (2010) Body temperatures of modern and extinct vertebrates from <sup>13</sup>C-<sup>18</sup>O bond abundances in bioapatite. *Proc. Natl. Acad. Sci.* **107**, 10377–10382.
- Ehleringer, J. R., Casale, J. F., Lott, M. J., and Ford, V. L. (2000) Tracing the geographical origin of cocaine. *Nature* **408**, 311–312.

- Eiler, J., Cesar, J., Chimiak, L., Dallas, B., Grice, K., Griep-Raming, J., Juchelka, D., Kitchen, N., Lloyd, M., Makarov, A., Robins, R., and Schwieters, J. (2017) Analysis of molecular isotopic structures at high precision and accuracy by Orbitrap mass spectrometry. *Int. J. Mass Spectrom.* **422**, 126–142.
- Eiler, J. M. (2007) “Clumped-isotope” geochemistry—The study of naturally-occurring, multiply-substituted isotopologues. *Earth Planet. Sci. Lett.* **262**, 309–327.
- Eiler, J. M. (2011) Paleoclimate reconstruction using carbonate clumped isotope thermometry. *Quat. Sci. Rev.* **30**, 3575–3588.
- Eiler, J. M. (2013) The isotopic anatomies of molecules and minerals. *Annu. Rev. Earth Planet. Sci.* **41**, 411–441.
- Eiler, J. M., Bergquist, B., Bourg, I., Cartigny, P., Farquhar, J., Gagnon, A., Guo, W., Halevy, I., Hofmann, A., and Larson, T. E. (2014) Frontiers of stable isotope geoscience. *Chem. Geol.* **372**, 119–143.
- Eiler, J. M., Clog, M., Magyar, P., Piasecki, A., Sessions, A., Stolper, D., Deerberg, M., Schlueter, H.-J., and Schwieters, J. (2013) A high-resolution gas-source isotope ratio mass spectrometer. *Int. J. Mass Spectrom.* **335**, 45–56.
- Eiler, J. M., and Schauble, E. (2004)  $^{18}\text{O}^{13}\text{C}^{16}\text{O}$  in Earth’s atmosphere. *Geochim. Cosmochim. Acta* **68**, 4767–4777.
- Elsila, J. E., Aponte, J. C., Blackmond, D. G., Burton, A. S., Dworkin, J. P., and Glavin, D. P. (2016) Meteoritic amino acids: Diversity in compositions reflects parent body histories. *ACS Cent. Sci.* **2**, 370–379.
- Elsila, J. E., Charnley, S. B., Burton, A. S., Glavin, D. P., and Dworkin, J. P. (2012) Compound-specific carbon, nitrogen, and hydrogen isotopic ratios for amino acids in CM and CR chondrites and their use in evaluating potential formation pathways. *Meteorit. Planet. Sci.* **47**, 1517–1536.
- Fedoseev, G., Chuang, K.-J., van Dishoeck, E. F., Ioppolo, S., and Linnartz, H. (2016) Simultaneous hydrogenation and UV-photolysis experiments of NO in CO-rich interstellar ice analogues; linking HNC, OCN<sup>-</sup>, NH<sub>2</sub>CHO, and NH<sub>2</sub>OH. *Mon. Not. R. Astron. Soc.* **460**, 4297–4309.
- Fernandez-de-Cossio, J. (2010) Efficient packing fourier-transform approach for ultrahigh resolution isotopic distribution calculations. *Anal. Chem.* **82**, 1759–1765.
- Ferris, J. P., Joshi, P. C., Edelson, E. H., and Lawless, J. G. (1978) HCN: A plausible source of purines, pyrimidines and amino acids on the primitive earth. *J. Mol. Evol.* **11**, 293–311.
- Fraga, C. G., Clowers, B. H., Moore, R. J., and Zink, E. M. (2010) Signature-discovery approach for sample matching of a nerve-agent precursor using liquid chromatography–mass spectrometry, XCMS, and chemometrics. *Anal. Chem.* **82**, 4165–4173.

- Fraga, C. G., Farmer, O. T., and Carman, A. J. (2011) Anionic forensic signatures for sample matching of potassium cyanide using high performance ion chromatography and chemometrics. *Talanta* **83**, 1166–1172.
- Galimov, E. M. (1985) CHAPTER 3 - Method of calculating the thermodynamic isotopic factors of polyatomic compounds. In *The Biological Fractionation of Isotopes* (ed. E. M. Galimov). Academic Press. pp. 42–93.
- Gardner, F. F., Godfrey, P. D., and Williams, D. R. (1980) Observations of the  $^{12}\text{C}$  and  $^{13}\text{C}$  isotopes of formamide at 19 cm. *Mon. Not. R. Astron. Soc.* **193**, 713–721.
- Gentile, N., Siegwolf, R. T. W., Esseiva, P., Doyle, S., Zollinger, K., and Delémont, O. (2015) Isotope ratio mass spectrometry as a tool for source inference in forensic science: A critical review. *Forensic Sci. Int.* **251**, 139–158.
- Gerakines, P. A., Moore, M. H., and Hudson, R. L. (2004) Ultraviolet photolysis and proton irradiation of astrophysical ice analogs containing hydrogen cyanide. *Icarus* **170**, 202–213.
- Ghoshdastidar, D., Ghosh, D., and Senapati, S. (2016) High nucleobase-solubilizing ability of low-viscous ionic liquid/water mixtures: measurements and mechanism. *J. Phys. Chem. B* **120**, 492–503.
- Giacomozzi, L., D'Angelo, G., Diaz-Tendero, S., de Ruelle, N., Stockett, M. H., Alcamí, M., Cederquist, H., Schmidt, H. T., and Zettergren, H. (2019) Decay pathways for protonated and deprotonated adenine molecules. *J. Chem. Phys.* **151**, 044306.
- Gilbert, A., Silvestre, V., Segebarth, N., Tcherkez, G., Guillou, C., Robins, R. J., Akoka, S., and Remaud, G. S. (2011) The intramolecular  $^{13}\text{C}$ -distribution in ethanol reveals the influence of the  $\text{CO}_2$ -fixation pathway and environmental conditions on the site-specific  $^{13}\text{C}$  variation in glucose. *Plant Cell Environ.* **34**, 1104–1112.
- Glaser, R., Hodgen, B., Farrelly, D., and McKee, E. (2007) Adenine synthesis in interstellar space: Mechanisms of prebiotic pyrimidine-ring formation of monocyclic HCN-pentamers. *Astrobiology* **7**, 455–470.
- Goesmann, F., Rosenbauer, H., Bredehöft, J. H., Cabane, M., Ehrenfreund, P., Gautier, T., Giri, C., Krüger, H., Roy, L. L., MacDermott, A. J., McKenna-Lawlor, S., Meierhenrich, U. J., Caro, G. M. M., Raulin, F., Roll, R., Steele, A., Steininger, H., Sternberg, R., Szopa, C., Thiemann, W., and Ulamec, S. (2015) Organic compounds on comet 67P/Churyumov-Gerasimenko revealed by COSAC mass spectrometry. *Science* **349**.
- Gonzalez-James, O. M., Zhang, X., Datta, A., Hrovat, D. A., Borden, W. T., and Singleton, D. A. (2010) Experimental evidence for heavy-atom tunneling in the ring-opening of cyclopropylcarbinyl radical from intramolecular  $^{12}\text{C}/^{13}\text{C}$  kinetic isotope effects. *J. Am. Chem. Soc.* **132**, 12548–12549.

- Gorshkov, M. V., Fornelli, L., and Tsybin, Y. O. (2012) Observation of ion coalescence in Orbitrap Fourier transform mass spectrometry. *Rapid Commun. Mass Spectrom.* **26**, 1711–1717.
- Greule, M., Huber, S. G., and Keppler, F. (2012) Stable hydrogen-isotope analysis of methyl chloride emitted from heated halophytic plants. *Atmos. Environ.* **62**, 584–592.
- Grinfeld, D., Stewart, H., Skoblin, M., Denisov, E., Monastyrsky, M., and Makarov, A. (2019) Space-charge dynamics in Orbitrap mass spectrometers. *Int. J. Mod. Phys. A* **34**, 1942007.
- Halfen, D. T., Woolf, N. J., and Ziurys, L. M. (2017) The  $^{12}\text{C}/^{13}\text{C}$  ratio in Sgr B2(N): Constraints for galactic chemical evolution and isotopic chemistry. *Astrophys. J.* **845**, 158.
- Hartmann, S. C., Keppler, F., Greule, M., Lauer, R., and Horst, A. (2023) Triple-element stable isotope analysis of chloromethane emitted by royal fern and degraded by club moss. *J. Geophys. Res. Biogeosciences* **128**, e2022JG007256.
- Hayes, J. M. (2001) Fractionation of Carbon and Hydrogen Isotopes in Biosynthetic Processes. *Rev. Mineral. Geochem.* **43**, 225–277.
- He, Y., Cao, X., and Bao, H. (2020) Ideas and perspectives: The same carbon behaves like different elements – an insight into position-specific isotope distributions. *Biogeosciences* **17**, 4785–4795.
- Hilkert, A., Böhlke, J. K., Mroczkowski, S. J., Fort, K. L., Aizikov, K., Wang, X. T., Kopf, S. H., and Neubauer, C. (2021) Exploring the potential of electrospray-Orbitrap for stable isotope analysis using nitrate as a model. *Anal. Chem.* **93**, 9139–9148.
- Hoegg, E. D., Barinaga, C. J., Hager, G. J., Hart, G. L., Koppenaal, D. W., and Marcus, R. K. (2016) Preliminary figures of merit for isotope ratio measurements: The liquid sampling-atmospheric pressure glow discharge microplasma ionization source coupled to an Orbitrap mass analyzer. *J. Am. Soc. Mass Spectrom.* **27**, 1393–1403.
- Hoegg, E. D., Godin, S., Szpunar, J., Lobinski, R., Koppenaal, D. W., and Marcus, R. K. (2021) Resolving severe elemental isobaric interferences with a combined atomic and molecular ionization source–Orbitrap mass spectrometry approach: The  $^{87}\text{Sr}$  and  $^{87}\text{Rb}$  geochronology pair. *Anal. Chem.* **93**, 11506–11514.
- Hoegg, E. D., Marcus, R. K., Koppenaal, D. W., Irvahn, J., Hager, G. J., and Hart, G. L. (2017) Determination of uranium isotope ratios using a liquid sampling atmospheric pressure glow discharge/Orbitrap mass spectrometer system. *Rapid Commun. Mass Spectrom.* **31**, 1534–1540.
- Hofmann, A. E., Chimiak, L., Dallas, B., Griep-Raming, J., Juchelka, D., Makarov, A., Schwieters, J., and Eiler, J. M. (2020) Using Orbitrap mass spectrometry to assess the isotopic compositions of individual compounds in mixtures. *Int. J. Mass Spectrom.* **457**, 116410.

- Hoggard, J. C., Wahl, J. H., Synovec, R. E., Mong, G. M., and Fraga, C. G. (2010) Impurity profiling of a chemical weapon precursor for possible forensic signatures by comprehensive two-dimensional gas chromatography/mass spectrometry and chemometrics. *Anal. Chem.* **82**, 689–698.
- Höger Holmgren, K., Mören, L., Ahlinder, L., Larsson, A., Wikteliuss, D., Norlin, R., and Åstot, C. (2021) Route determination of sulfur mustard using nontargeted chemical attribution signature screening. *Anal. Chem.* **93**, 4850–4858.
- Holbrook, M. T. (2003) Methyl chloride. In *Kirk-Othmer Encyclopedia of Chemical Technology* John Wiley & Sons, Ltd.
- Holt, B. D., Sturchio, N. C., Abrajano, T. A., and Heraty, L. J. (1997) Conversion of chlorinated volatile organic compounds to carbon dioxide and methyl chloride for isotopic analysis of carbon and chlorine. *Anal. Chem.* **69**, 2727–2733.
- Howa, J. D., Lott, M. J., Chesson, L. A., and Ehleringer, J. R. (2014) Carbon and nitrogen isotope ratios of factory-produced RDX and HMX. *Forensic Sci. Int.* **240**, 80–87.
- Hsu, C. S. (1984) Diophantine approach to isotopic abundance calculations. *Diophantine Approach Isot. Abundance Calc.* **56**, 1356–1361.
- Hu, Q., Noll, R. J., Li, H., Makarov, A., Hardman, M., and Graham Cooks, R. (2005) The Orbitrap: A new mass spectrometer. *J. Mass Spectrom.* **40**, 430–443.
- Hudson, J. S., Eberle, J. F., Vachhani, R. H., Rogers, L. C., Wade, J. H., Krishnamurthy, R., and Springsteen, G. (2012) A unified mechanism for abiotic adenine and purine synthesis in formamide. *Angew. Chem. Int. Ed.* **51**, 5134–5137.
- Janesko, B. G., Fisher, H. C., Bridle, M. J., and Montchamp, J.-L. (2015) P(=O)H to P–OH tautomerism: A theoretical and experimental study. *J. Org. Chem.* **80**, 10025–10032.
- Jeilani, Y. A., Nguyen, H. T., Cardelino, B. H., and Nguyen, M. T. (2014) Free radical pathways for the prebiotic formation of xanthine and isoguanine from formamide. *Chem. Phys. Lett.* **598**, 58–64.
- Jézéquel, T., Joubert, V., Giraudeau, P., Remaud, G. S., and Akoka, S. (2017) The new face of isotopic NMR at natural abundance. *Magn. Reson. Chem.* **55**, 77–90.
- Kamel, A. M., and Munson, B. (2004) Collision-induced dissociation of purine antiviral agents: Mechanisms of ion formation using gas-phase hydrogen/deuterium exchange and electrospray ionization tandem mass spectrometry. *Eur. J. Mass Spectrom.* **10**, 239–257.
- Karl, D. M., Beversdorf, L., Björkman, K. M., Church, M. J., Martinez, A., and Delong, E. F. (2008) Aerobic production of methane in the sea. *Nat. Geosci.* **1**, 473–478.
- Kaufmann, A., and Walker, S. (2018) Coalescence and self-bunching observed in commercial high-resolution mass spectrometry instrumentation. *Rapid Commun. Mass Spectrom.* **32**, 503–515.

- Kaufmann, A., and Walker, S. (2016) Extension of the Q Orbitrap intrascan dynamic range by using a dedicated customized scan. *Rapid Commun. Mass Spectrom.* **30**, 1087–1095.
- Keating, A. E., Merrigan, S. R., Singleton, D. A., and Houk, K. N. (1999) Experimental proof of the non-least-motion cycloadditions of dichlorocarbene to alkenes: Kinetic isotope effects and quantum mechanical transition states. *J. Am. Chem. Soc.* **121**, 3933–3938.
- Keppler, F., Ninja Röbling, A., Jaeger, N., Schroll, M., Christoph Hartmann, S., and Greule, M. (2020) Sources and sinks of chloromethane in a salt marsh ecosystem: constraints from concentration and stable isotope measurements of laboratory incubation experiments. *Environ. Sci. Process. Impacts* **22**, 627–641.
- Kharchenko, A., Vladimirov, G., Heeren, R. M. A., and Nikolaev, E. N. (2012) Performance of Orbitrap mass analyzer at various space charge and non-ideal field conditions: Simulation approach. *J. Am. Soc. Mass Spectrom.* **23**, 977–987.
- Koga, T., Takano, Y., Oba, Y., Naraoka, H., and Ohkouchi, N. (2024) Abundant extraterrestrial purine nucleobases in the Murchison meteorite: Implications for a unified mechanism for purine synthesis in carbonaceous chondrite parent bodies. *Geochim. Cosmochim. Acta* **365**, 253–265.
- Kostoudi, S., and Pampalakis, G. (2022) Improvements, variations and biomedical applications of the Michaelis–Arbuzov reaction. *Int. J. Mol. Sci.* **23**, 3395.
- Kostyukevich, Y., Kononikhin, A., Popov, I., and Nikolaev, E. (2015) Letter: Observation of the  $^{16}\text{O}/^{18}\text{O}$  exchange during electrospray ionization. *Eur. J. Mass Spectrom.* **21**, 109–113.
- Kruve, A., and Kaupmees, K. (2017) Adduct formation in ESI/MS by mobile phase additives. *J. Am. Soc. Mass Spectrom.* **28**, 887–894.
- Krzycki, J. A., Kenealy, W. R., DeNiro, M. J., and Zeikus, J. G. (1987) Stable carbon isotope fractionation by *Methanosarcina barkeri* during methanogenesis from acetate, methanol, or carbon dioxide-hydrogen. *Appl. Environ. Microbiol.* **53**, 2597–2599.
- Kubinyi, H. (1991) Calculation of isotope distributions in mass spectrometry. A trivial solution for a non-trivial problem. *Anal. Chim. Acta* **247**, 107–119.
- Kuhlbusch, N., Hilker, A., Juchelka, D., and Kohl, I. (2023) Orbitrap Exploris Isotope Solutions: Using multiple microscans to enhance precision and accuracy for the ratios of minor isotopologues.
- Landais, A., Barkan, E., Yakir, D., and Luz, B. (2006) The triple isotopic composition of oxygen in leaf water. *Geochim. Cosmochim. Acta* **70**, 4105–4115.
- Langer, W. D., and Penzias, A. A. (1990) C-12/C-13 isotope ratio across the Galaxy from observations of C-13/O-18 in molecular clouds. *Astrophys. J.* **357**, 477–492.
- Lehmann, W. D. (1998) Isotope-selective tandem mass spectrometry: A new tool for elucidation of fragmentation pathways. *J. Mass Spectrom.* **33**, 164–172.



- Levy, M., and Miller, S. L. (1998) The stability of the RNA bases: Implications for the origin of life. *Proc. Natl. Acad. Sci.* **95**, 7933–7938.
- Levy, M., Miller, S. L., Brinton, K., and Bada, J. L. (2000) Prebiotic synthesis of adenine and amino acids under Europa-like conditions. *Icarus* **145**, 609–613.
- Li, L., Kresh, J. A., Karabacak, N. M., Cobb, J. S., Agar, J. N., and Hong, P. (2008) A hierarchical algorithm for calculating the isotopic fine structures of molecules. *J. Am. Soc. Mass Spectrom.* **19**, 1867–1874.
- Liu, Q., Tossell, J. A., and Liu, Y. (2010) On the proper use of the Bigeleisen–Mayer equation and corrections to it in the calculation of isotopic fractionation equilibrium constants. *Geochim. Cosmochim. Acta* **74**, 6965–6983.
- Liu, Z., Wu, L.-F., Xu, J., Bonfio, C., Russell, D. A., and Sutherland, J. D. (2020) Harnessing chemical energy for the activation and joining of prebiotic building blocks. *Nat. Chem.* **12**, 1023–1028.
- Lloyd, M. K., Eldridge, D. L., and Stolper, D. A. (2021) Clumped  $^{13}\text{CH}_2\text{D}$  and  $^{12}\text{CHD}_2$  compositions of methyl groups from wood and synthetic monomers: Methods, experimental and theoretical calibrations, and initial results. *Geochim. Cosmochim. Acta* **297**, 233–275.
- Lock, C. M., and Meier-Augenstein, W. (2008) Investigation of isotopic linkage between precursor and product in the synthesis of a high explosive. *Forensic Sci. Int.* **179**, 157–162.
- Londry, K. L., Dawson, K. G., Grover, H. D., Summons, R. E., and Bradley, A. S. (2008) Stable carbon isotope fractionation between substrates and products of *Methanosarcina barkeri*. *Org. Geochem.* **39**, 608–621.
- López-Sepulcre, A., Balucani, N., Ceccarelli, C., Codella, C., Dulieu, F., and Theulé, P. (2019) Interstellar formamide ( $\text{NH}_2\text{CHO}$ ), a key prebiotic precursor. *ACS Earth Space Chem.* **3**, 2122–2137.
- Lu, X., Zhang, Z., Gao, R., Wang, H., and Xiao, J. (2021a) Recent progress in the chemical attribution of chemical warfare agents and highly toxic organophosphorus pesticides. *Forensic Toxicol.* **39**, 334–349.
- Lu, X., Zhang, Z., Liu, H., Tang, H., Gao, R., Pei, C., Wang, H., and Xiao, J. (2021b) Forensic signatures of a chemical weapon precursor DMPADC for determination of a synthetic route. *Talanta* **232**, 122476.
- Luz, B., and Barkan, E. (2010) Variations of  $^{17}\text{O}/^{16}\text{O}$  and  $^{18}\text{O}/^{16}\text{O}$  in meteoric waters. *Geochim. Cosmochim. Acta* **74**, 6276–6286.
- Makarov, A. (2000) Electrostatic axially harmonic orbital trapping: A high-performance technique of mass analysis. *Anal. Chem.* **72**, 1156–1162.

- Makarov, A., and Denisov, E. (2009) Dynamics of ions of intact proteins in the Orbitrap mass analyzer. *J. Am. Soc. Mass Spectrom.* **20**, 1486–1495.
- Makarov, A., Denisov, E., Kholomeev, A., Balschun, W., Lange, O., Strupat, K., and Horning, S. (2006a) Performance evaluation of a hybrid linear ion trap/Orbitrap mass spectrometer. *Anal. Chem.* **78**, 2113–2120.
- Makarov, A., Denisov, E., Lange, O., and Horning, S. (2006b) Dynamic range of mass accuracy in LTQ orbitrap hybrid mass spectrometer. *J. Am. Soc. Mass Spectrom.* **17**, 977–982.
- Makarov, A., Denisov, E., Lange, O., Kholomeev, A., and Horning, S. (2005) Dynamic range of mass accuracy in FTMS. In *Proceedings of the 53rd ASMS Conference on Mass Spectrometry and Allied Topics*. San Antonio, TX.
- Marcus, R. K., Quarles, C. D. Jr., Barinaga, C. J., Carado, A. J., and Koppelaar, D. W. (2011) Liquid sampling-atmospheric pressure glow discharge ionization source for elemental mass spectrometry. *Anal. Chem.* **83**, 2425–2429.
- Marlier, J. F., Dopke, N. C., Johnstone, K. R., and Wirdzig, T. J. (1999) A heavy-atom isotope effect study of the hydrolysis of formamide. *J. Am. Chem. Soc.* **121**, 4356–4363.
- Marlier, J. F., and O’Leary, M. H. (1990) Carbon kinetic isotope effects on the hydrolysis of aryl carbonates. *J. Am. Chem. Soc.* **112**, 5996–5998.
- Martin, Peter Eckels (2019) Detection and analysis of Martian low-temperature geochemistry. Diss., California Institute of Technology. *CaltechTHESIS*.
- Martins, Z. (2011) Organic chemistry of carbonaceous meteorites. *Elements* **7**, 35–40.
- Martins, Z., Botta, O., Fogel, M. L., Sephton, M. A., Glavin, D. P., Watson, J. S., Dworkin, J. P., Schwartz, A. W., and Ehrenfreund, P. (2008) Extraterrestrial nucleobases in the Murchison meteorite. *Earth Planet. Sci. Lett.* **270**, 130–136.
- Masbou, J., Drouin, G., Payraudeau, S., and Imfeld, G. (2018) Carbon and nitrogen stable isotope fractionation during abiotic hydrolysis of pesticides. *Chemosphere* **213**, 368–376.
- Mastryukova, T. A., and Kabachnik, M. I. (1991) Enolisation of the phosphoryl group. *Russ. Chem. Rev.* **60**, 1115.
- Mccortney, B. A. (1986) Kinetics of the methyl-iodide catalyzed and autocatalyzed Arbuzov rearrangement (methoxyphosphonium, conductivity, phosphorus NMR). Diss., Rice University.
- McNaught, A. D., Wilkinson, A., and Chalk, S. J. eds. (1997) *IUPAC. Compendium of Chemical Terminology, 2nd ed. (the “Gold Book”)*, Blackwell Scientific Publications, Oxford.
- Meier, U. C. (2023) Forensic analysis of the deuterium/hydrogen isotopic ratios of the nerve agent sarin, its reaction by-product diisopropyl methylphosphonate and their precursors by 2H SNIF-NMR. *Talanta* **253**, 123890.

- Metcalf, W. W., Griffin, B. M., Cicchillo, R. M., Gao, J., Janga, S. C., Cooke, H. A., Circello, B. T., Evans, B. S., Martens-Habbena, W., Stahl, D. A., and van der Donk, W. A. (2012) Synthesis of methylphosphonic acid by marine microbes: A source for methane in the aerobic ocean. *Science* **337**, 1104–1107.
- Miller, M. F., and Pack, A. (2021) Why measure 17O? Historical perspective, triple-isotope systematics and selected applications. *Rev. Mineral. Geochem.* **86**, 1–34.
- Miyakawa, S., Cleaves, H. J., and Miller, S. L. (2002) The cold origin of life: B. Implications based on pyrimidines and purines produced From frozen ammonium cyanide solutions. *Orig. Life Evol. Biosph.* **32**, 209–218.
- Moran, J. J., Fraga, C. G., and Nims, M. K. (2018) Stable-carbon isotope ratios for sourcing the nerve-agent precursor methylphosphonic dichloride and its products. *Talanta* **186**, 678–683.
- Mueller, E. P., Sessions, A. L., Sauer, P. E., Weiss, G. M., and Eiler, J. M. (2022a) Simultaneous, high-precision measurements of  $\delta^2\text{H}$  and  $\delta^{13}\text{C}$  in nanomole quantities of acetate using electrospray ionization-quadrupole-Orbitrap mass spectrometry. *Anal. Chem.* **94**, 1092–1100.
- Mueller, E. P., Wu, F., and Sessions, A. L. (2022b) Quantifying Isotopologue Reaction Networks (QIRN): A modelling tool for predicting stable isotope fractionations in complex networks. *Chem. Geol.* **610**, 121098.
- Murray, K. K., Boyd, R. K., Eberlin, M. N., Langley, G. J., Li, L., and Naito, Y. (2013) Definitions of terms relating to mass spectrometry (IUPAC Recommendations 2013). *Pure Appl. Chem.* **85**, 1515–1609.
- Nelson, C. C., and McCloskey, J. A. (1992) Collision-induced dissociation of adenine. *J. Am. Chem. Soc.* **114**, 3661–3668.
- Neubauer, C., Crémière, A., Wang, X. T., Thiagarajan, N., Sessions, A. L., Adkins, J. F., Dalleska, N. F., Turchyn, A. V., Clegg, J. A., Moradian, A., Sweredoski, M. J., Garbis, S. D., and Eiler, J. M. (2020) Stable isotope analysis of intact oxyanions using electrospray quadrupole-Orbitrap mass spectrometry. *Anal. Chem.* **92**, 3077–3085.
- Neubauer, C., Sweredoski, M. J., Moradian, A., Newman, D. K., Robins, R. J., and Eiler, J. M. (2018) Scanning the isotopic structure of molecules by tandem mass spectrometry. *Int. J. Mass Spectrom.* **434**, 276–286.
- Okumura, T., Takasu, N., Ishimatsu, S., Miyanoki, S., Mitsuhashi, A., Kumada, K., Tanaka, K., and Hinohara, S. (1996) Report on 640 victims of the Tokyo subway sarin attack. *Ann. Emerg. Med.* **28**, 129–135.
- Olsen, J. V., Godoy, L. M. F. de, Li, G., Macek, B., Mortensen, P., Pesch, R., Makarov, A., Lange, O., Horning, S., and Mann, M. (2005) Parts per million mass accuracy on an Orbitrap mass spectrometer via lock mass injection into a C-trap. *Mol. Cell. Proteomics* **4**, 2010–2021.

- Ostrom, N. E., and Ostrom, P. H. (2012) The isotopomers of nitrous oxide: Analytical considerations and application to resolution of microbial production pathways. In *Handbook of Environmental Isotope Geochemistry: Vol I* (ed. M. Baskaran). Advances in Isotope Geochemistry. Springer, Berlin, Heidelberg. pp. 453–476.
- Pérez, T., Garcia-Montiel, D., Trumbore, S., Tyler, S., Camargo, P. de, Moreira, M., Piccolo, M., and Cerri, C. (2006) Nitrous oxide nitrification and denitrification  $^{15}\text{N}$  enrichment factors from amazon forest soils. *Ecol. Appl.* **16**, 2153–2167.
- Pita, R., and Domingo, J. (2014) The use of chemical weapons in the Syrian conflict. *Toxics* **2**, 391–402.
- Pizzarello, S. (2014) The nitrogen isotopic composition of meteoritic HCN. *Astrophys. J.* **796**, L25.
- Poirier, R. A., Wang, Y., and Westaway, K. C. (1994) A theoretical study of the relationship between secondary alpha-deuterium kinetic isotope effects and the structure of  $\text{SN}_2$  transition states. *J. Am. Chem. Soc.* **116**, 2526–2533.
- Primrose, S., Woolfe, M., and Rollinson, S. (2010) Food forensics: Methods for determining the authenticity of foodstuffs. *Trends Food Sci. Technol.* **21**, 582–590.
- Prokhorov, I., Kluge, T., and Janssen, C. (2019) Optical clumped isotope thermometry of carbon dioxide. *Sci. Rep.* **9**, 4765.
- Ramaley, L., and Herrera, L. C. (2008) Software for the calculation of isotope patterns in tandem mass spectrometry. *Rapid Commun. Mass Spectrom.* **22**, 2707–2714.
- Repeta, D. J., Ferrón, S., Sosa, O. A., Johnson, C. G., Repeta, L. D., Acker, M., DeLong, E. F., and Karl, D. M. (2016) Marine methane paradox explained by bacterial degradation of dissolved organic matter. *Nat. Geosci.* **9**, 884–887.
- Rockwood, A. L. (1995) Relationship of Fourier transforms to isotope distribution calculations. *Rapid Commun. Mass Spectrom.* **9**, 103–105.
- Rockwood, A. L., Kushnir, M. M., and Nelson, G. J. (2003) Dissociation of individual isotopic peaks: predicting isotopic distributions of product ions in  $\text{MS}^n$ . *J. Am. Soc. Mass Spectrom.* **14**, 311–322.
- Rockwood, A. L., and Palmblad, M. (2020) Isotopic distributions. In *Mass Spectrometry Data Analysis in Proteomics* (ed. R. Matthiesen). Methods in Molecular Biology. Springer, New York, NY. pp. 79–114.
- Rockwood, A. L., and Van Orden, S. L. (1996) Ultrahigh-speed calculation of isotope distributions. *Anal. Chem.* **68**, 2027–2030.
- Rockwood, A. L., Van Orden, S. L., and Smith, R. D. (1996) Ultrahigh resolution isotope distribution calculations. *Rapid Commun. Mass Spectrom.* **10**, 54–59.

- Rosberg, M., Lendle, W., Pfeleiderer, G., Tögel, A., Dreher, E.-L., Langer, E., Rassaerts, H., Kleinschmidt, P., Strack, H., Cook, R., Beck, U., Lipper, K.-A., Torkelson, T. R., Löser, E., Beutel, K. K., and Mann, T. (2006) Chlorinated hydrocarbons. In *Ullmann's Encyclopedia of Industrial Chemistry* John Wiley & Sons, Ltd.
- Rotelli, L., Trigo-Rodríguez, J. M., Moyano-Camero, C. E., Carota, E., Botta, L., Mauro, E. D., and Saladino, R. (2016) The key role of meteorites in the formation of relevant prebiotic molecules in a formamide/water environment. *Sci. Rep.* **6**, 1–7.
- Roussis, S. G., and Proulx, R. (2003) Reduction of chemical formulas from the isotopic peak distributions of high-resolution mass spectra. *Anal. Chem.* **75**, 1470–1482.
- Roy, D., Najafian, K., and von Ragué Schleyer, P. (2007) Chemical evolution: The mechanism of the formation of adenine under prebiotic conditions. *Proc. Natl. Acad. Sci.* **104**, 17272–17277.
- Rustad, J. R. (2009) Ab initio calculation of the carbon isotope signatures of amino acids. *Org. Geochem.* **40**, 720–723.
- Saladino, R., Botta, L., and Di Mauro, E. (2018) The prevailing catalytic role of meteorites in formamide prebiotic processes. *Life* **8**, 6.
- Saladino, R., Crestini, C., Cossetti, C., Di Mauro, E., and Deamer, D. (2011) Catalytic effects of Murchison Material: Prebiotic Synthesis and Degradation of RNA Precursors. *Orig. Life Evol. Biospheres* **41**, 437.
- Saladino, R., Crestini, C., Pino, S., Costanzo, G., and Di Mauro, E. (2012) Formamide and the origin of life. *Phys. Life Rev.* **9**, 84–104.
- Sanchez, R. A., Ferris, J. P., and Orgel, L. E. (1968) Studies in prebiotic synthesis: IV. Conversion of 4-aminoimidazole-5-carbonitrile derivatives to purines. *J. Mol. Biol.* **38**, 121–128.
- Sauer, P. E., Schimmelmann, A., Sessions, A. L., and Topalov, K. (2009) Simplified batch equilibration for D/H determination of non-exchangeable hydrogen in solid organic material. *Rapid Commun. Mass Spectrom.* **23**, 949–956.
- S. Burton, A., C. Stern, J., E. Elsila, J., P. Glavin, D., and P. Dworkin, J. (2012) Understanding prebiotic chemistry through the analysis of extraterrestrial amino acids and nucleobases in meteorites. *Chem. Soc. Rev.* **41**, 5459–5472.
- Schimmelmann, A., Sessions, A. L., and Mastalerz, M. (2006) Hydrogen isotopic (d/H) composition of organic matter during diagenesis and thermal maturation. *Annu. Rev. Earth Planet. Sci.* **34**, 501–533.
- Secretary-General, U. N. (2013) Report of the United Nations mission to investigate allegations of the use of chemical weapons in the Syrian Arab Republic on the alleged use of chemical weapons in the Ghouta area of Damascus on 21 August 2013. *Organisation for the Prohibition of Chemical Weapons/United Nations*.

- Sephton, M. A. (2002) Organic compounds in carbonaceous meteorites. *Nat. Prod. Rep.* **19**, 292–311.
- Shao, X., Ge, H., Li, Z., Ren, C., and Wang, J. (2015) Solubility of methylphosphonic acid in selected organic solvents. *Fluid Phase Equilibria* **390**, 7–13.
- Sharp, Z. (2017) Principles of stable isotope geochemistry, 2nd Edition. *Open Textb.*
- Sharp, Z. D., Atudorei, V., and Durakiewicz, T. (2001) A rapid method for determination of hydrogen and oxygen isotope ratios from water and hydrous minerals. *Chem. Geol.* **178**, 197–210.
- Shaw, Elliott. (1950) A new synthesis of the purines adenine, hypoxanthine, xanthine, and isoguanine. *J. Biol. Chem.* **185**, 439–447.
- Singleton, D. A., Merrigan, S. R., Beno, B. R., and Houk, K. N. (1999) Isotope effects for Lewis acid catalyzed Diels-Alder reactions. The experimental transition state. *Tetrahedron Lett.* **40**, 5817–5821.
- Singleton, D. A., and Szymanski, M. J. (1999) Simultaneous determination of intermolecular and intramolecular  $^{13}\text{C}$  and  $^2\text{H}$  kinetic isotope effects at natural abundance. *J. Am. Chem. Soc.* **121**, 9455–9456.
- Singleton, D. A., and Thomas, A. A. (1995) High-precision simultaneous determination of multiple small kinetic isotope effects at natural abundance. *J. Am. Chem. Soc.* **117**, 9357–9358.
- Singleton, K. E., Cooks, R. Graham., and Wood, K. V. (1983) Utilization of natural isotopic abundance ratios in tandem mass spectrometry. *Anal. Chem.* **55**, 762–764.
- Slavova, S., and Enchev, V. (2020) Self-catalytic mechanism of prebiotic reactions: From formamide to purine bases. *Int. J. Quantum Chem.* **120**, e26362.
- Sleno, L. (2012) The use of mass defect in modern mass spectrometry. *J. Mass Spectrom.* **47**, 226–236.
- Smart, J. K. (1997) History of chemical and biological warfare: An American perspective. In *Medical Aspects of Chemical and Biological Warfare* (eds. F. R. Sidell, E. T. Takafuji, and D. R. Franz). Office of the Surgeon General, Washington DC.
- Snider, R. K. (2007) Efficient calculation of exact mass isotopic distributions. *J. Am. Soc. Mass Spectrom.* **18**, 1511–1515.
- Šponer, J. E., Mládek, A., Šponer, J., and Fuentes-Cabrera, M. (2012) Formamide-based prebiotic synthesis of nucleobases: A kinetically accessible reaction route. *J. Phys. Chem. A* **116**, 720–726.

- Stolper, D. A., Sessions, A. L., Ferreira, A. A., Santos Neto, E. V., Schimmelmann, A., Shusta, S. S., Valentine, D. L., and Eiler, J. M. (2014) Combined  $^{13}\text{C}$ -D and D-D clumping in methane: Methods and preliminary results. *Geochim. Cosmochim. Acta* **126**, 169–191.
- Strong, M. (2012) Variations in the stable isotope compositions of water vapor and precipitation in New Mexico: Links to synoptic-scale weather. *Earth Planet. Sci. ETDs*.
- Sutherland, J. D. (2016) The origin of life—Out of the blue. *Angew. Chem. Int. Ed.* **55**, 104–121.
- Taenzer, L., Carini, P. C., Masterson, A. M., Bourque, B., Gaube, J. H., and Leavitt, W. D. (2020) Microbial methane from methylphosphonate isotopically records source. *Geophys. Res. Lett.* **47**, e2019GL085872.
- Taenzer, Lina, Labidi, J., Masterson, A. L., Feng, X., Rumble, D., Young, E. D., and Leavitt, W. D. (2020) Low  $\Delta^{12}\text{CH}_2\text{D}_2$  values in microbialgenetic methane result from combinatorial isotope effects. *Geochim. Cosmochim. Acta* **285**, 225–236.
- Tagami, K., and Uchida, S. (2008) Online stable carbon isotope ratio measurement in formic acid, acetic acid, methanol and ethanol in water by high performance liquid chromatography–isotope ratio mass spectrometry. *Anal. Chim. Acta* **614**, 165–172.
- Taylor, J. (1997) Introduction to Error Analysis, the Study of Uncertainties in Physical Measurements, 2nd Edition. *University Science Books*.
- Toy, A. D. F., Forest, P., and Uhing, E. H. (1963) Method of Producing Methylphosphonic Acid and Derivatives. US3110727A.
- Toyoda, S., Kuroki, N., Yoshida, N., Ishijima, K., Tohjima, Y., and Machida, T. (2013) Decadal time series of tropospheric abundance of  $\text{N}_2\text{O}$  isotopomers and isotopologues in the Northern Hemisphere obtained by the long-term observation at Hateruma Island, Japan. *J. Geophys. Res. Atmospheres* **118**, 3369–3381.
- Toyoda, S., Yoshida, N., and Koba, K. (2017) Isotopocule analysis of biologically produced nitrous oxide in various environments. *Mass Spectrom. Rev.* **36**, 135–160.
- Tu, A. T. (2007) Toxicological and chemical aspects of Sarin terrorism in Japan in 1994 and 1995. *Toxin Rev.* **26**, 231–274.
- Uhing, E., Rattenbury, K., and Toy, A. D. F. (1961) Chemistry of chloromethylphosphinic acid. I. Preparation and alkaline hydrolysis. *ACS Publ.*
- Urey, H. C. (1947) The thermodynamic properties of isotopic substances. *J. Chem. Soc. Resumed*, 562–581.
- U.S. Army Chemical Materials Activity (2016) Recovered chemical materiel directorate fact sheet on former production facilities demolition. *Recovered Chemical Material Directorate Fact Sheet*.

- Valkenburg, D., Mertens, I., Lemière, F., Witters, E., and Burzykowski, T. (2012) The isotopic distribution conundrum. *Mass Spectrom. Rev.* **31**, 96–109.
- Van Stipdonk, M., Anbalagan, V., Chien, W., Gresham, G., Groenewold, G., and Hanna, D. (2003) Elucidation of the collision induced dissociation pathways of water and alcohol coordinated complexes containing the uranyl cation. *J. Am. Soc. Mass Spectrom.* **14**, 1205–1214.
- Vanninen, P., Lignell, H., Heikkinen, H. A., Kiljunen, H., Silva, O. S., Aalto, S. A., and Kauppila, T. J. (2020) Chemical forensics. In *21st Century Prometheus: Managing CBRN Safety and Security Affected by Cutting-Edge Technologies* (eds. M. Martellini and R. Trapp). Springer International Publishing, Cham. pp. 255–286.
- Wang, J., Gu, J., Nguyen, M. T., Springsteen, G., and Leszczynski, J. (2013a) From formamide to adenine: A self-catalytic mechanism for an abiotic approach. *J. Phys. Chem. B* **117**, 14039–14045.
- Wang, J., Gu, J., Nguyen, M. T., Springsteen, G., and Leszczynski, J. (2013b) From formamide to purine: A self-catalyzed reaction pathway provides a feasible mechanism for the entire process. *J. Phys. Chem. B* **117**, 9333–9342.
- Wang, J., Gu, J., Nguyen, M. T., Springsteen, G., and Leszczynski, J. (2013c) From formamide to purine: An energetically viable mechanistic reaction pathway. *J. Phys. Chem. B* **117**, 2314–2320.
- Wang, Y., Sessions, A. L., Nielsen, R. J., and Goddard, W. A. (2009) Equilibrium 2H/1H fractionations in organic molecules. II: Linear alkanes, alkenes, ketones, carboxylic acids, esters, alcohols and ethers. *Geochim. Cosmochim. Acta* **73**, 7076–7086.
- Wang, Z., Schauble, E. A., and Eiler, J. M. (2004) Equilibrium thermodynamics of multiply substituted isotopologues of molecular gases. *Geochim. Cosmochim. Acta* **68**, 4779–4797.
- Weber, T., Wiseman, N. A., and Kock, A. (2019) Global ocean methane emissions dominated by shallow coastal waters. *Nat. Commun.* **10**, 4584.
- Weiss, G. M., Sessions, A. L., Julien, M., Csernica, T., Yamada, K., Gilbert, A., Freeman, K. H., and Eiler, J. M. (2023) Analysis of intramolecular carbon isotope distributions in alanine by electrospray ionization Orbitrap mass spectrometry. *Int. J. Mass Spectrom.* **493**, 117128.
- Westaway, K. C. (2007) Determining transition state structure using kinetic isotope effects. *J. Label. Compd. Radiopharm.* **50**, 989–1005.
- Wilkes, E. B., Sessions, A. L., Zeichner, S. S., Dallas, B., Schubert, B., Jahren, A. H., and Eiler, J. M. (2022) Position-specific carbon isotope analysis of serine by gas chromatography/Orbitrap mass spectrometry, and an application to plant metabolism. *Rapid Commun. Mass Spectrom.* **36**, e9347.



- Yadav, M., Kumar, R., and Krishnamurthy, R. (2020) Chemistry of abiotic nucleotide synthesis. *Chem. Rev.* **120**, 4766–4805.
- Yergey, J. A. (1983) A general approach to calculating isotopic distributions for mass spectrometry. *Int. J. Mass Spectrom. Ion Phys.* **52**, 337–349.
- Yeung, L. Y. (2016) Combinatorial effects on clumped isotopes and their significance in biogeochemistry. *Geochim. Cosmochim. Acta* **172**, 22–38.
- Yeung, L. Y., Affek, H. P., Hoag, K. J., Guo, W., Wiegel, A. A., Atlas, E. L., Schauffler, S. M., Okumura, M., Boering, K. A., and Eiler, J. M. (2009) Large and unexpected enrichment in stratospheric  $^{16}\text{O}^{13}\text{C}^{18}\text{O}$  and its meridional variation. *Proc. Natl. Acad. Sci.* **106**, 11496–11501.
- Yeung, L. Y., Ash, J. L., and Young, E. D. (2015) Biological signatures in clumped isotopes of  $\text{O}_2$ . *Science* **348**, 431–434.
- Yeung, L. Y., Li, S., Kohl, I. E., Haslun, J. A., Ostrom, N. E., Hu, H., Fischer, T. P., Schauble, E. A., and Young, E. D. (2017) Extreme enrichment in atmospheric  $^{15}\text{N}^{15}\text{N}$ . *Sci. Adv.* **3**, eaao6741.
- Zeichner, S. S., Aponte, J. C., Bhattacharjee, S., Dong, G., Hofmann, A. E., Dworkin, J. P., Glavin, D. P., Elsila, J. E., Graham, H. V., Naraoka, H., Takano, Y., Tachibana, S., Karp, A. T., Grice, K., Holman, A. I., Freeman, K. H., Yurimoto, H., Nakamura, T., Noguchi, T., Okazaki, R., Yabuta, H., Sakamoto, K., Yada, T., Nishimura, M., Nakato, A., Miyazaki, A., Yogata, K., Abe, M., Okada, T., Usui, T., Yoshikawa, M., Saiki, T., Tanaka, Satoshi, Terui, F., Nakazawa, S., Watanabe, S., Tsuda, Y., Hamase, K., Fukushima, K., Aoki, D., Hashiguchi, M., Mita, H., Chikaraishi, Y., Ohkouchi, N., Ogawa, N. O., Sakai, S., Parker, E. T., McLain, H. L., Orthous-Daunay, F.-R., Vuitton, V., Wolters, C., Schmitt-Kopplin, P., Hertkorn, N., Thissen, R., Ruf, A., Isa, J., Oba, Y., Koga, T., Yoshimura, T., Araoka, D., Sugahara, H., Furusho, A., Furukawa, Y., Aoki, J., Kano, K., Nomura, S. M., Sasaki, K., Sato, H., Yoshikawa, T., Tanaka, Satoru, Morita, M., Onose, M., Kabashima, F., Fujishima, K., Yamazaki, T., Kimura, Y., and Eiler, J. M. (2023a) Polycyclic aromatic hydrocarbons in samples of Ryugu formed in the interstellar medium. *Science* **382**, 1411–1416.
- Zeichner, S. S., Chimiak, L., Elsila, J. E., Sessions, A. L., Dworkin, J. P., Aponte, J. C., and Eiler, J. M. (2023b) Position-specific carbon isotopes of Murchison amino acids elucidate extraterrestrial abiotic organic synthesis networks. *Geochim. Cosmochim. Acta* **355**, 210–221.
- Zeichner, S. S., Wilkes, E. B., Hofmann, A. E., Chimiak, L., Sessions, A. L., Makarov, A., and Eiler, J. M. (2022) Methods and limitations of stable isotope measurements via direct elution of chromatographic peaks using gas chromatography-Orbitrap mass spectrometry. *Int. J. Mass Spectrom.* **477**, 116848.
- Zhang, P., Chan, W., Ang, I. L., Wei, R., Lam, M. M. T., Lei, K. M. K., and Poon, T. C. W. (2019) Revisiting fragmentation reactions of protonated  $\alpha$ -amino acids by high-resolution

electrospray ionization tandem mass spectrometry with collision-induced dissociation.  
*Sci. Rep.* **9**, 6453.